Non-Covalent Interactions in the Design and Performance of Macromolecules for Biological Technologies

Allison Marie Pekkanen

Dissertation submitted to the faculty of the Virginia Polytechnic Institute and State University in partial fulfillment of the requirements for the degree of

Doctor of Philosophy
In
Biomedical Engineering

Timothy E. Long (Chair)
M. Nichole Rylander
Christopher B. Williams
Abby R. Whittington
Rong Tong

April 25, 2017
Blacksburg, VA

Keywords: Nanoparticle Modification, Polymer Chemistry, Biomaterials, Supramolecular Interactions

Non-Covalent Interactions in the Design and Performance of Macromolecules for Biological Technologies

Allison M. Pekkanen

Abstract

Supramolecular, or non-covalent, interactions remain a hallmark of biological systems, dictating biologic activity from the structure of DNA to protein folding and cell-substrate interactions. Harnessing the power of supramolecular interactions commonly experienced in biological systems provides numerous functionalities for modifying synthetic materials. Hydrogen bonding, ionic interactions, and metal-ligand interactions highlight the supramolecular interactions examined in this work. Their broad utility in the fields of nanoparticle formulations, polymer chemistry, and additive manufacturing facilitated the generation of numerous biological materials.

Metal-ligand interactions facilitated carbon nanohorn functionalization with quantum dots through the zinc-sulfur interaction. The incorporation of platinum-based chemotherapeutic cisplatin generated a theranostic nanohorn capable of real-time imaging and drug delivery concurrent with photothermal therapies. These nanoparticles remain non-toxic without chemotherapy, providing patient-specific. Furthermore, metal-ligand interactions proved vital to retaining quantum dots on nanoparticle surfaces for up to three days, both limiting their toxicity and enhancing their imaging potential.

Controlled release of biologics remain highly sought-after, as they remain widely regarded as next-generation therapeutics for a number of diseases. Geometry-controlled release afforded by additive manufacturing advances next-generation drug delivery solutions. Poly(ether ester) ionomers composed of sulfonated isophthalate and poly(ethylene glycol) provided polymers well suited for low-temperature material

extrusion additive manufacturing. Ionic interactions featured in the development of these ionomers and proved vital to their ultimate success to print from filament. Contrary to ionic interactions, hydrogen bonding ureas coupled poly(ethylene glycol) segments and provided superior mechanical properties compared to ionic interactions. Furthermore, the urea bond linking together poly(ethylene glycol) chains proved fully degradable over the course of one month in solution with urease. The strength of these supramolecular interactions demanded further examination in the photopolymerization of monofunctional monomers to create free-standing films. Furthermore, the incorporation of both hydrogen bonding acrylamides and ionic groups provided faster polymerization times and higher moduli films upon light irradiation. Vat photopolymerization additive manufacturing generated 3-dimensional parts from monofunctional monomers. These soluble parts created from additive manufacturing provide future scaffolds for controlled release applications. Controlled release, whether a biologic or chemotherapeutic, remains a vital portion of the biomedical sciences and supramolecular interactions provides the future of materials for these applications.

Non-Covalent Interactions in the Design and Performance of Macromolecules for Biological Technologies

Allison M. Pekkanen

General Audience Abstract

Biology remains the unprecedented expert in the manipulation of non-covalent (or supramolecular) interactions to maintain structure and function. As an example, the structure of DNA maintains many hydrogen bonding units which allow for dynamic reading of genetic material but retain its characteristic structure. Proteins, made from linear chains of amino acids, utilize these interactions to fold into conformations necessary for their function. Harnessing these interactions in the creation of next-generation materials lies at the center of this work.

Metal-sulfur bonds highlight initial work to encapsulate both drug and imaging agent onto a carbon nanoparticle. This complex revealed favorable biocompatibility and the ability to deliver drug in the elimination of bladder cancer cells *in vitro*. Furthermore, the complex revealed the maintenance of imaging capabilities over many days and continued to release low levels of chemotherapeutic during this time, potentially eradicating cancer cells long after initial treatment. Utilizing this nanoparticle, clinicians can monitor the location of nanoparticles in real-time and tailor doses specific to each patient.

Ionic interactions provided enhanced mechanical properties of both water-soluble and water-insoluble polymers. The water-soluble polymers experienced significantly increased melt viscosity upon the addition of divalent cations, potentially creating non-covalent crosslinks in the molten state. Water-insoluble polymers acted as effective biological adhesives, likely arising from the interaction of ionic groups with its

surrounding environment. Hydrogen bonding functioned to increase the mechanical integrity of water-soluble polymers for enhanced processing. The incorporation of urea groups into water-soluble polymers provided a readily available nitrogen source for plant growth while eliminating potential downstream environmental toxicity. Urethane functionality, generated with biologically-friendly byproducts, also provided hydrogen bonding to improve mechanical integrity of water-soluble polymers.

Traditionally, stereolithography 3D printing demanded the use of covalent (or permanent) crosslinking to generate 3D shapes. Hydrogen bonding and ionic interactions coupled together to provide rapidly-formed free-standing films held together only through non-covalent interactions. Comparison of hydrogen bonding, ionic bonding, and both together provided insights onto the kinetics and strength of these films. These interactions proved strong enough to generate well-defined 3D structures through 3D printing. Furthermore, these parts proved water-soluble after fully forming, proving the reversibility of these bonds.

Biologically-inspired interactions drive the future of materials research, and harnessing these interactions provides a better-performing material. Probing new materials for controlled release applications utilizing reversible interactions provided new families of ionic and hydrogen-bonding polymers. Whether soluble or insoluble, biological or not, these interactions pave the way to increase mechanical integrity of commonplace materials with the added reversibility hallmark of supramolecular interactions.

Acknowledgements

Firstly, I would like to thank my two advisors, Dr. Timothy E. Long and Dr. M. Nichole Rylander for their guidance throughout my graduate school career. Dr. Rylander brought me to Virginia Tech and provided support for my first two years of graduate school. I owe the ability to earn this degree to her faith in my skills coming out of my undergraduate career and for that I am extremely grateful. After Dr. Rylander moved back to Texas, I was fortunate yet again to be "adopted" by Dr. Long and his research group. Although the transition was difficult at the onset, I have grown immensely through working with Dr. Long and his group. With Dr. Long's guidance, I have blossomed into a unique researcher whose skills vary greatly from my peers and for that I am also eternally grateful. I have also gotten very lucky in the wonderful collaborators that I've had the opportunity to work with at Virginia Tech. Dr. Christopher B. Williams is unrivaled in his expertise in the world of additive manufacturing and has taught me everything I know in the area. Dr. Abby B. Whittington leads a fantastic group in Materials Science and Engineering and who has guided my learning in the area of enzyme structure and chemistry. I would also like to thank Dr. Stefan Duma for admitting me into the School of Biomedical Engineering and Science at Virginia Tech and encouraging my diverse graduate school experience.

I have had the great pleasure to work alongside fantastic lab-mates throughout my graduate school career. First, Matt DeWitt who was my partner in crime in the Rylander lab. We schemed and worked on many a project together during my first two years of graduate school. Manasa Gadde and Brittany Balhouse also helped out tremendously as

we navigated classes and the research group together. Upon my transition to Dr. Long's lab, I found another great friend and labmate in Ashley Nelson. Even though I only got one year with Ashley, she taught me everything I now know about polymer science and chemistry and I was fortunate to work directly with her on a project. She has also mentored me tremendously even after she left Virginia Tech about life, jobs, and research in general. Ryan Mondschein has remained my best friend in the research group for the past few years through every research talk, project, and as we transition into full writing mode. His brilliance and ability to bounce ideas off of was extremely important to my success in Dr. Long's group and I wish we had all the time in the world to execute even half of the ideas we've come up with. Evan Margaretta, who I was fortunate to work with on a funded project, also taught me a lot about dissertation writing in the final semester of his graduate school career. Finally, Joeseph Dennis has been a fabulous lab mate and whose intelligence is unrivaled. I've been extremely fortunate to work with him over the past few years. Others in the lab group, Katherine Valentine, Emily Wilts, Dr. Nicholas Moon, Dr. Maruti Hegde, Kevin Drummey, Mingtao Chen, and Philip Scott provided so many helpful discussions and ideas that I cannot count. I've also been extremely fortunate to work with other collaborators across campus, including Lindsey Anderson, Christopher Winkler, Steve McCartney, and Athena Tilley.

There are many other people behind the scenes who have also provided my support throughout my graduate career. Brent Bowden and Kristin Dorfler have made questions and issues seem like absolutely nothing in their infinite wisdom and calendar prowess. They've helped me through so many administrative hiccups throughout my time in Dr. Long's group. Tess Sentelle and Pam Stiff in the biomedical engineering

department have provided me with so much support during recruitment weekends and especially during my tenure as president of the Biomedical Engineering Society. They were instrumental to the execution of the 2015 SBES Graduate Student Symposium and I absolutely could not have done it without them. Tammy Jo Hiner in the Macromolecules Innovation Institute provided more than just administrative support, she became a trusted advisor throughout our overlap in Dr. Long's group. To all the other people in the Biomedical Engineering, Chemistry, and Macromolecules Innovation Institute departments at Virginia Tech, thank you so much for all your hard work!

I have been fortunate to work on projects funded by Proctor and Gamble, Align Technologies, Techulon, Inc., the National Institute of Health, and the National Science Foundation throughout my tenure at Virginia Tech. I was also extremely fortunate to receive the PEO International Women's Fellowship in my fourth year to help support me as I finished my graduate studies. These great funding partners were instrumental to the success I experienced on many of these projects. Specifically, Denis Guenette and Nrusingh Mohapatra at Techulon, Inc., Travis Hodgdon, Douglas Graham, Freddy Barnabas and Corey Kenneally at Proctor and Gamble were instrumental to each of the project's success and for that I am grateful.

Blacksburg has been very kind to me over the past five years and has provided me with many friendships that I will always treasure. Firstly, to Matt, Kelly, Anna, and Hudson Beeken who have supported me throughout my five years in Blacksburg and who have truly served as a second family to me. To everyone at Blacksburg United Methodist Church who lent me support and a helping hand when I needed, I am eternally grateful. Lindsey Anderson, you are more than just a collaborator, you are a true friend. You've

been there for me through some tough times (and tough workout classes!) and I always know that you'll save me a seminar seat! Megan Cox, I always know that I can come spend a few hours in the Verbridge lab getting lost on class assignments and talking about all the lab drama. And to everyone else on the 3rd floor of Kelly Hall, you have all been a tremendous part of my success at Virginia Tech.

To my family who supported me in my move to Virginia Tech five years ago and who have never stopped supporting me no matter what, I love you and I thank you. To my mom, Cindy Pekkanen who taught me so much about learning and what it means to be a good person. She has supported me in absolutely everything that I do and always told me to push myself as far as I can go. To my dad, Alan Pekkanen, I can't stress how much I love that you embody the typical electrical engineer. I love the pocket protector most of all ☺. You and mom have taught me so much about life and take the full credit for everything that I accomplish in life. I owe you everything! And to my baby brother Kyle, you wouldn't believe how proud I am of everything you do (like moving out!). You're going to do great things following in dad's footsteps and I hope I can convince you to move out here one day so that we can be closer! To the rest of my grandparents, Mary Lou and Lincoln Dearth and Vivian and Leo Pekkanen (who are always with me in spirit!), I can't express how much I value time that we have spent together and the support you've given me. To my aunts and uncles: Debbie and Terry Palmer, Cheryl and Roger Ritton, Bruce Dearth, Mark and Amy Spiegel, and Kathie and Willis Korb, you have all encouraged me so much in my five years at Virginia Tech. And to all my cousins: Jon, Kim, and Cameron Palmer, Andrew Palmer and TJ Alsept, Alex Ritton, Alex and Garrett Spiegel, and Kip, Holly, and Kelly Korb, growing up with all of you has

most definitely made me into the person I am today. To my whole family, I could do nothing without you!

Finally, and greatest of all, I have to thank my partner-in-life Matt Morgan. You came into my life in a great storm and I thank God every day that you did. You cheer me up when I have a bad day, make me laugh at every turn, and have been completely instrumental in helping me finish these last couple of years. I always know that you'll be there for me in a time of need and I know that we can celebrate all of the best things in life together. Without you, my sweet honey, I wouldn't have anything in this world and I can't wait to see where our lives take us. I also have to give a shout out to little Burt, who you've trained into a snuggling machine with so much personality. You (and Lucky and Burt, but only a little) are the only reasons I come home at night. You've also brought so many wonderful people into my life whom I adore: your mom Donna Farmer, your grandma Sylvia, and your awesome sisters and brother Madison and Haley Farmer and Nick Morgan. They have kept me sane this past year and helped me remember that there is a great life beyond graduate school! Your aunt and grandma Linda and Alma Morgan, along with your dad Mark Morgan are all amazing and I am so lucky to have them in my life too. Matt, I wouldn't be here without your love and support and I only hope that one day I can repay you with all the love I have to give ☺.

I know there are many more friends and classmates that have guided me throughout my graduate career than I can ever count. I thank everyone who has helped me during my time at Virginia Tech. To all of you, I am forever grateful. I could never have done this without any of you!

Attributions

Professor Timothy E. Long
Professor of Chemistry and Research Advisor

Professor M. Nichole Rylander
Associate Professor of Mechanical Engineering, The University of Texas at Austin, Research Advisor

Professor Christopher B. Williams
Associate Professor of Mechanical Engineering and collaborator on Chapters 4, 6, and 9

Professor Abby R. Whittington
Associate Professor of Materials Science and Engineering and Chemical Engineering and collaborator on Chapter 6

Professor Robert B. Moore
Professor of Chemistry and collaborator on Chapters 7 and 8

Chapter 2

Matthew R. DeWitt: Graduate student in Dr. M. Nichole Rylander's group who wrote the sections entitled "Photodynamic Therapies", "Photoacoustic Therapies" and "Photo-triggered Drug Release"

Chapter 3

Matthew R. DeWitt: Graduate student in Dr. M. Nichole Rylander's group who aided in experiment design and collected 12 h time points for drug release.

David B. Geohegan, Ph.D.: Researcher at Oak Ridge National Labs who provided the nanohorns used for the study.

Andrew Giordani: Graduate student in Materials Science and Engineering who performed XPS experiments.

Christopher Winkler: Instrument specialist at the Institute of Critical Technologies and Applied Sciences who collected images and EDS spectra for TEM studies.

Athena Tilley: ICP Spectroscopist in the Department of Crop and Soil Environmental Sciences who analyzed platinum content of water in drug release samples.

Chapter 5

Ryan J. Mondschein: Graduate student in Dr. Timothy E. Long's group who and myself performed all experimental design, peptide design, and collected data together. The work fully embodies the requirements of a co-first author.

Steve McCartney: Instrument specialist at the Institute of Critical Technologies and Applied Sciences who performed scanning electron microscopy on all fabric samples.

Andrew Giordani: Graduate student in Materials Science and Engineering who performed XPS experiments.

Nrusingh Mohapatra and Denis Guenette: Researchers at Techulon, Inc. who aided in the experimental design.

Chapter 6

Callie Zawaski: Graduate student in Dr. Christopher B. Williams's group who performed all material extrusion experiments.

Andre T. Stevenson: Graduate student in Dr. Abby R. Whittington's group who developed and executed protocols to determine dissolution rate of all polymers.

Ross Dickerman: Undergraduate student in Dr. Abby R. Whittington's group who developed and executed protocols to determine dissolution rate of all polymers.

Chapter 7

Kilian Horatz: Summer researcher under the direction of Timothy E. Long who synthesized and analyzed all PCL-containing ionomers.

Kevin Drummey: Graduate student in Dr. Timothy E. Long's group who performed peel testing of target PCL samples.

Samantha Talley: Graduate student in Dr. Robert Moore's group who performed small angle X-ray scattering on polymer films.

Chapter 8

Joseph M. Dennis: Graduate student in Dr. Timothy E. Long's group who aided in the experimental design and execution of polymer synthesis.

Lindsey J. Anderson: Graduate student in Dr. Robert B. Moore's group who performed variable temperature FTIR and conducted data analysis of resulting spectra.

Ryan J. Mondschein: Graduate student in Dr. Timothy E. Long's group who aided in the collection of ammonia release data and in the presentation of data.

Chapter 9

Emily M. Wilts: Graduate student in Dr. Timothy E. Long's group who performed dissolution experiments for all photopolymerized gels.

Donald A. Aduba, Ph.D.: Postdoctoral researcher in Dr. Christopher B. William's group who performed vat photopolymerization additive manufacturing of target ionic monomers.

Chapter 10

Emily M. Wilts: Graduate student in Dr. Timothy E. Long's group who aided in the synthesis and characterization of isocyanate-free polyurethanes.

Ryan J. Mondschein: Graduate student in Dr. Timothy E. Long's group who aided in refining experimental parameters to increase molecular weight of resulting polyurethanes.

Joseph M. Dennis: Graduate student in Dr. Timothy E. Long's group who aided in experimental design.

Table of Contents

Chapter 1. Introduction

1.1 Dissertation Overview

This work details the synthesis and characterization of nanomaterials and polymers containing non-covalent interactions for biological applications. Chapter 2 reviews the state of light interactions with nanomaterials, leading into Chapter 3 which describes the modification of a carbon-based nanomaterials. Chapter 4 introduces non-covalent interactions in polymers. Chapter 5 describes the role of peptides in coating of blended fabrics and a method of analysis. Chapters 6, 7, 8, and 10 detail the varied modification of poly(ethylene glycol) (PEG) or polycaprolactone for varied biological applications. Chapter 9 describes the use of combined ionic and hydrogen bonding interactions in the creation of soluble 3D parts generated by vat photopolymerization. Finally, Chapter 11 provides potential areas for future discovery.

Chapter 3 begins with a focus on zinc-sulfur interactions to effectively immobilize quantum dots onto carbon nanohorn surfaces. Simultaneously, cisplatin (a commonly used chemotherapeutic) is sequestered into nanohorn interiors to create a nanoparticle which acts as both an imaging agent and drug delivery vehicle. Coupling of analytical techniques to characterize the nanoparticle and *in vitro* testing to evaluate the drug delivery effectiveness highlighted the utility of this nanoparticle formulation. This novel nanoparticle enables future discovery as an *in vivo* bladder cancer agent to deliver both drug and, in concert with light irradiation, thermal treatment while acting as an imaging agent for real-time clinician feedback.

Chapter 5 details the coating of a small peptide onto the surface of Nylon/Cotton blended fabric as a model for peptide nucleic acid release. Design of the model peptide

included functional handles for analysis via UV-Vis spectroscopy (Phenylalanine) and elemental analysis (Cysteine). Significant characterization of peptide coatings served as a model of coating and release from these fabrics. Scanning electron microscopy proved useful in the characterization of surface roughness dictated by the peptide coating, a direct translation to peptide nucleic acid coatings onto fibers.

Ionic interactions in the polymeric properties of poly(ethylene glycol) (Chapter 6) and polycaprolactone (Chapter 7) reveal enhanced polymeric properties. Poly(ethylene glycol) polymerized alongside sulfonated isophthalate revealed a stark increase in melt viscosity upon successful incorporation. Ion exchange to a variety of monovalent and divalent cations provided a fundamental understanding of low levels of ion incorporation on changes in melt viscosity and thermomechanical properties. The calcium realization of these polymers proved useful in the creation of filament and subsequent material extrusion at low temperature, suitable for the incorporation of biological active ingredients. Polycaprolactone synthesized in a similar manner provided a water-insoluble analog to PEG. These polymers exhibited significant increases in melt viscosity upon ion incorporation and surprising tensile and compressive forces characteristic of ionic associations. These polymers proved useful as biological adhesives, exhibiting favorable cell attachment and peel strength at biological temperatures.

Hydrogen bonding in PEG, highlighted through the generation of low concentrations of either urea (Chapter 8) or urethane (Chapter 10), provided a direct comparison of polymer properties as a result of these supramolecular interactions. The urea group, introduced through melt polycondensation without solvent or catalyst, provided high molecular weight, water-soluble polyureas which exhibited significantly

increased melt viscosities. A series of these polymers probed the effect of weight percent urea on thermomechanical properties. These polyureas served as effective sources of nitrogen, degrading up to 100 % upon incubation with urease in solution after only one month. Polyurethanes, generated through reactions with carbonyldiimidazole, avoiding toxic isocyanate reagents, and resulting in only imidazole byproducts, provided an additional indication of low levels of hydrogen bonding on polymer properties. While these polymers fail to exhibit the mechanical properties observed by either ureas or ionic interactions, they provide a facile method for creating isocyanate-free polyurethanes.

Chapter 9 details the combination of ionic and hydrogen bond interactions in the creation of water-soluble 3D structures created from vat photopolymerization. Screening of varied monomer structure provided a metric for examining the role of supramolecular interactions on the resulting mechanical properties of the part. Interestingly, crystallinity in these parts also provides free-standing films which fail to dissolve in water. The reversibility of the supramolecular interactions provided water-solubility in these 3D structures.

Finally, Chapter 11 provides new avenues of current and future research of the role supramolecular interactions on polymer properties. The creation of biodegradable tissue scaffolds from PEG-PLGA copolymers provides a way to induce tissue regeneration while simultaneously releasing non-toxic byproducts of degradation. The utility of the urea and CDI reactions remains relatively unknown in the creation of high molecular weight polymers, providing significant framework in the creation of new materials.

Chapter 2. Nanoparticle Enhanced Optical Imaging and Phototherapy of Cancer

(Published in Journal of Biomedical Nanotechnology, **2014**, **10**(9), 1677-1712)

Allison M Pekkanen[†]*, Matthew R. DeWitt*[†]*, Marissa Nichole Rylander*[1]
[†]These authors contributed equally to the work.

[1]School of Biomedical Engineering and Sciences, Virginia Tech, Blacksburg, VA 24061

Keywords: Cancer, drug delivery, nanoparticles, photoacoustic therapy, photodynamic therapy, photothermal therapy, quantum dots, SERS

2.1 Abstract

Nanoparticle research has seen advances in many fields, including the imaging and treatment of cancer. Specifically, nanotechnology has been investigated for its potential to be used as a tool to deliver well-tested drugs in potentially safer concentrations through both passive and active tumor targeting, while additionally providing means for a secondary therapy or imaging contrast. In particular, the use of light in conjunction with nanoparticle-based imaging and therapies has grown in popularity in recent years due to advances in utilizing light energy. In this review, we will first discuss nanoparticle platforms that can be used for optical imaging of cancer, such as fluorescence generation with quantum dots and surface-enhanced Raman scattering with plasmonic nanoparticles. We then analyze nanoparticle therapies, including photothermal therapy, photodynamic therapies, and photoacoustic therapy and their differences in exploiting light for cancer treatment. For photothermal therapies in particular, we have aggregated data on key variables in gold nanoparticle treatment protocols, such as exposure energy and nanoparticle concentration, and hope to highlight the need for normalization of variable reporting across varying experimental conditions and energy

sources. We additionally discuss the potential to co-deliver chemotherapeutic drugs to the tumor using nanoparticles and how light can be harnessed for multifunctional approaches to cancer therapy. Finally, current *in vitro* methods of testing these therapies is discussed as well as the potential to improve on clinical translatability through 3D tissue phantoms. This review is focused on presenting, for the first time, a comprehensive comparison on a wide variety of photo based nanoparticle interactions leading to novel treatments and imaging tools from a basic science to clinical aspects and future directions.

2.2 Introduction

Cancer remains a leading cause of death worldwide and despite significant medical advances to reduce the mortality rate of other major diseases (such as heart disease), the number of cancer related deaths continues to increase every year[1]. While traditional cancer therapies, such as chemotherapy and radiation treatment, have had limited success in the fight against cancer, there is much room for improvement[2]. By capitalizing on tissue optical properties, the use of lasers for therapy has a wide variety of applications, including laser eye surgery and laser-induced thermal therapy for eradication of cancerous lesions[3-5]. With large ranges of potential wavelengths, laser powers, and treatment durations available for therapy, the light interactions with tissue can vary from photochemical interactions to induce a chemical change in tissue to photomechanical interactions to ablate away layers of tissue[6]. The efficacy and potential applications of lasers for biological applications is largely dependent on the depth to which the light will penetrate the tissue. Due to the high absorbance of visible light by hemoglobin in the bloodstream and the significant absorbance of far infrared light by

water, light penetration is maximized with wavelengths in the near infrared region (NIR, 700-1400 nm). NIR light can reach up to centimeters below the surface, while light penetration in other regions of the spectrum is limited to the sub-millimeter scale (making them attractive choices for ablation of surface layers of tissue). Surface and endoscopic-based light imaging based on visible and far infrared wavelengths is possible, but the high attenuation of light intensity limits the use of these wavelengths. Utilizing the NIR optical window provides the greatest penetration depth in tissue and is thus the gold standard for most light-based imaging and treatment of cancer [6].

Nanoparticles offer added advantages to light-based therapies due to their drug carrying capacity and ability to selectively deliver energy doses to target tissue for tumor destruction. While laser-tissue interactions are sufficient to cause heating or photochemical activation of sensitizers in tissue, the addition of nanoparticles makes this conversion both more efficient and more localized[7]. Photo-based therapies that utilize nanoparticles for energy conversion are able to deliver significant tissue changes at the nanoparticle level without altering the bulk properties of the tissue. This limits the collateral damage to surrounding healthy tissue when used for the treatment of tumors.

This review discusses the use of nanoparticles in conjunction with photo therapies for imaging and treatment of cancerous lesions. While other review papers have examined individual particles[8, 9] or photo-based applications[10, 11] separately, there has yet to be an comprehensive review to combine and compare both the nanoparticles as well as the type of therapy used for the treatment of cancer. In conjunction with therapies, nanoparticles have also been implicated for the imaging and detection of cancer, with significant advances in the field of quantum dots and Raman scattering leading the way.

Additionally, areas for future improvement will be discussed, including photo-triggered release of drug from nanoparticles and improved 3D testing platforms to better mimic *in vivo* tissue. We will focus on necessary parameters that should be considered when designing a nanoparticle for cancer treatment, as we envision that the capability to combine aspects of imaging, therapeutics, and drug release into one nanoparticle platform will ultimately be the future of cancer nanotechnology.

2.3 Imaging of Cancer with Nanoparticles

The most effective way to improve the prognosis of a cancer diagnosis is early detection. There are many different detection methods in practice today, including a wide variety of imaging modalities that can both detect tumors and act as a guide for clinicians to plan treatment. Some of these modalities, such as MRI [12, 13], CT[14], or nuclear imaging such as PET[15], are beyond the scope of this work and the reader is directed to other works. Though they have yet to be translated to clinical use, there are a few imaging modes that are based on light detection (i.e. Raman scattering and quantum dot imaging) that have yet to translate to clinical use; the status of the research surrounding these modes will be discussed.

2.3.1 Quantum Dots

Quantum dots (QDs) are semiconducting crystal lattice structures, usually containing one or more heavy metals, that absorb and emit light related to their size and elemental composition, as shown in **Figure 2.1** [16, 17]. This unique property enables researchers to precisely tune the fluorescence wavelength of the particles based solely on their size [16, 18]. Because their mechanism of fluorescence is different than traditional

fluorescent particles[19], QDs exhibit stable fluorescence over their lifetime and rarely photobleach [20, 21]. Of particular interest are the cadmium-selenide (CdSe) QDs that exhibit large quantum efficiencies[22] but biological applications using these QDs are limited because of cadmium toxicity[23]. Because of this heavy metal toxicity, QDs are often coated with materials such as zinc-sulfur (ZnS) [17] and attached to biocompatible ligands [24] for use *in vitro* and in animal studies. In addition to CdSe and other heavy metal-based QDs, heavy-metal-free QDs such as indium-phosphorous (InP) are currently under investigation to replace toxic cadmium-containing species [25]. However, quantum efficiencies of these particles are rarely over 50%, and their wavelength range is considerably smaller than cadmium-containing particles [17].

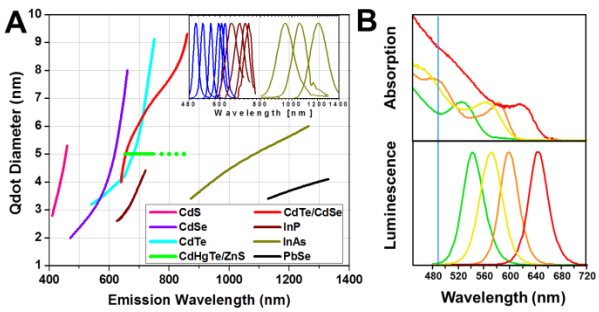

Figure 2.1. (a) Quantum dot emission range based on elemental composition and size. (b) Demonstration of varying emission wavelength QDs' ability to fluoresce with the same excitation wavelength. From: ref. 17, X. Michalet, F. F. Pinaud, L. A. Bentolila, J. M. Tsay, S. Doose, J. J. Li, G. Sundaresan, A. M. Wu, S. S. Gambhir, and S. Weiss, Quantum Dots for Live Cells, in Vivo Imaging, and Diagnostics. *Science*. 307, 538-544 (2005). Copyright@ AAAS.

QDs can be attached to a variety of surface-modifying moieties, such as poly(ethylene glycol) (PEG)[18, 24, 26, 27], arginine-glycine-aspartic acid peptides (RGD) [28], folic acid [24, 29-31], monoclonal antibodies [18, 20, 25, 32-34], trans-activator of transcription (TAT) protein [18, 27], transferrin [32], vascular endothelial growth factor (VEGF) [35], aptamers [36, 37], lysine[38], bovine serum albumin (BSA)[38], and epidermal growth factor (EGF) [39].

These targeted particles can then be used for a wide variety of applications, such as fixed cell imaging, biosensing of tissue components, optical surgical aids, and bioanalytical assays, just to name a few [17]. As a tool for cancer, QDs have immense potential for cancer diagnosis and detection; for example, conjugated QDs can be used to identify properties of tumors such as VEGF-receptor expression[35]. Gao et al. demonstrate the immense power of QDs as an imaging tool by conjugating a variety of targeting molecules and PEG to the surface of different sizes of CdSe-ZnS QDs [18]. Using 3 types of QDs (unmodified, PEG, and antibody-conjugated), they were able to demonstrate that localization of QDs to the cancer cells, both *in vitro* and *in vivo*, increases with conjugation to PEG and antibody. In addition to histological analysis, they imaged QDs *in vivo* to reveal the capability to resolve different emission wavelengths corresponding to quantum dot suspensions of varied color, as shown in **Figure 2.2**. Gao et al. established the potential of QDs for use in real-time, precise, *in vivo* imaging [18].

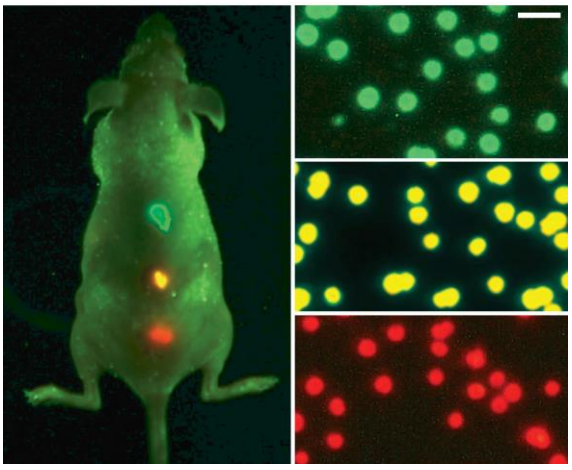

Figure 2.2. Demonstration of simultaneous quantum dot fluorescence to detect multiple species *in vivo*. From ref. 18, X. Gao, Y. Cui, R. M. Levenson, L. W. K. Chung, and S. Nie, In vivo cancer targeting and imaging with semiconductor quantum dots. *Nature Biotechnology*. 22, 969-76 (**2004**). Copyright@ Macmillan Publishers Ltd.

Characterizing tumor associated vasculature is a relatively new area of interest for cancer researchers and one in which developments in QDs have shown particular value. Diagaradjane et al. describe a method to use near infrared (NIR) QDs coupled to EGF for the detection of EGF receptor (EGFR) expression, which is commonly overexpressed within tumor vasculature [39]. They conjugated EGF to the surface of cadmium-selenide-tellurium (CdSeTe)/ZnS QDs via a maleimide reaction, yielding particles that selectively bind to EGF receptors on the endothelial cell surface. When injected into mice with colorectal tumors overexpressing EGFR, the targeted particles show an increased tumor-to-background ratio, indicating a significant difference in intratumoral accumulation between targeted and non-targeted QDs. They concluded that this class of targeted QD imaging probes could potentially be used in the future for early detection of cancers and image-guided biopsy[39]. Chen et al. detail a study in which CdTe/ZnS QDs are conjugated to the VEGF protein for the detection of tumor vasculature [35]. These particles were injected and imaged *in vivo*, demonstrating the effect of targeting and concentration on the intensity profile of fluorescence. A look at biodistribution of these particles revealed significant accumulation in liver, spleen, and bone along with the tumor tissue, indicating that while VEGF may be an effective target for examining tumor vasculature, it is likely ineffective as a target for therapy due to high accumulation in these other tissues. In a more detailed attempt to distinguish different species within tumors, Stroh et al. utilized CdSe/ZnCdS QDs conjugated either to PEG or TAT protein or encapsulated within a microsphere and imaged tumor structures using multiphoton microscopy[27]. They collected images of tumor vasculature, including GFP-perivascular cells resolved from

blood vessels while tagged with 470 nm QDs. In addition, QD-loaded silica microspheres showed heterogeneous extravasation, indicating that accessibility to the target perivascular cells is strongly dependent on local vasculature. The resolution and imaging properties of QDs make a valuable tool for characterizing tumor associated vasculature and gathering information on tumor component relationships, though advancements reducing toxicity and increasing specificity to the tumor microenvironment are still needed.

With developments in the creation of heavy metal-free QDs and QDs for use with NIR imaging, the field of QD imaging for biological applications has the potential to rapidly translate directly to clinical applications. For example, as previously mentioned, Diagaradjane et al. demonstrated the use of NIR CdSeTe/ZnS QDs for imaging of tumor vasculature[39]. Kim et al. discusses the use of CdTe/CdSe QDs with a fluorescence emission peak around 850 nm for sentinel lymph node mapping[21]. In that study, QDs were injected into either the paw or thigh of mice and imaged at the sentinel lymph node during surgery. These particles have the potential to give surgeons real-time feedback in order to avoid incomplete resections, which is especially important in surgeries for breast cancer and melanoma[21]. Yong details the use of manganese-doped CdTeSe/CdS with a fluorescence emission maximum around 822 nm for imaging of pancreatic cancer[34]. These particles were coated with lysine and subsequently conjugated to monoclonal antibodies specific to pancreatic cancer (anti-claudin 4, anti-mesothelin or anti-prostate stem-cell antigen) while maintaining quantum yield and fluorescence maximum. When injected into mice, the particles showed the ability to bind to and effectively image pancreatic cancer lesions while maintaining healthy levels of blood serum proteins,

demonstrating their impending use as a cancer diagnostic[34]. In an effort to demonstrate the potential of cadmium-free QDs for cancer imaging, Yong et al. detail the use of InP/ZnS QDs with a fluorescence emission maximum around 650 nm. Similar to cadmium-containing species, these QDs have the ability to conjugate targeting ligands on their surface, such as monoclonal antibodies demonstrated in that study. These particles showed no decrease in cell viability after 48 hours with concentrations up to 100 mg/mL, demonstrating their prospects as an *in vivo* diagnostic tool[25]. Choi et al. describe a QD composed of indium-arsenic (InAs)/ZnS which also fluoresces in the NIR range around 750 nm, combining the favorable qualities of cadmium-free QDs with the tissue penetration depth allowed by NIR imaging[26]. They conjugated PEG to the surface of the QDs and examined organ distribution as a function of PEG chain length; results suggest that longer PEG chains allow for increased circulation time and reticuloendothelial system (RES) escape, as shown in **Figure 2.3**. This study shows a technique that minimizes cytotoxicity, both by the exclusion of cadmium and inclusion of PEG chains, while utilizing the NIR optical window[26].

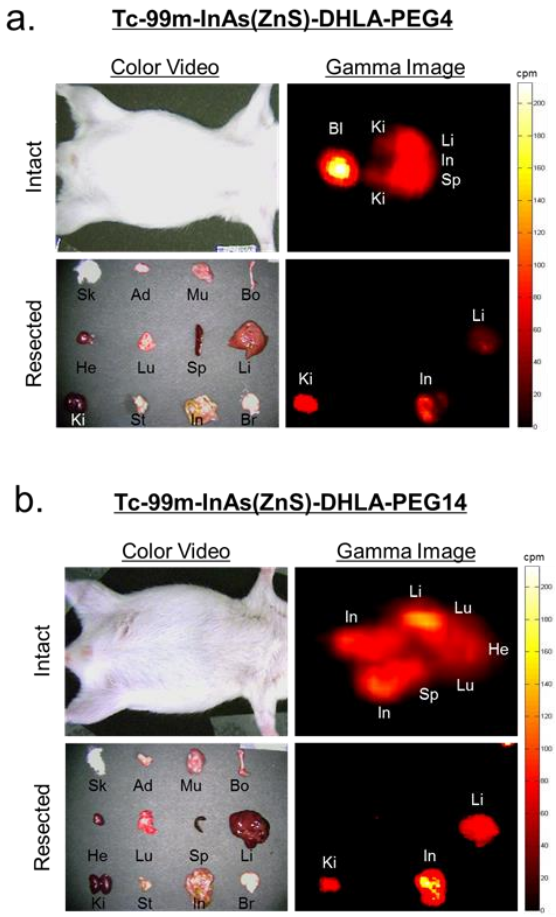

Figure 2.3. Organ distribution of InAs/ZnS QDs with varying PEG chain length. (a) QD-PEG4 (5.6 nm diameter) show accumulation in brain and RES organs. (b) QD-PEG14 (8.7 nm diameter) accumulates in RES organs. Abbreviations used are: Sk, skin; Ad, adipose; Mu, muscle; Bo, bone; He, heart; Lu, lungs; Sp, spleen; Li, liver; Ki, kidneys; St, stomach; In, intestine; Br, brain; and Bl, bladder. From ref 26, H. S. Choi, B. I. Ipe, P. Misra, J. H. Lee, M. G. Bawendi, and J. V. Frangioni, Tissue- and Organ-Selective Biodistribution of NIR Fluorescent Quantum Dots. *Nano Letters*. 9, 2354-2359 (**2009**). Copyright@ American Chemical Society.

As QDs develop further into widely-used imaging tools, they have the potential to be combined with other nanoparticle platforms to create a multifunctional nanocomposite. Hu et al. described how QDs can be conjugated to the surface of graphene oxide particles; upon conjugation, the composites could then be used both for imaging the tissue distribution of particles and for photothermal treatment upon

irradiation[31]. Interestingly, they observed a decrease in fluorescence intensity upon heating of the graphene oxide, which they were able to reproduce in a pure heating experiment. Additional experimentation on the interplay between surface chemistry, heating, and laser irradiation are needed to evaluate the potential for QDs to be used effectively in conjunction with photothermal therapies. Quantum dots have also been added to single-walled carbon nanohorns for use in characterizing transport of nanoparticles of varying properties and external conditions[40, 41]. This gives insight into nanoparticle-cell interactions that could otherwise not be imaged and has the capacity to give real time feedback into the cytotoxic effects of delivering drug payloads to cells.

Future work utilizing QDs for cancer imaging involves overcoming great obstacles. The development of heavy metal-free QDs to limit systemic toxicity while still retaining high quantum yield has yet to be accomplished. In addition, development of QDs capitalizing on the NIR region for deep tissue imaging still requires further research and optimization. The combination of QDs with other therapies to develop a multifunctional nanoparticle/nanocomposite will give the ability to image particles in real-time while simultaneously delivering a therapy directly to tumor tissue.

2.3.2 Surface-Enhanced Raman Scattering (SERS)

Raman scattering is based on the vibrational energy and relaxation experienced with different elemental bonds seen in complex structures. Parameters such as element size and bond length play an important role in the ability of particles to scatter and shift incident light to a particular band [42]. Detailed discussion of the mechanism is beyond the scope of this review; the reader is directed to more fundamental reviews for the mechanisms[42]. For imaging applications, SERS is most commonly studied in metals such

as gold, silver, and copper, though other metals have limited study[42]. Carbon nanotubes have also been used for SERS because of their characteristic graphite peak[43]. The concentration of these particles at a particular location corresponds to an increased intensity seen in the characteristic SERS spectra of the delivered nanomaterials[44].

Due to the unique Raman interactions found in metals and graphite-containing structures mentioned previously, there are a wide variety of particle types that can be used for SERS; these include gold nanorods[45, 46], gold nanospheres[47], silica core/gold shell nanoparticles[48-50], gold/silver core/shell particles[44], gold nanoparticles[51-54], silver nanoparticles[55, 56], carbon nanotubes[43, 57-60], metal coated carbon nanotubes[61], and polymers[62]. In addition to the large variety of particle materials used for SERS imaging, there are a number of surface modifications that can be made to particles, such as monoclonal antibodies[44, 45, 47, 48, 51, 53, 58, 63] or PEG[46, 48, 49, 51, 53, 59, 61], for enhanced delivery to cancer lesions. The combination of particle type and surface modification enables a large number of candidate molecules for effective SERS imaging.

In a classic example of Raman imaging with SERS, Lee et al. detail a hollow gold nanosphere used for SERS imaging that outperforms its silver counterpart, which is shown in **Figure 2.4** [47]. They adsorb the Raman reporter crystal violet and the anti-human epidermal growth factor receptor 2 (HER2) antibody to the surface of the particles, yielding a targeted particle for the detection of the breast cancer cell line MCF-7. Fluorescence imaging and Raman scattering showed that particles associate selectively with HER2-expressing cells, which exemplifies their capability to be a diagnostic and imaging agent *in vivo*. Huang et al. described the use of gold nanorods with a plasmonic resonance in the NIR region to selectively image human oral squamous cell carcinoma

through conjugation to the anti-EGFR antibody[45]. They also examined the effect of orientation on the strength of the Raman signal, indicating that cancer cells may align particles through the interactions with the EGFR and the antibody attached to the particle surface, thus enhancing the signal produced. Signals from cancer samples were sharper and had a greater intensity than those seen from normal cells, indicating that there may be an enhanced benefit to using gold nanorods for SERS imaging of cancer *in vivo*. In another regime of cancer detection, Wang et al. described the use of anti-EGFR conjugated gold nanoparticles with QSY reporter molecule for the detection of circulating tumor cells *ex vivo*[53]. Blood collected from patients was exposed to the SERS nanoparticle and subsequently imaged with Raman. They were able to correlate the intensity of the SERS signal with the concentration of cancer cells, as well as distinguish cancer and non-cancer cells. This procedure has the potential to selectively identify circulating tumor cells in patients and, with the application of additional surface molecule tags, could lead to information on the progression and prognosis of disease[53].

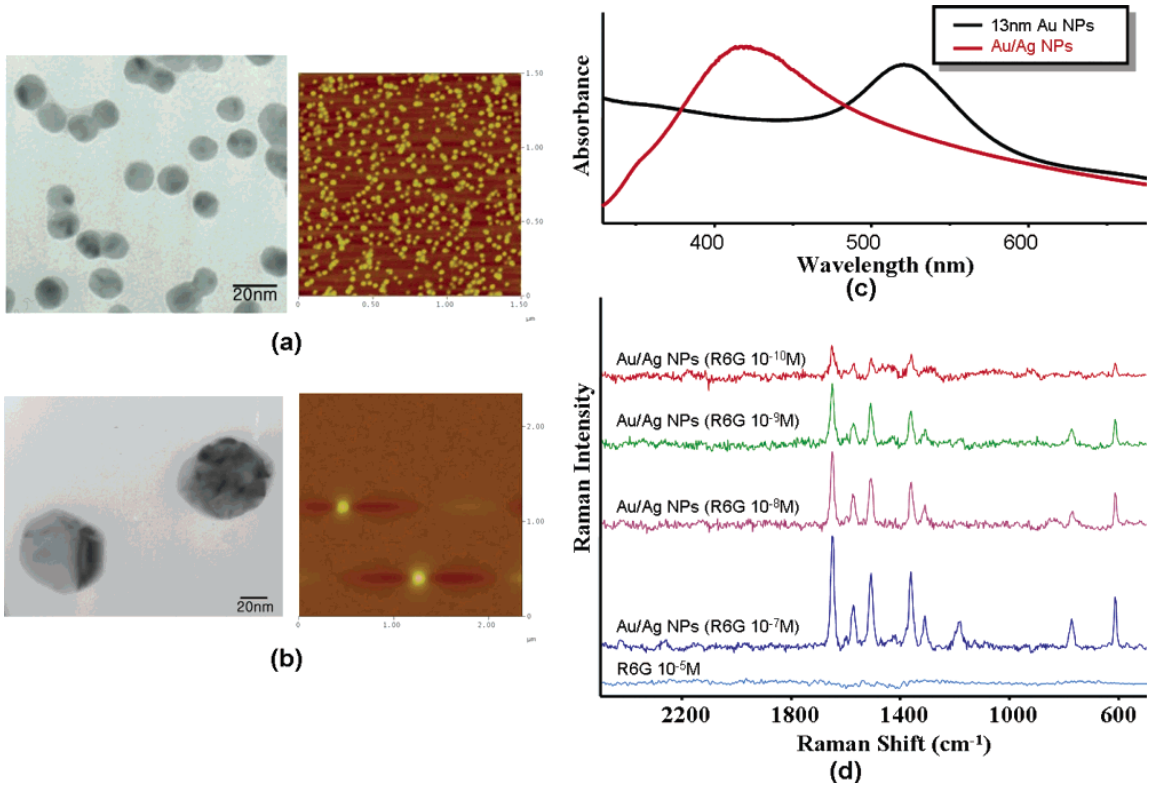

Figure 2.4. TEM and AFM of (a) gold nanoparticles and (b) antibody-conjugated Au/Ag core-shell nanoparticles. (c) Absorbance spectra of both particle types. (d) SERS spectra of R6G conjugated Au/Ag particles with varying concentrations. From ref 44, S. Lee, S. Kim, J. Choo, S. Y. Shin, Y. H. Lee, H. Y. Choi, S. Ha, K. Kang, and C. H. Oh, Biological Imaging of HEK293 Cells Expressing PLCγ1 Using Surface-Enhanced Raman Microscopy. *Analytical Chemistry*. 79, 916-922 (2007). Copyright@ American Chemical Society.

Exemplifying the next generation of SERS imaging, Feng et al. described a method to spatially map tissue constituents of cancerous vs. non-cancerous tissue with a signal enhancement from gold nanoparticles[52]. With the inclusion of gold nanoparticles, not only is the Raman signal more intense, but the sharpness of the peaks is also enhanced. Thus, it is possible to distinguish tissue constituents by scanning tissues and selecting specific bands corresponding to tissue components; 2D spatial maps can be created that can highlight microenvironmental differences between normal and cancerous tissues. In an extensive *in vivo* study, Qian et al. described the use of gold nanorods that have been modified with the fluorescent molecule 3,3′-diethylthiatricarbocyanine iodide

(DTTC) and PEG for *in vivo* imaging and biodistribution analysis, as shown in **Figure 2.5** [46]. This study examined NIR fluorescence and SERS to determine the spatial distribution of particles, identify sentinel lymph nodes, and evaluate excretion mechanisms of these modified gold nanoparticles. SERS in particular showed a sharp signal increase when gold particles were present and was able to bypass many issues associated with auto-fluorescing tissue commonly seen in mice studies. By utilizing only light-based imaging for their work, Qian et al. demonstrated the future of diagnostic tools that take advantage of favorable optical properties associates with using NIR light for tissue imaging.

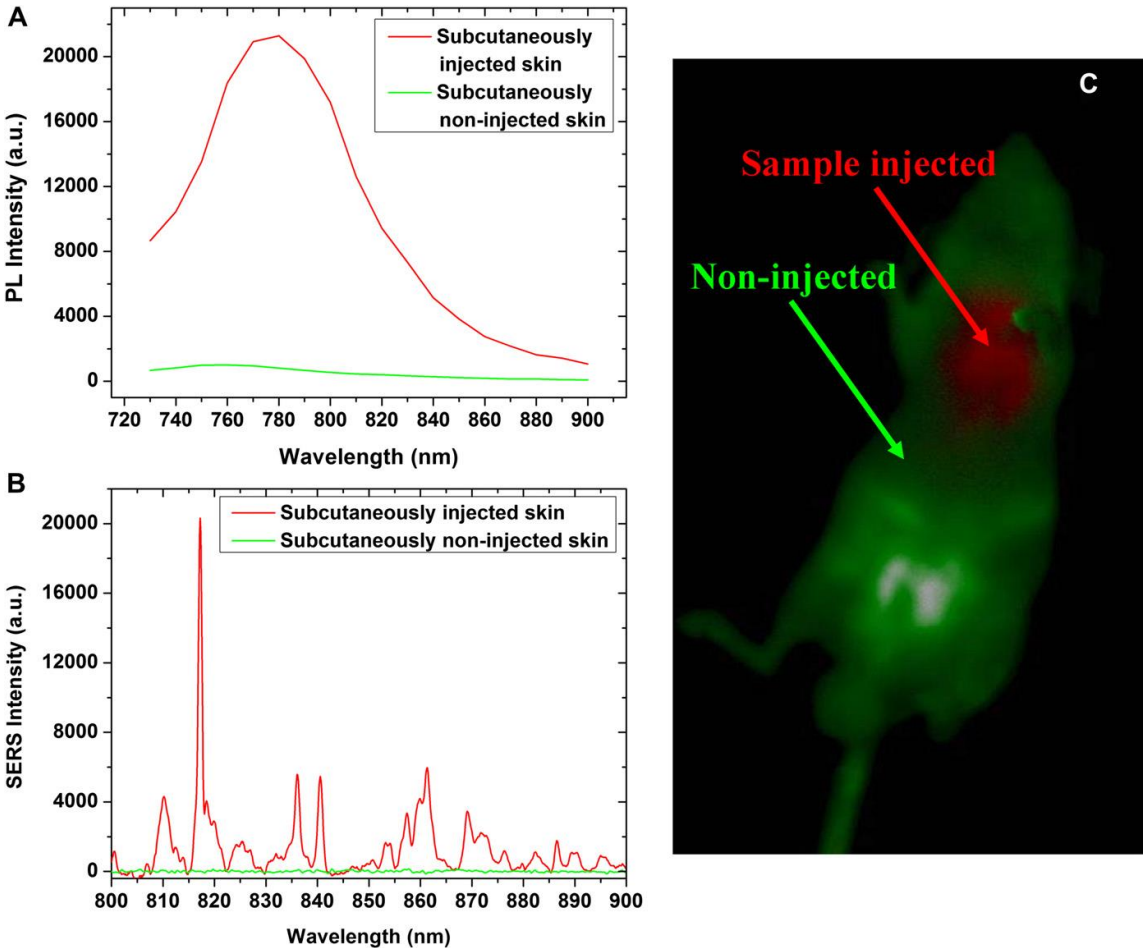

Figure 2.5. NIR fluorescence (a) and SERS spectra (b) from PEG-DTTR-GNR injected skin. (c) NIR fluorescence of injected particles showing diagnostic potential *in vivo*. From ref 46, J. Qian, L. Jiang, F. Cai, D. Wang, and S. He, Fluorescence-surface enhanced Raman scattering co-functionalized gold nanorods as near-infrared probes for purely optical in vivo imaging. *Biomaterials*. 32, 1601-1610 (2011). Copyright@ Elsevier.

The creation of a multifunctional nanoparticle has long been of interest in the scientific community. Wang et al. described a particle consisting of a single walled carbon nanotube (SWNT) coated with either gold or silver, made biocompatible with the addition of PEG, and targeted to cancer cells through attachment of folic acid [61]. These particles selectively bind to cancer cells *in vitro* and can be imaged with Raman spectroscopy. In addition to these favorable imaging qualities, the particle can also be used as a photothermal agent, as an increased change in temperature of gold-coated

SWNTs (SWNT-Au) compared to previously studied SWNTs was demonstrated. When compared to gold nanorods, SWNT-Au's showed an enhanced photostability after irradiation, indicating the potential of these particles to be used for imaging post-treatment. Although there are many parameters not discussed in the manuscript, such as degree of metal coating and its effect on imaging and therapy, these multi-component nanoparticles may indicate an exciting new direction for future study.

Raman scattering and its capacity for imaging cancer lesions *in vivo* is still a rapidly growing field. With recent developments such as spatial imaging and extensive *in vivo* work in mice, the field of SERS has demonstrated the capability to specifically identify tumors. Concerns about the clinical potential of using SERS particles for imaging, such as the effect of circulating gold in the body and significant clearance by the RES system, must be addressed. In addition, advancements in detection of Raman signals would enhance the resolution of spatial images gathered from *in vivo* work, a development that is essential for clinical translation of SERS particle research.

2.3.3 Photoacoustic Imaging

In photoacoustic imaging, nanoparticles absorb light (usually in the NIR range to maximize tissue penetration of light) to produce a surface plasmon and subsequently generate an acoustic wave in the tissue[64, 65]. With the use of an ultrasound detector, these waves can be identified and used for imaging the location of nanoparticles within the tissue[64]. When targeting agents are added to the surface of these particles (such as anti-EGFR antibody), determination of the location of these particles can be used as a diagnostic tool to distinguish surface markers and identify their location within tumors[64]. Common particle types for photoacoustic imaging include gold[64, 66-70], iron oxide [71, 72],

cobalt[73] and copper[65, 74] nanoparticles, although carbon[75] and polymers[76] have also demonstrated the capability to generate acoustic waves. Because generation of an acoustic wave also produces a local heating event, these particles are all good candidates for photothermal therapy when used with different laser parameters.

Mallidi et al. discuss the use of 50 nm gold nanospheres conjugated to the anti-EGFR antibody for the selective detection of human epithelial carcinoma cells *ex vivo* through photoacoustic imaging[64]. When these gold nanospheres were conjugated to the anti-EGFR antibody, they underwent a slight red shift from a 520 nm maximum and increased their absorbance across all wavelengths. Targeted, non-targeted, or no particles were incubated with cells; cellular mixtures were subsequently mixed in gelatin and injected into *ex vivo* mice skin (fourth injection of NIR dye for control). Images were taken at different wavelengths of light to highlight differences in the optical absorption properties of the implants (532 nm, 5 ns pulses; 680, 740, 800, 860 nm, 7 ns pulses) and are shown in **Figure 2.6**. While non-targeted particles are seen to some degree under 532 nm irradiation, targeted particles are seen at all wavelengths with a strong correlation to their corresponding absorption spectra. This method creates high-resolution images with high selectivity to anti-EGFR gold nanospheres while sacrificing the ability to image in real-time; the combination of these two elements will greatly enhance the value of photoacoustic imaging.

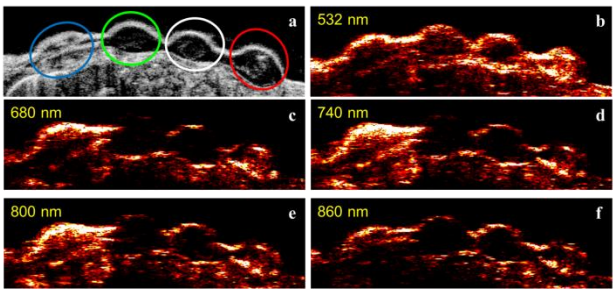

Figure 2.6. Ultrasound (a) and photoacoustic (b-f) imaging of implants in mouse tissue at varying wavelength. Blue inset: NIR dye, Green inset: non-targeted Au nanoparticles with A431 cells, White inset: control A431 cells, and Red inset: targeted Au nanoparticles with A431 cells. From ref 64, S. Mallidi, T. Larson, J. Tam, P. P. Joshi, A. Karpiouk, K. Sokolov, and S. Emelianov, Multiwavelength Photoacoustic Imaging and Plasmon Resonance Coupling of Gold Nanoparticles for Selective Detection of Cancer. *Nano Letters*. 9, 2825-2831 (**2009**). Copyright@ American Chemical Society.

Capitalizing on the optical properties of tissue, Zha et al. discuss the use of NIR light for photoacoustic imaging with the addition of copper sulfide particles (6-12 nm) in tissue phantoms[74]. When placed under a layer of chicken breast muscle up to 3.2 cm thick, focal patterns of nanoparticles were still able to be imaged (808 nm, 2.25 MHz transducer). They subsequently used this technique for imaging the cerebral cortex of mice injected with copper sulfide nanoparticles and demonstrated the ability to enhance contrast between blood vessels and brain parenchyma. With further refinement and additional studies, copper sulfide particles have the potential for widespread use due to their relatively small size and imaging capability in the NIR region.

Since photoacoustic imaging using nanoparticles is a relatively new field, significant advancements in both image quality and selectivity of nanoparticles used for imaging must be made before this becomes a viable clinical option for tumor imaging. For surface cancers, the use of shorter wavelength light (such as 532 nm) does not pose a significant barrier to detection; however, for use in most cancers, particles that can be used in the NIR region are ideal candidates. In addition, Bayer et al. discuss the enhancement of photoacoustic signals with increased accumulation of surface-plasmon

generating nanoparticles, an area that warrants further investigation as a potential quantitative measure for imaging [67]. Furthermore, the use of these particle types in photothermal therapies (discussed below) offers the ability to both image and treat tumors with minimal modifications.

2.4 Photothermal Therapies

As the name suggests, photothermal therapy is based around the conversion of light energy into heat, either through plasmon resonance energy transfer or a vibrational energy transfer from atoms in nanoparticles to atoms in surrounding media or tissue. Although irradiating tissue with laser light without the presence of nanoparticles will cause tissue heating, the capability to transfer heat efficiently in a localized area is unique to nanoparticle photothermal therapy. The specificity of nanoparticle heating is limited to the area directly surrounding the particle, thereby limiting damage to the surrounding healthy tissue. Specific mechanisms of energy transfer are beyond the scope of this review, but the reader is directed to specific papers for further information regarding the mechanisms behind photothermal therapy[77, 78].

Nanoparticles for use with photothermal therapy vary widely; the most commonly used particles revolve around the use of gold to transfer plasmon resonance from the particle to the surrounding tissue. These include gold nanorods, gold nanospheres, and silica core/gold shell particles, among others. A wide variety of other metals are also used, including silver particles, iron oxide-containing particles, and copper-containing particles. Carbon particles in photothermal therapy, including carbon nanotubes, graphene oxide, and carbon nanohorns, capitalize on the transfer of vibrational energy from the graphene atoms to the surrounding tissue. Polymer systems have also been

explored recently as a potential biodegradable particle for photothermal therapy, bypassing many common concerns of higher costs and tissue retention associated with metal particles[75]. Each of the particles retains the ability to modify their exterior with PEG or targeting molecules to both increase biocompatibility and circulation time and also selectively treat tumors. Between the wide variety of particle types, attachable moieties, and laser parameters used for treatment, few groups are able to compare results based on one parameter, such as concentration of particles, wavelength of light, or laser power used. As highlighted in **Table 2.1**, laser parameters for three main types of gold particles alone are highly variable; to effectively move nanoparticle-based photothermal therapy from the lab to the clinic, many of these variables must be controlled and industry standards established which will subsequently be discussed.

Variation in Parameters for Photothermal Therapy with Gold Nanoparticles					
Particle Type	Laser Wavelength	Nanoparticle Concentration	Laser Duration	Laser Irradiance (W/cm^2)	References
Gold Nanorod	671 nm	400 µg/mL	10 minutes	Not reported	[86]
	780 nm	Not reported	178.5 seconds	26.4, 41.5	[88]
	800 nm	Not reported	0.19-5.70 milliseconds	41.7, 27.8, 19.4, 13.9, 5.6	[85]
	808 nm	35 mg/kg	5 minutes	0.6, 2	[60]
		1000 µg/mL	4 minutes	4	[87]
		OD(800) = 40, 120; 15µL	10 minutes	1, 1.8	[89]
		75, 150, 300 µg/mL	2 minutes	1, 2, 3	[257]
		Varied	5 minutes	2	[255]
		200 µg	5 minutes	24	[83]
	810 nm	10 mgAu/kg	30 minutes	0.75	[258]
		1 mg/kg	Not reported	3.82	[259]
		20 mg/kg	5 minutes	2	[118]
Silica Core/Gold Shell	800 nm	1.7×10^{11} particles/mL	3 minutes	4	[99]
	808 nm	Varied	5 minutes	2	[255]
		2.4×10^{11} nanoshells/mL	3 minutes	4	[94]
		1.5×10^{11} particles/mL	3 minutes	4	[98]
		5×10^{9} nanoshells/mL	2-3 minutes	10	[260]
	820 nm	2.9×10^{9} particles/mL	7 minutes	0.8	[95]
		3×10^{9} nanoshells/mL	7 minutes	0.008	[96]
		4.4×10^{9} particles/mL	7 minutes	35	[97]
Gold Nanospheres	514 nm	0.2 nM	4 minutes	76, 57, 25, 19	[92]
	530 nm	0.13 nM	5 minutes	4, 7, 14	[261]
	660 nm	60 nM	10 minutes	5, 6.5, 8, 10	[93]
	800 nm	4 nM	2 minutes	0.14, 0.28, 0.56, 1.41, 2.82, 5.65, 8.95, 17.8	[90]

Table 2.1. Variation between groups investigating photothermal therapy with the three main forms of gold nanoparticle. Parameters not listed include cell type treated and injection site and variation becomes more marked when all particles currently being used for photothermal therapy is taken into account.

2.4.1 Gold Particles

2.4.1.1 Gold Nanorods Gold nanorods are particles composed of gold that are characterized by their high aspect ratio and tunability to resonate at a specific wavelength (usually in the NIR). They are most commonly formed by a seed-mediated growth method, where gold seeds are placed in growth solution that limits growth in only one direction to yield rods of high aspect ratio[79, 80]. For application in cancer therapy, particles are ordinarily tuned to absorb in the NIR range to maximize tissue penetration of light, thereby increasing the numbers of eligible lesions for photothermal therapy. Gold nanorods can be used with a simple silica coating or PEG[8, 81] or in conjunction with targeting molecules such as aptamers[82], RGD peptides [83], folate [84], anti-EGFR [45], or transferrin [85] to avoid cytotoxicity seen with cetyltrimethylammonium bromide (CTAB) used in nanorod synthesis.

Yi et al. describe a gold nanorod system designed that can identify high levels matrix metalloproteinase (MMP) expression while simultaneously providing therapy in the form of heat[86]. They develop a NIR fluorescent peptide coating for gold nanorods that is degraded by MMPs; the fluorescent signal from their reporter molecule Cy5.5 is quenched until there is peptide degradation by the MMPs, giving an indication of the number of MMPs expressed by a particular tumor. By using a NIR fluorescent dye, they simultaneously administered heat and captured fluorescence using a 671 nm laser (200 W, area not specified). Ultimately, these particles were used for simultaneous imaging and therapy of tumors, showing an increase in fluorescence and temperature corresponding to longer incubation and irradiation time. In an effort to minimize cytotoxicity caused by the use of CTAB commonly seen in gold nanorod studies, Choi et

al. describe the use of loading gold nanorods into a chitosan-Pluronic F 68 conjugate nanocarrier[87]. The use of a chitosan nanocarrier does not significantly change the diameter of particles while significantly decreasing the zeta potential of gold nanorods (from +35 mV to +10 mV). The chitosan-gold nanorod particle caused significant photothermal death of SCC7 squamous cell carcinoma cancer cells with limited destruction of non-cancerous NIH/3T3 cells (780 nm, 26.4 or 41.5 W/cm^2). When used *in vivo*, the chitosan-gold nanorod particles accumulated significantly at the tumor site, showing a remarkably similar percentage of injection dose accumulated in liver and tumor, which is rarely seen in nanoparticle biodistribution studies. As shown in **Figure 2.7**, the use of chitosan-gold nanorods with photothermal irradiation (808 nm, 4 W/cm^2) resulted in significantly stunted tumor growth; with the addition of a second irradiation after 48 hours, tumors exhibited complete disappearance.

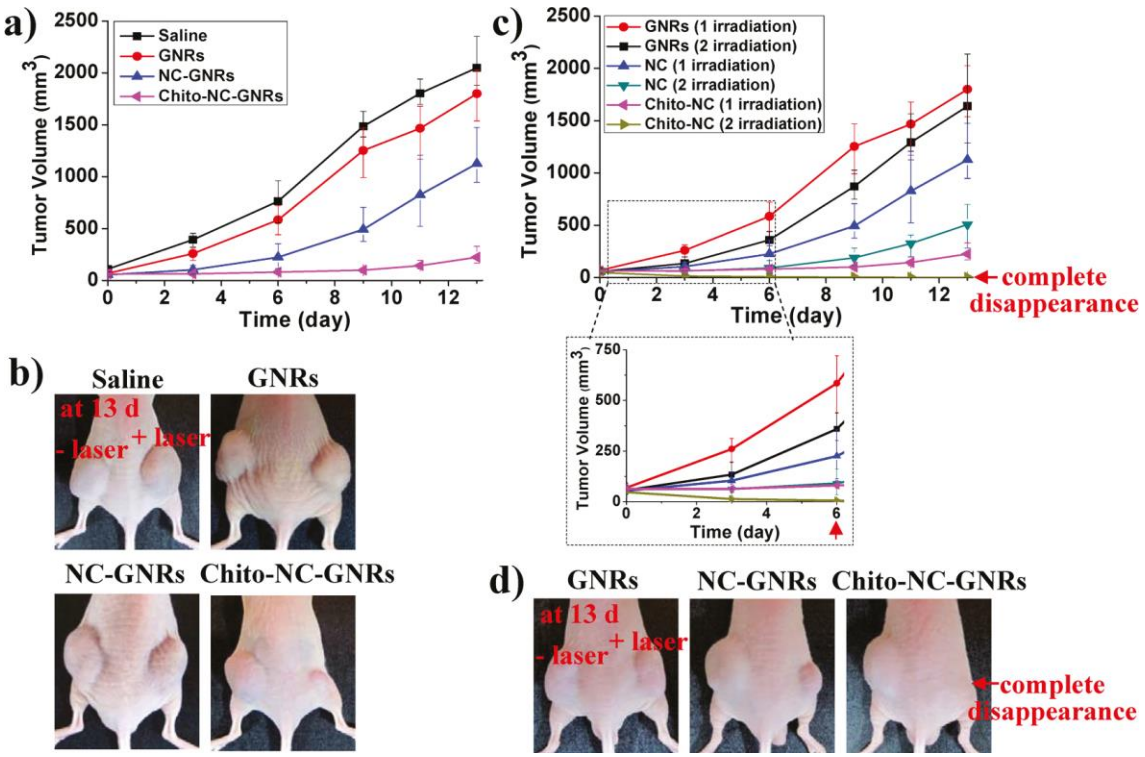

Figure 2.7. Use of gold nanorods for tumor regression. One-time laser irradiation on changes in tumor volume (a) and corresponding images (b). 24 hr and 48 hr irradiation (two-time irradiation) on changes in tumor volume (c) and corresponding images (d). From ref 87, W. I. Choi, J.-Y. Kim, C. Kang, C. C. Byeon, Y. H. Kim, and G. Tae, Tumor Regression In Vivo by Photothermal Therapy Based on Gold-Nanorod-Loaded, Functional Nanocarriers. *ACS Nano*. 5, 1995-2003 (**2011**). Copyright@ American Chemical Society.

In an effort to increase the conversion of light to thermal energy, Li et al. detail the use of circularly polarized light to specifically irradiate gold nanorods with laser powers that would ordinarily cause no particle heating with linearly polarized light[85]. Gold nanorods were conjugated to transferrin and PEG to facilitate specific uptake and biocompatibility, respectively. When particles were incubated with HeLa cells *in vitro*, the exposure time required for effective photothermal therapy was significantly less for circularly polarized light than for linearly polarized light, indicating energy efficiency. While the overall threshold of energy density required to kill cells was not different between the two types of polarization, the exposure time was significantly less than other

reported values. This is a significant finding because delivering less laser energy to tissue in an effort to eradicate cancer lesions is medically safer. While other groups have investigated the use of circularly polarized beams[88], more research into tissue effects and therapy effectiveness is needed.

Ultimately, the goal of gold nanorod work is to translate these therapies to a clinical setting; however, there are many factors requiring investigation before clinical translation that are not considered in many *in vivo* studies. One such consideration is how the gold nanorods will be delivered in a clinical setting. As shown in **Figure 2.8**, Dickerson et al. discuss the influence of injection site (direct injection or intravenous injection) on particle accumulation and effectiveness of photothermal therapy[89]. PEGylated gold nanorods were injected into either the tail vein or directly into tumor space and subsequently irradiated with a 800 nm laser. For direct injection of particles, photothermal treatment was performed after 2 minutes of accumulation at a power density of 0.9-1.1 W/cm^2; intravenous injections were allowed to accumulate for 24 hours and were irradiated with a power density of 1.7-1.9 W/cm^2. These varying protocols demonstrate similar temperature elevations in the tissue (20-22°C); direct injection treatments resulted in slightly lowered tumor volume, though the decrease was not significant. These findings highlight the potential use of a direct injection system for translatable photothermal therapies; not only does the therapy allow for more favorable laser parameters, it also limits time needed between injection and irradiation to have significant gold nanorod accumulation into targeted areas.

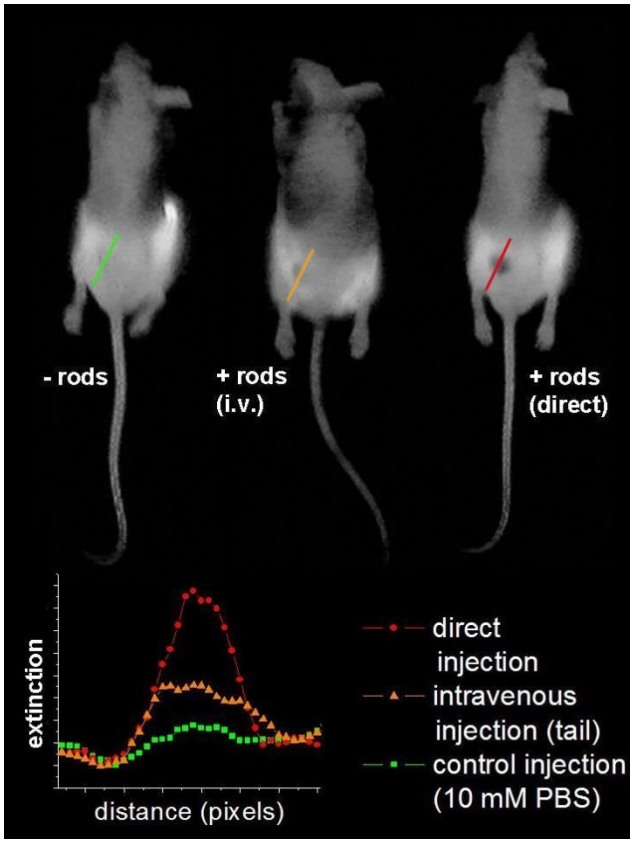

Figure 2.8. Injection site of PEGylated gold nanorods and the effects on the NIR extinction before treatment (corresponding to concentration of particles at tumor site). From ref 89, E. B. Dickerson, E. C. Dreaden, X. Huang, I. H. El-Sayed, H. Chu, S. Pushpanketh, J. F. McDonald, and M. A. El-Sayed, Gold nanorod assisted near-infrared plasmonic photothermal therapy (PPTT) of squamous cell carcinoma in mice. *Cancer Letters*. 269, 57-66 (**2008**). Copyright@ Elsevier.

2.4.1.2 Gold Nanospheres Gold nanospheres are solid spheres composed of all gold that can be tuned to absorb at a specific wavelength proportional to their size. Although photothermal therapies generally revolve around the use of NIR wavelengths, gold nanospheres are commonly tuned to wavelengths between 500-650 nm (green-red on the visible spectrum) limiting the formation of defects seen in NIR-absorbing larger spheres[90]. Because of the use of a different wavelength of light, tissue penetration becomes a factor when using these particles. As a consequence, gold nanospheres are commonly designed to target oral epithelial carcinoma[91, 92] or melanoma[93], both of which have easily accessible surfaces for photothermal treatment.

For treatment of oral carcinoma, El-Sayed et al. describe the use of anti-EGFR conjugate gold nanospheres combined with 514 nm light to eliminate malignant cells[92]. They examined a wide variety of laser power densities ranging from 13 W/cm^2 up to 64 W/cm^2 and evaluated the threshold laser power needed for destruction of both benign and malignant cells. The laser power density required to kill benign cells is more than twice that required to kill malignant cells, indicating a threshold where normal tissue would be unaffected by treatment. Because of the targeting agent associated with these gold nanospheres, more study is required to determine the effect of laser alone on tissue viability due to the decreased concentration of particles present in benign cells at the time of irradiation.

For the treatment of melanoma, Nam et al. describe a gold nanosphere that can selectively accumulate in tumors based on changes in pH[93]. Gold nanospheres were coated with a ligand, which while negatively charged at physiological pH, becomes positively charged in acidic environments commonly found in tumors and cancer cell endosomes. Because of this change in charge, the gold nanospheres aggregate and subsequently change their peak absorption to the NIR range; this quality makes them attractive candidates for photothermal therapy because of their activation upon aggregation at the tumor site. These particles were incubated with B16 F10 mouse melanoma cells and subsequently irradiated with a 660 nm laser with power densities ranging from 5-10 W/cm^2. The pH sensitive particles were able to destroy cancer cells at laser powers as low as 6.5 W/cm^2. Further *in vivo* study is needed to determine the potential of these pH sensitive particles to accumulate selectively in tumors and be subsequently used as a photothermal therapy.

2.4.1.3 Gold Shell Particles Since the generation of surface plasmons occurs exclusively at the surfaces of metal nanoparticles, gold shells surrounding a hollow core or a core of a different metal can offer a different option for photothermal therapies. As developed by Drs. Halas and West, the use of another compound at the core, such as silica, allows for specific control of layer thickness, thereby tuning the absorption of the particle to a particular wavelength[94-102]. The use of an iron core within a gold shell can give the particle magnetic properties favorable for MRI imaging or magnetic guided particle accumulation, while retaining the characteristics necessary for photothermal therapy[103, 104]. Other cores, such as hollow core gold nanoshells[105, 106], gold-gold sulfide particles [107, 108], and polymers coated with gold [109], are being explored as potential nanomaterials for photothermal therapy in an attempt to reduce the amount of gold used and to codeliver drugs[105]. Since gold shell particles retain exterior characteristics found with other gold particles, they can be conjugated to targeting moieties, PEG, or other ligands in a similar manner.

Lowery et al. describe an *in vitro* experiment to test the photothermal effectiveness of a targeted 110 nm diameter silica core/11 nm thick gold shell [95]. The particles were conjugated to the anti-HER2 antibody and PEG and were subsequently incubated with a combination of SK-BR-3 HER2 positive breast carcinoma cells and MCF-7 HER2 negative breast carcinoma cells and irradiated (820 nm, 0.8 W/cm^2). The particles selectively attached to the HER2 positive cells and demonstrated the capability to specifically eliminate HER2 positive cells when both cell types are incubated with particles and irradiated simultaneously. Day et al. examine a similar particle composed of 120 nm diameter silica cores surrounded with 15 nm thick gold shell for its photothermal

therapy potential *in vivo*[99]. The particles were coated with PEG and injected into the veins of mice with tumors of firefly luciferase expressing U373 glioma cells. Although significant accumulation was seen in the liver and spleen, a substantial portion of the nanoshells accumulated into tumor space and were demonstrated to be effective in eliminating cancerous lesions through photothermal heating (800 nm, 4 W/cm^2). Some of these lesions reoccurred around day 20, while some mice experienced complete remission with the laser + nanoshell therapy. Rylander et al. describe optimizing photothermal therapies *in vivo* using gold nanoshells around the production of heat-shock proteins (HSP) acting as cellular chaperones, increasing cell fortitude after initial non-lethal treatment[102]. With additional refinement in nanomaterial formulation resulting in optimized biodistribution and targeting, these silica core/gold shell nanoparticles have the potential to be an attractive choice for *in vivo* photothermal therapy.

Ji et al. describe a superparamagnetic iron oxide (SPIO) core-gold shell particle with a silica interface for use in both MR imaging and photothermal therapy[103]. SPIO particles with a 10 nm diameter core were coated with a 28 nm thick silica layer and subsequently underwent the deposition of an 8 nm thick gold exterior layer. These particles were then coated with PEG to yield both water solubility and biocompatibility. In addition to demonstrating the magnetic capabilities of the particles, the photothermal effect of these nanoshells was examined in solution for temperature increases as a function of concentration (808 nm, 10.4 W/cm^2). While these particles demonstrated favorable heating and magnetic properties on the benchtop, significant *in vitro* and *in vivo* work needs to be completed to determine the feasibility of these particles as a photothermal therapy. Dong et al. detail the synthesis of SPIO core-gold shell

nanoparticle via a one-pot synthesis method via the formation of polymeric micelles; this method encapsulates the SPIO particles and provides a surface onto which to deposit the gold shell[104]. The particles are tuned to absorb in the NIR region and are subsequently incubated with MCF-7 human breast adenocarcinoma cells. Without laser irradiation, the cells showed no change in viability; however, when irradiated with a laser (808 nm, 2 W/cm^2), the viability of cells dropped significantly. Similar heating results were seen *in vivo*, with the combination of MR imaging and photothermal heating demonstrated in mice. Additional work is needed to examine the particle's effect on *in vivo* tumors and the effect of adding targeting molecules.

An interesting new area of photothermal research revolves around the use of polymers as the core material surrounded by a gold shell. Ke et al. describe the use of poly(lactic acid), poly(vinyl alcohol), and poly(amine hydrochloride) in conjunction with a gold shell for photothermal therapy[110]. These particles exhibit no sharp peak in absorption and instead are highly absorptive across the entire NIR window, which lends itself to use with multiple laser wavelengths. In addition to photothermal properties, these particles can be used as an ultrasound contrast agent, demonstrating the capability to simultaneously image and treat tumors. When irradiated, this polymer system exhibited a large temperature increase and a correspondingly decreased viability of HeLa cells *in vitro* (808 nm, 4 or 8 W/cm^2). Although their potential *in vivo* has not been examined, these particles demonstrate the capability to be used as both an imaging and agent therapy for cancer. Park et al. describe the use of a poly(lactic-co-glycolic acid) (PLGA) gold half-shell nanoparticle system for both photothermal therapy and chemotherapeutic drug release for the eradication of cancerous lesions[109]. Doxorubicin-containing PLGA

particles in a monolayer were coated with a 15 nm thick gold layer, yielding particles with a half-shell of gold. Without the addition of doxorubicin, these particles did not cause significant photothermal heating (808 nm, 0.7 W/cm^2), but with the addition of chemotherapeutic drug, the therapy is extremely effective at eliminating HeLa cells *in vitro*. Interestingly, the amount of doxorubicin released from the particles increases with NIR irradiation (808 nm, 1.5 W/cm^2) and showed a change in nanoparticle morphology following irradiation, as shown in **Figure 2.9**. The combined chemotherapy and photothermal therapy gave a greatly enhanced therapeutic efficacy. The addition of targeting ligands and *in vivo* studies are necessary to determine the potential of this particle as a photothermal therapy, though initial *in vitro* experiments indicate favorable results.

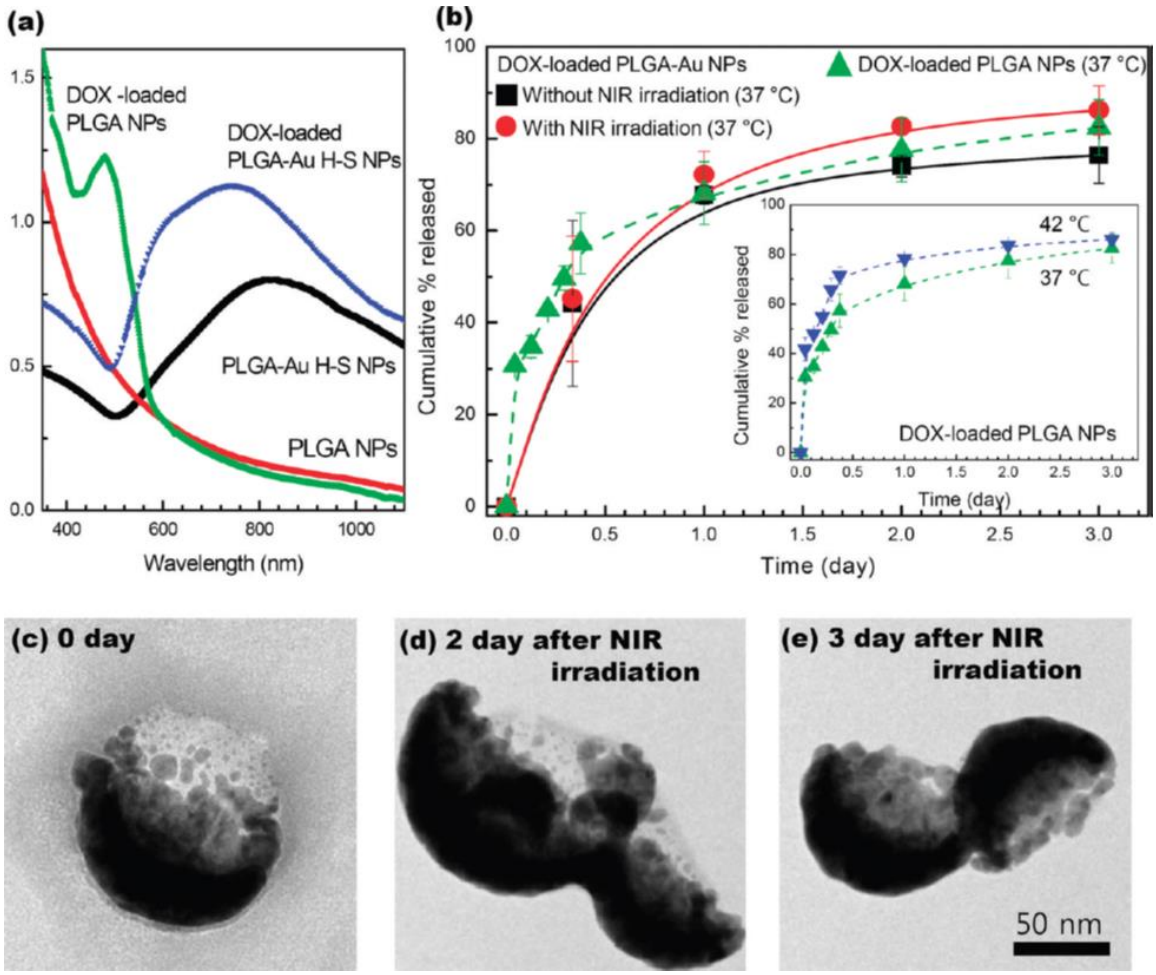

Figure 2.9. (a) Absorption spectra of PLGA NPs, PLGA-Au half-shell NPs, DOX-loaded PLGA NPs, and DOX-loaded PLGA-Au half-shell NPs. (b) DOX release from complex with and without NIR irradiation. TEM images of DOX-loaded PLGA-Au half-shell NPs as prepared (c), 2 days after NIR irradiation (d), and 3 days after NIR irradiation (e). From ref 109, H. Park, J. Yang, J. Lee, S. Haam, I.-H. Choi, and K.-H. Yoo, Multifunctional Nanoparticles for Combined Doxorubicin and Photothermal Treatments. *ACS Nano*. 3, 2919-2926 (**2009**). Copyright@ American Chemical Society.

2.4.1.4 Other gold particles Gold particles of variable shape are commonly examined as potential photothermal therapy options due to the potential for gold particles to have a high rate of conversion from light to heat through plasmon resonance. These particles include gold nanocages[111-114], stars[115-117], antennas[118] and popcorn-shaped particles[119, 120] just to name a few. These particles retain the capability to conjugate targeting ligands and PEG to their exterior similarly to other gold particles. Due to the

large number of particles and their variability, only a few examples will be discussed here.

Chen et al. describe a gold nanocage system conjugated with anti-HER2 to selectively target and eliminate HER2-positive breast cancer cells through photothermal heating[112]. Gold nanocages are cube-shaped particles with an edge length of 45 nm and wall thickness of 3.5 nm that highly absorb light in the NIR range. When HER2-targeted gold nanocages were incubated with SK-BR-3 breast cancer cells, there was significant heat generation to kill cells (810 nm, threshold power density of 1.5 W/cm^2 to kill cells). As expected, with increasing laser power density, cell viability decreased and the damage area was increased. Additional study with *in vivo* experiments to evaluate the potential to eliminate cancer lesions and biodistribution upon delivery is needed, but gold nanocages remain an alternate particle for use in photothermal therapy.

Yuan et al. describe the use of a gold nanostar conjugated to the TAT peptide for targeted photothermal therapy[115]. Gold nanostars offer an increased surface area to volume ratio compared to their spherical counterparts, offering the opportunity to conjugate a high concentration of ligands on their surface. In addition, these particles absorb light in the NIR region and, when incubated with BT549 breast cancer cells and irradiated, they demonstrated their therapeutic efficacy (850 nm, 0.4 W/cm^2). These gold nanostars demonstrated their thermal generating ability with a much lower power density than is required with other gold systems, making them an attractive candidate for a translatable photothermal therapy. Additional study *in vivo* is needed to fully demonstrate their capability to eliminate cancer lesions.

2.4.1.5 Issues and Advantages with Gold The use of gold nanoparticles for photothermal elimination of cancer lesions has many advantages. The ability to precisely control the size and shape of particles to create a material tailored to a particular application offers a unique opportunity to provide a personalized approach to photothermal therapy based on the type of cancer lesion. In addition, many gold particles can be imaged using SERS, as discussed in an earlier section. Conjugation to many types of ligands, including antibodies and PEG, is done relatively easily, which adds to the ability to tailor particles for a specific application. Gold particles are also well established in literature, with many groups already attempting animal studies with varied success.

Despite many advantages to working with gold particles, there are also a number of drawbacks. The quantities of gold needed for effective photothermal therapy may be harmful when concentrated in a specific area over an extended period of time; more study on the effects of long-term gold exposure at these elevated levels is needed before clinical translation can occur. In addition, many existing *in vivo* studies show significant accumulation of gold particles in organs of the RES system, including the spleen and liver. The cytotoxic side effects must be elucidated for the concentrations of particles being used for photothermal therapy. In terms of laboratory use, the reagents used to clean and break down gold residues (e.g. aqua regia) are extremely hazardous and corrosive. Large batch synthesis of these particles has many barriers associated with logistics and safety. In addition, the high cost of gold used in these reactions is a major barrier to the feasibility of gold particles in a clinical setting. If these obstacles can be overcome, gold particles offer a diverse and efficient platform for use with photothermal therapies.

2.4.2 Other Metals

Although gold offers many advantages as a photothermal therapy, there have been a number of groups investigating particles composed of other metals. Many of these offer an additional benefit of natural occurrence in the human body, alleviating many concerns of toxicity when translated to an *in vivo* therapy. The choice of metal is broad and can include silver[111, 121-124], silver/gold composites[124-127], copper[128-130], germanium[131, 132], silicon[133-135], iron/cobalt[136, 137], titanium oxide[138], and lanthanides[139], among others.

2.4.2.1 Silver and Silver/Gold Composites Although examples of pure silver nanoparticles are few and far between, silver is often used in combination with other metals, either in a core-shell form or in a composite[111, 122, 124-127, 140] Silver mimics many of the useful properties of gold, such as the ability to tune surface plasmons to a particular wavelength and the ability to heat significantly upon irradiation[111], while significantly reducing the high costs associated with gold. In addition, the ability to conjugate targeting molecules such as folic acid or aptamers is retained in particles with a silver surface [121, 124, 125].

Boca et al. describe a chitosan-coated silver triangular particle for *in vitro* photothermal treatment of human non-small cell lung cancer cells[121]. When this particle was incubated with healthy cells (HEK, human epithelial kidney cells), no cytotoxic effects were seen; however, when incubated with cancer cells, the chitosan-coated silver particle caused a decrease in cell viability by up to 25%. When irradiated, these particles demonstrated the ability to cause photothermal destruction to the cancer cells (800 nm, 12-54 W/cm^2). In addition to proving the feasibility of silver nanoparticles for photothermal applications, Boca et al. also compared the silver triangles to gold

nanorods, finding that gold had a greater cytotoxic effect on cells but needed more laser energy to induce photothermal damage. With additional work into the surface functionalization and *in vivo* work with these particles, they could become a viable option for photothermal treatments of cancer.

When used in a gold core-silver shell system, the silver coating has a significant effect on the properties of the particle; Lu et al describe a significant blue shift of the peak absorbance when the ratio of silver to gold was increased[140]. However, these particles can be used in the NIR range, as Wu et al have described the use of a gold-silver core-shell particle conjugated to a targeting aptamer that can be used for both SERS and photothermal therapy[125, 127]. When incubated for significant time intervals (5-60 minutes) under NIR radiation, these particles show the ability to photothermally destroy MCF-7 breast cancer cells (808 nm, 0.06-0.25 W/cm^2). As expected, with increased irradiation time and power density, the viability of the cells *in vitro* drops significantly (approaching zero at times nearing 1 hour and at power densities above 0.25 W/cm^2). Additionally, these targeted particles demonstrate the ability to selectively destroy cancer cells when compared to identical therapies experienced by MCF-10A normal breast epithelial cells. As a translatable therapy, concerns of long-term cytotoxicity and biodistribution associated with exposure to these metals must be overcome for these to be a significant contribution to the clinic. With additional work with *in vivo* studies, toxicity, and fine-tuning the ideal laser parameters, gold core-silver shell particles could be a viable choice as a translatable photothermal agent.

2.4.2.2 Copper Copper particles offer a biocompatible alternative to many other types of metals and provide a size advantage not seen with many other nanoparticles for

photothermal therapies. The size of copper particle necessary for significant heating is much smaller than its gold counterpart, making the overall metal dose less as well as offering a size that is more readily internalized into tumors and cancer cells[128]. While the photo-based generation of heat from gold particles is largely dependent on the formation of surface plasmons, heat generation of copper particles is based on energy band-band transitions, offering an alternate mechanism to generate heat in biological tissues[129]. While work with the attachment of targeting molecules to the surface of copper particles is not widespread, copper has demonstrated the ability to complex with amphiphilic polymers[128], drugs [74] and PEG[130].

Li et al. describe the formation and use of copper sulfide (CuS) nanoparticles for photothermal therapy[129]. The particles had an observable crystal lattice structure, with an average diameter of 3 nm and relatively high absorption of NIR light. In solution, copper sulfide particles demonstrated a significant rise in temperature, and *in vitro* studies show the capability to eliminate HeLa cells under irradiation (808 nm, 24, 40, or 64 W/cm^2). Although the copper chloride solution used to form particles causes significant cytotoxicity at high concentrations, copper sulfide nanoparticles do not exhibit this cytotoxicity and outperform gold nanorods at equivalent concentrations. There is no significant change in viability for any particle type below 10 μM. With the addition of targeting molecules and work *in vivo*, copper sulfide particles offer a biocompatible alternative to gold particles.

Hessel et al. demonstrate the use of a 16 nm copper selenide nanocrystal for use in photothermal therapy[128]. These particles are surrounded by amphiphilic poly(maleic anhydride)-based polymers that lend water stability while sequestering the nanocrystal

from interaction with biological entities. The exterior carboxylic acid groups on the polymer offer an opportunity to attach targeting or other ligands, though this work has not yet been performed. When compared with gold nanoshells and gold nanorods, the copper selenide nanocrystals demonstrate equivalent temperature changes while also exhibiting increased photothermal transduction efficiency. When incubated with HCT-116 colorectal cancer cells, no cytotoxicity was seen until irradiation (800 nm, 30 W/cm^2). These particles offer an alternative platform that outperforms gold, however significant work with *in vivo* studies and the addition of targeting ligands needs to be performed before their true potential can be elucidated.

2.4.2.3 Issues and Advantages to Other Metals While research into using metals other than gold for photothermal therapy is limited, they offer many advantages. Although each specific material has its own benefits, all metals used for photothermal therapies outside of the traditional gold have one outstanding benefit: reduced cost. With the expense of both the materials and the significant infrastructure needed for maintaining gold nanoparticles in a laboratory setting, alternative metals provide a viable choice for a less expensive alternative. This will influence the cost of future scale-up of nanoparticle synthesis if these are ever translated to a clinical setting.

However, despite all the individual advantages that alternative metals offer, gold remains the leading metal of choice for photothermal therapy. A significant amount of research is put into investigating gold nanoparticles every year by researchers spanning the globe; the rate of advancement of gold nanoparticle research far outpaces any other metal. In addition, the creation of surface plasmons and their relative intensity is well documented, bypassing years of research required for the use of a new particle type.

Finally, with the advances of SERS and photoacoustic imaging, the multifunctionality of gold particles has been demonstrated many more times than other particle compositions. Although the ultimate future of nanoparticle-mediated photothermal therapy may lie away from gold particles due to cost of materials, it will take years to reach the level of knowledge and research put into another particle type.

2.4.3 Carbon Particles

2.4.3.1 Graphene Oxide Graphene is a monolayer of carbon atoms forming a 2D (flat) structure. Graphene has a demonstrated potential as a drug carrier [141] and as a photothermal agent [142, 143] through the transfer of vibrational energy to surrounding biological media and induction of oxidative stress [142]. Its oxidized counterpart, graphene oxide, has been proven to have enhanced heating properties when compared to pristine graphene. Despite concerns of cytotoxicity associated with both of these forms of graphene, coating with biocompatible moieties alleviates much of this concern[141, 144, 145].

In a study to examine the effect of graphene oxide heating, Yang et al. describe attaching Cy7 fluorescence labeled PEG to the surface of graphene oxide to increase biocompatibility, water solubility, and lend fluorescence[146]. When irradiated in solution, the modified graphene exhibits a significant rise in temperature to 50°C (808 nm, 2 W/cm^2). Accordingly, when mice with 4T1 tumors were injected intravenously with the graphene oxide and subsequently irradiated, tumor volume drops to 0 and the survival rate of these mice remains at 100% after 40 days. Even more striking is the buildup of non-targeted particles into tumor space, with accumulation in tumors outnumbering accumulation in all other organs, as shown in **Figure 2.10**. With additional components such as chemotherapeutics and targeting agents and additional study in pharmacokinetics

and biodistribution, these particles have the potential to become a leading candidate for photothermal therapies.

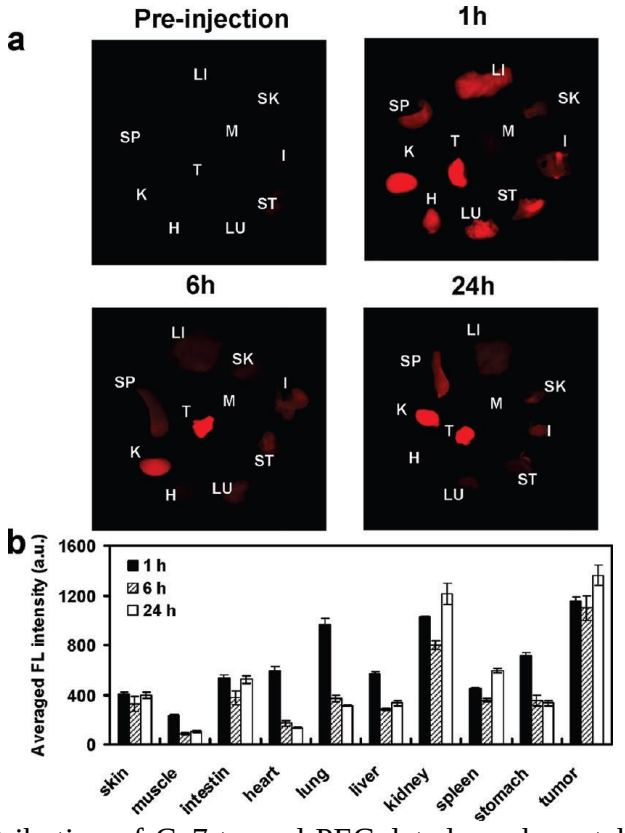

Figure 2.10. Biodistribution of Cy7-tagged PEGylated graphene taken at different time points. After initial accumulation in RES system (a, 1 hour), the tumor volume continues to retain high levels of the particles (a, 24 hour). Corresponding fluorescence intensity numbers shown in (b). From ref 146, K. Yang, S. Zhang, G. Zhang, X. Sun, S.-T. Lee, and Z. Liu, Graphene in Mice: Ultrahigh In Vivo Tumor Uptake and Efficient Photothermal Therapy. *Nano Letters*. 10, 3318-3323 (**2010**). Copyright@ American Chemical Society.

In seemingly contradictory results, Zhang et al. discuss the addition of doxorubicin to the graphene oxide-PEG conjugate for use as a photothermal therapy *in vivo*[141]. Doxorubicin was added to the graphene oxide through a simple mixing process, and when combined with NIR heating, showed an increase in the cellular inhibition rate compared with free doxorubicin (808 nm, 2 W/cm^2). When particles were injected intravenously into the tail veins of mice with EMT6 murine mammary tumors, growth of

tumors was inhibited only slightly with free doxorubicin or with NIR irradiation of particles alone. However, when both doxorubicin and heating treatments were combined, a significant decrease in tumor volume was seen in comparison to other treatment groups and controls. The addition of chemotherapy to graphene oxide is a seemingly good addition for use in photothermal therapies, but contradictions with other work should be examined in detail before the translational potential of graphene oxide can be realized.

Graphene oxide, like most nanoparticles, has the ability to conjugate to other nanomaterials to create a multifunctional complex. Ma et al. discuss the use of iron oxide superparamagnetic particles in conjunction with doxorubicin and graphene oxide to create a hybrid nanocomplex for magnetically targeted drug and photothermal therapy[147]. Although particles lacking doxorubicin are not cytotoxic at even high concentrations (up to 100 mg/L), graphene oxide-iron oxide-doxorubicin conjugates show a decrease in viability similar to that seen with free doxorubicin. When incubated with 4T1 murine breast cancer cells, they demonstrate the use of graphene oxide-iron oxide conjugated for magnetic targeting as well as the ability to photothermally destroy cells (808 nm, 1 W/cm^2). Although *in vivo* photothermal therapy and therapy in conjunction with doxorubicin was not examined, there is potential for these conjugates to deliver a magnetically targeted drug and photothermal therapy. In an effort to use fluorescence imaging, Hu et al. discuss a multifunctional particle composed of graphene oxide conjugated to QDs[31]. They use two different sized graphene oxide particles (38 nm and 260 nm) conjugated to three different colored QDs (550, 570, and 600 nm emission) and folic acid to demonstrate the ability to resolve different colored QDs *in vivo.* When used *in vitro*, they demonstrate the ability of these graphene oxide conjugates to kill cells as a

function of increased laser irradiation time (808 nm, 2 W/cm^2), as seen in **Figure 2.11**. It is also interesting to note that a loss of fluorescence signal is seen from the QDs upon irradiation, indicating that oxidation and heat could cause a loss of fluorescence signal. With further *in vivo* study and a better understanding of the loss of fluorescence signal, these particles could be used as an effective photothermal therapy with the added benefit of a marker to indicate therapeutic efficiency.

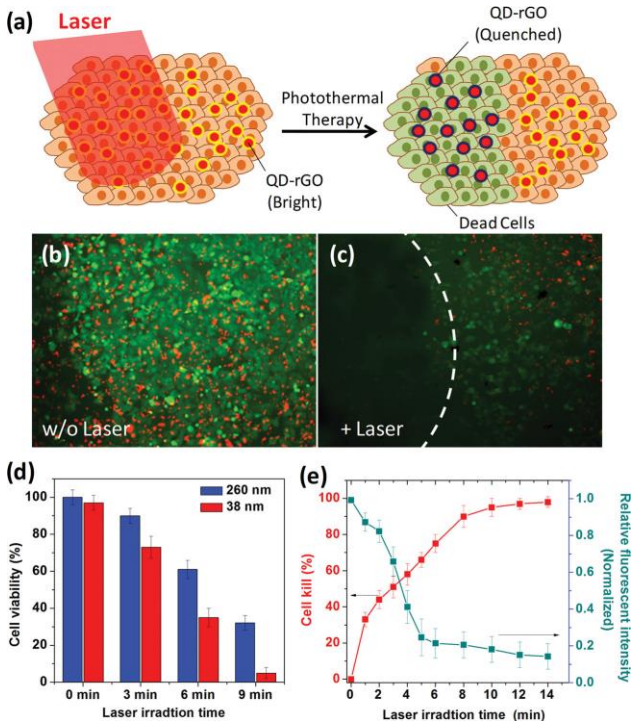

Figure 2.11. (a) Schematic of QD-graphene under irradiation and subsequent QD quenching. (b and c) Images corresponding to the schematic showing QD quenching. (d) Decrease in cell viability with increasing laser irradiation time and decreasing particle size (260 nm vs. 38 nm). (e) Cell death and normalized fluorescence intensity as a function of laser irradiation time, showing both QD quenching and increased cell death. From ref 31, S.-H. Hu, Y.-W. Chen, W.-T. Hung, I. W. Chen, and S.-Y. Chen, Quantum-Dot-Tagged Reduced Graphene Oxide Nanocomposites for Bright Fluorescence Bioimaging and Photothermal Therapy Monitored In Situ. *Advanced Materials*. 24, 1748-1754 (**2012**). Copyright@ John Wiley and Sons.

2.4.3.2 Carbon Nanotubes When graphene sheets roll into tubes via a chemical catalyst, they form a class of nanoparticles called carbon nanotubes (CNTs)[142]. These particles can reach up to a few microns in length and can be formed from either a single graphene sheet (single walled, SWNTs)[60, 148-154] or many graphene sheets (multi walled, MWNTs)[142, 155-158]. In the CNT form, the graphene sheets retain their high absorption in the NIR region coupled to significant heating and oxidative stress with the benefit of added surface area and volume to attach drugs[150] and targeting moieties [60, 142, 148]. In addition to these qualities, CNTs can be used for imaging with Raman spectroscopy, as discussed previously[60].

In a demonstration of photothermal therapy with SWNTs, Zhou et al. describe a method to use nanotubes with an average diameter of 0.81 nm that possess an intense absorption band at 980 nm for use in targeted therapy[148]. When irradiated with NIR light while in solution, these SWNTs induced a temperature rise up to 20°C more than laser alone (980 nm, 1 W/cm^2). For use *in vitro* with murine mammary tumor cells EMT6, SWNTs were conjugated to folic acid, incubated with cells, and irradiated; this caused a decrease in cell viability that corresponded to the concentration of particles and laser power (0.5 or 1 W/cm^2). When injected into tumors *in vivo*, these targeted particles demonstrated a similar rise in temperature compared to that seen in solution, while demonstrating the ability to induce cell death (1 W/cm^2). Interestingly, the percentage of cell death was higher in tumor sections than normal sections, and targeted particles irradiated in the normal section induced less cell death than their non-targeted counterparts. Additional study into the biodistribution and long-term effects still must be

performed with this particle to determine its potential as a translatable photothermal agent.

In an effort to demonstrate the use of SWNTs compared to gold nanorods for photothermal therapy with *in vivo* mouse tumors, Robinson et al. discuss a protocol using 140 nm SWNTs[60]. For this study, both gold nanorods and the SWNTs were conjugated to PEG to facilitate a longer circulation time and biocompatibility; in solution, SWNTs demonstrate an increased absorbance of light across all wavelengths at the same concentration. When SWNTs were injected into mice with 4T1 tumors on both shoulders, SWNTs demonstrated the ability to generate temperatures up to 55°C when irradiated (808 nm, 0.6W/cm^2) that resulted in a decrease in tumor volume and improved survival (100% for up to 60 days). When gold nanorods were injected into these mice and irradiated with similar laser parameters (808 nm, 0.6 W/cm^2), there was no significant rise in temperature when compared to the laser alone and tumors continued to grow; significant temperatures increases and decreases in tumor volumes were seen with a higher laser power (2 W/cm^2). Continued work with biodistribution to improve biocompatibility and addition of targeting agents and drugs to SWNTs will bring the next generation of photothermal therapy with SWNTs.

In addition to therapies with SWNTs, MWNTs are demonstrated as an effective therapy to eliminate breast cancer stem cells in work performed by Burke et al[155]. These MWNTs are around 591 nm in length with an average diameter of 29 nm and functionalized with amine groups. Cells grown *in vitro* and exposed to sub-cellularly localized heat showed a significant drop in surviving fraction when compared to controls; both stem cells and bulk cells were affected by this heat generation (1064 nm, 3 W/cm^2).

Cells exposed to MWNT therapy formed significantly smaller tumor spheres when compared to controls, indicating a decrease in both bulk cells and stem cells. In an effort to compare results with other forms of hyperthermia, experiments were done with water bath heating that indicated that stem cells did not respond to bulk heating (though bulk cancer cells responded similarly) and increased production of heat shock protein 90. This indicates the value of MWNT therapy to eliminate bulk and stem cells in tissue, a theory that is supported by the ability to improve survival in stem cell driven breast tumors *in vivo* that were administered localized heating by nanotube therapy. Further work performed by Fisher et al. and Burke et al. describe the use of MWNTs for NIR photothermal therapy to treat human prostate cancer (PC3) and murine renal carcinoma (RENCA)[156, 157]. These studies examined both *in vitro* and *in vivo* response of cancer cells to MWNTs under NIR irradiation (1064 nm, 3 and 15.3 W/cm^2), concluding that MWNTs are a viable option as a clinical photothermal agent. Although additional work into biodistribution and *in vivo* testing is needed, MWNTs combined with NIR light could prove to be a relevant method for use in resistant tumors.

2.4.3.3 Carbon Nanohorns Single-walled carbon nanohorns (SWNHs) are composed of graphene sheets that have been rolled into cones rather than tubes (such as seen in SWNTs)[159, 160]. Many of these individual nano-cones aggregate together to form an overall spherical structure[160] which has both an internal space for drug loading[161-166] and significantly increased surface area for conjugation[41, 167]. Because the method of synthesis involves laser ablation instead of chemical or metal catalysts, there is little concern for toxicity of the particles[159, 160, 168]. Like other forms of graphene, SWNHs have

demonstrated the capability to absorb significantly in the NIR region, making them attractive candidates for photothermal therapy[167, 169-173].

Whitney et al. describe the use of SWNHs in conjunction with laser irradiation to kill RENCA cells[169]. As expected, cell viability decreased with increased particle concentration and increased laser exposure time (1064 nm, 40 W/cm^2). In a subsequent study also by Whitney et al., the capability to induce cell death in MDA-MB-231 breast cancer cells with SWNHs in 3D tissue phantoms was determined[171]. Sodium alginate solutions seeded with MDA-MB-231 cells were exposed to varying concentrations of SWNHs and allowed to cross-link to form gel phantoms. When irradiated (1064 nm, 3.8 W/cm^2), three regions of cell viability were created within the phantom: kill zone (where cell viability was 0%), transition zone (where cell viability was between 0 and 75%), and untreated zone (where cell viability was above 75%). The corresponding temperature maps draw direct correlations between temperature and viability and highlight temperature variance as a function of depth into the phantom. This research not only highlights the use of SWNHs for photothermal therapy, but also demonstrates the importance of using 3D tissues and computations to both evaluate and predict the outcomes of photothermal treatments.

In addition, SWNHs have been demonstrated for their use in conjunction with other functionalities and devices, such as fiberoptic microneedles for delivery[173], QDs for fluorescence imaging[40], chemotherapeutic agents[41], or magnetite for MR imaging[174].

2.4.3.4 Issues and Advantages of Carbon Particles Carbon particles offer many advantages over metal particles including relatively inexpensive cost and prevalence of carbon in living systems. Biological systems are riddled with carbon species, which

makes carbon-based nanoparticles an attractive choice for use *in vivo*. In addition, the lack of toxic catalyst seen in some synthesis methods for carbon particles limits the exposure of cells to potentially harmful metals. Because graphene is readily available, synthesis procedures are often easier than fabricating metal particles with the added benefit of reduced cost.

Although carbon is readily found in living systems, the use of graphene in any form has posed cytotoxicity concerns possibly due to metal catalysts or aspect ratio, necessitating the use of polymers to lend biocompatibility. The use of metal catalysts may account for a fraction of toxicity concerns, but long-term effects of carbon particles has not been examined *in vivo*. Contrary to metal particles, carbon particles do not carry the capability to tune absorption to a specific wavelength due to the lack of surface plasmon resonance. This limits the wavelengths that can be used for photothermal therapy with carbon particles. In addition, similar to that seen with metals other than gold, the use of carbon particles for photothermal therapy is not as widespread as that seen with gold. This limits the research that is performed with carbon nanoparticles, which confines the number of scientific questions that can be answered in a given time period. With additional development of the biocompatibility aspects of carbon particles, they have the potential to become a leading candidate for photothermal therapies.

2.4.4 Polymers

Because many polymers dissolve readily in biological solvents, they are not widely thought of as platforms for significant heating selectively near particles. However, a few groups are examining dense polymers that form particles that can absorb in the NIR for use in photothermal therapies. Cheng et al. describe a PEGylated PEDOT:PSS

conductive polymer system conjugated to the fluorescent molecule Cy5 for use in treating 4T1 murine breast cancer *in vivo*[175]. When tumor-bearing mice injected with particles were irradiated, the tumor volume shrank to zero and the survival of the mice up to 45 days remained at 100% (808 nm, 0.5 W/cm^2). While these results are similar to those seen with other nanoparticle platforms, the novelty of this polymer system is its ability to accumulate in the tumor at significantly higher rates than many other particles. As shown in **Figure 2.12**, passive accumulation into tumor space mimics that seen in the liver; with the addition of a targeting agent to this system, particle accumulation in tumors may pass that seen in the liver or spleen. With many concerns of organ toxicity associated with nanoparticles, this system offers a viable alternative that can minimize damage seen to RES organs. When looking to the future, polymers offer the ability to fine tune structure and functionality relatively easily, while often offering features such as biodegradability. Polymers may ultimately be the future of photothermal therapies because of these unique features that bypass many concerns associated with other nanoparticle platforms.

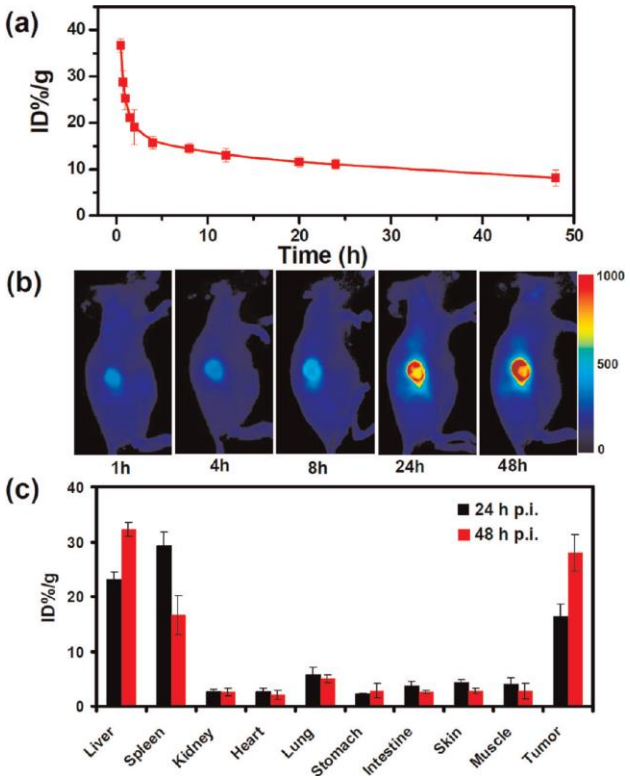

Figure 2.12. PEDOT:PSS-PEG-Cy5 polymer system demonstrating exit of circulation after injection (a) and accumulation of particle in tumor site with increased circulation time (b). Fluorescence intensity of organs indicating a large percentage of tumor uptake of particles (c). From ref 175, L. Cheng, K. Yang, Q. Chen, and Z. Liu, Organic Stealth Nanoparticles for Highly Effective in Vivo Near-Infrared Photothermal Therapy of Cancer. *ACS Nano*. 6, 5605-5613 (**2012**). Copyright@ American Chemical Society.

2.4.5 Translation of Photothermal Therapies to the Clinic

As photothermal cancer therapy approaches use in human patients, there are many considerations to take into account. When examining the change in temperature under particular laser and particle conditions, many studies use room temperature (~20°C) rather than physiological temperature (37°C) as a baseline. While this may give more favorable temperature changes for research, using these cool baseline temperatures does not give a correct indication of therapy parameters necessary for equivalent temperature changes that will be seen *in vivo*. In addition, the use of 2D *in vitro* culture setups does not lend data comparable to a 3D system. The difference in cell morphology and response

to other therapies is widely documented, motivating a movement to 3D culture systems for evaluation of these photothermal therapies. Finally, a major barrier to overcome before clinical use is the wide variety of parameters used for nanoparticle-based photothermal therapy, including the type of particle, laser wavelength, laser power, nanoparticle concentration, and exposure time. These major differences between the most widely used gold particles are highlighted in Table 1. There are no two groups using the same parameters listed in the table, which does not include the injection site for *in vivo* work or the type of cell treated. The standardization of these parameters is necessary before clinicians will attempt these therapies; using a different set of parameters for every specific application *in vivo* is not a viable option to present to clinicians. However, with these few changes, nanoparticle use with photothermal therapies presents an excellent choice for the treatment of a wide variety of cancers.

2.5 Photodynamic Therapies

Photodynamic therapy (PDT) is a relatively older treatment modality, originally developed and tested in the 1960s and 1970s, which is showing new promise due to the recent combination with nanomaterials. PDT is a minimally invasive treatment which utilizes localized photochemical reactions between delivered light and exogenous photosensitizing agents (PS). The mechanism behind PDT therapies has been extensively described elsewhere in detail[176, 177]. Briefly, PDT can be thought of as treatment comprised of 3 components: light, photosensitizers, and molecular oxygen[178]. The treatment itself occurs by initially administering the photosensitizer either locally or intravenously which subsequently begins to accumulate in fast dividing cells, making it ideal for use with cancer cells[179]. Light is then delivered to the tumor region to activate

the PS agent to its excited states which can then undergo two well defined mechanisms for producing cytotoxic reactive species[180]. The first of these reactions, a Type I reaction, occurs when free radicals or superoxide ions result from hydrogen or electron transfer; Type II reactions occur when $^1O_2$ (singlet oxygen) is generated from collisions of free oxygen with the excited PS agent. It is well documented that the singlet oxygen generated from the Type II reaction is the primary reactive oxygen species (ROS) produced in PDT and is responsible for damaging nearby biomolecules, resulting in cell death through apoptosis[181]. PDT provides a localized treatment option due to the short half-life of ROS produced under laser excitation, resulting in limited diffusion. PDT is currently clinically approved and is being tested to treat many types of cancers including prostate[182], pancreatic[183], and lung[184], along with many others[185]. Dolmans et al. provides a great review of the overall process of PDT which was briefly described above[176]

2.5.1 Photosensitizers

The overall effectiveness of PDT treatments and thus the ability to be clinically translatable is determined primarily by the degree of singlet oxygen production[186]. While many factors may affect how efficiently singlet oxygen species are generated such as light intensity and wavelength, much attention has been recently focused on how to improve photosensitizers and light properties[187]. Allison et al. recently reviewed current clinically used photosensitizers[188]. They discuss how there are a small number of structures that are capable of interacting with light to allow for an energy transfer capable of the Type II photochemical reaction necessary for ROS formation. Selection of PS agents is highly dependent upon finding a molecule with acceptable energy conversion at certain wavelengths of light. Since tumors are often found deep in the body, PS agents

have been developed to have higher activation at longer wavelengths of light as the NIR region boasts higher depth of penetration and lower absorption of endogenous chromophores. Of these potential PS agents, Photoforin®, ALA, Phthalocyanines, and methylene blue (MB) are the most studied due to their Type II reactions and optimized activation wavelength in the NIR region. Overall, a PS agent can be classified as a compound that is nontoxic until it is activated by a light source, which then starts a photochemical reaction resulting in ROS formation. The utilization of free PS agents, like previously mentioned agents, is currently limited by degree of accumulation in target tissue and degradation of the PS molecule by biological fluids.

2.5.2 Nanoparticle Carriers

It has previously been stated that PDT is defined by 3 major stages: excitation of a PS agent, generation of toxic O_2 molecules, and cell death[189]. However, we consider another important stage in the treatment which has a major effect on treatment efficacy: delivery of agent to the tumor. It is well known that selective delivery of drugs is one of the most important stages in many treatment modalities, with the possibility of higher drug localization occurring from more selective delivery and resulting in lower required dosage. Additionally, nanoparticles can be used to shield the PS from aqueous bodily fluids which often reduce the PS agent, thus limiting its ROS generating capabilities. Shielding the PS from the biological environment can also aide in retaining the agent in its monomeric form by reducing the potential for aggregation. Most importantly, nanoparticles can enable highly selective accumulation of the PS agent in the desired tumor region, reducing the dosage with little to no uptake by non-target cell. Nanoparticles offer the added benefit of lower prolonged skin photosensitivity after

treatment which a main side effect of PDT and one of the limitations of many PS agents[190].

2.5.3 Biodegradable Nanoparticles for PDT Treatment

Nanoparticles used in PDT have many primary functions, such as increasing circulation in blood and reducing interactions of the PS agent and water, but a feature that must be considered while developing a clinically feasible nano-delivery system is the biocompatibility of the carrier particle. Polymer based nanoparticles offer an avenue for exploration due to their tunability, both for biocompatibility and for biodegradability. Biodegradable polymer based nanoparticles were first explored in the early 1990s by Brasseur et al. in which they looked at the potential of loading the PS agent hematoporphyrin in poly(alkycyanoacrylate) nanoparticles[191]. Their results from this study were somewhat promising, but the polymer choice resulted in low carrying capacity and a steep release profile. Overall, polymers and liposomes make great choices for nanoparticle materials due to their adaptable chemistry which makes their properties easily tunable, which has been the primary focus of research in the past two decades, resulting in new material consideration to overcome the shortcomings mentioned in early studies. The main processes studied which will be mentioned subsequently are: polymer choice, drug loading properties, controlling drug release, and the addition of active targeting modalities to polymer-based systems to allow for greater intracellular accumulation in the tumor region[187].

2.5.3.1 Liposomes Liposomes are phospholipid nanosized vesicles comprised of either multilamellar (liposomes) or unilamellar (micelles) layers that allow for incorporation of hydrophilic drugs into their matrix through encapsulation of an aqueous

compartment containing drugs. This is accomplished through the spontaneous ordered arrangement of the hydrophilic heads and hydrophobic tails of the phospholipids. Liposomes can bind to cell membranes (also comprised of phospholipids) allowing for release of the carried PS directly into the intracellular space. Due to their ease of manufacturing and simple composition which do not require complex chemical steps, liposomes were some of the first biodegradable nanoparticles used for PDT[192]. Foslip® is a recently developed photosensitizer based on a new novel liposomal formulation[193]. Foslip® has shown greater efficacy and reduction of collateral damage compared to its non-liposomal formulation, Foscam. Additionally the PS agent ALA has been studied inside a cholesterol linked liposomal nanoparticle, showing greater stability in cell culture medium and increased penetration compared to free ALA[194].

In addition to taking advantage of the EPR effect, active targeting can be accomplished with liposomes through the conjugation of ligands to the liposomal surface. While many ligands have been studied, the addition of antibodies to the liposomes has shown great promise. This addition of antibodies to liposomes creates a new class of nanomaterial carriers coined immunoliposomes[195]. Recent studies have shown how PS agents such as pheophorbide can be encapsulated into immunoliposomes conjugated to antibodies against transferrin receptors which results in higher internalization[196]. Additionally, studies have shown that encapsulation of PS inside transferrin-conjugated PEG-liposomes can cause a 10-fold increase in efficacy compared to the free photosensitizer due to increased attachment of the nanoparticle and subsequent internalization of the drug[197]. The simple nature of liposomes, combined with the ability to add targeting modalities such as transferrin provide reasons to continue to study its

effects *in vivo* and provide a background to combine multiple modalities into one treatment option.

2.5.3.2 Polyacrylamide Nanoparticles Of the potential polymer material choices, poly(acrylamide)(PAA) has shown great promise as a biodegradable material for carrying PS agents[198]. While PAA possesses many qualities that make it a great nanoparticle choice for PDT therapy (including low inherent toxicity[199] and ease of functionalization through the addition of amine and carboxyl groups for surface modification[200]) one of its main features is its high hydrophilicity which reduces its likeliness to aggregate when administered systemically [201]. PAA nanoparticles used for carrying PS agents are usually produced to have an average diameter of 30-70nm, an optimal size range to harness many key events of the EPR effect[202]. PAA has been used to carry a variety of different PS agents including Photofrin® [203], MB[200, 204], and two photon adsorption PS agents[205].

Tang et al. describe how they were able to prevent reduction of the PS agent MB, by encapsulating the drug into a 30nm diameter PAA nanoparticle[204]. The PAA nanoparticles, by shielding the reduction effect of diaphorase plasma reducing enzymes, were able to improve the efficacy of the drug *in vitro* in C6 glioma cells. Using fluorescence emission at 680nm, they were able to show that the PAA nanoparticles remained stable in a PBS solution containing NADH and diaphorase for up to 60 minutes, whereas reduction of free MB occurred within minutes of excitation. This suggests that the embedded MB stayed intact during the administration of PAA particles. Building on this initial work, the Kopelman group was able to show an increased efficacy in an F3 peptide-targeted MB conjugated PAA nanoparticle[200]. The microemulsion polymerization used after conjugation of the MB dye to the PAA monomer resulted in

nanoparticles an average size of 50-60nm. The complexation of MB to PAA results in less leaching compared to encapsulated MB, which enables a greater control of the location of singlet oxygen production following light excitation. **Figure 2.13** shows confocal images of 4 different cancer cell lines (MDA-MB-435 and MCF-7 breast cancer cells, 9L glial cells, F98 glioblastoma cells) following illumination (647nm, 80μW, ca. 20J/cm^2) with either targeted or non-targeted MB-PAA nanoparticles. Their quantitative data, along with the confocal images, show how the targeting modality F3 enhances the efficiency of the PDT treatment. Additionally, this same nanoparticle formulation was used *in vivo* on 9L glioma tumor bearing rats and resulting in over 40% of the treated rats remaining tumor free after 60 days[203].

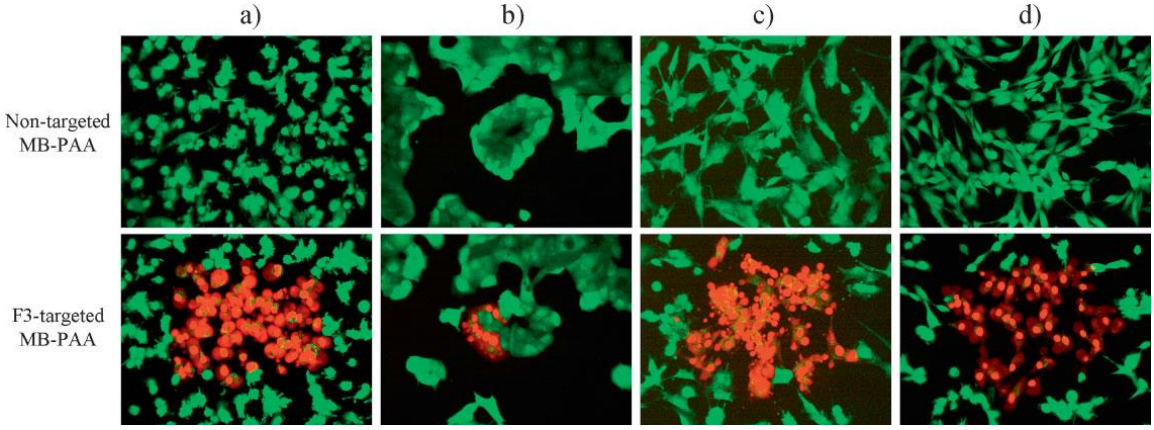

Figure 2.13. Confocal live (green)/dead (red) images of four cancer cell lines: (a) MDA-MB-435, (b) MCF-7, (c) 9L, and (d) F98 treated with PDT therapy with either F3 targeting (bottom) or non-targeted MB-conjugated PAA nanoparticles. From ref 200. H. J. Hah, G. Kim, Y. E. K. Lee, D. A. Orringer, O. Sagher, M. A. Philbert, and R. Kopelman, Methylene Blue-Conjugated Hydrogel Nanoparticles and Tumor-Cell Targeted Photodynamic Therapy. *Macromolecular Bioscience*. 11, 90-99 (**2011**). Copyright@ John Wiley and Sons.

Two-photon dyes have the ability to convert low-energy absorbed light into higher energy emissions and can therefore directly transfer this higher energy to oxygen to create singlet oxygen. They have an advantage due to lower energy light traveling deeper into tissue to activate the agents. While many dyes have been tested, they have inherent toxicity which makes them a non-ideal choice for PDT. However, by entrapping two-photon dyes into nanoparticles, toxicity can be reduced while still utilizing deeper light penetration for activation. Gao et al. used a microemulsion technique to incorporate porphyrin tetra(p-toluene-sulfonate) (TMPyP) into PAA nanoparticles[205]. The results of this study were promising, with cell death occurring after 90 minutes of treatment following exposure to 100mW/cm^2 780 nm pulsed light. This study provides a foundation for further research to test how to properly use nanoparticles to shield the toxic effect of the two-photon dies while allowing for PDT treatment with lower energy light.

2.5.3.3 PLGA Nanoparticles Recent work has been focused on utilizing biodegradable poly(D,L-lactide-co-glycolide)(PLGA) with second generation porphryin derivatives to create a delivery system for PS agents. PLGA is an optimal choice due to the ability to alter the properties of the polymer by varying the weight percentage of PLA and PGA monomers. PLA is less hydrophilic than PGA; by affecting the ratio of the two monomers, the nanoparticle drug loading properties can be varied. Konan et al. show that although different ratios of PLGA (50:50 PLGA, 75:25 PLGA, and PLA) have different *in vitro* phototoxicity despite having similar drug loading properties[206]. They were able to show that hydrophilicity can influence the uptake of the nanoparticle, resulting in differences in delivered drug concentration. Overall, PLGA nanoparticles are noted for high biocompatibility and ease in manufacturing, becoming the most extensively studied

polymers for PS delivery. Nanoparticles made of PLGA have been coupled with a variety of PS, including porphyrins, chlorins, and other second generation PS, and have shown great promise for clinical translation. Additionally, the properties of PLGA nanoparticles can be changed through PEGylation, improving their biodistribution and blood circulation time[207].

Fadel et al. recently used PLGA nanoparticles to carry the PS Zinc phthalocyanine(ZnPc) in order to enhance tissue uptake and target delivery. Using a solvent emulsion evaporation method, they were able to create the nanoparticles and subsequently characterize the nanoparticle shape, encapsulation properties, *in vitro* release, as well as determine *in vivo* photodynamic efficiency in tumor bearing rats. The antitumor activity of ZnPc-loaded PLGA nanoparticles was compared to that of free ZnPc, showing that rats treated with PLGA-carried ZnPc had the smallest tumors. They concluded that ZnPc loaded into PLGA nanoparticles were far superior to its free form, corresponding with results seen in similar studies[208, 209]. In another study, the PS agent Verteporfin was loaded into PLGA nanoparticles in order to optimize the carrier for intravenous injection and subsequent PDT[210] Two sizes of nanoparticles, 150 and 300nm in diameter, were studied after preparation with a salting-out technique. *In vitro* results showed a nearly 60% and 40% higher efficiency for the smaller nanoparticles compared to free verteporfin and the large nanoparticle loaded with Vertporfin, respectively. These results highlight the importance of size considerations for effective treatment. It was hypothesized that smaller nanoparticles resulted in increased rates of endocytosis compared to larger nanoparticles, while additionally showing higher drug release rates due to increased surface area to volume ratio.

While nanoparticles formed with PLGA aide in the accumulation of PS agent to the tumor space based on the EPR effect and longer circulation times, non-specific localization of the photosensitizer into healthy tissue or skin still remains a hurdle to reduce side effects. To help overcome this, McCarthy et al. has developed a new delivery system based on PLGA nanoparticles that results in lower side effects based on lower toxicity in extracellular space and a time dependent intracellular release of the PS[211, 212]. This is accomplished by the fact that the PS meso-tetraphenylporpholactol is non-phototoxic upon administration and only becomes toxic when released from the PLGA nanoparticle after cellular internalization. The polarity of the PS causes aggregation upon encapsulation, resulting in the quenching of the chromophore leading to an inability to be excited until release from the nanoparticle. After cellular internalization, the meso-tetraphenylporphyrin yields meso-tetraphenylporpholactol which has a 10 fold higher extinction coefficient at 646nm and thus a higher singlet oxygen quantum yield. Similar techniques have been utilized to create this double selective PDT treatment[213] and we envision therapies that use this activatable photosensitizer coupled with a targeted nanoparticles to further increase the selectivity of drug. These future steps will increase the likeliness of a polymer based nanoparticle becoming clinically translatable.

2.5.4 Non-biodegradable nanoparticles for PDT

While biodegradable nanoparticles show great promise for carrying PS agents for PDT, nanoparticles made from non-biodegradable materials also have shown preclinical success in the previous decade. As stated before, the main function of polymeric and other biodegradable nanoparticles is to act as a drug delivery vehicle, either through conjugation or encapsulation. Unlike these materials, non-biodegradable materials are

chosen due to a key feature of most PS agents, lack of their degradability. PS agents, which are released by organic nanoparticles, do not lose function after treatment with initial light activation and can be activated repeatedly. Therefore, non-biodegradable materials are chosen to act as carriers to reduce problems with the free drug that is released with the biodegradable nanoparticles, reducing possible collateral toxicity.

2.5.4.1 Ceramic One of the key attributes of non-polymer based nanoparticles is the ability to have great control over the size, shape, porosity, and surface chemistry. This is readily apparent in ceramic-based nanoparticles which can have photosensitizers non-covalently attached to their surface while having great control over their properties and a controllable size under 50 μm. Roy et al. effectively used ceramic based nanoparticles approximately 30nm in diameter to delivery encapsulated 2-devinyl-2-(1-hexyloxyethyl) pyropheophorbide(HPPH)[214]. Irradiation of the PS entrapped in the nanoparticles at 650nm showed efficient generation of singlet oxygen, likely due to the porous nature of the nanoparticle without the need for release of the drug. *In vivo* results showed significant damage to the tumor and showed that ceramic materials might viable options for PDT. One of the key features of this formulation was the ability of the PS agent to be activated without needing to be released from the nanoparticle, a feature that could overcome the shortcomings listed previously about biodegradable nanoparticles and residual toxicity.

2.5.4.2 Gold Gold nanoparticles may provide promise to be a highly selective delivery platform for PS agents in PDT. PEGylated gold nanoparticles are known for their inertness, long circulation times, minimal toxicity and tunability of size from 2-100nm[215]. Cheng et al. recently developed gold nanocages to deliver the PS agent, Pc4.

This delivery method greatly improved the long term (2 h) delivery of Pc4 to the target site in tumor bearing mice as seen in **Figure 2.14**. After determining the gold nanoparticle conjugates keep the drug stable in suspension for longer durations and determining minimal changes in singlet oxygen production due to shielding, they concluded that the gold nanoparticles provide a carrier system capable of improving PDT treatment[216]. Likewise, Wieder et al. developed a gold nanoparticle capable of delivering phthalocyanine with an average particle diameter of 2-4nm[217]. The PDT efficiency determined from the particle-PS agent conjugates were nearly twice that of the free phthalocyanine. They hypothesized that this difference was due to a difference in uptake between the free drug and the carried drug, which likely entered through endocytosis in a HeLa cell line. Overall their results were promising for gold nanoparticle delivery vehicles. However, their results lacked *in vivo* data which would provide information on accumulation of the drug and nanoparticles which would likely be different from the Cheng paper as there is a large size discrepancy.

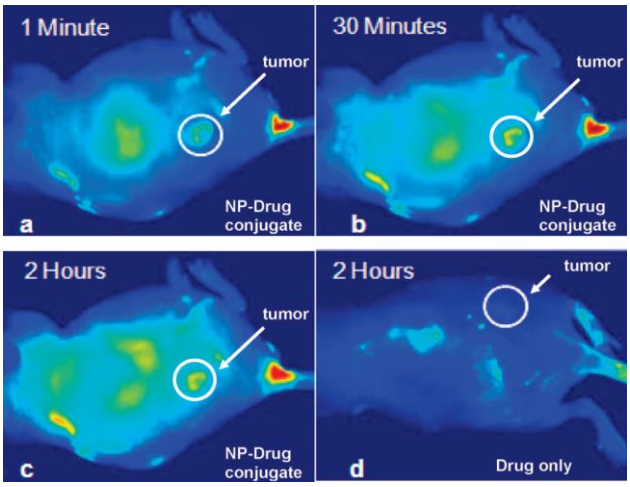

Figure 2.14. Fluorescent images of tumor-bearing rats injected with AuNP-Pc4 "PS agent" conjugated after (a) 1 minute, (b) 30 minutes, (c) 120 minutes compared to (d) 120 minutes with nude Pc4. Pc4 fluorescence shows increased accumulation into tumors after 2 hours with NP-drug conjugates compared to drug only. From ref 216, Y. Cheng, A. C. Samia, J. D. Meyers, I. Panagopoulos, B. W. Fei, and C. Burda, Highly efficient drug delivery with gold nanoparticle vectors for in vivo photodynamic therapy of cancer. *Journal of the American Chemical Society*. 130, 10643-10647 (**2008**). Copyright@ American Chemical Society.

Stuchinskaya et al. recently used anti-HER2 monoclonal antibodies as a targeting modality with gold nanoparticle-phthalocyanine conjugates[218]. After successfully confirming antibody attachment to the outside of the 2-3nm gold nanoparticles, they were able to show increased *in vitro* efficacy of the targeted nanoparticles compared to the non-antibody targeted nanoparticles after irradiation with 693nm light. They concluded that HER-2 antibody conjugation to nanoparticles containing a PS agent can increase efficacy of treatment in cells that overexpress HER2 while causing minimal changes in cells which do not overexpress this receptor. Once again, these results were promising *in vitro*, and *in vivo* data should be collected to determine if this active targeting regiment can increase accumulation in the tumor space in addition to increasing cellular uptake.

2.5.4.3 Quantum Dots QDs, as mentioned previously, are semiconductor nanoparticles that possess several characteristics that make them a potential great choice as a novel class of PS agents[219]. In general, QDs used in PDT for cancer treatment

include CdSe, CdTe, CdSe/ZnS and InP/ZnS. Unlike other nanoparticles mentioned previously, these nanoparticles do not act as delivery vehicles of PS agents but rather are PS agents themselves. These nanoparticles were first studied as a part of a two-step energy transfer mechanism and delivery vehicle capable of acting as an energy intermediate for activating the conjugated PS agent[186]. However, they determined that QDs alone are capable of producing singlet oxygen species without the need of a PS molecule. More importantly, QDs can be used to deliver localized ionizing radiation, circumventing the low tissue penetration of light which may additionally complement PDT for treatment. While PDT with QDs alone is possible, the emission quantum yield remains low, and efforts have been focused to continue to conjugate PS molecules to QDs, such as CdSe/ZnS via organic bridges[220].

While strides have been made in the past 5 years on studies with QDs acting as energy transfer components for PS molecules, one of the first to study generation of singlet oxygen species by fluorescence resonance energy transfer from QDs to phthalocyaninato was accomplished by Samia et al[221]. They were able to conjugate the PS molecule to the QD via an alkyl amino group and were able to show singlet oxygen formation via fluorescence resonance energy transfer (FRET). However, it should be noted that clinical translatability of this system is minimal due to the inability of the particles to be solubilized in water. To overcome this shortcoming, Tsay et al. has recently developed a water soluble peptide-coated QD that is conjugated to Rose Bengal and chlorin e6, both high yielding PS molecules. The CdSe/CdS/Zn QDs used in this study were capable of producing singlet oxygen species through FRET from the QD donor to the PS and through direct activation of the PS[222]. In the case with direct

activation, using two wavelengths for excitation, the QD-Ps conjugate could be used for simultaneous imaging and singlet oxygen generation. Overall singlet oxygen quantum yields as high as 0.31 were achieved under 532nm light.

2.5.4.4 Upconverting Nanoparticles Upconverting nanoparticles (UCNP) are composite nanoparticles which generate higher energy light from a lower energy source. Usually this is in the form of NIR light or infrared (IR) light which can be converted through the use of a transition metal, lanthanide, or actinide ion doped into a solid material that is capable of emitting higher energy light to activate PS molecules[223]. This is exceptionally useful in PDT as one of the main limitations of PS agents is the depth of penetration of the light normally used for activation (600-800nm). If an NIR or IR source can be used and coupled with a nanoparticle to produce these wavelengths at the site, greater clinical translation can be envisioned for deep tissue cancers. A variety of different materials have been demonstrated for UCNP with $NaYF_4$ being increasingly used as the core material of choice due to its high upconversion efficiencies in the regions necessary for PS molecules[224].

One UCNP of choice which allows for amine groups for attachment of biomolecules is a PEI/$NaYF_4$:Yb^{3+},Er^{3+} which emit in the green peaks(500-550nm) and red peaks(650-675) when excited by a 980 nm NIR laser. To take advantage of this unique fact, ZnPc PS molecules can be attached to the surface of these nanoparticles. The nanoparticle can then perform three functions: drug delivery vehicle capable of active or passive targeting, conversion of lower energy NIR light to the functional red peak for PS activation, and aiding in solubilizing the non-polar ZnPc. Chatterjee et al. showed effective adsorption of ZnPc to these UCNPs and demonstrated production of singlet

oxygen species with irradiation at 980 nm through the photobleaching of disodium, 9, 10-anthracenediproionic acid (ADPA). The ZnPc/PEI/$NaYF_4$ nanoparticles were studied in vitro using HT29 human colonic adenocarcinoma cells, and remarkable cell death (80-90%) was seen after 5 minutes of laser exposure. Many other studies have shown that UCNPs can be used *in vivo* for PDT. Ce6 loaded PEG-UCNPs were studied in mice bearing 4T1 murine breast tumors under 980 nm light (0.5 W/cm^2) resulting in complete suppression and clearance of the nanoparticles[225]. The *in vivo* work accomplished in this study can be seen in **Figure 2.15**. One of the key findings for this study is that UCNPs can be used to significantly improve treatments in tumors blocked by thick biological tissues.

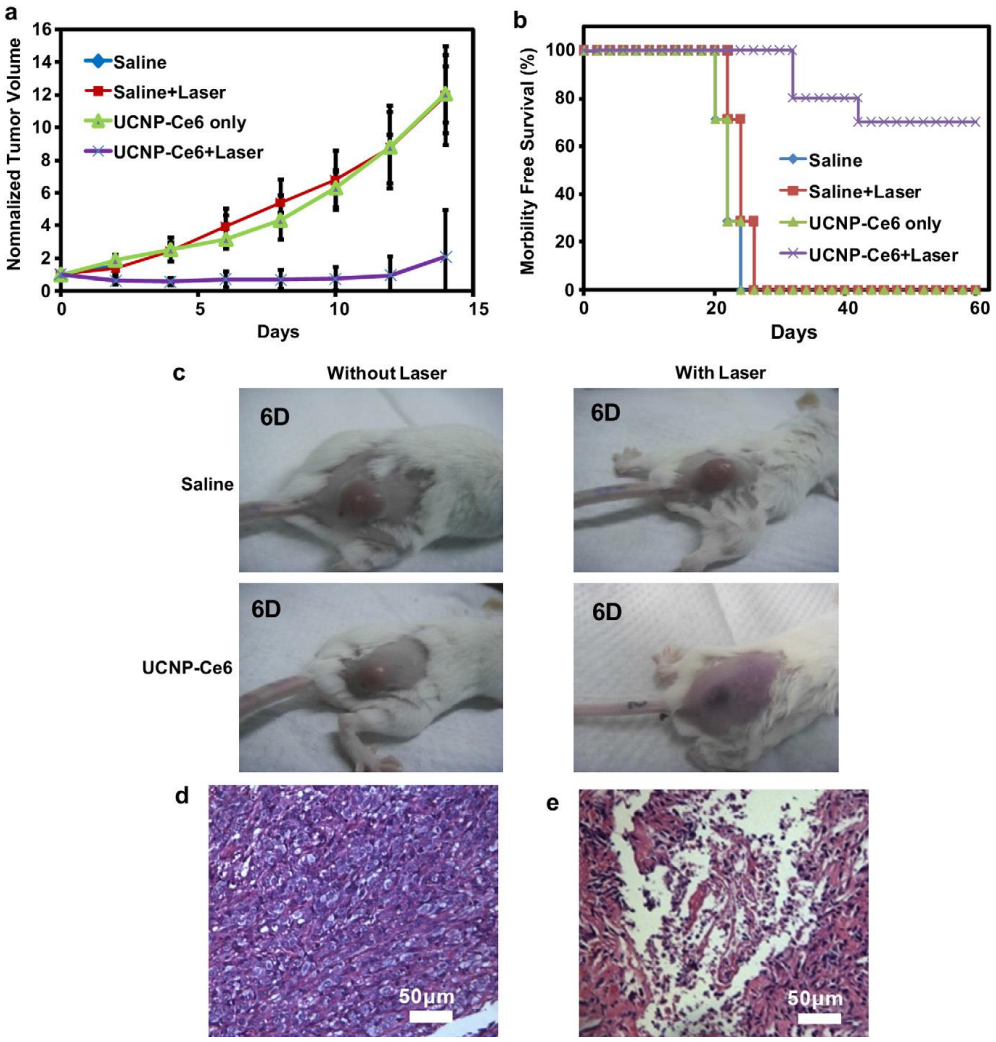

Figure 2.15. *in vivo* PDT treatment of tumor-bearing mice. (a) Comparison of tumor growth between controls and upconverting nanoparticle treatments. (b) Survival curves at 60 days for the same treatments. (c) Representative images of tumors after 6 days post-treatment. (d) and (e) H&E stains of untreated (d) and treated (e) tumors showing the localized destruction of tissue with the use of upconverting nanoparticles for PDT. From ref 225, C. Wang, H. Q. Tao, L. Cheng, and Z. Liu, Near-infrared light induced in vivo photodynamic therapy of cancer based on upconversion nanoparticles. *Biomaterials*. 32, 6145-6154 (**2011**). Copyright@ Elsevier.

2.5.5 Combination therapies with PDT

While nanoparticle-based PDT has developed into a broad field with many nanomaterials discussed here, there is great hope in using these nanomaterials for combination therapies. One of the key approaches using nanoparticles for combinatorial

PDT therapies is technique that combines it with photothermal therapy. Kah et al. recently used gold nanoparticles conjugated with hypercin to perform combination photothermal and photodynamic therapies and showed strong enhancement of the therapies compared to a single therapy with either PDT or PTT[226]. Additionally, a combination nanoparticle can be used to delivery both PDT and chemotherapy. Khadir et al. recently use aerosol OT alginate nanoparticles to deliver both the PS agent MB and the chemotherapeutic agent doxorubicin to overcome drug resistance problems [227]. They photoactivated the MB with 665 nm light with drug-resistant NCI/ADR-RES cells and showed that encapsulation of the two drugs followed by PDT have much improved efficacy. The multimodal therapies resulted in higher ROS production and concluded that the combination nanoparticles were effective in improving cytotoxicity in drug-resistant tumor cells.

Overall, there has been vast improvement in the field of nanomaterials and nanomedicine in the past decade and many of these materials can be used to create more effective PDT treatments. Whether the nanoparticle is used for dispersion purposes, increased targeting, or if the particle is degradable, the overwhelming consensus is that nanomedicine is providing a foundation for highly optimized treatments based on the delivery of drugs. Biodegradable nanoparticles make excellent choices for drug delivery and may provide the earliest clinical translation due to the ease of clearance and low toxicity, while non-biodegradable particles provide a range unique features such as upconversion of lower energy light allowing for deeper penetration or precise tunability for specific treatment options. Regardless, the goal of the nanoparticle should be to selectively deliver the PS agent, or in the case of QDs act as the PS agent, to the tumor

region, allowing for minimal residual toxicity and higher accumulation. Most likely this will occur via active targeting through the addition of ligands on the exterior of nanoparticles. Among the various material choices described in this review, there is great hope for developing a system to effectively utilize nanomedicine in photodynamic therapies.

2.6 Photoacoustic Therapy

Recent findings on the ignition of SWNTs and other nanoparticles exposed to pulsed light source have attracted attention for use in photoacoustic therapy. Light interactions with nanoparticles that can lead to photothermal effects are extensively mentioned previously. Similar interactions of light with the nanoparticles are capable of producing pressure bubbles after excitation causing mechanical destruction of tissues with little to no heat production. Traditionally, the interaction of these particles with light causing a pressure wave has excited research in the field of photoacoustic imaging of tumors, which can be used to visualize tumors during photothermal treatments[228, 229]. The magnitude of the photoacoustic pressure wave following excitation has a peak pressure of 100 MPa, likened to a firecracker-like explosion on the nanoscale[230]. The transduction of light into pressure capable of mechanically disrupting tissue might provide a new treatment utilizing these nanoparticles for cancer destruction and has only recently been studied[230-232].

Kang et al. recently functionalized SWNTs with folate to develop a photoacoustic "bomb" agent that can selectively enter into cancer cells receptor and subsequently kill cells through a pressure explosion under the excitation of a Q-switched millisecond pulsed 1064nm laser (532 nm) at 800 mW/cm^2 [230]. They found that 85% of cancer cells

with SWNH uptake died within 20 seconds of treatment while 90% of cells without SWNT uptake remained alive. Using infrared thermometers, they were able to show that no more than a 3 degree rise in temperature was seen, ruling out the possibility of a thermal mechanism of cell death. Mitochondria are considered a promising therapeutic target for cancer therapy due to their intricate interactions with proteins in the cell apoptosis pathway[233]. A moderate decline in mitochondrial function is known to trigger cell death[234]. With this in mind, Zhou et al. targeted the mitochondria in EMT-6 cells for photoacoustic therapy utilizing SWNTs[235]. Using similar conditions to the Kang paper, they were able to additionally show that the pressure waves caused through the photoacoustic interaction results in mitochondrial damage and apoptosis (**Figure 2.16**). Additionally, *in vivo* results in mice containing EMT6 flank tumors showed mitochondrial localization of the SWNTs in the tumor with excitation of 17.5 mJ for 60s of a Q-switched 1064nm laser showed cytotoxic results with little thermal creation. While the mechanism cannot be completely decoupled from a thermal mechanism, there is increasing promise in photoacoustic therapies for tumors that are highly vascularized, limiting the possibility of photothermal treatments due to the heat sink nature of the vascular bed.

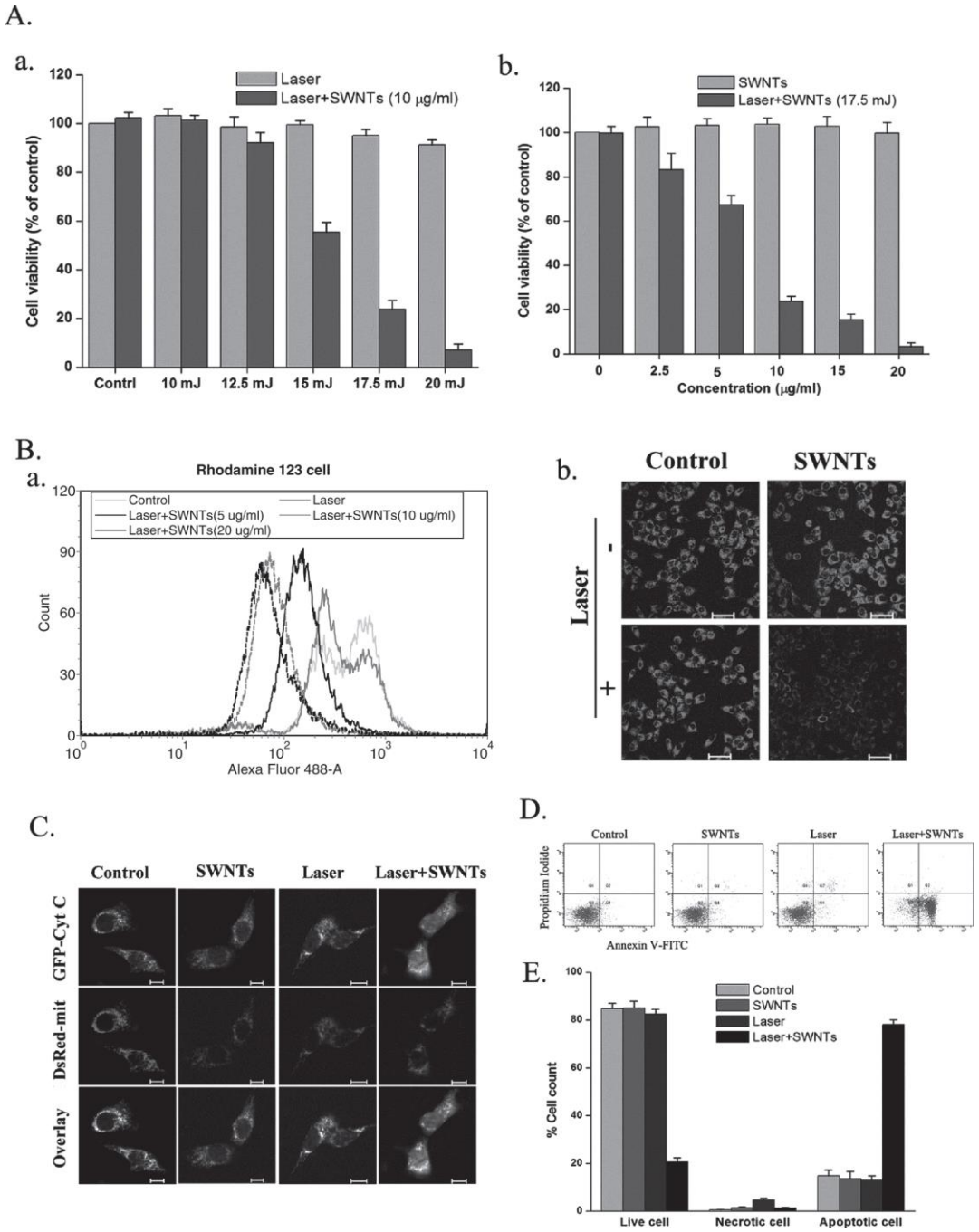

Figure 2.16. Photoacoustic effects of SWNTs on EMT6 cells. (a) Viability at different energies and concentrations of particles. (b) Mitochondrial trans-membrane potential exhibited by Rhodamine staining and visualized with flow cytometry and confocal imaging. (c) Cytochrome c release analysis for 30 minutes before laser irradiation. Fluorescent images recorded with confocal microscopy. (d) and (e) Cell viability 30 minutes after treatment studied annexin V-FITC. From ref 235, F. F. Zhou, S. N. Wu, Y. Yuan, W. R. Chen, and D. Xing, Mitochondria-Targeting Photoacoustic Therapy Using Single-Walled Carbon Nanotubes. *Small*. 8, 1543-1550 (**2012**). Copyright@ John Wiley and Sons.

2.7 Photo-Triggered Drug Release

As previously stated, there are many advantages for nanoparticles acting as drug carriers compared to free systemic drug delivery. While enabling greater accumulation in a targeted tumor site either through a passive or active targeting technique is a key attribute of nanoparticle delivery vehicles, one of the biggest advantageous of nanoparticle carriers is that they can shield the drug from normal tissue. This shielding effect not only mitigates degradation of the drug in the harsh in vivo environment, but additionally reduces undesirable side effects caused by drugs throughout the body. Although traditional nanoparticle delivery vehicles aide in this effect simply by acting as a one-step delivery vehicle, the problem of shielding the payload with controlled release still exists. After shielding the drug from the environment and the environment from the drug, nanoparticles must be able to release the drug at the desired location. Therefore, increasing the control of the time and location of the release of drugs within nanoparticles remains a topic in nanomedicine research. Greater control of the release of drugs can result in not only higher local concentration in the desired tumor region but also reduce collateral damage to healthy tissue while reducing the systemic dosage required. Development of a triggered release mechanism could provide this greater control of spatial and temporal delivery of drugs with nanoparticles.

While many intrinsic signals such as pH and enzymatic degradation and external triggers such as ultrasound, temperature, and light are currently studied to create a controllable switch for drug release from nanoparticles, light is especially promising. The attractiveness of light is that it has highly controllable temporal resolution with the development of femtosecond laser and the capability of having micron level spatial

resolution. Additionally, low energy light in the NIR region is capable of deep tissue penetration (up to 10cm), allowing it to be used possibly as an external trigger with minimal invasiveness. There are many mechanisms for light to be used as a trigger for photo-responsive nanoparticles including photo-oxidation, photothermal effects, photo-crosslinking, and photo-based polymer backbone fragmentation; the mechanism is determined and optimized by nanomaterial selection and formulation. Specific examples of these mechanisms of photo-triggered release will be mentioned presently.

The photothermal properties of nanoparticles used to generate heat such as gold nanoparticles were previously mentioned. Briefly, gold nanoparticles can absorb light efficiently in the visible and NIR regions and subsequently undergo plasmonic resonance which creates a highly localized heating event. In order for a photothermal triggered drug release to occur, this heating effect must be coupled with a thermal sensitive polymer or hydrogel that carriers the drug and releases only when it is heated due to the thermal event. Typically this is accomplished by incorporating photothermal nanostructures into polymer capsules that contain drug molecules. One of the first studies on this mechanism was described by Radt et al. in which polyelectrolyte microparticles were prepared by incorporating 6nm gold nanospheres with lysozymes[236]. They observed lysozyme release after 5 minute exposure of 10ns switched 1064 nm NIR light and provided the fundamental proof of concept for this technology. Since this initial study, many groups have looked at using photothermal mechanism to release drugs[237, 238].

Recently, Yavuz et al. demonstrated their ability to create a novel photothermal responsive gold-polymer nanoparticle capable of controllable release of the chemotherapeutic drug doxorubicin[239]. After loading the drug into a gold nanocage, they

were able to cover the naturally porous nanocage with a nonporous and, more importantly, thermo-sensitive smart polymer pNIPAAm-co-pAAm which is seen in **Figure 2.17**. Under NIR excitation, the gold nanocage is able to convert light efficiently into heat, causing the polymer surrounding the nanocage to collapse. The collapse of the polymer then allows for the drug to leach from the porous gold nanocage and interact with cells. After the NIR laser is switched off, the polymer is able to relax back to its full size and then shield the remaining drug inside the nanocage, reducing toxicity during clearance of the nanoparticle. The use of these nanoparticles offer many other advantages such as bio-inertness of the particles and the surface can be easily functionalized using gold-thiolate chemistry to introduce active targeting modalities[240].

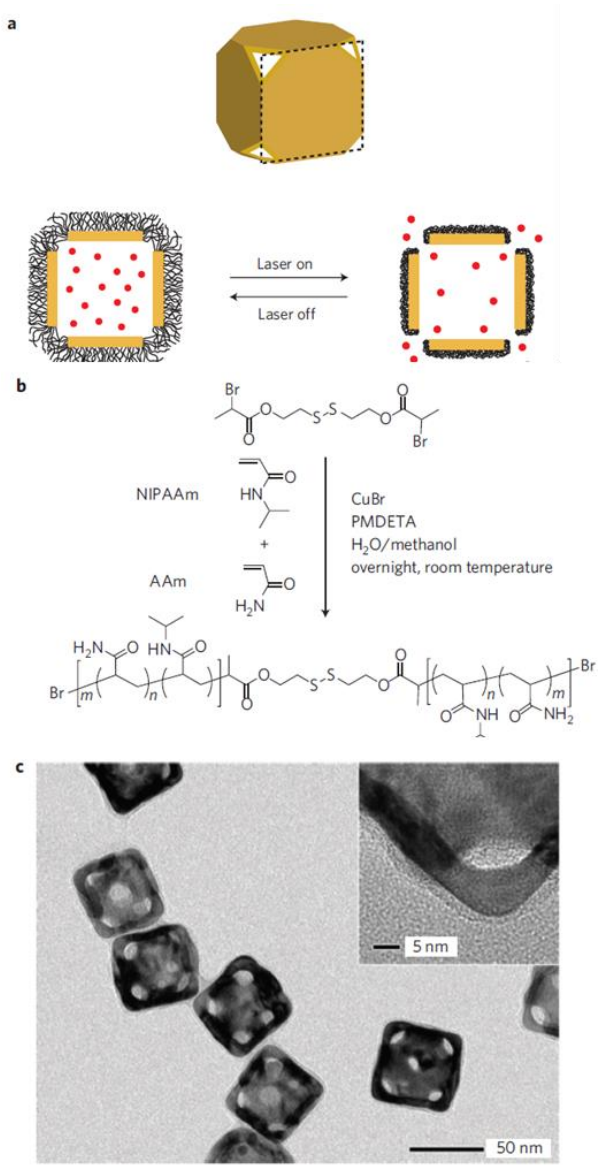

Figure 2.17. (a) Schematic illustrating how gold nanocage-smart polymer drug release system works. (b) Illustration of atom-transfer radical polymerization of NIPAAm and AAm monomers. (c) TEM images of gold nanocages covered with smart polymer, with insert showing the corner of a nanocage with smart polymer. From ref 239, M. S. Yavuz, Y. Y. Cheng, J. Y. Chen, C. M. Cobley, Q. Zhang, M. Rycenga, J. W. Xie, C. Kim, K. H. Song, A. G. Schwartz, L. H. V. Wang, and Y. N. Xia, Gold nanocages covered by smart polymers for controlled release with near-infrared light. *Nature Materials*. 8, 935-939 (**2009**). Copyright@ Macmillan Publishers Ltd.

One of the major concerns with gold nanoparticle mediated photothermal release of drug cargo is the stability of the drug in the high temperature environment locally surrounding the resonating nanoparticle, which can reach 600-800°C. While careful

shielding of the drug from the nanoparticle can reduce this effect, other photo-triggered mechanisms of drug release provide similar controllable release kinetics without potentially damaging molecules. One mechanism is a photochemical reaction much like the one that occurs to create singlet oxygen species in PDT therapy, where the singlet oxygen degrades the polymer carrying a drug chemically, releasing the molecule in a similar fashion to photothermal release. These nanocarrying systems must therefore have a particle to carry payloads, an attached photosensitizer that is able to convert the light into a singlet oxygen species, and a polymer that can hold a drug molecules and degrade after production of the singlet oxygen following laser irradiation.

Early work with singlet oxygen created-phototriggered release of drug was accomplished by Thompson et al[241, 242]. They were able to show that singlet oxygen species can release drugs from liposomes by breaking down the liposomes through oxidation of the plasminogen vinyl ether linkage. The breaking of this linkage allows for greater membrane fusion of the liposome to the membrane and therefore greater release of the drug from the intraliposomal space. They used the PS agent bacteriochlorophylla and an 800nm wavelength laser to create the singlet oxygen species which was able to trigger release of the liposome with great results. Building from this initial study, many have used similar liposomal photodynamic techniques to create triggered release of molecules.

Additionally, NIR light can be used to trigger release of drugs or other molecules through chemical changes induced by light interaction with either changing the chemical structure of materials or through a two-step process that utilize UCNPs as mentioned in the PDT review. This was first accomplished in amphiphilic molecules created by

Goodwin et al. which contained a hydrophobic and light sensitive 2-diazonapthoquinone (DNQ) and a hydrophilic PEG chain[243]. This copolymer forms a micelle at pH 7.4 and is capable of drug or dye loading. In order to test the phototriggered release capability of this novel material, Nile red was encapsulated as a reporter dye. Under NIR light (795nm), the DNQ undergoes Wolff rearrangement and forms a hydrophilic molecule, 3-indone carboxylic acid, thus destroying the drug containing micelle and releasing the drug or dye. This was confirmed with a 75% decrease in the fluorescence of Nile Red which was then able to diffuse into the medium. There are many other ways for light interaction with the chemical backbone of polymers, but most of these interactions occur in the UV range. Since UV has a low depth of penetration, the use of UCNPs can be used which are capable of converting the high depth penetrating NIR light into ultraviolet (UV) light at the site [244]. Yang et al. developed a photochemical release based on these UCNPs by caging D-luciferin in a 1-(2-nitrophenyl) ethyl group which is known to be degraded by UV light[245]. By attaching these caged molecules in the polymer to a UCNP made up of a Tm/Td doped $NaYF_4$, they were able to excite with a 980nm light and uncage the molecule due to UV degradation of the polymer *in vitro* and *in vivo* with great results.

Regardless of the mechanism for phototriggered release, there is great promise in creating new strategies for releasing drugs in a targeted region using NIR light in both space and time. Photothermal and photodynamic release both represent creative ways to use previous technologies used for single modal destruction of tumors to create this controllable release. While there are still many hurdles that must be overcome for

ultimate clinical translation, there is great hope in using NIR controlled drug release from nanoparticle drug delivery vehicles.

2.8 3D Tumor Mimics for in vitro Testing of Photo-based Therapies

As more definitive knowledge emerges on the differences between 2-dimensional and 3-dimensional cell behavior and morphology, testing strategies must evolve to better reflect *in vivo* tissue[246, 247]. Discrepancies between 2D and 3D culture may account for the inability of many therapies to translate from *in vitro* settings to *in vivo* environments. 3D models suitable for testing with photo therapies should mimic the optical properties of tissue while also retaining the ability to maintain normal cellular functions and responses. Tumor mimics must either retain porosity for subsequent nanoparticle treatment or allow polymerization or setting to occur around pre-treated cells.

The specific type of material for tissue phantoms is application and biologically driven. For example, collagen, a natural polysaccharide that is found in many biological tissues, is used for many imaging applications [248, 249]. Poly(vinyl alcohol) has been widely used for photoacoustic imaging for its minimal optical absorption and capability to scatter light similar to tissues [70, 71, 250]. Photoacoustic imaging in particular has taken advantage of tissue phantoms for imaging uses, with other phantom materials including agar gels [66, 251, 252], gelatin [67], and porcine gel [73]. While examples of tissue phantom use are uncommon in imaging applications, photo-based therapies have shown even less use of tumor mimics. The use of sodium alginate tissue phantoms has been used for photothermal therapies and imaging with carbon-based nanoparticles [170, 171, 253] due to its high thermal stability compared to collagen and other protein-based hydrogels, while the use of other materials is scarce [254, 255]. For photodynamic applications, tumor mimics

have yet to be used. The potential for future work on the differences between the 2D and 3D response to nanoparticle mediated photo-based therapies for cancer is great. The large number of available materials for the creation of these tissue mimics that retain both favorable imaging and cellular characteristics can give significant insight into how 3D *in vivo* tumors will respond to any given photo-therapy. For a more detailed discussion on the available types of tissue phantoms, the reader is directed to a review by Pogue et al[256].

2.9 Conclusion

Photo-based imaging and therapy for the battle against cancer is emerging as a field with great potential. Research into novel nanomaterials is attempting to catch up with the variety of potential applications of light for both imaging and treatment. This wide variety of applications of light both in imaging (from fluorescence to photoacoustic imaging) and in therapies (from thermal to photodynamic therapies) give a significant number of potential applications from similar materials. The use of nanoparticles to aid in photo-therapies has made them more focused and effective, increasing the chance of cancer cell death while also minimizing the collateral damage to surrounding healthy tissue. While there are still challenges to be met before translation to clinical practice, nanoparticle-mediated photo-therapies for use in cancer applications is poised to meet these challenges and emerge as the next generation of cancer imaging and therapy.

2.10 Acknowledgements

Funding for this work was provided by the National Science Foundation Early CAREER Award CBET 0955072 and 0933571, the National Institutes of Health Grants R21 CA156078 and R21 CA135230, Institute for Critical Technology and Applied Sciences (ICTAS, Virginia Tech) Grant, and the National Science Foundation Graduate Research Fellowship Program.

References

1 R. Siegel, D. Naishadham, and A. Jemal, Cancer statistics, 2013. *CA: A Cancer Journal for Clinicians*. 63, 11-30 (**2013**)

2 D. Hanahan, and Robert A. Weinberg, Hallmarks of Cancer: The Next Generation. *Cell*. 144, 646-674 (**2011**)

3 T. Sakimoto, M. I. Rosenblatt, and D. T. Azar, Laser eye surgery for refractive errors. *The Lancet*. 367, 1432-1447

4 T. J. Vogl, P. K. Müller, R. Hammerstingl, N. Weinhold, M. G. Mack, C. Philipp, M. Deimling, J. Beuthan, W. Pegios, and H. Riess, Malignant liver tumors treated with MR imaging-guided laser-induced thermotherapy: technique and prospective results. *Radiology*. 196, 257-265 (**1995**)

5 T. J. Vogl, R. Straub, K. Eichler, O. Söllner, and M. G. Mack, Colorectal Carcinoma Metastases in Liver: Laser-induced Interstitial Thermotherapy—Local Tumor Control Rate and Survival Data. *Radiology*. 230, 450-458 (**2004**)

6 S. L. Jacques, Laser-tissue interactions. Photochemical, photothermal, and photomechanical. *Surg. Clin. N. Am*. 72, 531-558 (**1992**)

7 M. H. Niemz, *Laser-tissue interactions: fundamentals and applications*, Springer, (**2007**)

8 W. Choi, A. Sahu, Y. Kim, and G. Tae, Photothermal Cancer Therapy and Imaging Based on Gold Nanorods. *Ann. Biomed. Eng*. 40, 534-546 (**2012**)

9 L. C. Kennedy, L. R. Bickford, N. A. Lewinski, A. J. Coughlin, Y. Hu, E. S. Day, J. L. West, and R. A. Drezek, A New Era for Cancer Treatment: Gold-Nanoparticle-Mediated Thermal Therapies. *Small*. 7, 169-183 (**2011**)

10 E. S. Shibu, M. Hamada, N. Murase, and V. Biju, Nanomaterials formulations for photothermal and photodynamic therapy of cancer. *J. Photoch. Photobio. C*. 15, 53-72 (**2013**)

11 S. Jiang, K. Y. Win, S. Liu, C. P. Teng, Y. Zheng, and M.-Y. Han, Surface-functionalized nanoparticles for biosensing and imaging-guided therapeutics. *Nanoscale*. 5, 3127-3148 (**2013**)

12 C. Sun, J. S. H. Lee, and M. Zhang, Magnetic nanoparticles in MR imaging and drug delivery. *Adv. Drug Delivery. Rev*. 60, 1252-1265 (**2008**)

13 O. Veiseh, J. W. Gunn, and M. Zhang, Design and fabrication of magnetic nanoparticles for targeted drug delivery and imaging. *Adv. Drug Deliver. Rev*. 62, 284-304 (**2010**)

14 R. Popovtzer, A. Agrawal, N. A. Kotov, A. Popovtzer, J. Balter, T. E. Carey, and R. Kopelman, Targeted Gold Nanoparticles Enable Molecular CT Imaging of Cancer. *Nano Lett*. 8, 4593-4596 (**2008**)

15 O. M. Koo, I. Rubinstein, and H. Onyuksel, Role of nanotechnology in targeted drug delivery and imaging: a concise review. *Nanomed-Nanotechnol*. 1, 193-212 (**2005**)

16 W. K. Leutwyler, S. L. Bürgi, and H. Burgl, Semiconductor clusters, nanocrystals, and quantum dots. *Science*. 271, 933 (**1996**)

17 X. Michalet, F. F. Pinaud, L. A. Bentolila, J. M. Tsay, S. Doose, J. J. Li, G. Sundaresan, A. M. Wu, S. S. Gambhir, and S. Weiss, Quantum Dots for Live Cells, in Vivo Imaging, and Diagnostics. *Science*. 307, 538-544 (**2005**)

18 X. Gao, Y. Cui, R. M. Levenson, L. W. K. Chung, and S. Nie, In vivo cancer targeting and imaging with semiconductor quantum dots. *Nat. Biotechnol*. 22, 969-76 (**2004**)
19 U. Resch-Genger, M. Grabolle, S. Cavaliere-Jaricot, R. Nitschke, and T. Nann, Quantum dots versus organic dyes as fluorescent labels. *Nat. Methods*. 5, 763-775 (**2008**)
20 X. Wu, H. Liu, J. Liu, K. N. Haley, J. A. Treadway, J. P. Larson, N. Ge, F. Peale, and M. P. Bruchez, Immunofluorescent labeling of cancer marker Her2 and other cellular targets with semiconductor quantum dots. *Nature Biotechnol*. 21, 41-46 (**2002**)
21 S. Kim, Y. T. Lim, E. G. Soltesz, A. M. De Grand, J. Lee, A. Nakayama, J. A. Parker, T. Mihaljevic, R. G. Laurence, D. M. Dor, L. H. Cohn, M. G. Bawendi, and J. V. Frangioni, Near-infrared fluorescent type II quantum dots for sentinel lymph node mapping. *Nature Biotechnol*. 22, 93-97 (**2004**)
22 B. O. Dabbousi, J. Rodriguez-Viejo, F. V. Mikulec, J. R. Heine, H. Mattoussi, R. Ober, K. F. Jensen, and M. G. Bawendi, (CdSe)ZnS Core−Shell Quantum Dots: Synthesis and Characterization of a Size Series of Highly Luminescent Nanocrystallites. *J. Phys. Chem. B.* 101, 9463-9475 (**1997**)
23 A. M. Smith, H. Duan, A. M. Mohs, and S. Nie, Bioconjugated quantum dots for in vivo molecular and cellular imaging. *Adv. Drug Deliver. Rev*. 60, 1226-1240 (**2008**)
24 F. Erogbogbo, K.-T. Yong, I. Roy, G. Xu, P. N. Prasad, and M. T. Swihart, Biocompatible Luminescent Silicon Quantum Dots for Imaging of Cancer Cells. *ACS Nano*. 2, 873-878 (**2008**)
25 K.-T. Yong, H. Ding, I. Roy, W.-C. Law, E. J. Bergey, A. Maitra, and P. N. Prasad, Imaging Pancreatic Cancer Using Bioconjugated InP Quantum Dots. *ACS Nano*. 3, 502-510 (**2009**)
26 H. S. Choi, B. I. Ipe, P. Misra, J. H. Lee, M. G. Bawendi, and J. V. Frangioni, Tissue- and Organ-Selective Biodistribution of NIR Fluorescent Quantum Dots. *Nano Lett*. 9, 2354-2359 (**2009**)
27 M. Stroh, J. P. Zimmer, D. G. Duda, T. S. Levchenko, K. S. Cohen, E. B. Brown, D. T. Scadden, V. P. Torchilin, M. G. Bawendi, D. Fukumura, and R. K. Jain, Quantum dots spectrally distinguish multiple species within the tumor milieu in vivo. *Nat. Med*. 11, 678-682 (**2005**)
28 W. Cai, D.-W. Shin, K. Chen, O. Gheysens, Q. Cao, S. X. Wang, S. S. Gambhir, and X. Chen, Peptide-Labeled Near-Infrared Quantum Dots for Imaging Tumor Vasculature in Living Subjects. *Nano Lett*. 6, 669-676 (**2006**)
29 M. Koyakutty, J. Seby, T. Deepa, S. Sonali, M. Deepthy, and N. Shantikumar, Bio-conjugated luminescent quantum dots of doped ZnS: a cyto-friendly system for targeted cancer imaging. *Nanotechnology*. 20, 065102 (**2009**)
30 J. Pan, and S.-S. Feng, Targeting and imaging cancer cells by Folate-decorated, quantum dots (QDs)- loaded nanoparticles of biodegradable polymers. *Biomaterials*. 30, 1176-1183 (**2009**)
31 S.-H. Hu, Y.-W. Chen, W.-T. Hung, I. W. Chen, and S.-Y. Chen, Quantum-Dot-Tagged Reduced Graphene Oxide Nanocomposites for Bright Fluorescence Bioimaging and Photothermal Therapy Monitored In Situ. *Adv. Mater*. 24, 1748-1754 (**2012**)
32 J. Qian, K.-T. Yong, I. Roy, T. Y. Ohulchanskyy, E. J. Bergey, H. H. Lee, K. M. Tramposch, S. He, A. Maitra, and P. N. Prasad, Imaging Pancreatic Cancer Using Surface-Functionalized Quantum Dots. *J. Phys. Chem. B.* 111, 6969-6972 (**2007**)

33 H. Tada, H. Higuchi, T. M. Wanatabe, and N. Ohuchi, In vivo Real-time Tracking of Single Quantum Dots Conjugated with Monoclonal Anti-HER2 Antibody in Tumors of Mice. *Cancer Res*. 67, 1138-1144 (**2007**)
34 K.-T. Yong, Mn-doped near-infrared quantum dots as multimodal targeted probes for pancreatic cancer imaging. *Nanotechnology*. 20, 015102 (**2009**)
35 K. Chen, Z.-B. Li, H. Wang, W. Cai, and X. Chen, Dual-modality optical and positron emission tomography imaging of vascular endothelial growth factor receptor on tumor vasculature using quantum dots. *Eur. J. Nucl. Med. Mol. I.* 35, 2235-2244 (**2008**)
36 Z. Li, P. Huang, R. He, J. Lin, S. Yang, X. Zhang, Q. Ren, and D. Cui, Aptamer-conjugated dendrimer-modified quantum dots for cancer cell targeting and imaging. *Mater. Lett*. 64, 375-378 (**2010**)
37 R. Savla, O. Taratula, O. Garbuzenko, and T. Minko, Tumor targeted quantum dot-mucin 1 aptamer-doxorubicin conjugate for imaging and treatment of cancer. *J. Control Release*. 153, 16-22 (**2011**)
38 H. C. Fischer, L. Liu, K. S. Pang, and W. C. W. Chan, Pharmacokinetics of Nanoscale Quantum Dots: In Vivo Distribution, Sequestration, and Clearance in the Rat. *Adv Funct Mater*. 16, 1299-1305 (**2006**)
39 P. Diagaradjane, J. M. Orenstein-Cardona, N. E. Colón-Casasnovas, A. Deorukhkar, S. Shentu, N. Kuno, D. L. Schwartz, J. G. Gelovani, and S. Krishnan, Imaging Epidermal Growth Factor Receptor Expression In vivo: Pharmacokinetic and Biodistribution Characterization of a Bioconjugated Quantum Dot Nanoprobe. *Clin Cancer Res*. 14, 731-741 (**2008**)
40 K. Zimmermann, D. Inglefield, Jr., J. Zhang, H. Dorn, T. Long, C. Rylander, and M. N. Rylander, Single-walled carbon nanohorns decorated with semiconductor quantum dots to evaluate intracellular transport. *J. Nanopart Res*. 16, 1-18 (**2013**)
41 M. DeWitt, A. Pekkanen, J. Robertson, C. G. Rylander, and M. N. Rylander, Influence of Hyperthermia on Efficacy and Uptake of Carbon Nanohorn-Cisplatin Conjugates. *J. Biomech. Eng.-T. ASME*. 132, 021003 (**2014**)
42 A. Campion, and P. Kambhampati, Surface-enhanced Raman scattering. *Chem. Soc. Rev*. 27, 241-250 (**1998**)
43 C. Zavaleta, A. de la Zerda, Z. Liu, S. Keren, Z. Cheng, M. Schipper, X. Chen, H. Dai, and S. S. Gambhir, Noninvasive Raman Spectroscopy in Living Mice for Evaluation of Tumor Targeting with Carbon Nanotubes. *Nano Lett*. 8, 2800-2805 (**2008**)
44 S. Lee, S. Kim, J. Choo, S. Y. Shin, Y. H. Lee, H. Y. Choi, S. Ha, K. Kang, and C. H. Oh, Biological Imaging of HEK293 Cells Expressing PLCγ1 Using Surface-Enhanced Raman Microscopy. *Anal. Chem.* 79, 916-922 (**2007**)
45 X. Huang, I. H. El-Sayed, W. Qian, and M. A. El-Sayed, Cancer Cells Assemble and Align Gold Nanorods Conjugated to Antibodies to Produce Highly Enhanced, Sharp, and Polarized Surface Raman Spectra: A Potential Cancer Diagnostic Marker. *Nano Lett*. 7, 1591-1597 (**2007**)
46 J. Qian, L. Jiang, F. Cai, D. Wang, and S. He, Fluorescence-surface enhanced Raman scattering co-functionalized gold nanorods as near-infrared probes for purely optical in vivo imaging. *Biomaterials*. 32, 1601-1610 (**2011**)
47 S. Lee, H. Chon, M. Lee, J. Choo, S. Y. Shin, Y. H. Lee, I. J. Rhyu, S. W. Son, and C. H. Oh, Surface-enhanced Raman scattering imaging of HER2 cancer markers

overexpressed in single MCF7 cells using antibody conjugated hollow gold nanospheres. *Biosens Bioelectron*. 24, 2260-2263 (**2009**)
48 J. V. Jokerst, Z. Miao, C. Zavaleta, Z. Cheng, and S. S. Gambhir, Affibody-Functionalized Gold–Silica Nanoparticles for Raman Molecular Imaging of the Epidermal Growth Factor Receptor. *Small*. 7, 625-633 (**2011**)
49 Y. Huang, V. P. Swarup, and S. W. Bishnoi, Rapid Raman Imaging of Stable, Functionalized Nanoshells in Mammalian Cell Cultures. *Nano Lett*. 9, 2914-2920 (**2009**)
50 C. L. Zavaleta, K. B. Hartman, Z. Miao, M. L. James, P. Kempen, A. S. Thakor, C. H. Nielsen, R. Sinclair, Z. Cheng, and S. S. Gambhir, Preclinical Evaluation of Raman Nanoparticle Biodistribution for their Potential Use in Clinical Endoscopy Imaging. *Small*. 7, 2232-2240 (**2011**)
51 C. T. Nguyen, J. T. Nguyen, S. Rutledge, J. Zhang, C. Wang, and G. C. Walker, Detection of chronic lymphocytic leukemia cell surface markers using surface enhanced Raman scattering gold nanoparticles. *Cancer Lett*. 292, 91-97 (**2010**)
52 S. Feng, J. Lin, M. Cheng, Y.-Z. Li, G. Chen, Z. Huang, Y. Yu, R. Chen, and H. Zeng, Gold Nanoparticle Based Surface-Enhanced Raman Scattering Spectroscopy of Cancerous and Normal Nasopharyngeal Tissues Under Near-Infrared Laser Excitation. *Appl. Spectrosc*. 63, 1089-1094 (**2009**)
53 X. Wang, X. Qian, J. J. Beitler, Z. G. Chen, F. R. Khuri, M. M. Lewis, H. J. C. Shin, S. Nie, and D. M. Shin, Detection of Circulating Tumor Cells in Human Peripheral Blood Using Surface-Enhanced Raman Scattering Nanoparticles. *Cancer Res*. 71, 1526-1532 (**2011**)
54 D. Lin, S. Feng, J. Pan, Y. Chen, J. Lin, G. Chen, S. Xie, H. Zeng, and R. Chen, Colorectal cancer detection by gold nanoparticle based surface-enhanced Raman spectroscopy of blood serum and statistical analysis. *Opt Express*. 19, 13565-13577 (**2011**)
55 S. Feng, R. Chen, J. Lin, J. Pan, G. Chen, Y. Li, M. Cheng, Z. Huang, J. Chen, and H. Zeng, Nasopharyngeal cancer detection based on blood plasma surface-enhanced Raman spectroscopy and multivariate analysis. *Biosens Bioelectron*. 25, 2414-2419 (**2010**)
56 J. Lin, R. Chen, S. Feng, Y. Li, Z. Huang, S. Xie, Y. Yu, M. Cheng, and H. Zeng, Rapid delivery of silver nanoparticles into living cells by electroporation for surface-enhanced Raman spectroscopy. *Biosens Bioelectron*. 25, 388-394 (**2009**)
57 Z. Liu, X. Li, S. M. Tabakman, K. Jiang, S. Fan, and H. Dai, Multiplexed Multicolor Raman Imaging of Live Cells with Isotopically Modified Single Walled Carbon Nanotubes. *J. Am. Chem. Soc*. 130, 13540-13541 (**2008**)
58 Z. Liu, S. Tabakman, S. Sherlock, X. Li, Z. Chen, K. Jiang, S. Fan, and H. Dai, Multiplexed five-color molecular imaging of cancer cells and tumor tissues with carbon nanotube Raman tags in the near-infrared. *Nano Res*. 3, 222-233 (**2010**)
59 Z. Liu, C. Davis, W. Cai, L. He, X. Chen, and H. Dai, Circulation and long-term fate of functionalized, biocompatible single-walled carbon nanotubes in mice probed by Raman spectroscopy. *P. Natl. Acad. Sci*. 105, 1410-1415 (**2008**)
60 J. Robinson, K. Welsher, S. Tabakman, S. Sherlock, H. Wang, R. Luong, and H. Dai, High performance in vivo near-IR (>1 μm) imaging and photothermal cancer therapy with carbon nanotubes. *Nano Res*. 3, 779-793 (**2010**)

61 X. Wang, C. Wang, L. Cheng, S.-T. Lee, and Z. Liu, Noble Metal Coated Single-Walled Carbon Nanotubes for Applications in Surface Enhanced Raman Scattering Imaging and Photothermal Therapy. *J. Am. Chem. Soc*. 134, 7414-7422 (**2012**)
62 T. Chernenko, C. Matthäus, L. Milane, L. Quintero, M. Amiji, and M. Diem, Label-Free Raman Spectral Imaging of Intracellular Delivery and Degradation of Polymeric Nanoparticle Systems. *ACS Nano*. 3, 3552-3559 (**2009**)
63 J.-H. Kim, J.-S. Kim, H. Choi, S.-M. Lee, B.-H. Jun, K.-N. Yu, E. Kuk, Y.-K. Kim, D. H. Jeong, M.-H. Cho, and Y.-S. Lee, Nanoparticle Probes with Surface Enhanced Raman Spectroscopic Tags for Cellular Cancer Targeting. *Anal. Chem*. 78, 6967-6973 (**2006**)
64 S. Mallidi, T. Larson, J. Tam, P. P. Joshi, A. Karpiouk, K. Sokolov, and S. Emelianov, Multiwavelength Photoacoustic Imaging and Plasmon Resonance Coupling of Gold Nanoparticles for Selective Detection of Cancer. *Nano Lett*. 9, 2825-2831 (**2009**)
65 D. Pan, X. Cai, C. Yalaz, A. Senpan, K. Omanakuttan, S. A. Wickline, L. V. Wang, and G. M. Lanza, Photoacoustic Sentinel Lymph Node Imaging with Self-Assembled Copper Neodecanoate Nanoparticles. *ACS Nano*. 6, 1260-1267 (**2012**)
66 Q. Zhang, N. Iwakuma, P. Sharma, B. M. Moudgil, C. Wu, J. McNeill, H. Jiang, and S. R. Grobmyer, Gold nanoparticles as a contrast agent for in vivo tumor imaging with photoacoustic tomography. *Nanotechnology*. 20, 395102 (**2009**)
67 C. L. Bayer, S. Y. Nam, Y.-S. Chen, and S. Y. Emelianov, Photoacoustic signal amplification through plasmonic nanoparticle aggregation. *J. Biomed. Opt*. 18, 016001-016001 (**2013**)
68 M. F. Kircher, A. de la Zerda, J. V. Jokerst, C. L. Zavaleta, P. J. Kempen, E. Mittra, K. Pitter, R. Huang, C. Campos, F. Habte, R. Sinclair, C. W. Brennan, I. K. Mellinghoff, E. C. Holland, and S. S. Gambhir, A brain tumor molecular imaging strategy using a new triple-modality MRI-photoacoustic-Raman nanoparticle. *Nat. Med*. 18, 829-834 (**2012**)
69 S. Kim, Y.-S. Chen, G. P. Luke, and S. Emelianov, In vivo three-dimensional spectroscopic photoacoustic imaging for monitoring nanoparticle delivery. *Biomed. Opt. Express*. 2, 2540-2550 (**2011**)
70 Y.-S. Chen, W. Frey, S. Kim, P. Kruizinga, K. Homan, and S. Emelianov, Silica-Coated Gold Nanorods as Photoacoustic Signal Nanoamplifiers. *Nano Lett*. 11, 348-354 (**2011**)
71 M. Qu, M. Mehrmohammadi, and S. Emelianov, Detection of Nanoparticle Endocytosis Using Magneto-Photoacoustic Imaging. *Small*. 7, 2858-2862 (**2011**)
72 J. R. Cook, W. Frey, and S. Emelianov, Quantitative Photoacoustic Imaging of Nanoparticles in Cells and Tissues. *ACS Nano*. 7, 1272-1280 (**2013**)
73 L.-S. Bouchard, M. S. Anwar, G. L. Liu, B. Hann, Z. H. Xie, J. W. Gray, X. Wang, A. Pines, and F. F. Chen, Picomolar sensitivity MRI and photoacoustic imaging of cobalt nanoparticles. *P. Natl. Acad. Sci*. 106, 4085-4089 (**2009**)
74 Z. Zha, S. Zhang, Z. Deng, Y. Li, C. Li, and Z. Dai, Enzyme-responsive copper sulphide nanoparticles for combined photoacoustic imaging, tumor-selective chemotherapy and photothermal therapy. *Chem. Commun*. 49, 3455-3457 (**2013**)
75 L. Wu, X. Cai, K. Nelson, W. Xing, J. Xia, R. Zhang, A. Stacy, M. Luderer, G. Lanza, L. Wang, B. Shen, and D. Pan, A green synthesis of carbon nanoparticles from honey and their use in real-time photoacoustic imaging. *Nano Res*. 6, 312-325 (**2013**)

76 Y. Kohl, C. Kaiser, W. Bost, F. Stracke, M. Fournelle, C. Wischke, H. Thielecke, A. Lendlein, K. Kratz, and R. Lemor, Preparation and biological evaluation of multifunctional PLGA-nanoparticles designed for photoacoustic imaging. *Nanomed-Nanotechnol*. 7, 228-237 (**2011**)
77 P. K. Jain, X. Huang, I. H. El-Sayed, and M. A. El-Sayed, Noble Metals on the Nanoscale: Optical and Photothermal Properties and Some Applications in Imaging, Sensing, Biology, and Medicine. *Accounts Chem. Res*. 41, 1578-1586 (**2008**)
78 X. Huang, P. Jain, I. El-Sayed, and M. El-Sayed, Plasmonic photothermal therapy (PPTT) using gold nanoparticles. *Laser Med. Sci*. 23, 217-228 (**2008**)
79 B. Nikoobakht, and M. A. El-Sayed, Preparation and Growth Mechanism of Gold Nanorods (NRs) Using Seed-Mediated Growth Method. *Chem. Mater*. 15, 1957-1962 (**2003**)
80 L. Gou, and C. J. Murphy, Fine-Tuning the Shape of Gold Nanorods. *Chem. Mater*. 17, 3668-3672 (**2005**)
81 Z. Zhang, L. Wang, J. Wang, X. Jiang, X. Li, Z. Hu, Y. Ji, X. Wu, and C. Chen, Mesoporous Silica-Coated Gold Nanorods as a Light-Mediated Multifunctional Theranostic Platform for Cancer Treatment. *Adv. Mater*. 24, 1418-1423 (**2012**)
82 Y.-F. Huang, K. Sefah, S. Bamrungsap, H.-T. Chang, and W. Tan, Selective Photothermal Therapy for Mixed Cancer Cells Using Aptamer-Conjugated Nanorods. *Langmuir*. 24, 11860-11865 (**2008**)
83 Z. Li, P. Huang, X. Zhang, J. Lin, S. Yang, B. Liu, F. Gao, P. Xi, Q. Ren, and D. Cui, RGD-Conjugated Dendrimer-Modified Gold Nanorods for in Vivo Tumor Targeting and Photothermal Therapy†. *Mol. Pharm*. 7, 94-104 (**2009**)
84 T. B. Huff, L. Tong, Y. Zhao, M. N. Hansen, J.-X. Cheng, and A. Wei, Hyperthermic effects of gold nanorods on tumor cells. *Nanomedicine*. 2, 125-132 (**2007**)
85 J. L. Li, D. Day, and M. Gu, Ultra-Low Energy Threshold for Cancer Photothermal Therapy Using Transferrin-Conjugated Gold Nanorods. *Adv. Mater*. 20, 3866-3871 (**2008**)
86 D. K. Yi, I.-C. Sun, J. H. Ryu, H. Koo, C. W. Park, I.-C. Youn, K. Choi, I. C. Kwon, K. Kim, and C.-H. Ahn, Matrix Metalloproteinase Sensitive Gold Nanorod for Simultaneous Bioimaging and Photothermal Therapy of Cancer. *Bioconjugate Chem*. 21, 2173-2177 (**2010**)
87 W. I. Choi, J.-Y. Kim, C. Kang, C. C. Byeon, Y. H. Kim, and G. Tae, Tumor Regression In Vivo by Photothermal Therapy Based on Gold-Nanorod-Loaded, Functional Nanocarriers. *ACS Nano*. 5, 1995-2003 (**2011**)
88 H. Kang, B. Jia, J. Li, D. Morrish, and M. Gu, Enhanced photothermal therapy assisted with gold nanorods using a radially polarized beam. *Appl. Phys. Lett*. 96, - (**2010**)
89 E. B. Dickerson, E. C. Dreaden, X. Huang, I. H. El-Sayed, H. Chu, S. Pushpanketh, J. F. McDonald, and M. A. El-Sayed, Gold nanorod assisted near-infrared plasmonic photothermal therapy (PPTT) of squamous cell carcinoma in mice. *Cancer Lett*. 269, 57-66 (**2008**)
90 X. Huang, W. Qian, I. H. El-Sayed, and M. A. El-Sayed, The potential use of the enhanced nonlinear properties of gold nanospheres in photothermal cancer therapy. *Laser Surg. Med*. 39, 747-753 (**2007**)

91 X. Huang, P. K. Jain, I. H. El-Sayed, and M. A. El-Sayed, Determination of the Minimum Temperature Required for Selective Photothermal Destruction of Cancer Cells with the Use of Immunotargeted Gold Nanoparticles. *Photochem. Photobiol*. 82, 412-417 (**2006**)
92 I. H. El-Sayed, X. Huang, and M. A. El-Sayed, Selective laser photo-thermal therapy of epithelial carcinoma using anti-EGFR antibody conjugated gold nanoparticles. *Cancer Lett*. 239, 129-135 (**2006**)
93 J. Nam, N. Won, H. Jin, H. Chung, and S. Kim, pH-Induced Aggregation of Gold Nanoparticles for Photothermal Cancer Therapy. *J. Am. Chem. Soc*. 131, 13639-13645 (**2009**)
94 D. P. O'Neal, L. R. Hirsch, N. J. Halas, J. D. Payne, and J. L. West, Photo-thermal tumor ablation in mice using near infrared-absorbing nanoparticles. *Cancer Lett*. 209, 171-176 (**2004**)
95 A. R. Lowery, A. M. Gobin, E. S. Day, N. J. Halas, and J. L. West, Immunonanoshells for targeted photothermal ablation of tumor cells. *Int. J. Nanomed*. 1, 149-154 (**2006**)
96 C. Loo, A. Lowery, N. Halas, J. West, and R. Drezek, Immunotargeted Nanoshells for Integrated Cancer Imaging and Therapy. *Nano Lett*. 5, 709-711 (**2005**)
97 L. R. Hirsch, R. J. Stafford, J. A. Bankson, S. R. Sershen, B. Rivera, R. E. Price, J. D. Hazle, N. J. Halas, and J. L. West, Nanoshell-mediated near-infrared thermal therapy of tumors under magnetic resonance guidance. *P. Natl. Acad. Sci*. 100, 13549-13554 (**2003**)
98 A. M. Gobin, M. H. Lee, N. J. Halas, W. D. James, R. A. Drezek, and J. L. West, Near-Infrared Resonant Nanoshells for Combined Optical Imaging and Photothermal Cancer Therapy. *Nano Lett*. 7, 1929-1934 (**2007**)
99 E. Day, P. Thompson, L. Zhang, N. Lewinski, N. Ahmed, R. Drezek, S. Blaney, and J. West, Nanoshell-mediated photothermal therapy improves survival in a murine glioma model. *J Neuro-Oncol*. 104, 55-63 (**2011**)
100 S. Lal, S. E. Clare, and N. J. Halas, Nanoshell-Enabled Photothermal Cancer Therapy: Impending Clinical Impact. *Accounts of Chem. Res*. 41, 1842-1851 (**2008**)
101 M.-R. Choi, K. J. Stanton-Maxey, J. K. Stanley, C. S. Levin, R. Bardhan, D. Akin, S. Badve, J. Sturgis, J. P. Robinson, R. Bashir, N. J. Halas, and S. E. Clare, A Cellular Trojan Horse for Delivery of Therapeutic Nanoparticles into Tumors. *Nano Lett*. 7, 3759-3765 (**2007**)
102 M. N. Rylander, R. J. Stafford, J. Hazle, J. Whitney, and K. R. Diller, Heat shock protein expression and temperature distribution in prostate tumours treated with laser irradiation and nanoshells. *Int. J. Hyperther*. 27, 791-801 (**2011**)
103 X. Ji, R. Shao, A. M. Elliott, R. J. Stafford, E. Esparza-Coss, J. A. Bankson, G. Liang, Z.-P. Luo, K. Park, J. T. Markert, and C. Li, Bifunctional Gold Nanoshells with a Superparamagnetic Iron Oxide−Silica Core Suitable for Both MR Imaging and Photothermal Therapy. *J. Phys. Chem. C*. 111, 6245-6251 (**2007**)
104 W. Dong, Y. Li, D. Niu, Z. Ma, J. Gu, Y. Chen, W. Zhao, X. Liu, C. Liu, and J. Shi, Facile Synthesis of Monodisperse Superparamagnetic Fe3O4 Core@hybrid@Au Shell Nanocomposite for Bimodal Imaging and Photothermal Therapy. *Adv. Mater*. 23, 5392-5397 (**2011**)

105 J. You, G. Zhang, and C. Li, Exceptionally High Payload of Doxorubicin in Hollow Gold Nanospheres for Near-Infrared Light-Triggered Drug Release. *ACS Nano*. 4, 1033-1041 (**2010**)
106 M. P. Melancon, W. Lu, Z. Yang, R. Zhang, Z. Cheng, A. M. Elliot, J. Stafford, T. Olson, J. Z. Zhang, and C. Li, In vitro and in vivo targeting of hollow gold nanoshells directed at epidermal growth factor receptor for photothermal ablation therapy. *Mol Cancer Ther*. 7, 1730-1739 (**2008**)
107 A. M. Gobin, E. M. Watkins, E. Quevedo, V. L. Colvin, and J. L. West, Near-Infrared-Resonant Gold/Gold Sulfide Nanoparticles as a Photothermal Cancer Therapeutic Agent. *Small*. 6, 745-752 (**2010**)
108 E. S. Day, L. Bickford, J. Slater, N. Riggall, R. Drezek, and J. L. West, Antibody-conjugated gold-gold sulfide nanoparticles as multifunctional agents for imaging and therapy of breast cancer. *Int. J. Nanomed.* 5, 445-454 (**2010**)
109 H. Park, J. Yang, J. Lee, S. Haam, I.-H. Choi, and K.-H. Yoo, Multifunctional Nanoparticles for Combined Doxorubicin and Photothermal Treatments. *ACS Nano*. 3, 2919-2926 (**2009**)
110 H. Ke, J. Wang, Z. Dai, Y. Jin, E. Qu, Z. Xing, C. Guo, X. Yue, and J. Liu, Gold-Nanoshelled Microcapsules: A Theranostic Agent for Ultrasound Contrast Imaging and Photothermal Therapy. *Angew. Chem*. 123, 3073-3077 (**2011**)
111 B. N. Khlebtsov, V. A. Khanadeev, I. L. Maksimova, G. S. Terentyuk, and N. G. Khlebtsov, Silver nanocubes and gold nanocages: Fabrication and optical and photothermal properties. *Nanotechnol. Russia*. 5, 454-468 (**2010**)
112 J. Chen, D. Wang, J. Xi, L. Au, A. Siekkinen, A. Warsen, Z.-Y. Li, H. Zhang, Y. Xia, and X. Li, Immuno Gold Nanocages with Tailored Optical Properties for Targeted Photothermal Destruction of Cancer Cells. *Nano Lett*. 7, 1318-1322 (**2007**)
113 L. Au, D. Zheng, F. Zhou, Z.-Y. Li, X. Li, and Y. Xia, A Quantitative Study on the Photothermal Effect of Immuno Gold Nanocages Targeted to Breast Cancer Cells. *ACS Nano*. 2, 1645-1652 (**2008**)
114 S. E. Skrabalak, J. Chen, Y. Sun, X. Lu, L. Au, C. M. Cobley, and Y. Xia, Gold Nanocages: Synthesis, Properties, and Applications. *Accounts Chem. Res*. 41, 1587-1595 (**2008**)
115 H. Yuan, A. M. Fales, and T. Vo-Dinh, TAT Peptide-Functionalized Gold Nanostars: Enhanced Intracellular Delivery and Efficient NIR Photothermal Therapy Using Ultralow Irradiance. *J. Am. Chem. Soc.* 134, 11358-11361 (**2012**)
116 C. L. Nehl, H. Liao, and J. H. Hafner, Optical Properties of Star-Shaped Gold Nanoparticles. *Nano Lett*. 6, 683-688 (**2006**)
117 B. Kang, M. A. Mackey, and M. A. El-Sayed, Nuclear Targeting of Gold Nanoparticles in Cancer Cells Induces DNA Damage, Causing Cytokinesis Arrest and Apoptosis. *J. Am. Chem. Soc.* 132, 1517-1519 (**2010**)
118 G. von Maltzahn, J.-H. Park, A. Agrawal, N. K. Bandaru, S. K. Das, M. J. Sailor, and S. N. Bhatia, Computationally Guided Photothermal Tumor Therapy Using Long-Circulating Gold Nanorod Antennas. *Cancer Res*. 69, 3892-3900 (**2009**)
119 A. K. Singh, W. Lu, D. Senapati, S. A. Khan, Z. Fan, T. Senapati, T. Demeritte, L. Beqa, and P. C. Ray, Long-Range Nanoparticle Surface-Energy-Transfer Ruler for Monitoring Photothermal Therapy Response. *Small*. 7, 2517-2525 (**2011**)

120 W. Lu, A. K. Singh, S. A. Khan, D. Senapati, H. Yu, and P. C. Ray, Gold Nano-Popcorn-Based Targeted Diagnosis, Nanotherapy Treatment, and In Situ Monitoring of Photothermal Therapy Response of Prostate Cancer Cells Using Surface-Enhanced Raman Spectroscopy. *J. Am. Chem. Soc.* 132, 18103-18114 (**2010**)
121 S. C. Boca, M. Potara, A.-M. Gabudean, A. Juhem, P. L. Baldeck, and S. Astilean, Chitosan-coated triangular silver nanoparticles as a novel class of biocompatible, highly effective photothermal transducers for in vitro cancer cell therapy. *Cancer Lett*. 311, 131-140 (**2011**)
122 R. Di Corato, D. Palumberi, R. Marotta, M. Scotto, S. Carregal-Romero, P. Rivera_Gil, W. J. Parak, and T. Pellegrino, Magnetic Nanobeads Decorated with Silver Nanoparticles as Cytotoxic Agents and Photothermal Probes. *Small*. 8, 2731-2742 (**2012**)
123 S. Ilknur, C. Dilek, K. Mehmet, B. Asli, and C. Mustafa, Interaction of multi-functional silver nanoparticles with living cells. *Nanotechnology*. 21, 175104 (**2010**)
124 P. Yang, Q.-Z. Xu, S.-Y. Jin, Y. Lu, Y. Zhao, and S.-H. Yu, Synthesis of Multifunctional Ag@Au@Phenol Formaldehyde Resin Particles Loaded with Folic Acids for Photothermal Therapy. *Chem–Eur. J.* 18, 9294-9299 (**2012**)
125 P. Wu, Y. Gao, H. Zhang, and C. Cai, Aptamer-Guided Silver–Gold Bimetallic Nanostructures with Highly Active Surface-Enhanced Raman Scattering for Specific Detection and Near-Infrared Photothermal Therapy of Human Breast Cancer Cells. *Anal. Chem*. 84, 7692-7699 (**2012**)
126 L.-C. Cheng, J.-H. Huang, H. M. Chen, T.-C. Lai, K.-Y. Yang, R.-S. Liu, M. Hsiao, C.-H. Chen, L.-J. Her, and D. P. Tsai, Seedless, silver-induced synthesis of star-shaped gold/silver bimetallic nanoparticles as high efficiency photothermal therapy reagent. *J. Mater. Chem*. 22, 2244-2253 (**2012**)
127 P. Wu, Y. Gao, Y. Lu, H. Zhang, and C. Cai, High specific detection and near-infrared photothermal therapy of lung cancer cells with high SERS active aptamer-silver-gold shell-core nanostructures. *Analyst*. 138, 6501-6510 (**2013**)
128 C. M. Hessel, V. P. Pattani, M. Rasch, M. G. Panthani, B. Koo, J. W. Tunnell, and B. A. Korgel, Copper Selenide Nanocrystals for Photothermal Therapy. *Nano Lett*. 11, 2560-2566 (**2011**)
129 Y. Li, W. Lu, Q. Huang, M. Huang, C. Li, and W. Chen, Copper sulfide nanoparticles for photothermal ablation of tumor cells. *Nanomedicine*. 5, 1161-1171 (**2010**)
130 M. Zhou, R. Zhang, M. Huang, W. Lu, S. Song, M. P. Melancon, M. Tian, D. Liang, and C. Li, A Chelator-Free Multifunctional [64Cu]CuS Nanoparticle Platform for Simultaneous Micro-PET/CT Imaging and Photothermal Ablation Therapy. *J. Am. Chem. Soc*. 132, 15351-15358 (**2010**)
131 T. N. Lambert, N. L. Andrews, H. Gerung, T. J. Boyle, J. M. Oliver, B. S. Wilson, and S. M. Han, Water-Soluble Germanium(0) Nanocrystals: Cell Recognition and Near-Infrared Photothermal Conversion Properties. *Small*. 3, 691-699 (**2007**)
132 K.-W. Hu, F.-Y. Jhang, C.-H. Su, and C.-S. Yeh, Fabrication of Gd2O(CO3)2[middle dot]H2O/silica/gold hybrid particles as a bifunctional agent for MR imaging and photothermal destruction of cancer cells. *J. Mater. Chem.* 19, 2147-2153 (**2009**)

133 S. Regli, J. A. Kelly, A. M. Shukaliak, and J. G. C. Veinot, Photothermal Response of Photoluminescent Silicon Nanocrystals. *J. Phys. Chem. Lett*. 3, 1793-1797 (**2012**)
134 C. Lee, H. Kim, C. Hong, M. Kim, S. S. Hong, D. H. Lee, and W. I. Lee, Porous silicon as an agent for cancer thermotherapy based on near-infrared light irradiation. *J. Mater. Chem*. 18, 4790-4795 (**2008**)
135 C. Lee, C. Hong, J. Lee, M. Son, and S.-S. Hong, Comparison of oxidized porous silicon with bare porous silicon as a photothermal agent for cancer cell destruction based on in vitro cell test results. *Laser Med. Sci*. 27, 1001-1008 (**2012**)
136 S. P. Sherlock, S. M. Tabakman, L. Xie, and H. Dai, Photothermally Enhanced Drug Delivery by Ultrasmall Multifunctional FeCo/Graphitic Shell Nanocrystals. *ACS Nano*. 5, 1505-1512 (**2011**)
137 S. Sherlock, and H. Dai, Multifunctional FeCo-graphitic carbon nanocrystals for combined imaging, drug delivery and tumor-specific photothermal therapy in mice. *Nano Res*. 4, 1248-1260 (**2011**)
138 C. Lee, C. Hong, H. Kim, J. Kang, and H. M. Zheng, TiO2 Nanotubes as a Therapeutic Agent for Cancer Thermotherapy. *Photochem. Photobiol*. 86, 981-989 (**2010**)
139 L. Cheng, K. Yang, Y. Li, X. Zeng, M. Shao, S.-T. Lee, and Z. Liu, Multifunctional nanoparticles for upconversion luminescence/MR multimodal imaging and magnetically targeted photothermal therapy. *Biomaterials*. 33, 2215-2222 (**2012**)
140 L. Lu, G. Burkey, I. Halaciuga, and D. V. Goia, Core–shell gold/silver nanoparticles: Synthesis and optical properties. *J. Colloid Interf. Sci*. 392, 90-95 (**2013**)
141 W. Zhang, Z. Guo, D. Huang, Z. Liu, X. Guo, and H. Zhong, Synergistic effect of chemo-photothermal therapy using PEGylated graphene oxide. *Biomaterials*. 32, 8555-8561 (**2011**)
142 Z. M. Markovic, L. M. Harhaji-Trajkovic, B. M. Todorovic-Markovic, D. P. Kepić, K. M. Arsikin, S. P. Jovanović, A. C. Pantovic, M. D. Dramićanin, and V. S. Trajkovic, In vitro comparison of the photothermal anticancer activity of graphene nanoparticles and carbon nanotubes. *Biomaterials*. 32, 1121-1129 (**2011**)
143 J. T. Robinson, S. M. Tabakman, Y. Liang, H. Wang, H. Sanchez Casalongue, D. Vinh, and H. Dai, Ultrasmall Reduced Graphene Oxide with High Near-Infrared Absorbance for Photothermal Therapy. *J. Am. Chem. Soc*. 133, 6825-6831 (**2011**)
144 K. Yang, J. Wan, S. Zhang, B. Tian, Y. Zhang, and Z. Liu, The influence of surface chemistry and size of nanoscale graphene oxide on photothermal therapy of cancer using ultra-low laser power. *Biomaterials*. 33, 2206-2214 (**2012**)
145 S. K. Singh, M. K. Singh, P. P. Kulkarni, V. K. Sonkar, J. J. A. Grácio, and D. Dash, Amine-Modified Graphene: Thrombo-Protective Safer Alternative to Graphene Oxide for Biomedical Applications. *ACS Nano*. 6, 2731-2740 (**2012**)
146 K. Yang, S. Zhang, G. Zhang, X. Sun, S.-T. Lee, and Z. Liu, Graphene in Mice: Ultrahigh In Vivo Tumor Uptake and Efficient Photothermal Therapy. *Nano Lett*. 10, 3318-3323 (**2010**)
147 X. Ma, H. Tao, K. Yang, L. Feng, L. Cheng, X. Shi, Y. Li, L. Guo, and Z. Liu, A functionalized graphene oxide-iron oxide nanocomposite for magnetically targeted drug delivery, photothermal therapy, and magnetic resonance imaging. *Nano Res*. 5, 199-212 (**2012**)

148 F. Zhou, D. E. Resasco, W. R. Chen, D. Xing, Z. Ou, and B. Wu, Cancer photothermal therapy in the near-infrared region by using single-walled carbon nanotubes. *J. Biomed. Opt*. 14, 021009-021009-7 (**2009**)
149 H. K. Moon, S. H. Lee, and H. C. Choi, In Vivo Near-Infrared Mediated Tumor Destruction by Photothermal Effect of Carbon Nanotubes. *ACS Nano*. 3, 3707-3713 (**2009**)
150 Z. Liu, A. C. Fan, K. Rakhra, S. Sherlock, A. Goodwin, X. Chen, Q. Yang, D. W. Felsher, and H. Dai, Supramolecular Stacking of Doxorubicin on Carbon Nanotubes for In Vivo Cancer Therapy. *Angew. Chem. Int. Edit*. 48, 7668-7672 (**2009**)
151 X. Liu, H. Tao, K. Yang, S. Zhang, S.-T. Lee, and Z. Liu, Optimization of surface chemistry on single-walled carbon nanotubes for in vivo photothermal ablation of tumors. *Biomaterials*. 32, 144-151 (**2011**)
152 N. Huang, H. Wang, J. Zhao, H. Lui, M. Korbelik, and H. Zeng, Single-wall carbon nanotubes assisted photothermal cancer therapy: Animal study with a murine model of squamous cell carcinoma. *Laser Surg. Med*. 42, 798-808 (**2010**)
153 P. Chakravarty, R. Marches, N. S. Zimmerman, A. D.-E. Swafford, P. Bajaj, I. H. Musselman, P. Pantano, R. K. Draper, and E. S. Vitetta, Thermal ablation of tumor cells with antibody-functionalized single-walled carbon nanotubes. *P. Natl. Acad. Sci*. 105, 8697-8702 (**2008**)
154 F. Zhou, S. Wu, B. Wu, W. R. Chen, and D. Xing, Mitochondria-Targeting Single-Walled Carbon Nanotubes for Cancer Photothermal Therapy. *Small*. 7, 2727-2735 (**2011**)
155 A. R. Burke, R. N. Singh, D. L. Carroll, J. C. S. Wood, R. B. D'Agostino Jr, P. M. Ajayan, F. M. Torti, and S. V. Torti, The resistance of breast cancer stem cells to conventional hyperthermia and their sensitivity to nanoparticle-mediated photothermal therapy. *Biomaterials*. 33, 2961-2970 (**2012**)
156 A. Burke, X. Ding, R. Singh, R. A. Kraft, N. Levi-Polyachenko, M. N. Rylander, C. Szot, C. Buchanan, J. Whitney, J. Fisher, H. C. Hatcher, R. D'Agostino, N. D. Kock, P. M. Ajayan, D. L. Carroll, S. Akman, F. M. Torti, and S. V. Torti, Long-term survival following a single treatment of kidney tumors with multiwalled carbon nanotubes and near-infrared radiation. *P. Natl. Acad. Sci*. 106, 12897-12902 (**2009**)
157 J. W. Fisher, S. Sarkar, C. F. Buchanan, C. S. Szot, J. Whitney, H. C. Hatcher, S. V. Torti, C. G. Rylander, and M. N. Rylander, Photothermal Response of Human and Murine Cancer Cells to Multiwalled Carbon Nanotubes after Laser Irradiation. *Cancer Res*. 70, 9855-9864 (**2010**)
158 L. Mocan, F. Tabaran, T. Mocan, C. Bele, A. I. Orza, C. Lucan, R. Stiufiuc, I. Manaila, F. Iulia, I. Dana, F. Zaharie, G. Osian, L. Vlad, and C. Iancu, Selective ex-vivo photothermal ablation of human pancreatic cancer with albumin functionalized multiwalled carbon nanotubes. *Int. J. Nanomed*. 6, 915-928 (**2011**)
159 G. Duscher, M. Chisholm, A. Puretzky, C. Rouleau, and D. Geohegan, Atomic Structure of Single Walled Carbon Nanohorns. *Microsc. Microanal*. 17, 1510-1511 (**2011**)
160 S. Iijima, M. Yudasaka, R. Yamada, S. Bandow, K. Suenaga, F. Kokai, and K. Takahashi, Nano-aggregates of single-walled graphitic carbon nano-horns. *Chem. Phys. Lett.* 309, 165-170 (**1999**)

161 T. Murakami, J. Fan, M. Yudasaka, S. Iijima, and K. Shiba, Solubilization of Single-Wall Carbon Nanohorns Using a PEG−Doxorubicin Conjugate. *Molecular Pharmaceutics*. 3, 407-414 (**2006**)
162 T. Murakami, K. Ajima, J. Miyawaki, M. Yudasaka, S. Iijima, and K. Shiba, Drug-Loaded Carbon Nanohorns: Adsorption and Release of Dexamethasone in Vitro. *Mol. Pharm*. 1, 399-405 (**2004**)
163 K. Ajima, M. Yudasaka, T. Murakami, A. Maigné, K. Shiba, and S. Iijima, Carbon Nanohorns as Anticancer Drug Carriers. *Mol. Pharm.* 2, 475-480 (**2005**)
164 K. Ajima, T. Murakami, Y. Mizoguchi, K. Tsuchida, T. Ichihashi, S. Iijima, and M. Yudasaka, Enhancement of In Vivo Anticancer Effects of Cisplatin by Incorporation Inside Single-Wall Carbon Nanohorns. *ACS Nano*. 2, 2057-2064 (**2008**)
165 J. Xu, M. Yudasaka, S. Kouraba, M. Sekido, Y. Yamamoto, and S. Iijima, Single wall carbon nanohorn as a drug carrier for controlled release. *Chem. Phys. Lett*. 461, 189-192 (**2008**)
166 T. Murakami, H. Sawada, G. Tamura, M. Yudasaka, S. Iijima, and K. Tsuchida, Water-dispersed single-wall carbon nanohorns as drug carriers for local cancer chemotherapy. *Nanomedicine*. 3, 453-463 (**2008**)
167 M. Zhang, T. Murakami, K. Ajima, K. Tsuchida, A. S. D. Sandanayaka, O. Ito, S. Iijima, and M. Yudasaka, Fabrication of ZnPc/protein nanohorns for double photodynamic and hyperthermic cancer phototherapy. *P. Natl. Acad. Sci*. 105, 14773-14778 (**2008**)
168 J. Miyawaki, M. Yudasaka, T. Azami, Y. Kubo, and S. Iijima, Toxicity of Single-Walled Carbon Nanohorns. *ACS Nano*. 2, 213-226 (**2008**)
169 J. R. Whitney, S. Sarkar, J. Zhang, T. Do, T. Young, M. K. Manson, T. A. Campbell, A. A. Puretzky, C. M. Rouleau, K. L. More, D. B. Geohegan, C. G. Rylander, H. C. Dorn, and M. N. Rylander, Single walled carbon nanohorns as photothermal cancer agents. *Laser Surg. Med*. 43, 43-51 (**2011**)
170 J. R. Whitney, A. Rodgers, E. Harvie, W. F. Carswell, S. Torti, A. A. Puretzky, C. M. Rouleau, D. B. Geohegan, C. G. Rylander, and M. N. Rylander, Spatial and temporal measurements of temperature and cell viability in response to nanoparticle-mediated photothermal therapy. *Nanomedicine*. 7, 1729-1742 (**2012**)
171 J. Whitney, M. DeWitt, B. M. Whited, W. Carswell, A. Simon, C. G. Rylander, and M. N. Rylander, 3D viability imaging of tumor phantoms treated with single-walled carbon nanohorns and photothermal therapy. *Nanotechnology*. 24, 275102 (**2013**)
172 E. Miyako, T. Deguchi, Y. Nakajima, M. Yudasaka, Y. Hagihara, M. Horie, M. Shichiri, Y. Higuchi, F. Yamashita, M. Hashida, Y. Shigeri, Y. Yoshida, and S. Iijima, Photothermic regulation of gene expression triggered by laser-induced carbon nanohorns. *P. Natl. Acad. Sci*. 109, 7523-7528 (**2012**)
173 R. L. Hood, W. Carswell, A. Rodgers, M. Kosoglu, M. Rylander, D. Grant, J. Robertson, and C. Rylander, Spatially controlled photothermal heating of bladder tissue through single-walled carbon nanohorns delivered with a fiberoptic microneedle device. *Laser Med. Sci*. 28, 1143-1150 (**2013**)
174 J. Miyawaki, M. Yudasaka, H. Imai, H. Yorimitsu, H. Isobe, E. Nakamura, and S. Iijima, In Vivo Magnetic Resonance Imaging of Single-Walled Carbon Nanohorns by Labeling with Magnetite Nanoparticles. *Adv. Mater*. 18, 1010-1014 (**2006**)

175 L. Cheng, K. Yang, Q. Chen, and Z. Liu, Organic Stealth Nanoparticles for Highly Effective in Vivo Near-Infrared Photothermal Therapy of Cancer. *ACS Nano*. 6, 5605-5613 (**2012**)
176 D. E. J. G. J. Dolmans, D. Fukumura, and R. K. Jain, Photodynamic therapy for cancer. *Nat. Rev. Cancer*. 3, 380-387 (**2003**)
177 I. J. MacDonald, and T. J. Dougherty, Basic principles of photodynamic therapy. *J. Porphyr. Phthalocya.* 5, 105-129 (**2001**)
178 B. W. Henderson, and T. J. Dougherty, How Does Photodynamic Therapy Work. *Photochem. Photobiol*. 55, 145-157 (**1992**)
179 G. W. Sledge, and K. D. Miller, Exploiting the hallmarks of cancer: the future conquest of breast cancer. *Eur. J. Cancer*. 39, 1668-1675 (**2003**)
180 M. C. DeRosa, and R. J. Crutchley, Photosensitized singlet oxygen and its applications. *Coordin. Chem. Rev*. 233, 351-371 (**2002**)
181 M. W. Wiedmann, and K. Caca, General principles of photodynamic therapy (PDT) and gastrointestinal applications. *Curr. Pharm. Biotechno.* 5, 397-408 (**2004**)
182 T. R. Nathan, D. E. Whitelaw, S. C. Chang, W. R. Lees, P. M. Ripley, H. Payne, L. Jones, M. C. Parkinson, M. Emberton, A. R. Gillams, A. R. Mundy, and S. G. Bown, Photodynamic therapy for prostate cancer recurrence after radiotherapy: A phase I study. *J. Urology*. 168, 1427-1432 (**2002**)
183 S. G. Bown, A. Z. Rogowska, D. E. Whitelaw, W. R. Lees, L. B. Lovat, P. Ripley, L. Jones, P. Wyld, A. Gillams, and A. W. Hatfield, Photodynamic therapy for cancer of the pancreas. *Gut*. 50, 549-57 (**2002**)
184 K. Moghissi, and K. Dixon, Is bronchoscopic photodynamic therapy a therapeutic option in lung cancer? *Eur. Respir. J*. 22, 535-541 (**2003**)
185 S. B. Brown, E. A. Brown, and I. Walker, The present and future role of photodynamic therapy in cancer treatment. *Lancet Oncol*. 5, 497-508 (**2004**)
186 W. Chen, and J. Zhang, Using nanoparticles to enable simultaneous radiation and photodynamic therapies for cancer treatment. *J. Nanosci. Nanotechno*. 6, 1159-1166 (**2006**)
187 D. K. Chatterjee, L. S. Fong, and Y. Zhang, Nanoparticles in photodynamic therapy: An emerging paradigm. *Adv. Drug Deliver. Rev*. 60, 1627-1637 (**2008**)
188 R. R. Allison, and C. H. Sibata, Oncologic photodynamic therapy photosensitizers: A clinical review. *Photodiagn. Photodyn*. 7, 61-75 (**2010**)
189 M. Triesscheijn, P. Baas, J. H. M. Schellens, and F. A. Stewart, Photodynamic therapy in oncology. *Oncologist*. 11, 1034-1044 (**2006**)
190 T. J. Dougherty, C. J. Gomer, B. W. Henderson, G. Jori, D. Kessel, M. Korbelik, J. Moan, and Q. Peng, Photodynamic therapy. *J. Natl. Cancer I.* 90, 889-905 (**1998**)
191 N. Brasseur, D. Brault, and P. Couvreur, Adsorption of Hematoporphyrin onto Polyalkylcyanoacrylate Nanoparticles - Carrier Capacity and Drug Release. *Int. J. Pharm*. 70, 129-135 (**1991**)
192 H. L. L. M. Vanleengoed, V. Cuomo, A. A. C. Versteeg, N. Vanderveen, G. Jori, and W. M. Star, In-Vivo Fluorescence and Photodynamic Activity of Zinc Phthalocyanine Administered in Liposomes. *Brit. J. Cancer*. 69, 840-845 (**1994**)
193 M. A. D'Hallewin, D. Kochetkov, Y. Viry-Babel, A. Leroux, E. Werkmeister, D. Dumas, S. Grafe, V. Zorin, F. Guillemin, and L. Bezdetnaya, Photodynamic therapy with

intratumoral administration of lipid-based mTHPC in a model of breast cancer recurrence. *Laser Surg. Med*. 40, 543-549 (**2008**)
194 Y. P. Fang, P. C. Wu, Y. H. Tsai, and Y. B. Huang, Physicochemical and safety evaluation of 5-aminolevulinic acid in novel liposomes as carrier for skin delivery. *J. Liposome Res*. 18, 31-45 (**2008**)
195 D. Kozlowska, P. Foran, P. MacMahon, M. J. Shelly, S. Eustace, and R. O'Kennedy, Molecular and magnetic resonance imaging: The value of immunoliposomes. *Adv. Drug Deliver. Rev.* 61, 1402-1411 (**2009**)
196 P. Sapra, and T. M. Allen, Internalizing antibodies are necessary for improved therapeutic efficacy of antibody-targeted liposomal drugs. *Cancer Res*. 62, 7190-7194 (**2002**)
197 J. Morgan, A. G. Gray, and E. R. Huehns, Specific Targeting and Toxicity of Sulfonated Aluminum Phthalocyanine Photosensitized Liposomes Directed to Cells by Monoclonal-Antibody Invitro. *Brit. J. Cancer*. 59, 366-370 (**1989**)
198 Y. E. K. Lee, and R. Kopelman, Polymeric Nanoparticles for Photodynamic Therapy. *Biomed. Nanoetechnol: Meth. Prot.* 726, 151-178 (**2011**)
199 F. A. Anderson, Amended final report on the safety assessment of polyacrylamide and acrylamide residues in cosmetics. *Int J Toxicol*. 24 Suppl 2, 21-50 (**2005**)
200 H. J. Hah, G. Kim, Y. E. K. Lee, D. A. Orringer, O. Sagher, M. A. Philbert, and R. Kopelman, Methylene Blue-Conjugated Hydrogel Nanoparticles and Tumor-Cell Targeted Photodynamic Therapy. *Macromol. Biosci*. 11, 90-99 (**2011**)
201 Y. E. L. Koo, G. R. Reddy, M. Bhojani, R. Schneider, M. A. Philbert, A. Rehemtulla, B. D. Ross, and R. Kopelman, Brain cancer diagnosis and therapy with nanoplatforms. *Adv. Drug Deliver. Rev*. 58, 1556-1577 (**2006**)
202 H. Maeda, G. Y. Bharate, and J. Daruwalla, Polymeric drugs for efficient tumor-targeted drug delivery based on EPR-effect. *Eur. J. Pharm. Biopharm*. 71, 409-419 (**2009**)
203 G. R. Reddy, M. S. Bhojani, P. McConville, J. Moody, B. A. Moffat, D. E. Hall, G. Kim, Y. E. L. Koo, M. J. Woolliscroft, J. V. Sugai, T. D. Johnson, M. A. Philbert, R. Kopelman, A. Rehemtulla, and B. D. Ross, Vascular targeted nanoparticles for imaging and treatment of brain tumors. *Clin. Cancer Res*. 12, 6677-6686 (**2006**)
204 W. Tang, H. Xu, E. J. Park, M. A. Philbert, and R. Kopelman, Encapsulation of methylene blue in polyacrylamide nanoparticle platforms protects its photodynamic effectiveness. *Biochem. Biophys. Res. Co*. 369, 579-583 (**2008**)
205 D. Gao, R. R. Agayan, H. Xu, M. A. Philbert, and R. Kopelman, Nanoparticles for two-photon photodynamic therapy in living cells. *Nano Lett*. 6, 2383-2386 (**2006**)
206 Y. N. Konan, M. Berton, R. Gurny, and E. Allemann, Enhanced photodynamic activity of meso-tetra(4-hydroxyphenyl)porphyrin by incorporation into sub-200 nm nanoparticles. *Eur. J. Pharm. Sci.* 18, 241-249 (**2003**)
207 E. Allemann, J. Rousseau, N. Brasseur, S. V. Kudrevich, K. Lewis, and J. E. vanLier, Photodynamic therapy of tumours with hexadecafluoro zinc phthalocyanine formulated in PEG-coated poly(lactic acid) nanoparticles. *Int. J. Cancer*. 66, 821-824 (**1996**)
208 B. Pegaz, E. Debefve, J. P. Ballini, Y. N. Konan-Kouakou, and H. van den Bergh, Effect of nanoparticle size on the extravasation and the photothrombic activity of meso(p-tetracarboxyphenyl)porphyrin. *J. Photoch. Photobio. B*. 85, 216-222 (**2006**)

209 E. Ricci-Junior, and J. M. Marchetti, Zinc(II) phthalocyanine loaded PLGA nanoparticles for photodynamic therapy use. *Int. J. Pharm*. 310, 187-195 (**2006**)
210 Y. N. Konan-Kouakou, R. Boch, R. Gurny, and E. Allemann, In vitro and in vivo activities of verteporfin-loaded nanoparticles. *J. Control. Release*. 103, 83-91 (**2005**)
211 J. R. McCarthy, J. M. Perez, and R. Weissleder, PLGA encapsulated porphyrin nanoparticles as activateable photodynamic therapy and imaging agents. *Abstr. Pap. Am. Chem. S*. 229, U352-U352 (**2005**)
212 M. Jr, J. M. Perez, C. Bruckner, and R. Weissleder, Polymeric nanoparticle preparation that eradicates tumors. *Nano Lett*. 5, 2552-2556 (**2005**)
213 J. Bhaumik, R. Weissleder, and J. R. McCarthy, Synthesis and Photophysical Properties of Sulfonamidophenyl Porphyrins as Models for Activatable Photosensitizers. *J. Org. Chem*. 74, 5894-5901 (**2009**)
214 I. Roy, T. Y. Ohulchanskyy, H. E. Pudavar, E. J. Bergey, A. R. Oseroff, J. Morgan, T. J. Dougherty, and P. N. Prasad, Ceramic-based nanoparticles entrapping water-insoluble photosensitizing anticancer drugs: A novel drug-carrier system for photodynamic therapy. *J. Am. Chem. Soc*. 125, 7860-7865 (**2003**)
215 M. C. Daniel, and D. Astruc, Gold nanoparticles: Assembly, supramolecular chemistry, quantum-size-related properties, and applications toward biology, catalysis, and nanotechnology. *Chem. Rev*. 104, 293-346 (**2004**)
216 Y. Cheng, A. C. Samia, J. D. Meyers, I. Panagopoulos, B. W. Fei, and C. Burda, Highly efficient drug delivery with gold nanoparticle vectors for in vivo photodynamic therapy of cancer. *J. Am. Chem. Soc*. 130, 10643-10647 (**2008**)
217 M. E. Wieder, D. C. Hone, M. J. Cook, M. M. Handsley, J. Gavrilovic, and D. A. Russell, Intracellular photodynamic therapy with photosensitizer-nanoparticle conjugates: cancer therapy using a 'Trojan horse'. *Photoch. Photobio. Sci*. 5, 727-734 (**2006**)
218 T. Stuchinskaya, M. Moreno, M. J. Cook, D. R. Edwards, and D. A. Russell, Targeted photodynamic therapy of breast cancer cells using antibody-phthalocyanine-gold nanoparticle conjugates. *Photoch. Photobio. Sci*. 10, 822-831 (**2011**)
219 P. Juzenas, W. Chen, Y. P. Sun, M. A. N. Coelho, R. Generalov, N. Generalova, and I. L. Christensen, Quantum dots and nanoparticles for photodynamic and radiation therapies of cancer. *Adv. Drug Deliver. Rev*. 60, 1600-1614 (**2008**)
220 J. M. Hsieh, M. L. Ho, P. W. Wu, P. T. Chou, T. T. Tsai, and Y. Chi, Iridium-complex modified CdSe/ZnS quantum dots; a conceptual design for bi-functionality toward imaging and photosensitization. *Chem. Commun (Camb)*. 615-7 (**2006**)
221 A. C. Samia, X. Chen, and C. Burda, Semiconductor quantum dots for photodynamic therapy. *J. Am. Chem. Soc*. 125, 15736-7 (**2003**)
222 J. M. Tsay, M. Trzoss, L. Shi, X. Kong, M. Selke, M. E. Jung, and S. Weiss, Singlet oxygen production by Peptide-coated quantum dot-photosensitizer conjugates. *J. Am. Chem. Soc*. 129, 6865-71 (**2007**)
223 J. C. Boyer, F. Vetrone, L. A. Cuccia, and J. A. Capobianco, Synthesis of colloidal upconverting NaYF4 nanocrystals doped with Er3+, Yb3+ and Tm3+, Yb3+ via thermal decomposition of lanthanide trifluoroacetate precursors. *J. Am. Chem. Soc*. 128, 7444-5 (**2006**)
224 S. Heer, K. Kompe, H. U. Gudel, and M. Haase, Highly efficient multicolour upconversion emission in transparent colloids of lanthanide-doped NaYF4 nanocrystals. *Adv. Mater*. 16, 2102-+ (**2004**)

225 C. Wang, H. Q. Tao, L. Cheng, and Z. Liu, Near-infrared light induced in vivo photodynamic therapy of cancer based on upconversion nanoparticles. *Biomaterials*. 32, 6145-6154 (**2011**)
226 J. C. Kah, R. C. Wan, K. Y. Wong, S. Mhaisalkar, C. J. Sheppard, and M. Olivo, Combinatorial treatment of photothermal therapy using gold nanoshells with conventional photodynamic therapy to improve treatment efficacy: an in vitro study. *Lasers Surg. Med*. 40, 584-9 (**2008**)
227 A. Khdair, H. Handa, G. Z. Mao, and J. Panyam, Nanoparticle-mediated combination chemotherapy and photodynamic therapy overcomes tumor drug resistance in vitro. *Eur. J. Pharma. Biopharma*. 71, 214-222 (**2009**)
228 S. Y. Emelianov, P. C. Li, and M. O'donnell, Photoacoustics for molecular imaging and therapy. *Phys. Today*. 62, 34-39 (**2009**)
229 Z. F. Li, Y. B. Liu, H. Li, W. R. Chen, H. Y. Chen, and H. Wang, Monitoring tissue temperature for photothermal cancer therapy based on photoacoustic imaging: a pilot study. *Biophotonics and Immune Responses Viii*. 8582, (**2013**)
230 B. Kang, D. C. Yu, Y. D. Dai, S. Q. Chang, D. Chen, and Y. T. Ding, Cancer-Cell Targeting and Photoacoustic Therapy Using Carbon Nanotubes as "Bomb" Agents. *Small*. 5, 1292-1301 (**2009**)
231 J. P. Zhong, S. H. Yang, X. H. Zheng, T. Zhou, and D. Xing, In vivo photoacoustic therapy with cancer-targeted indocyanine green-containing nanoparticles. *Nanomedicine*. 8, 903-919 (**2013**)
232 H. Y. Ju, R. A. Roy, and T. W. Murray, Gold nanoparticle targeted photoacoustic cavitation for potential deep tissue imaging and therapy. *Biomed. Opt. Express*. 4, 66-76 (**2013**)
233 A. S. Don, and P. J. Hogg, Mitochondria as cancer drug targets. *Trends Mol. Med*. 10, 372-378 (**2004**)
234 S. Desagher, and J. C. Martinou, Mitochondria as the central control point of apoptosis. *Trends Cell Biol*. 10, 369-377 (**2000**)
235 F. F. Zhou, S. N. Wu, Y. Yuan, W. R. Chen, and D. Xing, Mitochondria-Targeting Photoacoustic Therapy Using Single-Walled Carbon Nanotubes. *Small*. 8, 1543-1550 (**2012**)
236 B. Radt, T. A. Smith, and F. Caruso, Optically addressable nanostructured capsules. *Adv. Mater*. 16, 2184-+ (**2004**)
237 R. Huschka, A. Barhoumi, Q. Liu, J. A. Roth, L. Ji, and N. J. Halas, Gene Silencing by Gold Nanoshell-Mediated Delivery and Laser-Triggered Release of Antisense Oligonucleotide and siRNA. *Acs Nano*. 6, 7681-7691 (**2012**)
238 R. M. Uda, E. Hiraishi, R. Ohnishi, Y. Nakahara, and K. Kimura, Morphological Changes in Vesicles and Release of an Encapsulated Compound Triggered by a Photoresponsive Malachite Green Leuconitrile Derivative. *Langmuir*. 26, 5444-5450 (**2010**)
239 M. S. Yavuz, Y. Y. Cheng, J. Y. Chen, C. M. Cobley, Q. Zhang, M. Rycenga, J. W. Xie, C. Kim, K. H. Song, A. G. Schwartz, L. H. V. Wang, and Y. N. Xia, Gold nanocages covered by smart polymers for controlled release with near-infrared light. *Nat. Mater*. 8, 935-939 (**2009**)

240 S. E. Skrabalak, J. Y. Chen, Y. G. Sun, X. M. Lu, L. Au, C. M. Cobley, and Y. N. Xia, Gold Nanocages: Synthesis, Properties, and Applications. *Accounts Chem. Res*. 41, 1587-1595 (**2008**)
241 D. H. Thompson, O. V. Gerasimov, J. J. Wheeler, Y. J. Rui, and V. C. Anderson, Triggerable plasmalogen liposomes: Improvement of system efficiency. *BBA-Biomembranes*. 1279, 25-34 (**1996**)
242 O. V. Gerasimov, M. Qualls, Y. Rui, and D. H. Thompson, Intracellular drug delivery using pH- and light-activated diplasmenylcholine liposomes. *Abstr. Pap. Am. Chem. S*. 213, 303-PMSE (**1997**)
243 A. P. Goodwin, J. L. Mynar, Y. Z. Ma, G. R. Fleming, and J. M. J. Frechet, Synthetic micelle sensitive to IR light via a two-photon process. *J. Am. Chem. Soc.* 127, 9952-9953 (**2005**)
244 G. Y. Chen, C. H. Yang, and P. N. Prasad, Nanophotonics and Nanochemistry: Controlling the Excitation Dynamics for Frequency Up- and Down-Conversion in Lanthanide-Doped Nanoparticles. *Accounts Chem. Res*. 46, 1474-1486 (**2013**)
245 Y. M. Yang, Q. Shao, R. R. Deng, C. Wang, X. Teng, K. Cheng, Z. Cheng, L. Huang, Z. Liu, X. G. Liu, and B. G. Xing, In Vitro and In Vivo Uncaging and Bioluminescence Imaging by Using Photocaged Upconversion Nanoparticles. *Angew. Chem. Int. Edit*. 51, 3125-3129 (**2012**)
246 D. W. Hutmacher, R. E. Horch, D. Loessner, S. Rizzi, S. Sieh, J. C. Reichert, J. A. Clements, J. P. Beier, A. Arkudas, O. Bleiziffer, and U. Kneser, Translating tissue engineering technology platforms into cancer research. *J.Cell. Mol. Med*. 13, 1417-1427 (**2009**)
247 C. S. Szot, C. F. Buchanan, J. W. Freeman, and M. N. Rylander, 3D< i> in vitro</i> bioengineered tumors based on collagen I hydrogels. *Biomaterials*. 32, 7905-7912 (**2011**)
248 A. L. Timothy, B. James, A. Jesse, and S. Konstantin, Hybrid plasmonic magnetic nanoparticles as molecular specific agents for MRI/optical imaging and photothermal therapy of cancer cells. *Nanotechnology*. 18, 325101 (**2007**)
249 S. Mallidi, T. Larson, J. Aaron, K. Sokolov, and S. Emelianov, Molecular specific optoacoustic imaging with plasmonic nanoparticles. *Opt. Express*. 15, 6583-6588 (**2007**)
250 J. Shah, L. Ma, K. Sokolov, K. Johnston, T. Milner, S. Y. Emelianov, S. Park, S. Aglyamov, and T. Larson, Photoacoustic imaging and temperature measurement for photothermal cancer therapy. *J. Biomed. Opt*. 13, 034024-034024-9 (**2008**)
251 Z. Zha, Z. Deng, Y. Li, C. Li, J. Wang, S. Wang, E. Qu, and Z. Dai, Biocompatible polypyrrole nanoparticles as a novel organic photoacoustic contrast agent for deep tissue imaging. *Nanoscale*. 5, 4462-4467 (**2013**)
252 X. Liang, Z. Deng, L. Jing, X. Li, Z. Dai, C. Li, and M. Huang, Prussian blue nanoparticles operate as a contrast agent for enhanced photoacoustic imaging. *Chem. Commun*. 49, 11029-11031 (**2013**)
253 S. Sarkar, A. A. Gurjarpadhye, C. G. Rylander, and M. Nichole Rylander, Optical properties of breast tumor phantoms containing carbon nanotubes and nanohorns. *J. Biomed. Opt*. 16, 051304-051304-11 (**2011**)
254 S. Sarkar, K. Zimmermann, W. Leng, P. Vikesland, J. Zhang, H. Dorn, T. Diller, C. Rylander, and M. Rylander, Measurement of the Thermal Conductivity of Carbon

Nanotube–Tissue Phantom Composites with the Hot Wire Probe Method. *Ann. Biomed. Eng*. 39, 1745-1758 (**2011**)
255 V. P. Pattani, and J. W. Tunnell, Nanoparticle-mediated photothermal therapy: A comparative study of heating for different particle types. *Laser Surg. Med*. 44, 675-684 (**2012**)
256 B. W. Pogue, and M. S. Patterson, Review of tissue simulating phantoms for optical spectroscopy, imaging and dosimetry. *J. Biomed. Opt*. 11, 041102-041102-16 (**2006**)
257 R. Guo, L. Zhang, H. Qian, R. Li, X. Jiang, and B. Liu, Multifunctional Nanocarriers for Cell Imaging, Drug Delivery, and Near-IR Photothermal Therapy. *Langmuir*. 26, 5428-5434 (**2010**)
258 J.-H. Park, G. von Maltzahn, M. J. Xu, V. Fogal, V. R. Kotamraju, E. Ruoslahti, S. N. Bhatia, and M. J. Sailor, Cooperative nanomaterial system to sensitize, target, and treat tumors. *P. Natl. Acad. Sci*. 107, 981-986 (**2010**)
259 B. Jang, J.-Y. Park, C.-H. Tung, I.-H. Kim, and Y. Choi, Gold Nanorod−Photosensitizer Complex for Near-Infrared Fluorescence Imaging and Photodynamic/Photothermal Therapy In Vivo. *ACS Nano*. 5, 1086-1094 (**2011**)
260 I. L. Maksimova, G. G. Akchurin, B. N. Khlebtsov, G. S. Terentyuk, G. G. Akchurin, I. A. Ermolaev, A. A. Skaptsov, E. P. Soboleva, N. G. Khlebtsov, and V. V. Tuchin, Near-infrared laser photothermal therapy of cancer by using gold nanoparticles: Computer simulations and experiment. *Med. Laser Appl*. 22, 199-206 (**2007**)
261 J.-L. Li, L. Wang, X.-Y. Liu, Z.-P. Zhang, H.-C. Guo, W.-M. Liu, and S.-H. Tang, In vitro cancer cell imaging and therapy using transferrin-conjugated gold nanoparticles. *Cancer Lett*. 274, 319-326 (**2009**)

Chapter 3. Functionalization of Single Walled Carbon Nanohorns for Simultaneous Fluorescence Imaging and Cisplatin Delivery

(Under review at Carbon)

Allison M. Pekkanen[1], Matthew R. DeWitt[1], David B. Geohegan[2], Timothy E. Long[3], M. Nichole Rylander[1]

[1]School of Biomedical Engineering and Sciences, Virginia Tech, Blacksburg, VA 24061

[2] Center for Nanophase Materials Sciences, Oak Ridge National Laboratories, Oak Ridge, TN 37831

[3]Macromolecules Innovation Institute, Department of Chemistry, Virginia Tech, Blacksburg, VA 24061

Keywords: Carbon Nanohorn, Fluorescent Imaging, Cancer, Chemotherapy, Drug Delivery

3.1 Abstract

Single walled carbon nanohorns (SWNHs) were previously investigated for their capability to serve as photothermal and drug delivery agents for potential cancer therapy, particularly for the eradication of bladder cancer lesions. In this study, the potential for SWNHs to serve as a nanotheranostic vehicle with the capability for both treatment delivery and dynamic imaging is demonstrated through simultaneous delivery of the chemotherapeutic cisplatin from SWNH cone interiors and imaging of nanoparticle transport using quantum dots (QDs) conjugated to SWNH surfaces. Following successful formation of SWNH-QD + cisplatin conjugates and subsequent characterization, drug release profiles show that QDs imaging do not hinder the therapeutic ability of SWNHs. In addition, the conjugates were trackable over the course of 3 d, which reveals that endocytosed SWNHs continue to deliver therapy after removal of the nanoparticle

solution. This unique SWNH will ultimately enable the optimization of nanoparticle properties to achieve maximum efficacy.

3.2 Introduction

Bladder cancer continues to affect many Americans, with over 70,000 new cases diagnosed each year[1]. Even with locally-administered therapy, over 40% of bladder cancer cases will progress to an invasion of surrounding tissue[2]. The low efficacy of traditional treatments can primarily be explained by potential penetration issues for drugs into the bladder wall and subsequent cytotoxic action on bladder cancer cells[3]. Complete cystectomy has proven to be an effective treatment for bladder cancer. However, while this method significantly improves survival rates, the quality of life following cystectomy is pointedly diminished and requires adaptation to a more restrictive lifestyle[4, 5]. Nanomedicine offers great potential to eradicate bladder cancer without the need for invasive cystectomies through a direct injection method, which also avoids many common problems with systemically delivered nanotherapeutics[2, 3].

The capability and diversity of therapeutic nanotechnology has advanced significantly in recent years. In particular, thermal enhancement of chemotherapeutic is widely documented, where delivered drug is heated to induce additional local cell death[6-13]. This thermal dose can be delivered more efficiently with the use of thermally-activated nanoparticles.[14] Nanoparticles capable of delivering this therapeutic load alongside a thermal dose are often composed of metal and employ magnetic resonance imaging (MRI) to evaluate tissue distribution[8, 16-18]. While these options show great promise for bulk tissue evaluation *in vivo*, MRI-based imaging enhancement lacks the necessary

resolution for precise determination of the location of single nanoparticles or low concentrations on nanoparticles within the tumor microenvironment. Effective refinement of nanoparticle parameters necessitates the use of an alternative imaging method to ensure maximum therapeutic efficacy.

Fluorescence monitoring of nanoparticle transport within the tumor microenvironment allows for precise evaluation of single particle or small concentrations of nanoparticles with the ability to easily distinguish signals between cells and nanoparticles. There are nanoparticle formulations that have a fluorescent molecule such as rhodamine or fluorescein isothiocyanate (FITC) coupled to other imaging or therapeutic modalities; however, many of these molecules have a limited lifetime for fluorescence monitoring and thus have a limited capacity for long-term imaging and monitoring for transport studies[15, 16]. Quantum dots (QDs) serve as fluorescent beacons for tumor imaging both *in vitro* and *in vivo* for detection while having a decreased potential to photobleach as compared to traditional fluorescent molecules[17-19]. QDs have also shown the ability for conjugation to other nanoparticles to lend multifunctionality to nanoparticles, either acting as a dual-imaging modality or as a dual imaging-photothermal agent[20-23]. To this end, there are few nanoparticle formulations capable of studying the interplay between nanoparticle transport via QD fluorescence monitoring and subsequent cell death due to chemotherapy[24, 25]. The development of such a particle would allow for real-time monitoring of injected chemotherapeutic nanoparticles.

A highly unexplored nanoparticle with tremendous promise for dual imaging and treatment are single walled carbon nanohorns (SWNHs). These particles are formed upon laser ablation of graphene sheets, which induces the formation of cones that subsequently

self-aggregate into dahlia-like structures[26, 27]. The synthesis of SWNHs proceeds without a metal catalyst, which eliminates the need for purification and the concern over catalyst toxicity[27]. The aspect ratio of the aggregated structure approaches unity (near spherical), and the cone architecture has a significant impact on the available surface area for chemical conjugation[27]. SWNHs were implemented as a photothermal agent that, when combined with 1064 nm irradiation, generates sufficient thermal energy to induce regions of cell death[28]. When utilized in 3D tissue phantoms, there is a strong spatio-temporal relationship between laser irradiation of SWNHs and cell death[29].

When oxidized, the graphene structure of SWNH cones is disrupted, forming 0.5 nm - 3 nm pores [26, 30]. These pores induce movement of small molecules into the cone interior through capillary action, which was shown earlier for a number of drugs and C_{60} to demonstrate the SWNH's drug-carrying potential[30-34]. In addition to the formation of pores, the oxidation process introduces carboxylic acid groups onto the graphene surface for further functionalization[35, 36]. Specifically, Zimmerman et al. demonstrate the potential of SWNHs functionalized with quantum dots (QDs) for the monitoring of intracellular trafficking of SWNH conjugates but did not examine concurrent drug delivery[37]. Additionally, DeWitt et al. examined the capability of SWNHs for delivery of the chemotherapeutic agent cisplatin for use in thermally-enhanced chemotherapy treatments, but did not utilize QD attachment for concurrent monitoring. The combination of photothermal capability, the ability to load small molecules within cone interiors, and the potential to conjugate ligands to SWNH exteriors makes them an ideal candidate for a combination photothermal-chemotherapy nanoparticle for cancer treatment.

While SWNHs are used extensively as drug delivery vehicles or fluorescent beacons through functionalization, there has yet to be a SWNH conjugate that can act as both a therapeutic and a real-time imaging modality. The potential of SWNHs as a nanotheranostic agent (dual therapeutic-imaging agent) through incorporation of the chemotherapeutic drug cisplatin within SWNH cone interiors and QD attachment on the SWNH surface (SWNH-QD + cis) is demonstrated through this work. SWNH-cisplatin conjugates were characterized to confirm the desired structure, evaluate drug release, and confirm cytotoxicity of SWNH-QD + cis. The bright fluorescence signal from the QDs is demonstrated to image the conjugates *in vitro* over the course of three days, showing potential to track particle transport and distribution. Since SWNHs were characterized extensively, this effort focused on the characterization of the novel SWNH-QD + cis conjugate to examine whether the addition of QDs to SWNHs would interfere with its drug delivery capabilities.

3.3 Methods

3.3.1 SWNH Modification

3.3.1.1 Oxidation of SWNHs Pristine SWNHs were generously donated from Dr. David Geohegan from Oak Ridge National Laboratory. Pristine SWNHs were oxidized as described previously[37]; briefly, SWNHs were exposed to 8M HNO_3 under reflux at 110°C for 24 h. Reprotonation of carboxylic acid groups was accomplished through 1 M HCl under reflux at 110°C overnight. The resulting oxidized SWNHs (SWNHox, **Figure 3.1a**) were dried at 60°C under reduced pressure for 48-72 h.

3.3.1.2 Attachment of AET Ligand SWNHox were sonicated at a concentration of 0.25 mg/mL in water for 1-2 h until the solution was homogenous. The resulting

suspension was transferred to a round bottom flask and diluted further in water to a concentration of 0.1 mg/mL. The carbodiimide reaction for the addition of cysteamine hydrochloride (Sigma Aldrich; AET) proceeded as discussed previously[37]. 1-Ethyl-3-(3-dimethylaminopropyl) carbodiimide (Sigma Aldrich; EDC) was added to the vigorously stirred solution to a final concentration of 0.1M and allowed to stir for 5 mins. Subsequently, N-Hydroxysulfosuccinimide sodium salt (Sigma-Aldrich; sulfo-NHS) was added to the solution to a final concentration of 5mM and allowed to stir for 5 min. Finally, AET was added to the solution at a final concentration of 0.2M. The pH of the solution was adjusted to 5-6 with HCl/NaOH, covered with parafilm, and allowed to stir for 16 h. The solution was then filtered with a 0.1 μm PVDF membrane (Millipore) and washed thoroughly with water to remove excess reactants. SWNH-AET (**Figure 3.1b**) were isolated from the membrane by submergence in water and sonication.

3.3.1.3 Quantum Dot Conjugates Following filtration, SWNH-AET were resuspended in water at a concentration of 0.1 mg/mL in water. To this solution, 630 nm CdSe/ZnS core/shell QDs (OceanNanotech) suspended in chloroform (Sigma-Aldrich) were added to the stirred solution at a w/w of 2.5:1 of QD to SWNH-AET. The solution was stirred vigorously for 24 h to induce movement of QDs from the chloroform layer to the aqueous layer via interfacial complexation. The aqueous layer was isolated via separatory funnel and filtered through a 0.1 μm PVDF filter, which yielded dried SWNH-QD (**Figure 3.1c**).

3.3.1.4 Cisplatin Incorporation into SWNH Conjugates To incorporate cisplatin (Sigma-Aldrich) into cone interiors, SWNH conjugates (**Figure 3.1a-c**) were sonicated at a concentration of 0.25 mg/mL in water for approximately 1 h until all aggregates were

dispersed. Concurrently, cisplatin was dissolved in dimethyl sulfoxide (Sigma-Aldrich; DMSO) at a concentration of 2 mg/mL and stirred for 1 h. SWNH conjugates were added to the stirring cisplatin solution to yield a 1:1 w/w SWNH:cisplatin solution that was allowed to stir for 2 h; the solution was then dried under nitrogen. The final SWNH-cisplatin conjugates are depicted in **Figure 3.1d-f**. Each SWNH conjugate with and without drug, as well as pristine SWNHs, was analyzed via X-ray photoelectron spectroscopy (PHI Quantera SXM scanning photoelectron spectrometer microprobe; XPS) for elemental composition.

3.3.2 Transmission Electron Microscopy and Energy Dispersive Spectroscopy

Transmission electron microscopy (TEM) grids were prepared by introducing SWNH-QD + cis diluted in water to Lacey Carbon Mesh grids (Electron Microscopy Sciences). Imaging was performed with a JEOL 2100 TEM equipped with a silicon drift detector for energy dispersive spectroscopy (EDS) analysis.

3.3.3 Drug Release

Dried SWNH samples were suspended in water (0.2 mg/mL) and sonicated until the solution was homogenous. The solution was transferred to a dialysis membrane, (Spectra/Por® 3; MWCO~10,000 D) and subsequently suspended in 500 mL of water. Drug release was performed at 37 °C in an incubator fitted with a water bath into which the beaker was placed and stirred vigorously. All water was equilibrated to 37 °C before use. 20 mL of water surrounding the dialysis membrane was isolated at each time point for analysis by inductively coupled plasma-atomic emission spectrometer (Spectro Analytical Instruments, CirOS VISION model; ICP-AES) for trace concentrations of platinum.

3.3.4 Determination of IC50

N-(4-[5-nitro-2-furyl]-2-thiazolyl)formamide-induced rat bladder transitional cell carcinoma cells (AY-27) developed by Dr. S. Selman and Dr. J. Hampton (Medical College of Ohio, Toledo, Ohio) were donated by Dr. John Robertson (Virginia Tech, Blacksburg, VA). AY-27 cells were cultured in RPMI-1640 (HyClone Laboratories) supplemented with 10% fetal bovine serum (Sigma-Aldrich) and 1% penicillin/streptomycin (Invitrogen) at 37°C with 5% CO_2. Cells were detached from the plate with 0.25% Trypsin-EDTA (Life Technologies), which was subsequently quenched to yield a cell suspension. 50,000 cells/well were seeded onto a 24-well tissue culture treated plate and allowed to attach and proliferate overnight to approximately 50% confluence. Following seeding, cells were treated for 1 h with dilutions of free cisplatin or SWNH conjugates (with and without drug) in media (n=4). Following incubation, cells were washed thoroughly with phosphate buffered saline (Fisher Scientific; PBS) and fresh media was added to each well. Cells were allowed to proliferate for 72 h, and subsequently an alamarBlue® assay (Fisher Scientific) was completed to determine relative cell viability. Cell media was replaced with complete media supplemented with 10% alamarBlue® and allowed to incubate for 1-2 h until control cells had sufficiently reduced alamarBlue®. Following alamarBlue® reduction, each well was subsampled 3 x into a 96 well plate. Absorbance of test wells was measured at 570 and 600 nm with a plate reader (Molecular Devices SprectaMax M2). Cell viability for each experiment was normalized to internal controls and scaled between 0 (alamarBlue® with no cells) and 100 (cells with no SWNH treatment); logarithmic curve fits and ANOVA were completed in JMP software (p=0.05).

3.3.5 Cellular Staining and Fluorescence Imaging SWNH-QD + cis

For all imaging experiments, AY-27 cells were seeded at a density of 50,000 cells per well in a 24 well plate and allowed to attach and grow for 24 h. Cell media was aspirated and cells were rinsed with PBS, and the cells were treated with SWNH-QD at the calculated 50% inhibitory concentration (IC50) for 1 h. Following treatment, cells were washed vigorously with PBS and fresh media was added. Cells were then allowed to proliferate for 24, 48, or 72 h (staining began directly following incubation for 1 h experiments). All imaging experiments were performed on a Leica DMI-6000 B fluorescent microscope.

3.3.5.1 Actin/DAPI Stain Following incubation, cells were washed with PBS and fixed with 3.7% paraformaldehyde (Fisher Scientific) in PBS at room temperature for 15 min. Cells were rehydrated with PBS and permeabilized with 0.5% Triton X-100 (Sigma-Aldrich) in water for 15 min. Cells were again rinsed with PBS and then incubated with 1% Bovine Serum Albumin (Fisher Scientific) in PBS for 30 min. Following blocking, Oregon Green®-tagged phalloidin (Invitrogen) was added to each well at a dilution of 1:40 and allowed to incubate for 20 min. After washing with PBS, DAPI (Biotium) was added to wells with 100 µL of PBS for 1-2 min. Wells were protected with Vectashield (Vector Labs) and kept at 4°C imaged.

3.3.5.2 Live/Dead Stain Following incubation, cell media was removed and replaced with media that included dilute Calcein AM (Invitrogen; 1µL/mL), and cells were allowed to incubate for 30 min. Following the removal of Calcein AM-doped media, media with Propidium Iodide (Invitrogen; 30µL/mL) was added and allowed to

incubate with cells for 5 min. Subsequently, PI was removed and 100 µL of PBS was added to each well and cells were imaged.

3.3.6 Statistical Analysis.

Statistical analysis was performed in JMP software. Analysis of variance (ANOVA) tests were performed to determine statistical differences between groups. For determination of IC50, logarithmic curve fits were performed in JMP software (parameters and equation provided in Table S2). The IC50 was calculated from these curve fits.

3.4 Results

3.4.1 Nanoparticle Characterization

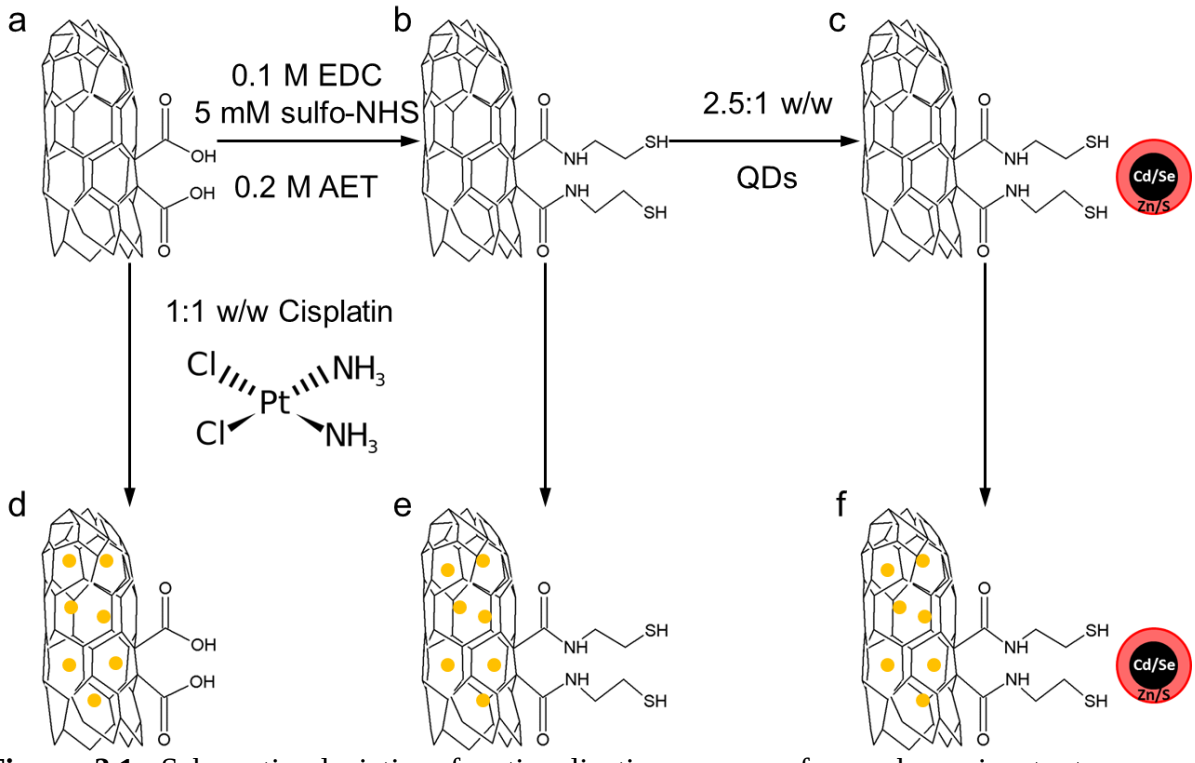

Figure 3.1. Schematic depicting functionalization process for each conjugate type: SWNHox (a), SWNH-AET (b), SWNH-QD (c), SWNHox+cisplatin (d), SWNH-AET+cisplatin (e), SWNH-QD+cisplatin (f). Cisplatin is depicted as yellow circles within SWNH cones, QDs are depicted as black/red circles associated with terminal thiol groups from AET. Cisplatin is loaded through capillary action into cone interiors through defects created by the oxidation process.

The functionalization of SWNHs proceeded as expected, with XPS results showing a progression in elemental composition as predicted (**Table 3.1**). Pristine SWNHs had a high carbon content with oxygen and nitrogen present in low amounts. Following acid oxidation, the oxygen content of SWNHs increased significantly, indicating successful oxidation. When further modified with AET, there was a rise in sulfur content from the elements in the ligand, with trace amounts of chlorine observed from the hydrochloric acid required in the synthetic process. QDs were added to the SWNH-AET and showed presence of cadmium and zinc indicating successful functionalization to QDs. Following cisplatin addition to each of these conjugates (as seen in shaded rows), an increase in chlorine and nitrogen content as well as the presence of platinum was detected, all of which indicated that cisplatin had been successfully added to the conjugates. The remaining trace elements were attributed to known sources including PVDF filter paper, DMSO, HCl, NaOH, and borosilicate glass.

Conjugate	C	N	O	S	Cl	Zn	Cd	Pt	Total %
Pristine SWNHs	91.76	0.52	7.72	0	0	0	0	0	100
SWNHox	79.56	2.2	16.65	0.19	0	0	0	0	98.6
SWNHox + Cis	67.31	3.25	19.76	1.51	3.12	0	0	1.51	96.46
SWNH-AET	78.31	2.35	15.06	0.57	0.21	0	0	0	96.5
SWNH-AET + Cis	75.67	2.94	16.53	1.24	1.73	0	0	0.92	99.03
SWNH-QD	80.78	1.29	14.82	1.39	0.4	0.21	0.8	0	99.69
SWNH-QD + Cis	75.13	1.94	15.05	2.52	2.87	0.08	0.11	1.75	99.45

Table 3.1. XPS of SWNH conjugates as they are functionalized. Shaded rows indicate conjugates that have been loaded with cisplatin. Trace elements include silicon, fluorine, and sodium, which are from known sources.

3.4.2 TEM and EDS Analysis

Energy dispersive spectroscopy (EDS) was performed on both bulk sample and on a small portion of the SWNH-QD + cis sample (supplementary information). As shown in the spectra, there was no difference in elemental composition between the bulk sample and the small sample, indicating that the SWNH-QD + cis sample was homogenous. In addition, the target elements (carbon, cadmium, selenium, zinc, sulfur, platinum, chlorine) were observed in the sample with additional peaks only from the grid (copper) and the instrument.

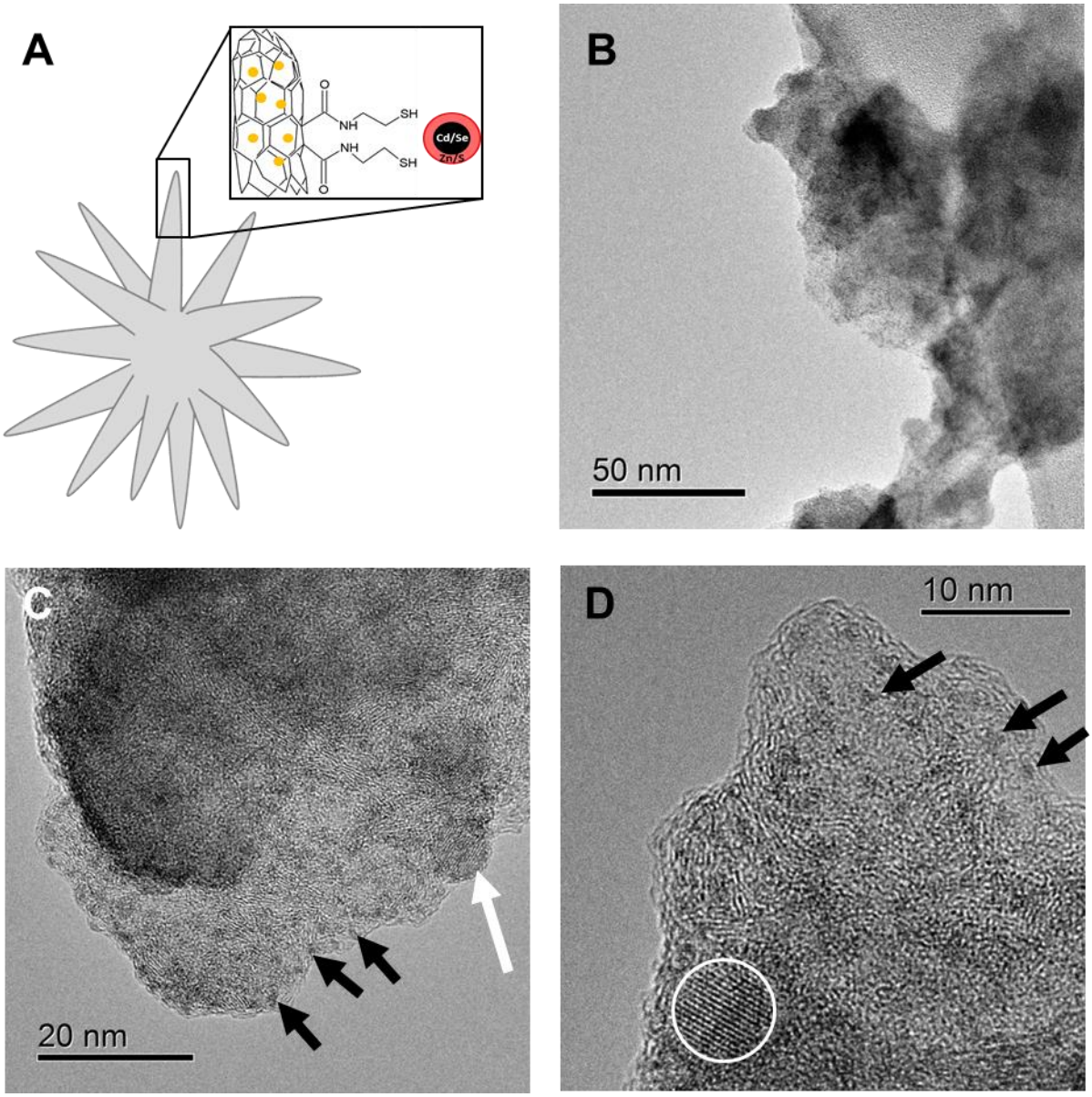

Figure 3.3. TEM images of SWNH-QD + cis showing the presence of both cisplatin and QDs. (a) Schematic of SWNH-QD + cis. (b) Images of SWNH aggregates indicating sizes similar to those seen with DLS. (c-d) Images of SWNH-QD + cis to visualize individual QDs and cisplatin molecules. Black arrows in C and D denote presence of cisplatin (small dark spots) and white arrows and the white circle show the presence of QDs (highly ordered lattice structure from CdSe crystal).

TEM images as shown in **Figure 3.3 (a-d)** indicate the presence of both cisplatin and QDs in the sample. In **Figure 3.3 (c, d),** the white arrow indicates the location of a QD in the sample, which are apparent by the highly ordered lattice structure with an overall size of 7-8 nm[40, 41]. The CdSe crystal lattice remains clearly visible despite the

carbon sheet background, indicating successful functionalization to SWNH surfaces[42, 43]. The black arrows indicate the presence of cisplatin in the sample, which is evidenced by small dark spots within the carbon mesh. Cisplatin appears as a dark spot within the carbon matrix due to the presence of the platinum atom. The other lines visible that are longer and slightly wavy are the result of the graphene sheet. These results indicate that SWNH can be modified to include a physical loading of cisplatin and an attachment of QD to SWNH surfaces to create SWNH-QD + cis.

3.4.3 Drug Release Properties

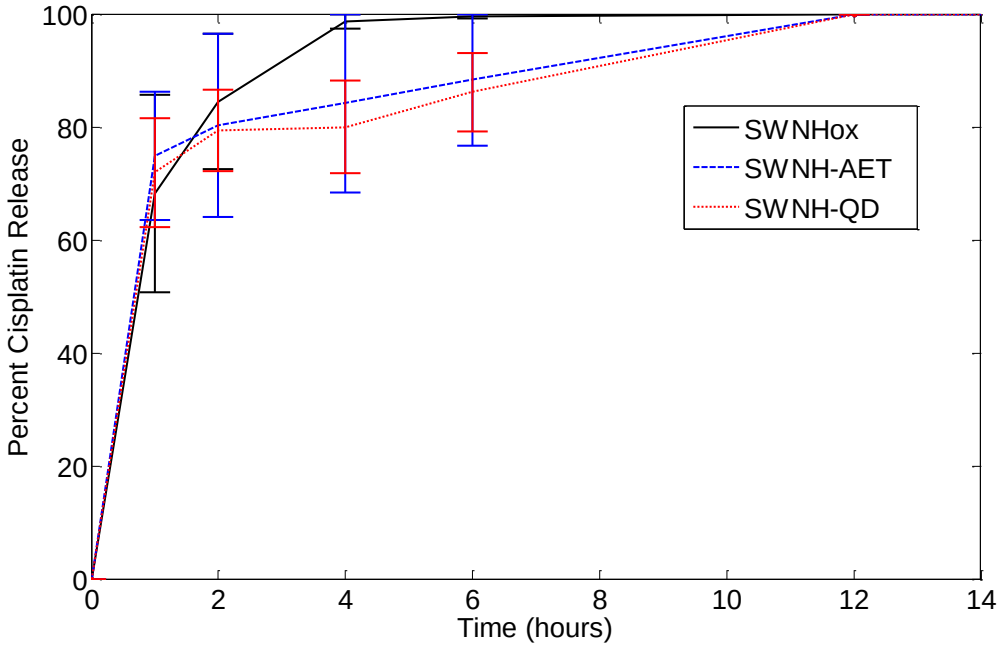

Figure 3.4. ICP-AES results indicating the percentage of released cisplatin as a function of total amount of drug released from each conjugate (n=3). There is no significant difference between any of the conjugates over the entire time period, indicating that functionalization does not inhibit the potential to use SWNHs as drug delivery vehicles.

ICP-AES results show the amount of platinum content in water surrounding the dialysis bag containing SWNH-cisplatin conjugates. This corresponds to a cisplatin release from the SWNH conjugates and is presented as a percentage of total cisplatin released during the course of the experiment (**Figure 3.4**). Each conjugate releases

between 60% and 70% of cisplatin within the first hour. After this first hour, SWNHox exhibits a slightly, though not significant, faster release as compared to the SWNH-AET and SWNH-QD. These slight differences are expected because of steric hindrance that the drug must move through to be released from the functionalized nanoparticles. Since there is no significant difference in drug release between the three conjugates, the addition of the QD to the SWNH surface does not hinder its ability to act as a drug delivery vehicle.

3.4.4 IC50 determination

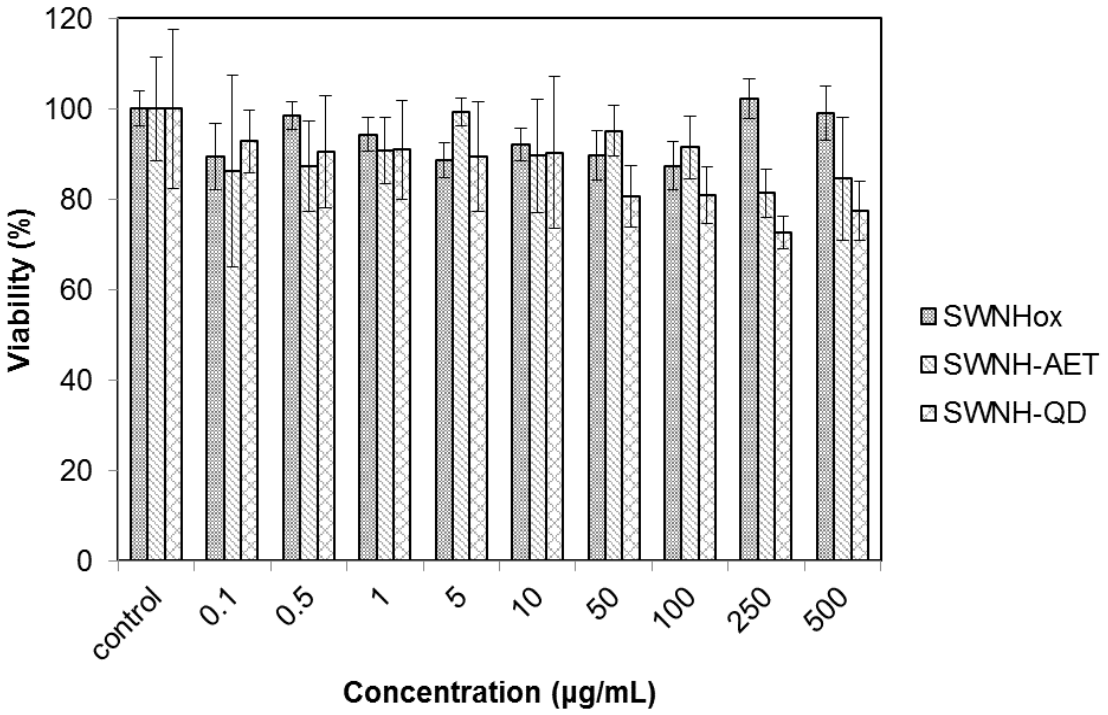

Figure 3.5. SWNH functionalization does not induce toxicity at the concentration ranges used for cisplatin therapy. Data is presented as average ± standard deviation. Significantly different viability as compared to controls follows no unifying trend, indicating that all dramatic drops in viability in SWNH-drug conjugates are due to cisplatin and not SWNH conjugates.

Percent reduction of alamarBlue® for a wide concentration range of cisplatin was determined for each conjugate and free cisplatin. Viability was determined as the percent reduction as compared to control cells with no treatment and data was normalized from 0-100 (with 0 being the negative alamarBlue® controls with no cells and 100 being control cells with no treatment). When SWNH conjugates without cisplatin are incubated with AY-27 cells, there is no significant trend in the data as a function of concentration, as shown in **Figure 3.5**. Slight variation exists and several concentrations of each conjugate induce significantly reduced cell viability, however these do not constitute an overall trend.

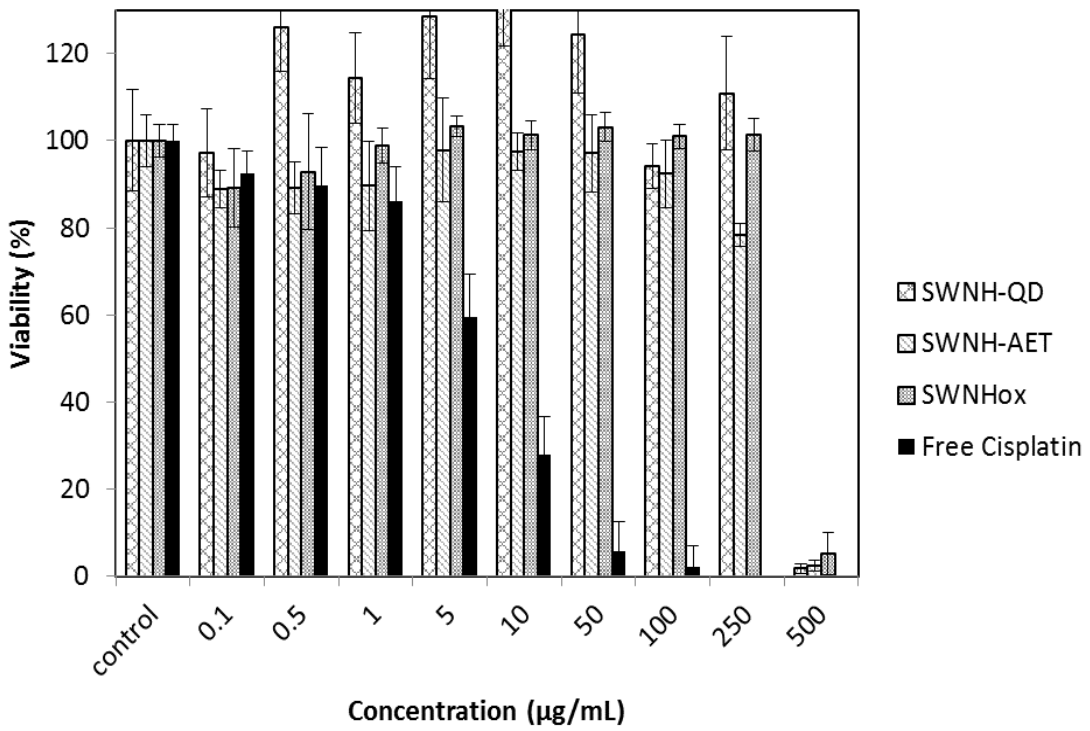

Conjugate	Free Cisplatin	SWNHox	SWNH-AET	SWNH-QD
IC50 (µg/mL)	4.68 ± 1.7	333 ± 55	302 ± 13	273 ± 56

Figure 3.6. Viability data collected from incubations with SWNH-cisplatin conjugates (n=4). SWNH-cisplatin conjugates demonstrate an increase in IC50 by two orders-of-magnitude. Data is presented as an average +/- standard deviation, with the IC50 values calculated from a logarithmic curve fit of each conjugate type (supplementary information).

AY-27 cells incubated with SWNH-cisplatin conjugates, as well as free cisplatin as a control, showed significant reductions in viability with increasing concentration, as shown in **Figure 3.6**. The solid black bars denoting free cisplatin exhibited a dramatic drop-off in viability at lower concentrations compared to the SWNH conjugates, which is demonstrated by the calculated IC50 as shown in Figure 6. Each of these data sets was fit to an S-curve in JMP to generate IC50 values (detail in supplementary information). There is no difference between the conjugates in IC50, but all are 2 orders-of-magnitude

higher than free cisplatin likely due to the different mechanism of uptake between free cisplatin and nanoparticle bound cisplatin[35].

3.4.5 Cellular Staining and Fluorescence Imaging SWNH-QD + cis

SWNH-QD + cis conjugates were incubated with AY-27 cells at the calculated IC50 concentration to evaluate the potential of these conjugates to both act as a chemotherapy delivery and an imaging vehicle. As evidenced in **Figure 3.7**, over the course of 3 d, control cells which were not incubated with any nanoparticle show substantial proliferation. After 72 h, there is a confluent monolayer over the entire well. However, in the treatment groups, there is a significant inhibition in proliferation as cells uptake the SWNH-QD + cis conjugates and the drug is allowed to act on the cells. This is especially evident after 24 h, with a significant population of cells dying and being washed away before staining occurs. After 72 h, the cells begin to recover and proliferate, which validates the calculated IC50 value, as it will only inhibit cellular proliferation by 50% as compared to controls. Dead cells stained in these experiments recently died upon staining. Additionally, the fluorescent signal from Calcein AM and PI is strong enough to limit the ability to visualize the QD signal from individual SWNH-QD+cis conjugates.

In addition to observing cell death over the course of 72 h, actin/DAPI staining was performed to evaluate the potential to image the cellular distribution of QDs over the course of the experiment, as shown in **Figure 3.7**. Similar trends in proliferation were observed with these cells, implying the action of the drug on inhibition of cell growth. However, with these images, the position of SWNH-QD + cis conjugates is clearly monitored through the bright red fluorescent signal from the QDs. At this concentration, AY-27 cells uptake a significant amount of SWNH-QD+cis which prevented the

evaluation of cellular trafficking of SWNH conjugates. These images demonstrate the potential to use this QD conjugation scheme in combination with cisplatin treatment to monitor nanoparticle transport and subsequent therapy.

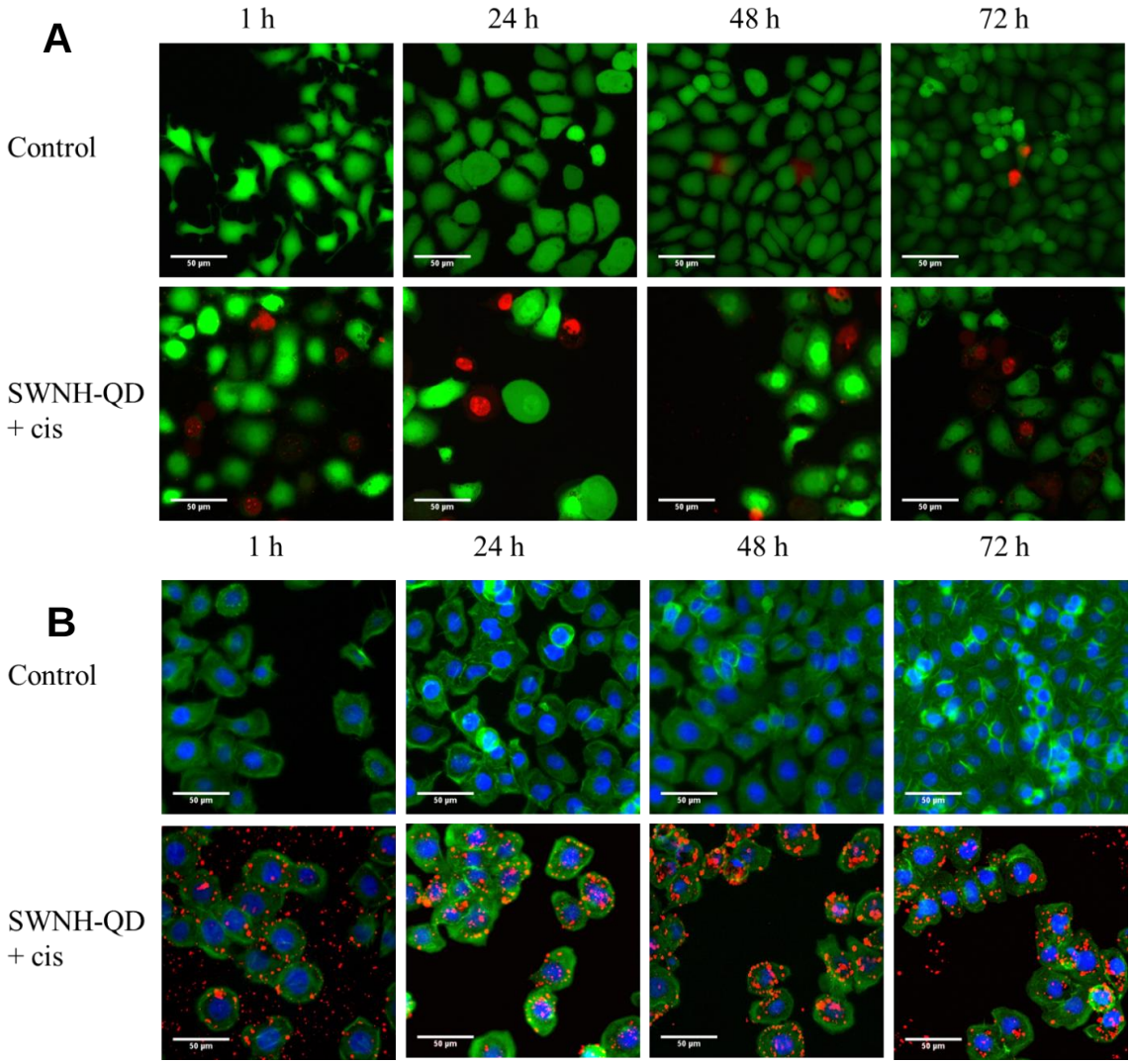

Figure 3.7. (a)Live/dead staining of AY-27 cells over 72 h following 1 h SWNH-QD + cis treatment. SWNH-QD + cis demonstrate a significant inhibition of proliferation of cell growth and cells continue to die over the 3 d period relative to cells exposed to no treatment. Green: calcein AM, live cells; Red: Propidium Iodide, dead cells, Scale bar = 50 µm. (b)Actin/DAPI staining of AY-27 cells over the course of 72 h following 1 h SWNH-QD + cis incubation. Green: Oregon-Green® Phalloidin, F-Actin; Blue: DAPI, Nuclei; Red: QDs; Scale bar = 50 µm. SWNH conjugates maintain their capabilities as an imaging tool over the course of 72 h, with cells retaining and trafficking conjugates over time. Increased intracellular time for conjugates translates to an increased dose of cisplatin available for therapy.

3.5 Discussion

In this work, SWNHs were evaluated for their capability to synthesize and evaluate its ability to act as an imaging and drug delivery probe simultaneously. In particular, QDs are utilized as the fluorescent probe for real-time imaging over extended periods of time due to its resistance to photobleaching[17]. Additionally, our focus on bladder cancer led us to utilize the chemotherapeutic drug cisplatin within SWNHs for the eradication of cancer cells. The enormous surface area of SWNHs make them an ideal platform to attach a significant number of QDs for a strong fluorescence signal, and the corresponding large internal space can sequester a substantial drug load. While SWNH-QD and SWNH+cis complexes have been evaluated separately, there has yet to be an examination of a dual imaging and drug delivery capable SWNH[35, 37]. Therefore, our efforts focused on the characterization of this SWNH-QD + cis, to examine whether the addition of QDs to the nanoparticle conjugate would interfere with the drug delivery capabilities of SWNHs. The development of SWNH-QD+cis will afford a dual photothermal-chemotheraputic nanoparticle with added fluorescent functionality for real-time feedback on the tissue distribution of injected nanoparticles for the eradication of bladder cancer.

Synthesis of SWNH conjugates proceeded as expected, with XPS elemental trends agreeing with the predicted reaction scheme (**Figure 3.1, Table 3.1**). Despite the presence of predicted elements (S, Cd, Pt, etc.) and a logical progression, XPS fails to include spatial information about the specific structure of the SWNH conjugates. TEM imaging of separate SWNH-QD and SWNHox + cis were previously performed in our laboratories[35, 37]. In these images, cisplatin was successfully incorporated in SWNH cone

interiors and QDs attached to the surface of SWNHs. Because of this previous body of work, SWNH-QD + cis were the focus of this study to evaluate the presence of cisplatin and QDs in relation to the SWNH cones. Qualitatively, cisplatin tended to aggregate towards the edges of the carbon mesh, which was consistent with findings by Ajima et al. to examine the material storage mechanism of SWNHs[30]. EDS spectra over a large and small area also indicate homogeneity of the sample, eliminating any SWNH-QD + cis that lack either cisplatin or QD tagging. In addition, cisplatin appeared within the carbon mesh, indicating successful internalization into SWNH cones, compared to surface attachment[35]. In contrast to XPS analysis, the combination of EDS and TEM confirmed that the platinum is from internalized cisplatin and not from residual cisplatin either on the surface of SWNHs or unassociated with SWNHs. In addition to the confirmation of internalized cisplatin, TEM also revealed the surface functionalization of SWNHs with QDs, as seen by the highly ordered lattice structure. The lattice is undisturbed by the graphene sheets, indicating that the QDs rest on the surface of the SWNH as predicted. Furthermore, the presence of cadmium and selenide characterized by EDS confirms the structure of SWNH-QD + cis.

Cisplatin's therapeutic action is directly dependent on its release from SWNH conjugates; its cytotoxic effect is attributed to its interaction with DNA to form adducts, which lead to apoptosis[45]. The release profile of cisplatin from SWNHs is necessary to predict cytotoxic action of SWNH-cisplatin conjugates. These SWNH conjugates exhibited a burst release of cisplatin from cone interiors with insignificant difference between the three conjugates. These profiles indicated that the functionalization procedure to attach QDs to SWNH surfaces did not significantly affect their ability to

release cisplatin. These release profiles were consistent with previous SWNH work, with the majority of sequestered compound released within the first few hours of incubation[46, 47]. The vigorously stirred environment (sink conditions) created in these dialysis experiments is extreme compared to fluid dynamics experienced by nanoparticles *in vitro*. This work is a commonly utilized technique to study drug release from nanoparticle formulations and will serve as a baseline to predict the maximum amount of drug released from these conjugates at any given time[35].

Following particle characterization, the cytotoxic potential of the SWNH-cisplatin conjugates was evaluated against AY-27 rat bladder cancer cells. Additionally, the SWNH conjugates themselves should not induce cytotoxicity, as the potential for errant cell death would increase significantly. The results of the cytotoxicity experiments indicated both the presence of active drug and the absence of errant cytotoxicity from SWNH conjugates without cisplatin. There was no significant decrease in cell viability as a function of concentration in SWNH conjugates without cisplatin, indicating that SWNH conjugates alone did not induce toxicity. When AY-27 cells were incubated with SWNH-cisplatin conjugates, there was a significant decrease in cell viability. Despite this decrease in viability, the IC50 value increased by 2 orders-of-magnitude as compared to free drug. This increase in IC50 is in agreement with previous literature involving the use of SWNH-drug conjugates, with typical increases of 1 or 2 orders-of-magnitude[48-51]. Clearly, sequestering the cisplatin within SWNH cones affects the amount of cisplatin that cells experience within the 1 h incubation time. Furthermore, incubation for a short time followed by a latency period of 72 h is a conservative replication of predicted *in vivo* exposure times and represents a conservative estimate of expected cell death[31-33, 48-53]. In

addition, the IC50 of the SWNH-drug conjugates will decrease and approach that of free drug with longer exposure times[50]. Although the majority of drug released from the SWNHs occurs in the first hour (shown in **Figure 3.4**), this represents a reduced concentration exposed to the cells as compared to free drug solutions. In addition, previous work in our laboratory postulates that cisplatin does not necessitate an endocytotic pathway as is necessary for SWNH conjugates[35]. Although there is drug released within the 1 h incubation period, a significant amount of cisplatin acted on cells through endocytosed SWNHs. In this scenario, increased concentrations of SWNH-cisplatin conjugates induced both more cells containing at least one conjugate and more conjugates per cell on average. As a result of endocytosis, these SWNH conjugates increased IC50 values by 2 orders-of-magnitude as compared to free cisplatin, but would allow for increased exposure to cisplatin following the initial incubation period.

To further confirm the SWNH-cisplatin conjugates' ability to continue to treat cells after 72 h, AY-27 cells were exposed to the IC50 concentration of SWNH-QD + cis and stained with Calcein AM and Propidium iodide to evaluate live and dead cells. Following treatment, there was a remarkable decrease in proliferation of AY-27 cells, suggesting a successful drug treatment. Additionally, in live/dead stains of both control cells and treatment cells (shown in **Figure 3.7a**), cells continued dying at the 72 h mark due to the presence of SWNH-QD + cis conjugates, indicating that SWNH conjugates were likely still releasing drug intracellularly, which was then acting on the AY-27 cells.

Following live/dead viability staining, the QD's imaging capability over the course of 3 d was examined and the SWNH intercellular position monitored. QDs are known as very effective imaging tools both *in vitro* and *in vivo* with little to no evidence

of photobleaching over the course of several days and the ability to conjugate to larger nanoparticle structures[17-19, 23, 37]. As seen in the images in Figure 3.7b, cells continue to retain the SWNH-cisplatin conjugates after 72 h, which would allow any residual cisplatin from SWNH cone interiors to exit and continue to act on cells. In particular, internalized SWNH-cisplatin conjugates continued to treat cells long after the removal of SWNH-doped media. Interestingly, there appeared to be no difference in the amount of internalized SWNH-QD + cis over 72 h, indicating that cells were not expelling SWNH conjugates over this time period. These images helped to validate the mechanism of continued cell death over the 72 h period, as internalized SWNH conjugates remain within the cell and can deliver cisplatin therapy over time.

3.5 Conclusion

This work represents the first theranostic SWNH, with the capabilities to both perform fluorescence imaging with the conjugation to QDs and deliver significant payloads of the chemotherapeutic cisplatin. Successful conjugation of SWNHs with both QDs and cisplatin, confirmed through TEM, XPS, and drug release studies, enabled cellular characterization. SWNH-QD + cis provided a valuable nanoparticle to monitor SWNHs and drug release over time, confirming the significant cell death and revealing continual drug release over 72 h. The ability to both deliver chemotherapy to elucidate cell death as well as monitor the position of the SWNH-QD + cis through fluorescence imaging are key parameters for the nanotechnology of the future.

3.6 Acknowledgements

The authors would like to thank Andrew Giordani for his assistance with XPS, Athena Tilley for her assistance with ICP-AES, and Chris Winkler for his assistance with TEM. Funding for this work was provided by the National Science Foundation Early CAREER Award CBET 0955072 and 0933571, the National Institutes of Health Grant R211R21CA158454-01A1, and the National Science Foundation Graduate Research Fellowship Program.

3.7 Supplementary Information

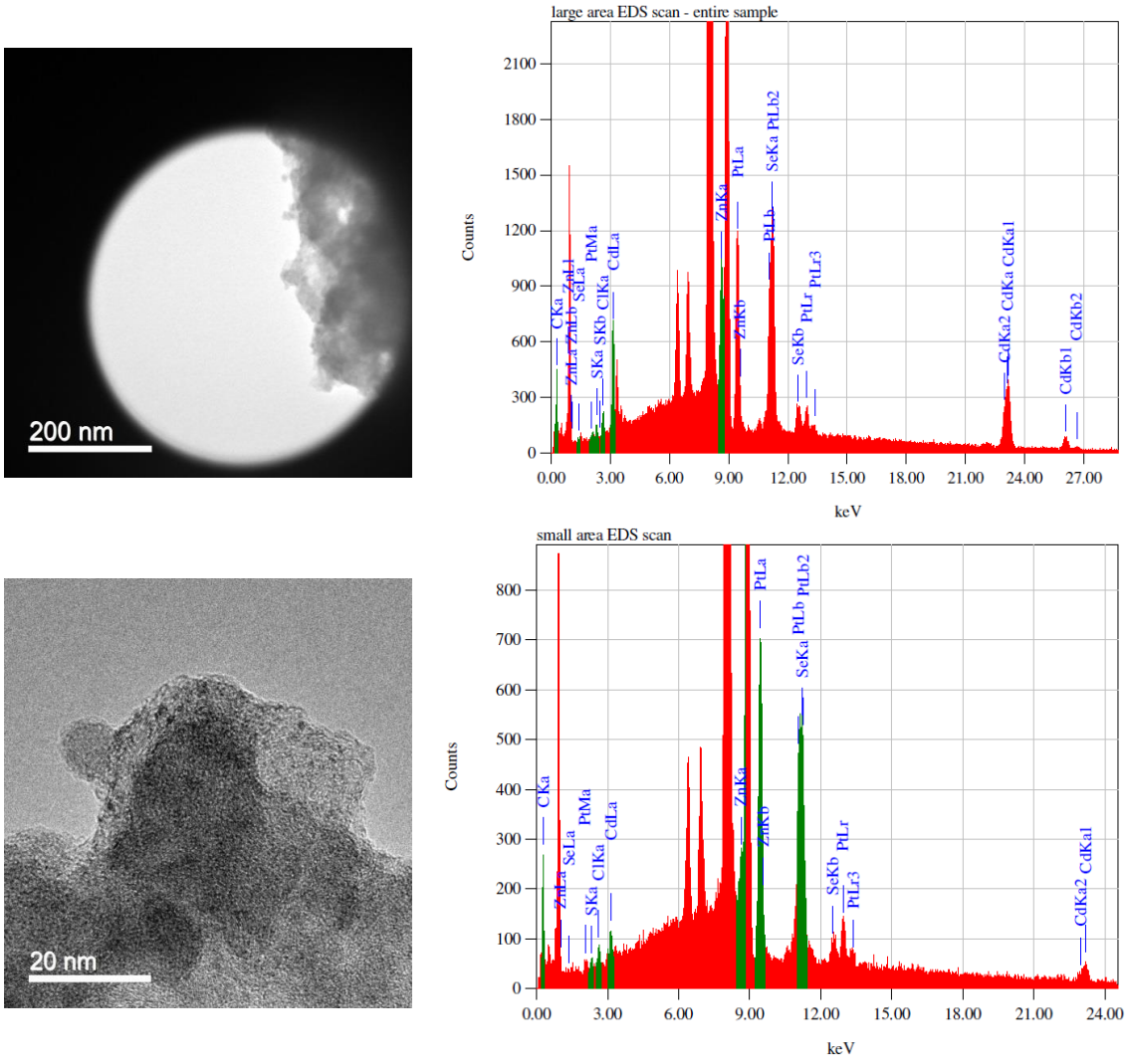

Figure 3.S1. EDS Spectra of a large and small area of SWNH-QD + cis. The elements present in each spectra correspond to successful functionalization. In addition, there is no difference in elemental composition between the large and small spectra, indicating sample homogeneity.

SWNHox

Concentration (mg/mL)					Least Sq Mean
10	A				122.67485
50	A	B			118.13635
5	A	B	C		114.27107
100		B	C	D	109.26374
1		B	C	D	109.12458
0.5		B	C	D	108.65733
0.1			C	D	105.36424
0.01			C	D	103.41095
0.05				D	100.29443
control				D	100.00000
0.001				D	98.78740
0.005				D	98.60724

SWNH-AET

Concentration (mg/mL)					Least Sq Mean
5	A				110.98215
0.5	A				110.35237
1	A				109.06426
control	A	B			100.00000
50		B	C		95.63338
10		B	C		95.56201
0.1		B	C	D	89.95304
100		B	C	D	88.46100
0.05			C	D	86.26449
0.01			C	D	85.25324
0.001				D	83.25441
0.005				D	81.07784

SWNH-QD

Concentration (mg/mL)					Least Sq Mean
control	A				100.00000
control2	A	B			95.55257
0.05	A	B	C		94.37206
0.1	A	B	C		94.30898
1	A	B	C		92.83216
water	A	B	C		92.82520
0.5	A	B	C		92.43079
10	A	B	C		92.29542
5	A	B	C		91.65304
0.01	A	B	C	D	89.81836
100		B	C	D	84.73189
50		B	C	D	84.65670
500			C	D	82.12920
250				D	78.16934

Table 3.S1. Statistics table including cytotoxicity of SWNH conjugates without cisplatin.

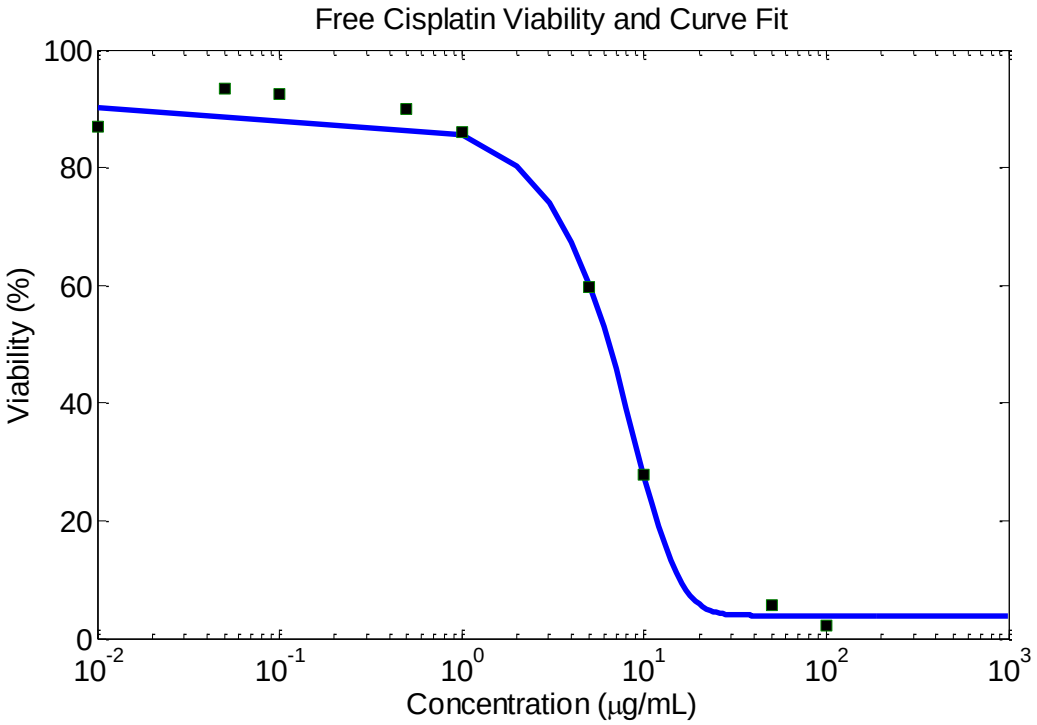

Figure 3.S2. Example of curve fitting to SWNH-cisplatin and free drug concentrations in JMP. Each of the data sets of viability vs concentration were fitted to a Logistic 4P S-curve and IC50 concentrations were calculated from these curves.

Conjugate	A: "growth rate"	B: "inflection point"	C: "lower asymptote"	D: "upper asymptote"	R^2
Free Cisplatin	-0.275118	5.5021996	3.9145743	109.3357	0.9934185
SWNHox	-0.045923	374.02847	3.2070048	100.88207	0.9948283
SWNH-AET	-0.02354	320.50486	0.8686549	93.221408	0.9920392
SWNH-QD	-0.011311	218.21189	-0.947627	100.17781	0.9934192

Table 3.S2. Examples of fitted parameters from Logistic 4P S-curve fits of each of the conjugates and the corresponding equation:

$$Viability = c + \frac{d - c}{1 + e^{(-a*(concentration - b))}}$$

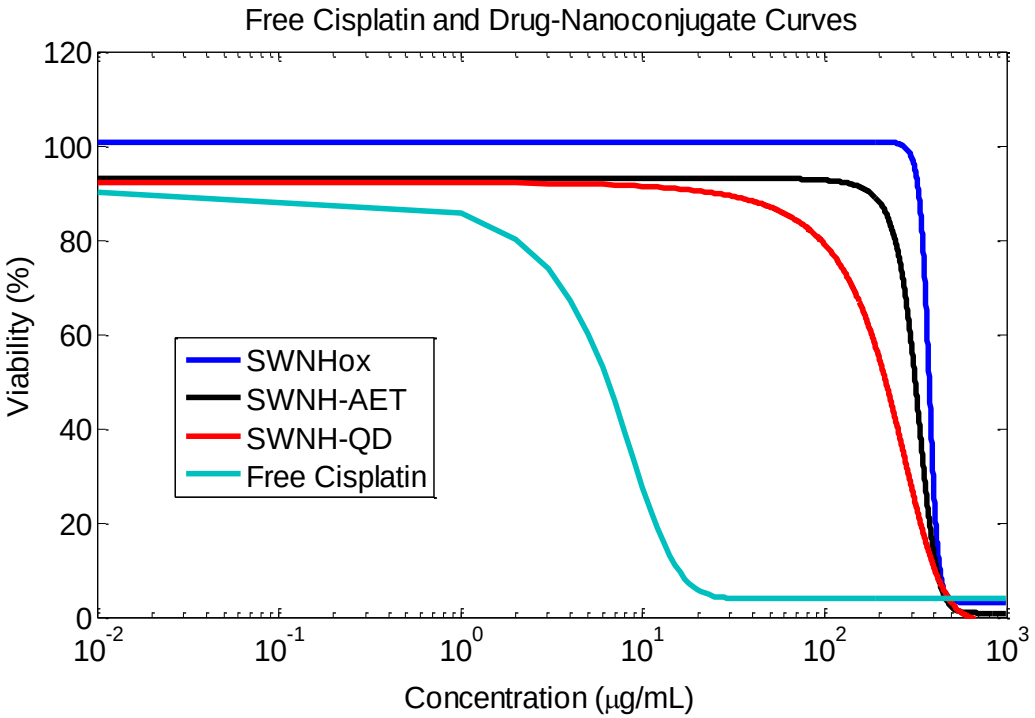

Figure 3.S3. Curve fits of each of the SWNH-cisplatin conjugates and free cisplatin. The curves show the change in IC50 pictorially by two orders of magnitude, with no significant difference between to different SWNH conjugates.

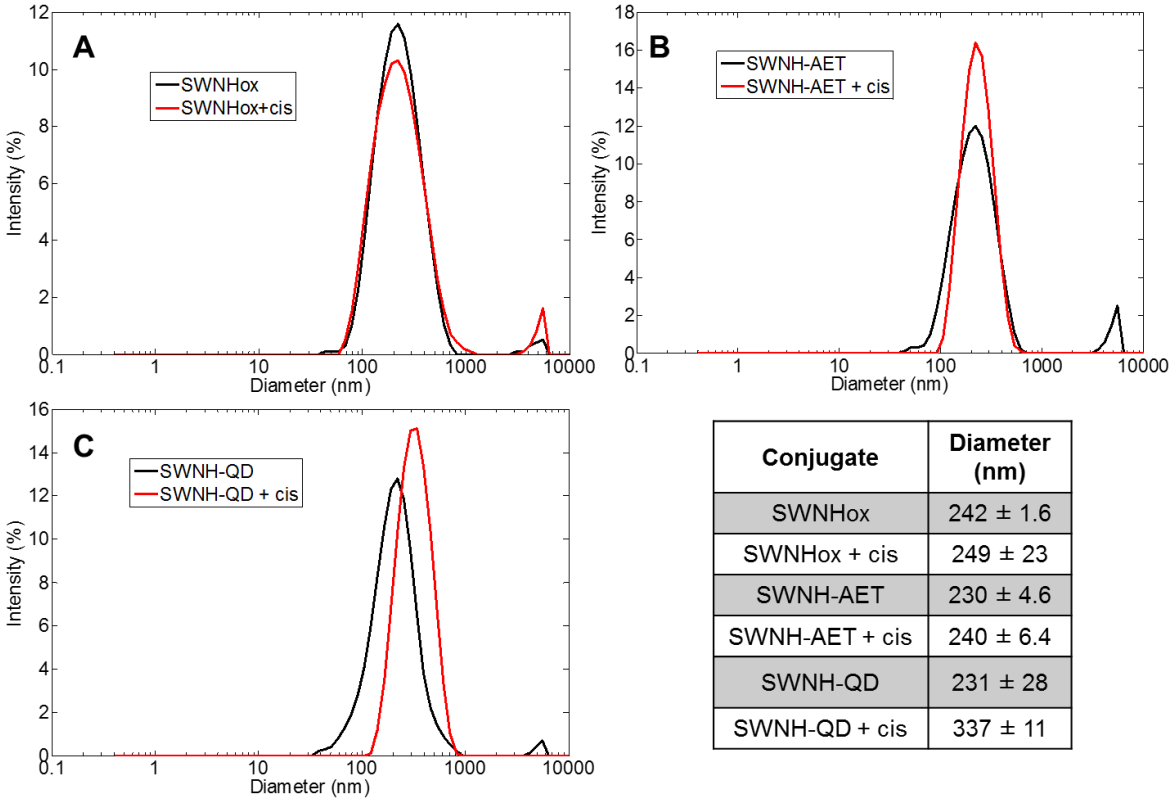

Conjugate	Diameter (nm)
SWNHox	242 ± 1.6
SWNHox + cis	249 ± 23
SWNH-AET	230 ± 4.6
SWNH-AET + cis	240 ± 6.4
SWNH-QD	231 ± 28
SWNH-QD + cis	337 ± 11

Figure 3.S4. Dynamic light scattering of SWNH conjugates, including before and after drug incorporation.

References

1 R. Siegel, J. Ma, Z. Zou, and A. Jemal, Cancer statistics, 2014. *CA: A Cancer Journal for Clinicians*. 64, 9-29 (**2014**)

2 D. T. Martin, C. J. Hoimes, H. Z. Kaimakliotis, C. J. Cheng, K. Zhang, J. Liu, M. A. Wheeler, W. K. Kelly, G. N. Tew, W. M. Saltzman, and R. M. Weiss, Nanoparticles for urothelium penetration and delivery of the histone deacetylase inhibitor belinostat for treatment of bladder cancer. *Nanomedicine : nanotechnology, biology, and medicine*. 9, 1124-1134 (**2013**)

3 Z. Lu, T.-K. Yeh, M. Tsai, J. L.-S. Au, and M. G. Wientjes, Paclitaxel-Loaded Gelatin Nanoparticles for Intravesical Bladder Cancer Therapy. *Clinical Cancer Research*. 10, 7677-7684 (**2004**)

4 J. P. Stein, G. Lieskovsky, R. Cote, S. Groshen, A.-C. Feng, S. Boyd, E. Skinner, B. Bochner, D. Thangathurai, M. Mikhail, D. Raghavan, and D. G. Skinner, Radical Cystectomy in the Treatment of Invasive Bladder Cancer: Long-Term Results in 1,054 Patients. *Journal of Clinical Oncology*. 19, 666-675 (**2001**)

5 S. Hart, E. C. Skinner, B. E. Meyerowitz, S. Boyd, G. Lieskovsky, and D. G. Skinner, QUALITY OF LIFE AFTER RADICAL CYSTECTOMY FOR BLADDER CANCER IN PATIENTS WITH AN ILEAL CONDUIT, OR CUTANEOUS OR URETHRAL KOCK POUCH. *The Journal of Urology*. 162, 77-81 (**1999**)

6 F.-Y. Cheng, C.-H. Su, P.-C. Wu, and C.-S. Yeh, Multifunctional polymeric nanoparticles for combined chemotherapeutic and near-infrared photothermal cancer therapy in vitro and in vivo. *Chemical Communications*. 46, 3167-3169 (**2010**)

7 W. Zhang, Z. Guo, D. Huang, Z. Liu, X. Guo, and H. Zhong, Synergistic effect of chemo-photothermal therapy using PEGylated graphene oxide. *Biomaterials*. 32, 8555-8561 (**2011**)

8 J.-H. Park, G. von Maltzahn, L. L. Ong, A. Centrone, T. A. Hatton, E. Ruoslahti, S. N. Bhatia, and M. J. Sailor, Cooperative Nanoparticles for Tumor Detection and Photothermally Triggered Drug Delivery. *Advanced Materials*. 22, 880-885 (**2010**)

9 T. S. Hauck, T. L. Jennings, T. Yatsenko, J. C. Kumaradas, and W. C. W. Chan, Enhancing the Toxicity of Cancer Chemotherapeutics with Gold Nanorod Hyperthermia. *Advanced Materials*. 20, 3832-3838 (**2008**)

10 A. M. Pekkanen, M. R. DeWitt, and M. N. Rylander, Nanoparticle enhanced optical imaging and phototherapy of cancer. *Journal of Biomedical Nanotechnology*. 10, 1677-1712 (**2014**)

11 F. Mohamed, P. Marchettini, O. A. Stuart, M. Urano, and P. Sugarbaker, Thermal Enhancement of New Chemotherapeutic Agents at Moderate Hyperthermia. *Annals of Surgical Oncology*. 10, 463-468 (**2003**)

12 M. Urano, and C. C. Ling, Thermal enhancement of melphalan and oxaliplatin cytotoxicity in vitro. *International Journal of Hyperthermia*. 18, 307-315 (**2002**)

13 R. E. Meyn, P. M. Corry, S. E. Fletcher, and M. Demetriades, Thermal Enhancement of DNA Damage in Mammalian Cells Treated with cis-Diamminedichloroplatinum(II). *Cancer Research*. 40, 1136-1139 (**1980**)

14 S. P. Sherlock, S. M. Tabakman, L. Xie, and H. Dai, Photothermally Enhanced Drug Delivery by Ultrasmall Multifunctional FeCo/Graphitic Shell Nanocrystals. *ACS Nano*. 5, 1505-1512 (**2011**)

15 J. E. Lee, N. Lee, H. Kim, J. Kim, S. H. Choi, J. H. Kim, T. Kim, I. C. Song, S. P. Park, W. K. Moon, and T. Hyeon, Uniform Mesoporous Dye-Doped Silica Nanoparticles Decorated with Multiple Magnetite Nanocrystals for Simultaneous Enhanced Magnetic Resonance Imaging, Fluorescence Imaging, and Drug Delivery. *Journal of the American Chemical Society*. 132, 552-557 (**2009**)
16 J.-H. Lee, Y.-w. Jun, S.-I. Yeon, J.-S. Shin, and J. Cheon, Dual-Mode Nanoparticle Probes for High-Performance Magnetic Resonance and Fluorescence Imaging of Neuroblastoma. *Angewandte Chemie International Edition*. 45, 8160-8162 (**2006**)
17 U. Resch-Genger, M. Grabolle, S. Cavaliere-Jaricot, R. Nitschke, and T. Nann, Quantum dots versus organic dyes as fluorescent labels. *Nat Meth*. 5, 763-775 (**2008**)
18 X. Gao, Y. Cui, R. M. Levenson, L. W. K. Chung, and S. Nie, In vivo cancer targeting and imaging with semiconductor quantum dots. *Nat Biotech*. 22, 969-976 (**2004**)
19 H. Tada, H. Higuchi, T. M. Wanatabe, and N. Ohuchi, In vivo Real-time Tracking of Single Quantum Dots Conjugated with Monoclonal Anti-HER2 Antibody in Tumors of Mice. *Cancer Research*. 67, 1138-1144 (**2007**)
20 D. Wang, J. He, N. Rosenzweig, and Z. Rosenzweig, Superparamagnetic Fe2O3 Beads−CdSe/ZnS Quantum Dots Core−Shell Nanocomposite Particles for Cell Separation. *Nano Letters*. 4, 409-413 (**2004**)
21 R. Di Corato, N. C. Bigall, A. Ragusa, D. Dorfs, A. Genovese, R. Marotta, L. Manna, and T. Pellegrino, Multifunctional Nanobeads Based on Quantum Dots and Magnetic Nanoparticles: Synthesis and Cancer Cell Targeting and Sorting. *ACS Nano*. 5, 1109-1121 (**2011**)
22 F. Erogbogbo, K.-T. Yong, R. Hu, W.-C. Law, H. Ding, C.-W. Chang, P. N. Prasad, and M. T. Swihart, Biocompatible Magnetofluorescent Probes: Luminescent Silicon Quantum Dots Coupled with Superparamagnetic Iron(III) Oxide. *ACS Nano*. 4, 5131-5138 (**2010**)
23 S.-H. Hu, Y.-W. Chen, W.-T. Hung, I. W. Chen, and S.-Y. Chen, Quantum-Dot-Tagged Reduced Graphene Oxide Nanocomposites for Bright Fluorescence Bioimaging and Photothermal Therapy Monitored In Situ. *Advanced Materials*. 24, 1748-1754 (**2012**)
24 R. Savla, O. Taratula, O. Garbuzenko, and T. Minko, Tumor targeted quantum dot-mucin 1 aptamer-doxorubicin conjugate for imaging and treatment of cancer. *Journal of Controlled Release*. 153, 16-22 (**2011**)
25 V. Bagalkot, L. Zhang, E. Levy-Nissenbaum, S. Jon, P. W. Kantoff, R. Langer, and O. C. Farokhzad, Quantum Dot−Aptamer Conjugates for Synchronous Cancer Imaging, Therapy, and Sensing of Drug Delivery Based on Bi-Fluorescence Resonance Energy Transfer. *Nano Letters*. 7, 3065-3070 (**2007**)
26 G. Duscher, M. Chisholm, A. Puretzky, C. Rouleau, and D. Geohegan, Atomic Structure of Single Walled Carbon Nanohorns. *Microscopy and Microanalysis*. 17, 1510-1511 (**2011**)
27 M. Yudasaka, S. Iijima, and V. Crespi, in *Carbon Nanotubes*, Edited by A. Jorio, G. Dresselhaus and M. Dresselhaus, Springer Berlin Heidelberg, (**2008**) Vol. 111, pp. 605-629.
28 J. R. Whitney, S. Sarkar, J. Zhang, T. Do, T. Young, M. K. Manson, T. A. Campbell, A. A. Puretzky, C. M. Rouleau, K. L. More, D. B. Geohegan, C. G. Rylander,

H. C. Dorn, and M. N. Rylander, Single walled carbon nanohorns as photothermal cancer agents. *Lasers in Surgery and Medicine*. 43, 43-51 (**2011**)
29 J. Whitney, M. DeWitt, B. M. Whited, W. Carswell, A. Simon, C. G. Rylander, and M. N. Rylander, 3D viability imaging of tumor phantoms treated with single-walled carbon nanohorns and photothermal therapy. *Nanotechnology*. 24, 275102 (**2013**)
30 K. Ajima, M. Yudasaka, K. Suenaga, D. Kasuya, T. Azami, and S. Iijima, Material Storage Mechanism in Porous Nanocarbon. *Advanced Materials*. 16, 397-401 (**2004**)
31 K. Ajima, M. Yudasaka, T. Murakami, A. Maigné, K. Shiba, and S. Iijima, Carbon Nanohorns as Anticancer Drug Carriers. *Molecular Pharmaceutics*. 2, 475-480 (**2005**)
32 S. Matsumura, K. Ajima, M. Yudasaka, S. Iijima, and K. Shiba, Dispersion of Cisplatin-Loaded Carbon Nanohorns with a Conjugate Comprised of an Artificial Peptide Aptamer and Polyethylene Glycol. *Molecular Pharmaceutics*. 4, 723-729 (**2007**)
33 K. Ajima, T. Murakami, Y. Mizoguchi, K. Tsuchida, T. Ichihashi, S. Iijima, and M. Yudasaka, Enhancement of In Vivo Anticancer Effects of Cisplatin by Incorporation Inside Single-Wall Carbon Nanohorns. *ACS Nano*. 2, 2057-2064 (**2008**)
34 J. Xu, M. Yudasaka, S. Kouraba, M. Sekido, Y. Yamamoto, and S. Iijima, Single wall carbon nanohorn as a drug carrier for controlled release. *Chemical Physics Letters*. 461, 189-192 (**2008**)
35 M. R. DeWitt, A. M. Pekkanen, J. Robertson, C. G. Rylander, and M. Nichole Rylander, Influence of Hyperthermia on Efficacy and Uptake of Carbon Nanohorn-Cisplatin Conjugates. *Journal of Biomechanical Engineering*. 136, 021003-021003 (**2014**)
36 J. Zhang, J. Ge, M. D. Shultz, E. Chung, G. Singh, C. Shu, P. P. Fatouros, S. C. Henderson, F. D. Corwin, D. B. Geohegan, A. A. Puretzky, C. M. Rouleau, K. More, C. Rylander, M. N. Rylander, H. W. Gibson, and H. C. Dorn, In Vitro and in Vivo Studies of Single-Walled Carbon Nanohorns with Encapsulated Metallofullerenes and Exohedrally Functionalized Quantum Dots. *Nano Letters*. 10, 2843-2848 (**2010**)
37 K. Zimmermann, D. Inglefield, Jr., J. Zhang, H. Dorn, T. Long, C. Rylander, and M. N. Rylander, Single-walled carbon nanohorns decorated with semiconductor quantum dots to evaluate intracellular transport. *Journal of Nanoparticle Research*. 16, 1-18 (**2013**)
38 D. H. Everett, in *Basic Principles of Colloid Science*, The Royal Society of Chemistry, (**1988**), pp. 127-145.
39 I. O. f. S. (ISO), (**2008**)
40 B. O. Dabbousi, J. Rodriguez-Viejo, F. V. Mikulec, J. R. Heine, H. Mattoussi, R. Ober, K. F. Jensen, and M. G. Bawendi, (CdSe)ZnS Core−Shell Quantum Dots: Synthesis and Characterization of a Size Series of Highly Luminescent Nanocrystallites. *The Journal of Physical Chemistry B*. 101, 9463-9475 (**1997**)
41 X. Peng, L. Manna, W. Yang, J. Wickham, E. Scher, A. Kadavanich, and A. P. Alivisatos, Shape control of CdSe nanocrystals. *Nature*. 404, 59-61 (**2000**)
42 Y.-T. Kim, J. H. Han, B. H. Hong, and Y.-U. Kwon, Electrochemical Synthesis of CdSe Quantum-Dot Arrays on a Graphene Basal Plane Using Mesoporous Silica Thin-Film Templates. *Advanced Materials*. 22, 515-518 (**2010**)

43 Y. Wang, H.-B. Yao, X.-H. Wang, and S.-H. Yu, One-pot facile decoration of CdSe quantum dots on graphene nanosheets: novel graphene-CdSe nanocomposites with tunable fluorescent properties. *Journal of Materials Chemistry*. 21, 562-566 (**2011**)
44 R. Singh, and J. W. Lillard Jr, Nanoparticle-based targeted drug delivery. *Experimental and Molecular Pathology*. 86, 215-223 (**2009**)
45 Z. H. Siddik, Cisplatin: mode of cytotoxic action and molecular basis of resistance. *Oncogene*. 22, 7265-7279 (**2003**)
46 K. Yin Win, and S.-S. Feng, Effects of particle size and surface coating on cellular uptake of polymeric nanoparticles for oral delivery of anticancer drugs. *Biomaterials*. 26, 2713-2722 (**2005**)
47 L. Linlin, C. Dong, Z. Yanqi, D. Zhengtao, R. Xiangling, M. Xianwei, T. Fangqiong, R. Jun, and Z. Lin, Magnetic and fluorescent multifunctional chitosan nanoparticles as a smart drug delivery system. *Nanotechnology*. 18, 405102 (**2007**)
48 T. Murakami, H. Sawada, G. Tamura, M. Yudasaka, S. Iijima, and K. Tsuchida, Water-dispersed single-wall carbon nanohorns as drug carriers for local cancer chemotherapy. *Nanomedicine*. 3, 453-463 (**2008**)
49 A. T. Horowitz, Y. Barenholz, and A. A. Gabizon, In vitro cytotoxicity of liposome-encapsulated doxorubicin: dependence on liposome composition and drug release. *Biochimica et Biophysica Acta (BBA) - Biomembranes*. 1109, 203-209 (**1992**)
50 N. Nishiyama, Y. Kato, Y. Sugiyama, and K. Kataoka, Cisplatin-Loaded Polymer-Metal Complex Micelle with Time-Modulated Decaying Property as a Novel Drug Delivery System. *Pharmaceutical Research*. 18, 1035-1041 (**2001**)
51 F. M. Veronese, O. Schiavon, G. Pasut, R. Mendichi, L. Andersson, A. Tsirk, J. Ford, G. Wu, S. Kneller, J. Davies, and R. Duncan, PEG−Doxorubicin Conjugates: Influence of Polymer Structure on Drug Release, in Vitro Cytotoxicity, Biodistribution, and Antitumor Activity. *Bioconjugate Chemistry*. 16, 775-784 (**2005**)
52 Z. Liu, J. T. Robinson, X. Sun, and H. Dai, PEGylated Nanographene Oxide for Delivery of Water-Insoluble Cancer Drugs. *Journal of the American Chemical Society*. 130, 10876-10877 (**2008**)
53 T. Murakami, J. Fan, M. Yudasaka, S. Iijima, and K. Shiba, Solubilization of Single-Wall Carbon Nanohorns Using a PEG−Doxorubicin Conjugate. *Molecular Pharmaceutics*. 3, 407-414 (**2006**)

Chapter 4. 3D Printing Polymers with Supramolecular Functionality for Biological Applications

(Submitted to Biomacromolecules)

Allison M. Pekkanen[1], Christopher B. Williams[2], Timothy E. Long[3]

[1]School of Biomedical Engineering and Sciences, Virginia Tech, Blacksburg, VA 24061

[2]Department of Mechanical Engineering, Virginia Tech, Blacksburg, VA 24061

[3]Department of Chemistry, Macromolecules Innovation Institute (MII), Virginia Tech, Blacksburg, VA 24061

*To whom correspondence should be addressed. E-mail: telong@vt.edu. TEL: (540) 231-2480 FAX: (540) 231-8517

Keywords: Additive Manufacturing, Hydrogen Bonding, Supramolecular, Tissue Engineering, Tissue Scaffolds

4.1 Abstract

Supramolecular chemistry continues to experience widespread growth, as fine-tuned chemical structures lead to well-defined bulk materials. Historically, significant research revolved around the use of supramolecular chemistry to develop tissue engineered scaffolds for biological applications. Recently, supramolecular polymers and additive manufacturing merged to develop scaffolds with definition on the molecular, macromolecular, and feature levels. This review details the progress of supramolecular polymer use in additive manufacturing for biological applications, including drug delivery and complex tissue scaffold formation. The potential for supramolecular polymers to generate isotropic parts and hierarchical structures provides a path for future investigation.

4.2 Introduction

The field of polymers containing supramolecular interactions describes a class of molecules in polymer chemistry that precisely control both the polymer structure and the interactions between polymer chains.[1, 2] Supramolecular interactions between polymer chains include ionic interactions, hydrogen bonding, guest/host interactions, and π-π stacking, each with varying degrees of strength.[2-5] Traditional supramolecular chemistry revolves around interactions between small molecules or polymers that possess a well-defined 2D or 3D structure.[1, 4] Importantly, the reversibility of supramolecular interactions facilitates part manufacturing with the ability to break supramolecular bonds during printing and form these interactions again in the final structure. The combination of supramolecular polymers with biologically-relevant hydrogels reveals a promising approach to complex tissue engineering, combining reversible, supramolecular bonds and water to lower the glass transition temperature (T_g) and lend chain mobility.[6, 7]

Tissue engineering involves the replication of native biological tissues *in vitro* for a variety of applications such as drug discovery, disease characterization, and organ replacement.[8] Tissue scaffolds generated from non-specific molding or precisely tuned 3D structure closely mimics a cell or organ type of choice.[9-11] The field of tissue engineering includes both synthetic and natural polymers, lending great diversity to the field.[12-14] Specifically, common tissue engineering constructs closely mimic native cartilage, which is generated from chondrocytes.[15-17] Stem cells, which differentiate into specific tissue types, tune differentiation based on the modulus and chemical environment of the resulting scaffold.[18, 19] Recent advances for *in vitro* 3D cell culture include complex tissues such as skin (keratinocytes, fibroblasts)[20], liver (hepatocytes)[21], brain and

spinal cord (neurons)[22], blood vessels (endothelial)[23], and heart (aortic valve, smooth muscle)[24], which forge the way for future tissue engineered scaffolds capable of mimicking complete organs.[25, 26] The advancement of tissue engineering to create biologically-active and hierarchical structures drives the future of tissue engineering.[27]

Additive manufacturing (AM), also known as 3D printing or rapid prototyping, emerged to generate previously unattainable geometric structures and functions from well-characterized materials. While AM generated new structural geometries composed of existing materials, biology also benefited from creation of novel drug delivery devices and tissue scaffolds.[28] Material extrusion AM, vat photopolymerization, and inkjet printing commonly generated novel structures suitable for incorporation into the human body.[29, 30] Specifically, the control of not only geometry but also porosity aided in formulation of complex biological structures capable of sustaining cellular viability and proliferation. Furthermore, recent advances in bioprinting allow for cell encapsulation into polymers for simultaneous deposition into complex tissue scaffolds.[31] While advances in additive manufacturing open opportunities for new tissue scaffolds, the breadth of cell sensing requires the incorporation of supramolecular functionality to create distinct structures (**Figure 4.1**). Resolution of common AM techniques, while improving rapidly, remains limited in scope compared to cell sensing capabilities. This review describes the use of polymers imbibed with supramolecular functionality, both natural and synthetic, for AM designed for biological applications, both with and without encapsulated cells.

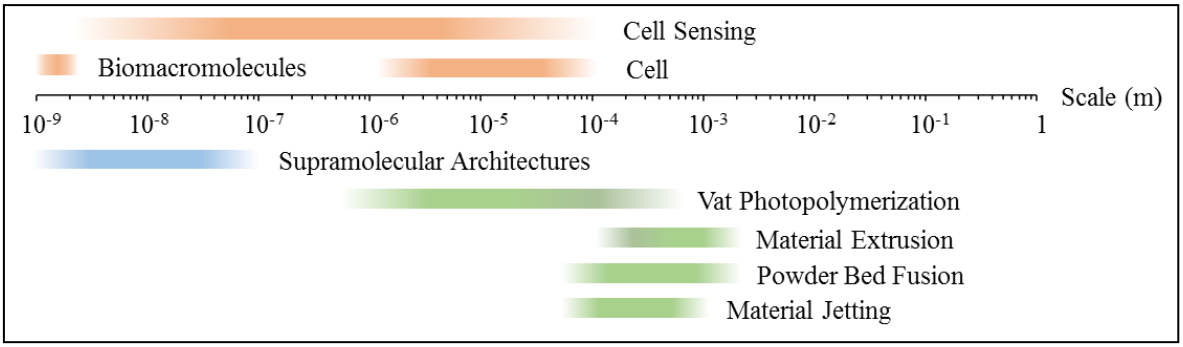

Figure 4.1. Resolution of common AM techniques fails to reach the breadth of cellular sensing capabilities, necessitating the use of both additive manufacturing and supramolecular interactions to reach control of fine features.[19, 32]

4.3 Synthesis and Characterization of 3D-Printable Supramolecular Polymers

Utilizing both synthetic methods and modifications of naturally-occurring biopolymers enabled supramolecular polymers appropriate for AM. The modulus, viscosity, and functionality of supramolecular polymers enables their use in AM.[33] Commonly, naturally-occurring polymers possess a high molecular weight, which translates to an inherently viscous polymer solution suitable for material extrusion AM.[34] Interestingly, most modified biopolymers combine with a photocurable group or synthetic copolymer to enhance mechanical integrity upon printing. Alternatively, synthetic polymers offer tunable viscosities and functionality, expanding the potential printing techniques suitable for tissue scaffolds or drug delivery and eliminating manufacturing limitations. Resulting modulus and physical characteristics of the printed polymers also drive their application, with high modulus materials best for applications such as bone tissue engineering and low modulus materials fit for soft tissue applications.[35, 36] Supramolecular functionality, modulus, and viscosity dictate both the AM technique used and resulting biological applications.[37]

4.3.1 Modifications of Natural Polymers.

Naturally-occurring polymers or biopolymers offer supramolecular functionality, which while often weaker than synthetic polymers, occurs naturally within the materials.[38] These polymers, however, often necessitate modifications to achieve tailored geometry while printing, such as the inclusion of a photocurable group for direct modification of the biopolymer.[39]

The polysaccharide hyaluronic acid (HA) acts as lubrication throughout the body and possesses sites for both hydrogen bonding and chemical modification (**Figure 4.2**).[40] HA possesses a high degree of biocompatibility and biodegradability, ensuring parts created with HA exhibit favorable biological properties.[40, 41] HA undergoes a number of reactions to introduce functionality along the polymer backbone. HA reacted at primary alcohols with methacrylic anhydride to yield methacrylated HA suitable for photocrosslinking.[42] Ouyang *et al.* described the functionalization of HA with adamantine (Ad) and β-cyclodextrin (CD) to facilitate enhanced supramolecular behavior via guest-host interactions.[43, 44] The primary alcohol group catalyzed Ad functionality,[44] while the carboxylic acid group modified to include CD functionality.[43] Additionally, EDC coupling through the carboxylic acid group yielded thiol-functionalized HA.[45] A thiol-ene reaction through thiol-HA included diaminohexane (DAH) or cucurbit[6]uril (CB[6]) into the biopolymer, which acted as guest-host supramolecular functionality facilitating the formation of hydrogels.[46, 47] In addition to the inherent hydrogen bonding found in HA, the addition of functionality to either induce additional supramolecular interactions or provide chemical crosslinking to bolster HA mechanical properties provides a robust biopolymer suitable for AM.

While HA dominates polysaccharides used for AM, others such as chondroitin sulfate (CS), dextran, chitosan, sodium alginate, and gellan gum also possess favorable functionalities (**Figure 4.2**).[39] CS acts as an extracellular matrix (ECM) protein capable of withstanding compressive load and absorbing water within cartilage in the human body.[48] Its abundance of ionic groups and hydrogen bonding groups, together with sites for chemical modification, make CS an attractive choice for biologically-sound structures. Abbadessa *et al.* described the creation of CS-methacrylate for AM through a reaction at the primary alcohol group with glycidyl methacrylate.[49] In parallel to a partially methacrylated triblock copolymer, CS-methacrylate created synthetic cartilage tissue scaffolds.[49] CS also reacted with 2-aminoethyl methacrylate through EDC coupling to form methacrylated CS.[50] Dextran, a colloidal biopolymer, functions to resist to protein adsorption and enables numerous *in vitro* characterizations of synthetic tissue scaffolds.[51] The primary alcohol on dextran reacted with hydroxyethyl methacrylate to form photocurable polymers.[52] Gellan gum, a polysaccharide commonly isolated from bacteria, possesses a number of hydroxyl groups, both primary for functionalization and secondary to serve solely as hydrogen bonding units.[53] EDC coupling through the carboxylic acid group on gellan gum afforded peptide-modified gellan gum for enhanced cell proliferation.[54] Characterization of the degree of functionality of these biopolymers provides a unique challenge due to the size and complexity of natural polymer structures.

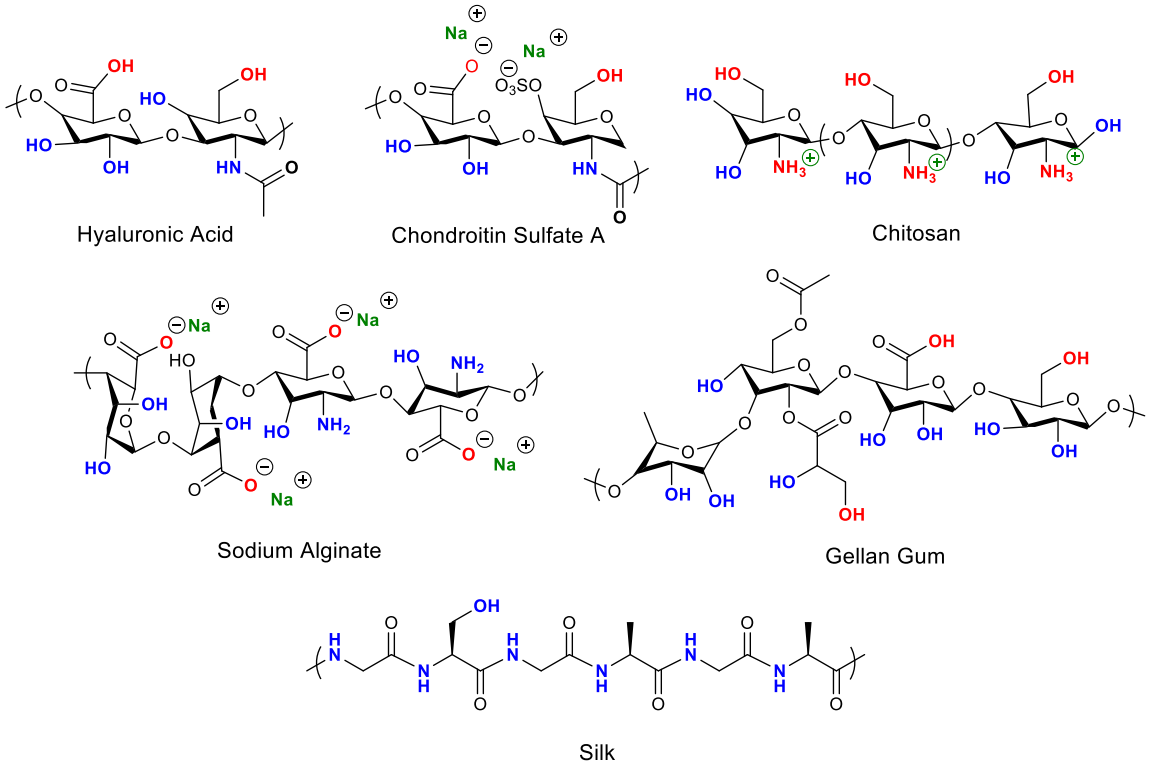

Figure 4.2. Structures of commonly used natural polymers for AM, including polysaccharides and polypeptides. These biopolymers have been chemically modified (sites marked in red) as well as utilized for their supramolecular behavior either from hydrogen bonding (blue) or ionic (green) interactions.

Due to the combination of high molecular weight and supramolecular functionality, biopolymers often undergo printing in their natural state. Other polysaccharides commonly used in hydrogel formation include chitosan, which is often used in its natural form due to its intrinsic positive charge to create ionically-based hydrogels.[55, 56] Chitosan also reacted through acid-base chemistry to yield N,O-carboxymethyl chitosan, which results in carboxylic acid groups attached to the amine and primary alcohol.[57] Sodium alginate's native state also provided charged biopolymers capable of physical crosslinking in the presence of divalent cations, typically calcium.[58] Agarose, with a gel point below room temperature, underwent successful inkjet printing to form well-defined structures in its native state.[59] While these biopolymers often

facilitate AM in their native state, their plethora of functional groups provides additional handles for chemical modifications.

Natural polymers also include polyamides generated from the polymerization of amino acids (polypeptides). The naturally occurring ECM protein collagen and its derivatives act as structural proteins and often display natural cell adhesion sequences to promote tissue generation. The arginine-glycine-aspartic acid (RGD) sequence as well as its triple helix structure make collagen an ideal candidate for the formation of tissue scaffolds. In traditional tissue engineering, collagen crosslinks during the neutralization of acid-soluble collagen to form an insoluble network, suffering from significant variation and lack of control.[60] Due to these factors, along with its substantial molecular weight, collagen alone rarely permits processing through AM.[61] Instead, its derivative gelatin facilitates AM to form complex 3D structures while maintaining the biocompatibility and biodegradability benefits of collagen.[56, 62, 63] Commonly, reactions of methacrylic anhydride with the amine group of gelatin generated photo-crosslinkable functionality, which lent additional structural support to the printed scaffold following material extrusion AM.[62, 63] Acetylation of gelatin is also accomplished at the amine group through a similar reaction.[64] Klotz *et al.* provided a comprehensive review of reactions with gelatin to generate 3D-printable gelatin through a variety of chemical modifications.[61] Polypeptides, while potentially offering tuned microstructure through the polymerization of different amino acids, represent only a portion of current research into biopolymer AM.

4.3.2 Synthetic Supramolecular Polymers

Synthetic supramolecular polymers are achieved through one of two routes: synthesis or self-assembly of a new supramolecular polymer system or modification of existing synthetic polymers. Synthetic polymers offer the ability to tune specific properties and supramolecular interactions. This control enables the selective creation of well-defined AM parts across many length scales, achieved through both printing parameters and the supramolecular chemistry employed.

4.3.2.1 Synthesis and Self-Assembly of Supramolecular Polymers

Synthetic chemistry facilitates precise tuning of polymeric structure, achieving control over the final printed part free from heterogeneity. Ionic interactions strongly influence hydrogel integrity, as exemplified by a zwitterionic system containing photocrosslinkable, synthetic monomers carboxybetaine acrylamide and carboxybetaine dimethacrylate which created hydrogels of varying stiffness for the preservation of human stem cells.[65] Varying ratios of acrylamide to dimethacrylate enabled construction of low modulus gels to precisely tune modulus and direct stem cell differentiation.[65] Schultz *et al.* described the creation of a novel charged phosphonium monomer, which was co-printed with PEG dimethacrylate through vat photopolymerization.[66] These parts demonstrated the capability to print synthetic ionic monomers to create a supramolecular, crosslinked network.[66]

Hydrogen bonding remains one of the most prevalent and versatile form of supramolecular interactions between synthetic polymers. Free radical polymerization to form precursor copolymers of poly[(ethylene glycol methyl ether mechacrylate)-co-*N*,*N*-dimethylacrylamide] demonstrated significant hydrogen bonding capabilities when co-

printed with cellulose nanofibrils.[67] Wang *et al.* detailed the creation of this copolymer to specifically eliminate ionic interactions, which could cause premature gelation, and instead designed the copolymer to tailor interactions with cellulose through hydrogen bonding.[67] Acrylamide monomers containing Ad and cucurbit[7]uril (CB[7]) polymerized through free radical polymerization formed crosslinked hydrogels upon mixing.[68] Controlled free radical polymerization yielded poly(*N*-(2-hydroxypropyl) methacrylamide lactate-co-PEG) (Poly(HPMAm-lactate)-PEG) triblock copolymers with controlled hydrophilic/hydrophobic interactions.[69] The thermal behavior of poly(HPMAm-lactate) blocks afforded dynamic hydrogels capable of supramolecular interactions controlled through temperature, which precisely tuned the deposition of fluorescent beads (**Figure 4.3**).[69]

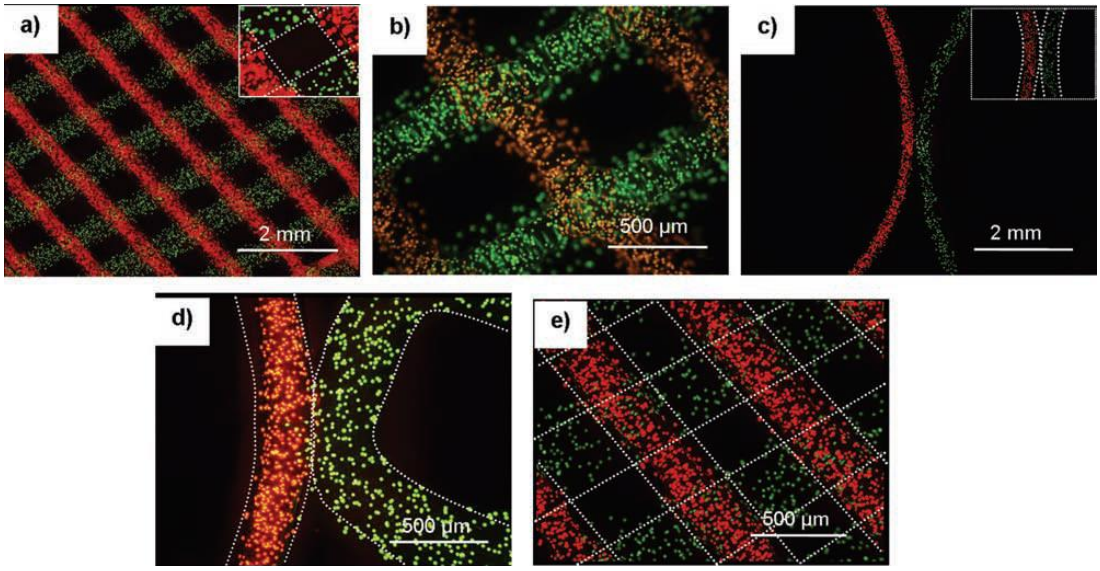

Figure 4.3. Material extrusion AM of poly(HPMAm-lactate)-PEG triblock copolymer generates precisely-controlled deposition of polymer strands doped with fluorescent beads, including layers (a, b, e) and curves (c, d). Adapted from Censi *et al.*[69]

Step-growth polymerization to form polyurethanes that possess water solubility and biodegradability underwent a multi-step procedure ending with chain extension of polycaprolactone (PCL) or poly(ether-*b*-amide) (PEBA)-based diisocyanates with

ethylene diamine to form high molecular weight polymers.[70] These multifaceted hydrogen-bonding polymers form complex tissue scaffolds for material extrusion AM.[70, 71] Release of chondrogenic growth factors and mesenchymal stem cell proliferation and differentiation furthered the use of AM with biodegradable polyurethanes for tissue engineering.[71]

Supramolecular interactions also accomplished the self-assembly of synthetic small molecules to form complex microstructures. Amphiphilic pyrene pyridinium and 2,4,7-trinitrofluorenone combined to create hydrogels through charge-transfer supramolecular interactions.[72] These injectable small molecules formed defined hydrogels, which also underwent self-recovery upon strain, highlighting the strength of these supramolecular bonds.[72] Wei *et al.* detailed the synthesis of a hydrogel, which underwent self-assembly to form a partially gelled intermediate through supramolecular interactions of amino acid-modified acrylic acid.[73] Following initial gel formation, crosslinking achieved through enzymatic polymerization formed an interpenetrating network resulting in superior mechanical properties than either gel alone.[73, 74] This research exemplifies the incorporation of supramolecular interactions into commonly-utilized AM technologies to enhance mechanical properties of the final part.

In each of these cases, new monomer synthesis enabled the creation of novel supramolecular polymers or fueled direct AM with a functional copolymer. As the field of supramolecular chemistry moves towards AM of isotropic parts, both new monomers and creative microstructures of commercially available monomers will enable precise control of structure, both at the molecular and printing scales.

4.3.2.2 Modifications of Existing Synthetic Polymers

Extensive research revealed classes of polymers suitable for use as tissue scaffolds, including poly(ethylene glycol) (PEG) and PCL, each undergo chemical modifications to lend 3D-printable and supramolecular functionality. High molecular weight PCL lacks printability by methods other than extrusion AM, but offers favorable biomechanical properties.[75] To create PCL amenable to other AM techniques, modification of low molecular weight diols with supramolecular functionality is necessary.[76] Hart *et al.* discussed the modification of PCL diols with a multitude of hydrogen bonding and π-stacking moieties through 2,4-toluene diisocyanate end-capping reactions.[76] The inclusion of these groups at relatively low concentrations led to the formation of supramolecular networks that exhibited shear thinning behavior and successful inkjet printing, a property commonly observed in high molecular weight polymers (**Figure 4.4**).[76] Synthetic groups tailored to contain multiple hydrogen bonding groups facilitated supramolecular interactions, such as 2-ureido-4[1H]-pyrimidinone (UPy) developed by Meijer *et al.*, which found use in a wide variety of polymeric systems.[1, 38, 77] UPy engaged in quadruple hydrogen-bonding and facilitated self-assembly polymers, exhibited through end-capping reactions with PCL and peptides.[77]

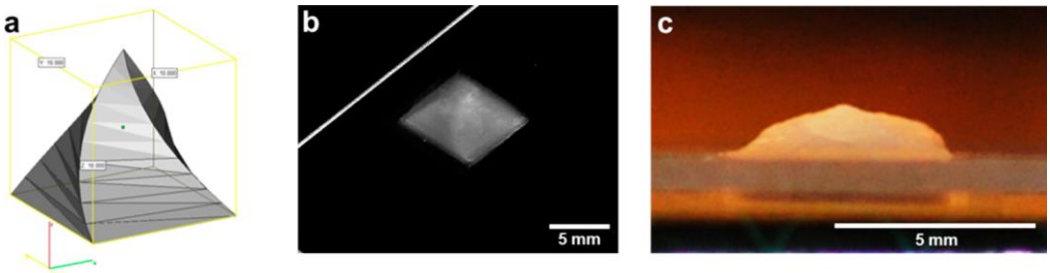

Figure 4.4. Inkjet printing of modified PCL from modeling (a) reveals structural integrity (b) and merging of layers (c) to produce a homogenous pyramid. Adapted from Hart *et al.*[76]

PEG possesses a significant portion of tissue engineered scaffolds due to its well-characterized biocompatibility and ease-of-use.[78] While the vast majority of PEG utilized for additive manufacturing exists as PEG-acrylate, the primary alcohol end-groups provided a facile route to introduce supramolecular functionality. Hydrogen bonding urethane-containing groups added to PEG diol ends through reactions with diisocyanate HMDI yielded photo-crosslinkable oligomers.[79]

4.4 Additive Manufacturing of Supramolecular Polymers

AM consists of many forms to successfully manufacture tissue scaffolds, including material extrusion, vat photopolymerization, inkjet printing, and bioprinting.[80] Bioprinting refers to cell-laden polymer solutions or resins, which subsequently undergo the printing process. Many scaffolds, however, undergo the printing process before introducing cells, eliminating additional printing parameters which could compromise the printability of the supramolecular polymer. Sterilization of tissue scaffolds occurs either before the printing process to yield sterile scaffolds directly or following scaffold formation through traditional sterilization of the pre-formed tissue scaffold. Sterilization adds another hidden parameter to AM tissue scaffolds, which potentially affects the structural integrity, anisotropy, and resolution of manufactured parts.

4.4.1 Material Extrusion Additive Manufacturing

Material extrusion AM traditionally relies on thermoplastics printed from either a hot-melt or filament. Extensive research refined the printing parameters, temperatures, and geometries for printing common polymers such as acrylonitrile-butadiene-styrene

(ABS) and polycarbonate. In recent years, however, material extrusion AM of biocompatible polymers such as PCL and natural biopolymers proved valuable to the creation of tissue scaffolds for personalized medicine.

Supramolecular polymers are prevalent in material extrusion AM, both in fused filament formation and direct-write systems, largely due to the abundance of extrudable natural polymers and their inherent supramolecular functionality. Naturally occurring polymers often print with a combination of material extrusion and photo-crosslinking, as they generally have sufficient molecular weight, and thus viscosity, to achieve part fidelity upon extrusion but require photo-crosslinking to lend additional mechanical support.

4.4.1.1 Natural Polymers.

HA features prominently for AM of tissue scaffolds, with a variety of chemical modifications resulting in the successful creation of hydrogels. HA successfully underwent modification with supramolecular functionality or photo-crosslinking groups for use in extrusion AM as described above. Highley *et al.* detailed the extrusion of Ad, CD and methacrylated HA, to form supramolecular bonds after exiting the nozzle.[43, 44] Following successful extrusion, photo-crosslinking the methacrylates further bostered the hydrogel, yielding self-supporting structures.[43, 44] Furthermore, microchannels within the part, created through the removal of excess uncrosslinked HA, utilized CD solutions.[44] Use of fibroblast cells confirmed functional structures capable of sustaining life, which drove future research to include the introduction of mesenchymal stem cells.[44]

Gellan gum, with combinations of other macromolecules or modified with methacrylates, encouraged successful material extrusion AM.[81-83] When modified with

RGD, gellan gum formed complex layered structures without further modification or co-extrusion.[54] Gellan gum and alginate supported mesenchymal stem cell proliferation and differentiation following material extrusion AM.[81] Cell seeding with human mesenchymal stem cells confirmed the improvement in cellular attachment and proliferation on composite hydrogels as compared to alginate alone.[81] Modified chitosan, co-extruded with polyphosphates and alginate, formed durable hydrogels capable of additional crosslinking with calcium.[57] Osteogenic cells seeded onto these scaffolds revealed biomineralization, suggesting a strong correlation between combination hydrogels and mineralization potential.[57]

Due to their high molecular weight and native supramolecular functionality, material extrusion AM of biopolymers in their natural state catalyzes the formation of distinct tissue scaffolds. Material extrusion of alginate created hydrogels with well-defined structure.[84] Liu *et al.* evaluated the effect of varying deposition parameters on the resulting ionically-crosslinked hydrogel, providing valuable metrics for future study.[84] Gelatin, also extruded in its native form, created 3D structures with homogenous polymer distribution throughout, generating high-fidelity parts.[85] Gelatin also extruded with silk to create stable, implantable hydrogels suitable for soft tissue reconstruction of precisely-controlled features imaged with CT scans of patient defects.[86] Alginate and gellan gum in their natural state provided hydrogels capable of releasing a number of growth factors to stimulate endothelial cell proliferation for the correction of bone defects.[87] Collagen co-extruded with hydroxyapatite to sustain bone marrow stromal cell viability when seeded after printing.[88] The 3D tissue scaffold induced cell differentiation and new bone formation following implantation into a rabbit.[88] Collagen also sustained and induced

proliferation of mesenchymal stromal cells following material extrusion into complex tissue scaffolds.[89] These combinations of natural polymers commonly exist as either blends or core/shell filaments, as seen in **Figure 4.5**.[90] A novel deposition system afforded core/shell scaffold materials to capitalize on the benefits of each biopolymer for the creation of precise tissue scaffolds with tunable modulus.[90]

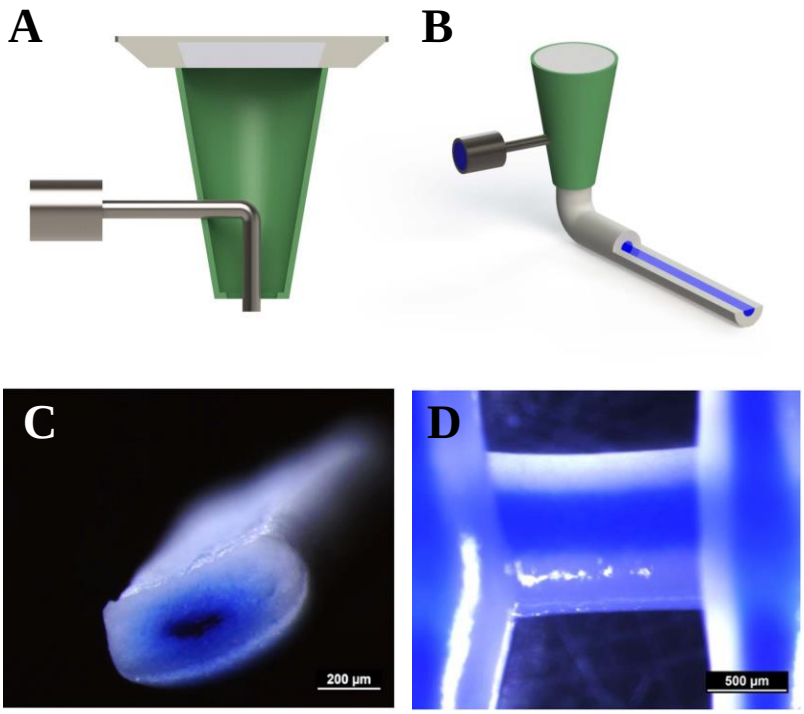

Figure 4.5. Schematic representation of core-shell biopolymer deposition (A-B) with dye-loaded filament (C-D) maintaining core-shell structure following material extrusion. Adapted from Akkineni *et al.*[90]

Tissue scaffolds remain a vital portion of biological applications of 3D printing, however printing controlled release tablets to precisely tune drug therapies emerged as new materials for 3D printing continue to develop. Hydroxypropyl methylcellulose (HPMC) extruded with active ingredients formed controlled-release tablets.[91] A paste of HPMC with the drug guaifenesin produced bilayer tablets capable of controlled release.[91] This emerging aspect of natural polymer material extrusion, along with the traditional

formation of tissue scaffolds, holds tremendous promise for creation of complex AM parts.

4.4.1.2 Synthetic Polymers.

Synthetic polymers offer substantial control over supramolecular interactions and their distribution along the polymer backbone. However, introducing cells onto these novel polymers generates additional unknown factors, such as biocompatibility, cell attachment, and potential cell differentiation. Furthermore, cells must produce ECM rather than embed themselves into an extruded ECM, offering the benefit of a naturally-occurring ECM with the drawback of substantial time required to generate complex tissues (**Figure 4.6**).

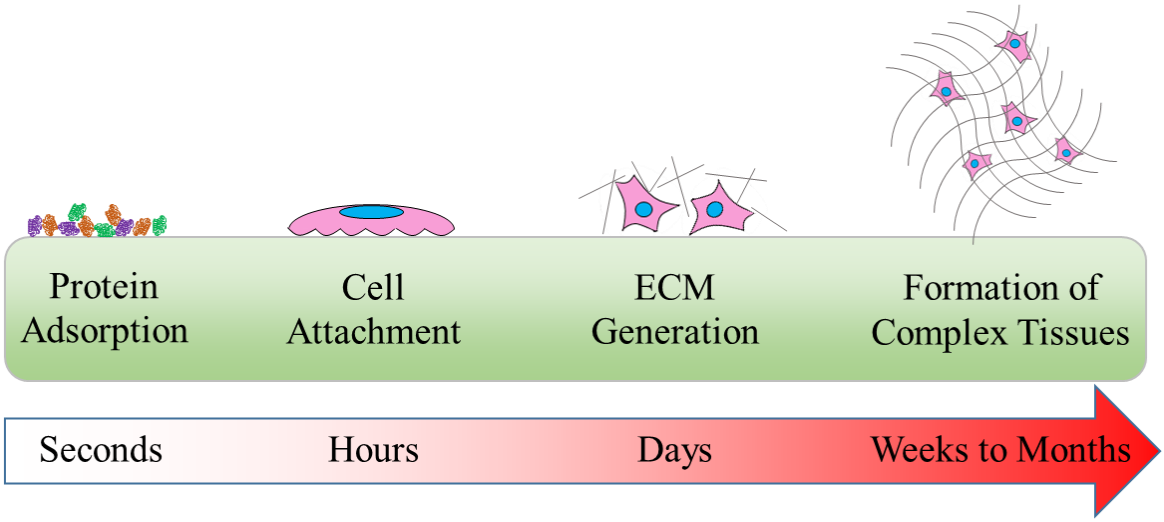

Figure 4.6. Time-scale of interactions with tissue scaffolds. Upon initial immersion into biological media, proteins undergo adsorption to the surface, both specific and non-specific.[92] Cell attachment to the polymer progresses over the course of hours. ECM generation begins within days and progresses to the formation of complex tissues over the course of weeks.[93]

Material extrusion AM of the commercial ion-containing polymer Eudragrit® afforded a wide array of parts for drug delivery applications. Ethyl acrylate, methyl methacrylate, and trimethylammonioethyl methacrylate chloride copolymerized to form Eudagrit®, which possessed a T_g of 63 °C. Pietrzak *et al.* detailed the creation of drug-doped filament and successful extrusion AM to create well-defined tablets, examining the effect of print resolution on dosing and controlled release.[94] Eudragrit® also inspired use as a hot-melt extruded transdermal patch,[95] extruded granules,[96, 97] and floating pellets[98], driving future use to control pharmaceutical release.

The high degree of hydrogen bonding inherent to the urethane bond catalyzes polyurethane use in synthetic supramolecular polymers.[70] Polyurethane resins successfully extruded to create complex parts with favorable surface roughness.[99] The use of shape-memory polymers resulted in parts for robotic mechanisms, resulting in a gripper suitable for grasping fine objects which operates through transition through the polymer's glass transition temperature.[99] PCL-based polyurethane tissue scaffolds provided support for mesenchymal stem cell proliferation and differentiation, as well as released growth factors to induce new cartilage formation.[70, 71]

Tuned supramolecular interactions provide a mechanically robust material compared to polymers with non-specific supramolecular interactions. Chen *et al.* detailed the coextrusion of polyacrylamides containing CB[7] and Ad to form guest-host interactions between polymer chains.[68] Upon mixing, a strong hydrogel formed that exhibited bulk properties and compressive hysteresis.[68] Polyion complexes composed of poly(sodium *p*-styrenesulfonate) (anionic) and poly(3-(methacryloylamino)propyl-trimethylammonium chloride) (cationic), extruded in the presence of saline, demonstrated

the power of ionic interactions to form stiff hydrogels.[100] With the diffusion of counterions out of the printed hydrogel, the polyelectrolytes formed a tough network based solely on supramolecular interactions.[100] While relations between extruded synthetic polymers and biologics are in their infancy, the vast array of potential new polymers for material extrusion AM make it an attractive choice for future investigations.

4.4.1.3 Polymer Blends.

Blends of synthetic and natural polymers often co-extrude to exert control over polymer structure inherent to synthetic polymers, while harnessing the naturally-occurring supramolecular functionality and biocompatibility present on biopolymers. Khaled *et al.* detailed the material extrusion AM of a hydroxyl methylcellulose-poly(acrylic acid) hydrogel for sustained release drug tablets which exhibited enhanced mechanical properties compared to commercially available products.[91] The interactions between the synthetic and natural polymer, tuned through their weight ratios, revealed a low amount of poly(acrylic acid) needed to provide superior mechanical properties.[91] PEG continues to capture the majority of tissue scaffold generation due to its biocompatibility and precedence. PEG-diacrylate coupled with gelatin, agarose, and alginate extruded into a concentrated salt solution to yield distinct scaffolds onto which myoblast cells were seeded.[101] Abbadessa *et al.* co-printed PEG-tetracrylate with CS to yield well-defined, porous structures capable of sustaining chondrogenic cells for at least 6 d.[49] These hydrogels capitalize on the favorable supramolecular properties of biopolymers coupled with the well-known biocompatibility of PEG.

PCL also exhibits favorable biodegradability and biocompatibility, catalyzing its use in tissue engineered scaffolds. UPy-modified PCL and peptides co-printed to create 3D structures with significantly enhanced mechanical and biological properties as compared to either polymer individually.[77] Hydrogen bonding between the two oligomers afforded a structurally sound scaffold upon extrusion which sustained fibroblast viability.[77] Methacrylated poly(hydroxymethylglycolide-co-ε-caprolactone) (poly(MHMGCL)) codeposited with gelatin-methacrylate yielded strong hydrogels with both complex hydrogen bonding and covalent crosslinking.[102] These hydrogels, implanted in rats, sustained chondrocyte viability and promoted collagen production *in vivo*.

Due to its high charge density and facile crosslinking through calcium, alginate in its native form offers an extrudable biopolymer without need for chemical modification. Alginate and PEG-diacrylate coextruded to form mechanically robust hydrogels capable of self-healing, approaching properties of native hydrogel.[103] These self-healing characteristics also enabled layer interactions to form parts that approached mechanical properties of bulk material. Human mesenchymal stem cells embedded in the tissue scaffolds underwent elongation upon hydrogel straining, suggesting strong cellular attachments and the potential to differentiate cells based on elongation.[103] Alginate also extruded alongside *N,N'*-methylenebisacrylamide to form hydrogels crosslinked ionically by calcium chloride and covalently by UV irradiation.[104] Stress-strain behavior of extruded hydrogels tuned with varying ratios of alginate to acrylamide changed the degree of ionic associations to covalent networks to reveal idealized hydrogels.[104]

Nucleic acids are known for their extreme hydrogen bonding capabilities, highlighted through the material extrusion AM of polystyrene or polyacrylamide beads coated with complementary DNA strands.[105] These materials successfully formed well-defined 3D structures without the need for support material or solvent for printing, demonstrating the power of supramolecular interactions in structure formation.[105] Human skin cells seeded onto these colloidal gels maintained viability and exhibited proliferation and colonization within the gel, emphasizing both the mechanical and chemical properties of the resulting hydrogel.[105]

Material extrusion AM offers the ability to employ commercially-available polymers and biopolymers to generate tissue scaffolds of millimeter-scale resolution without the need for extensive chemical modifications. Furthermore, the natural properties of biopolymers act in conjunction with extrusion-based AM due to their high molecular weight and high viscosity. The diversity of supramolecular polymers suitable for material extrusion AM provide a solid foundation for future innovation and tissue scaffold development.

4.4.2 Vat Photopolymerization

Vat photopolymerization revolves around the use of light and a photo-active polymer to create intricate 3D structures. Either a top-down or bottom-up approach coupled with a movable stage and masks or mirrors patterns a specific structure in a layer-by-layer fashion. Control of light intensity, photopolymer characteristics, and photointiator/photoabsorber content catalyzes the creation of fine features, which is well reviewed elsewhere. Biologically-friendly photoinitiators govern biological interactions with 3D tissue scaffolds, with few water-soluble and biologically-compatible

photoinitiators currently in use. Vat photopolymerization affords a number of scaffolds relevant for tissue engineering due to its resolution capabilities, but lacks significant examples of supramolecular polymers.[106, 107]

Traditional vat photopolymerization of PEG incorporated supramolecular and biodegradable functionality with the addition of dipsipeptide, a derivative of L-alanine.[108] Degradation and cell viability measured with depsipepetide-PEG scaffolds revealed that mass loss and cell proliferation occurred simultaneously, indicating a hydrogel supportive of cell growth and complex tissue formation.[108] Lutrol F127, a copolymer of PEG and poly(propylene glycol), modified with dipsipeptide, also successfully printed by vat photopolymerization.[109] The inclusion of dipsipeptide to the copolymers resulted in enhanced cell viability as compared to the copolymer alone, suggesting the importance of depsipeptide in both printing processes and maintenance of cell viability.[109] Highlighting the diversity of PEG in tissue scaffold formation, PEG diacrylate photocrosslinked with chitosan revealed ear-shaped tissue scaffolds with varying porosity which, upon seeding with mesenchymal stem cells, maintained high cell viability.[55]

Hydrogen bonding urethanes facilitate AM of isocyanate-free polyurethane oligomers, which accomplishes gradient structures.[110] Mouse fibroblast cells seeded onto polyurethane scaffolds exhibited high cell viability suggesting potential for future *in vivo* applications.[110] Tissue scaffolds generated with urethane diacrylate sustained bone marrow stromal cells, with enhanced proliferation and metabolic activity than their 2D counterparts, as shown in **Figure 4.6**.[111] Bone marrow stromal cells spread in 3D to completely cover pores generated during vat photopolymerization, facilitating the creation of functional bone tissue.[111] Chung *et al.* reported modification of PEG with

urethane moieties to induce hydrogen bonded, well-defined parts through vat photopolymerization.[79] Cell viability exceeded 75 % for all scaffolds, with the highest viability resulting from higher molecular weight PEG oligomers.[79] End-capping reactions of polyesters also imparted hydrogen bonding to allow successful vat photopolymerization of engineered tissue scaffolds.[112] Hydrogen bonding and ionic interactions coupled through the printing of diurethanedimethacrylate, glycerol dimethacrylate, and quaternary ammonium-modified methacrylates formed semi-interpenetrating networks.[113] This system not only exhibited superior anti-microbial activity, but also provided a facile system to introduce hydrogen-bonding into the AM part.[113]

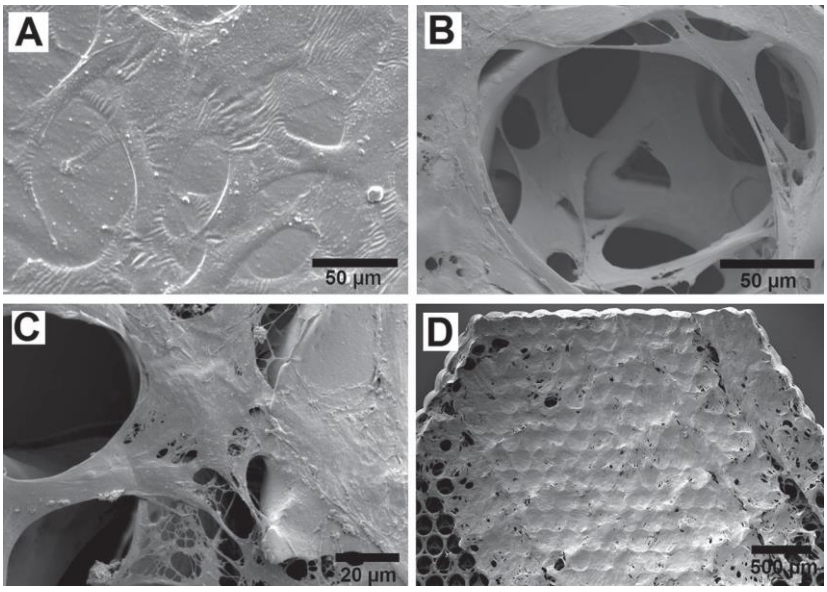

Figure 4.6. Bone marrow stromal cells exhibit 3D growth (a-c) and differentiation (d) upon seeding into urethane diacrylate tissue scaffolds printed with vat photopolymerization. Adapted from Petrochenko *et al.*[111]

Natural polymers leverage a large portion of the vat photopolymerization printing for biological applications due to their expected cell affinities and established chemistries used to modify their complex structures. HA in particular experiences widespread use in printing cell scaffolds from vat photopolymerization.[41, 114, 115] Chitosan co-printed with PEG-diacrylate yielded ear-shaped scaffolds suitable for chondrocyte culturing.[55] Both high and low molecular weight charged chitosan and varied ratios of PEG-diacrylate enabled successful vat photopolymerization to form porous, complex scaffolds.[55] Supramolecular biomaterials also include deoxyribonucleic acid (DNA) and proteins, which formed 3D structures containing photo-crosslinked DNA through vat photopolymerization.[116] Bovine serum albumin, DNA, and gelatin printed both with two-photon microfabrication and vat photopolymerization to produce precise structures.[116] Photo-crosslinkable keratin hydrogels synthesized by vat photopolymerization revealed the maintenance of fibroblast viability, expanding the collection of biopolymers created with this approach.[117]

Hydrogels synthetized using water-soluble, biocompatible photoinitiators drive the future of vat photopolymerization for biologically-relevant scaffolds. Pawar *et al.* synthesized water-soluble nanoparticles containing photoinitiator to print aqueous acrylamide solutions with high resolution when co-printed with PEG-diacrylate.[118] These scaffolds sustained cell viability and contained ~80 % water, previously unachievable due to the lack of water-soluble photoinitiators.[118] Vat photopolymerization research thrusts, both in the area of water-soluble photoinitiators and supramolecular oligomers, stimulates the generation of increasingly complex tissue scaffolds with enhanced resolution as compared to its AM counterparts.

4.4.3 Bioprinting

Bioprinting involves AM of a cell-laden polymer solution by either microextrusion, inkjet printing, or laser-assisted printing, which often blurs the lines between traditional AM techniques and bioprinting.[119, 120] These types of printing are well reviewed elsewhere.[31] Briefly, microextrusion bioprinting revolves around the syringe deposition of cell-laden material. Inkjet involves the deposition of droplets onto a surface to create a 3D-structured object. Laser-assisted deposition utilizes a laser pulse to transfer material containing cells onto a substrate. In each of these techniques, cells undergo the printing process, necessitating a biological ink that sustains cell viability throughout the print as well as provides structural integrity suitable for a particular biological application.[121-123]

Cartilage and cartilage-forming cells (chondrocytes) often find widespread use in the field of tissue engineering due to their ease of handling and resiliency towards modified biopolymers and synthetic polymers. Chondrocytes also induce the formation of complex ECM structures, easing characterization of healthy cell-laden tissue scaffolds.[82] Dextran-HA hydrogels formed through microextrusion and subsequent photocuring yielded semi-interpenetrating network scaffolds suitable for cartilage tissue engineering.[52] Precise control of printing parameters and hydrogel swelling evaluated for a number of hydrogel compositions all sustained chondrocyte viability.[52] Thermally-sensitive poly(HPMAm-lactate)-PEG hydrogels printed in a similar fashion yielded hydrogels structured through hydrophobic interactions arising from the microstructure of the triblock copolymer.[69] Encapsulated chondrocytes maintained viability throughout the printing process to produce well-defined structures possessing precise control of cell

localization.[69] Chondrocyte-laden methacrylated and acetylated gelatin solutions underwent inkjet printing to impart well-defined droplets on pre-formed gelatin hydrogels.[64] These inks sustained cell viability despite the degree of functionality of gelatin and varying incubation times (up to 240 min) prior to printing, indicating the ability of gelatin inks to afford complex tissue scaffolds with high cell viability.[64]

Stem cells specifically differentiate into varied daughter cells based on their chemical and physical environment. Based on the stem cell origin, differentiated cells could manifest as a wide variety of cell types, adding a layer of complexity to the printing process to prevent stem cell differentiation. Supramolecular microextrusion bioprinting accomplished with PCL, atelocollagen, and modified hyaluronic acid yielded 3D structured scaffolds embedded with turbinate-derived mesenchymal stromal cells for osteochondral tissue regeneration.[47] These multi-material scaffolds successfully promoted cartilage generation in a rabbit knee joint and paved the way for future multi-material printing without the need for harmful crosslinking agents.[47]

Inkjet bioprinting with mesenchymal stem cell-laden methacrylated gelatin accomplished by Gurkan *et al.* formed anisotropic fibrocartilage.[124] To closely mimic the transition between tendon and bone, gelatin droplets containing cells and one of two growth factors deposited side-by-side to produce a complex tissue geometry containing a biochemical gradient suitable for personalized medicine and new drug therapy testing.[124] Supramolecular interactions derived from peptides enhanced both function and cell viability of inkjet-printed PEG-diacrylate to form mesenchymal stem cell-laden hydrogels.[125] Gao *et al.* described stem cell differentiation, subsequent production of cartilage, and detailed the ability of bioprinting to produce homogenous, cell-laden

scaffolds.[125] While these examples highlight the use of bioprinting to generate non-vascular tissues, the use of stem cells to derive differentiated tissues with specific phenotypes will drive future work in synthetic tissue engineering.

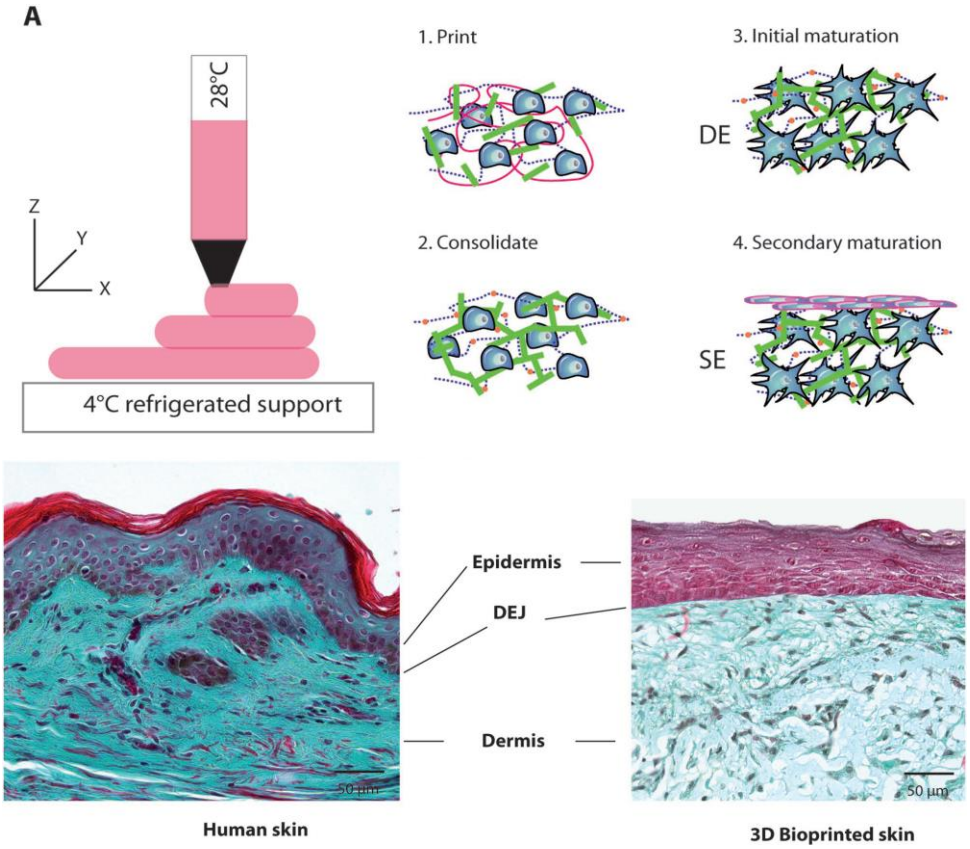

Figure 4.7. A. Schematic representation of skin tissue printing, growth, and maturation upon 3D printing with natural ECM. B. Following 26 d incubation, synthetic skin mimicked healthy human donor skin, revealing a bioprinting route to functional, synthetic skin. Adapted from Pourchet *et al.*[126]

Multi-material and multi-cell bioprinting carries the ability to achieve complex scaffolds that closely mimic native tissues and organs. Gelatin served as an effective biopolymer for bioink AM, especially when mixed with other natural (collagen, fibrinogen) or synthetic (PEG amine) macromolecules to enhance physical properties of

the resulting 3D printed part.[63] Multi-material printing controlled both the bioactivity of human dermal fibroblasts as well as the structural characteristics of the 3D printed part to allow for diverse tissue scaffold properties as a function of polymer blend.[63] Complex skin tissue formed through inkjet bioprinting of fibroblast and keratinocyte-containing bioinks composed of alginate and EDTA.[127] Precise control of layered structures varying between fibroblast and keratinocyte-laden inks successfully afforded functional skin tissue.[127] Pourchet *et al.* detailed the creation of functional human skin that mimics healthy donor tissue following culture for 26 d, as shown in **Figure 4.7**. Engineering synthetic neurons remains the pinnacle of avascular tissue engineering due to the complexity and sensitivity of neuronal cells. Lozano *et al.* detailed the microextrusion bioprinting of modified gellan gum with and without cortical neurons, producing a layered structure capable of maintaining cell viability.[54] Interestingly, the neurons remodeled and infiltrated the neighboring layers, suggesting not only an enhancement of cell activity but also the reversible ionic physical crosslinks.[54] While avascular tissue engineering limits the complexity needed in scaffolds, the cell types and potential supramolecular polymer utilization requires precise control for the creation of biologically-mimicking scaffolds.

Scaffolds of complex metabolic function capable of examining drug discovery and disease states require printing of complex cells types and the subsequent generation of characteristic phenotypes. Gelatin, alginate, and fibronigen mixtures microextruded with adipose-derived cells yielded scaffolds with high porosity capable of supporting cell viability.[128] After introducing pancreatic islets to the scaffolds, characterization of insulin release rate as a function of glucose concentration afforded a complex tissue scaffold

suitable for disease examination and drug discovery (**Figure 4.8**).[128] Gelatin methacrylate printed via microextrusion followed by UV irradiation afforded porous tissue scaffolds laden with hepatocytes for synthetic liver tissue.[129] Localization of the cells and the effect of nozzle types probed cell viability and hydrogel fidelity, forging the way for future studies to examine drug metabolism.[129] Complex biological tissues generated through microextrusion bioprinting to yield renal proximal tubules results in the accomplishment of biologically-active renal structures.[130] Casting fibroblast-laden gelatin and fibrinogen ECM along with microextrusion of sacrificial Pluronic F127 formed complex tubule structures.[130] Perfusion with renal cells yielded a polarized epithelium mimicking natural renal structures, vital to the development of *in vitro* models to evaluate drug meatbolism.[130] While significant research revealed the generation of metabolically-active tissue *in vitro,* the full utilization of synthetic tissue scaffolds for drug metabolism and disease characterization remain unexplored.

Generating vascularized tissues adds additional complications to the printing process, but affords scaffolds with increasing complexity to better mimic native tissues.[131] Skardal *et al.* discussed the ability of thiolated-HA and PEG of varying topology to form hydrogels and successfully microextrude cell-containing filaments.[45] Following deposition of high-viscosity filaments of HA-PEG and agarose into vessel-containing hydrogels, cellular activity remained for up to 4 weeks.[45] Furthermore, harnessing base crosslinking (NaOH) to form hydrogels prior to microextrusion bioprinting eliminated the use of harmful UV radiation and photoinitiator.[45] Laser-assisted transfer of cell-laden droplets to form complex vessel-like structures yielded high-density tissue scaffolds, which required low concentrations of alginate to produce

successful prints.[132] A high concentration of cells (6 x 10^7 cells/mL) printed onto a fibrinogen gel substrate facilitated well-defined areas of cells of high density and viability.[132] Even the high density of cells printed in this system required the addition of small amounts of supramolecular alginate to form well-defined structures. Vascularized liver tissue, involving AM of hepatocytes and endothelial cells together, drives the generation of functional, engineered tissue for liver regeneration.[133] The inclusion of fibroblasts into the tissue scaffold proved essential for albumin secretion and urea production, facilitating future design of multi-cell tissue scaffolds for biomimetic tissues.[133] The generation of vascularized tissues stimulates additional complexity for organ regeneration and tissue regeneration, many aspects of which remain unexplored.

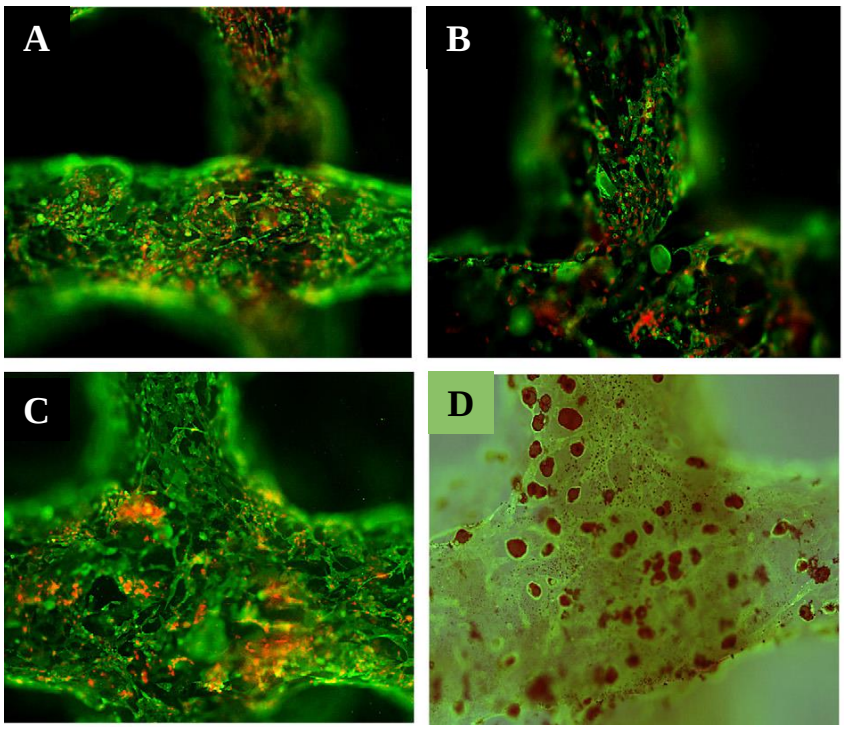

Figure 4.8. Adipocyte stem cell and endothelial cell bioprinting retained viability immediately following printing (green: CD34+, red: PI; A-B). Maturation of endothelial cells (C, green: CD31+, red: PI) cultured with epidermal growth factor. Adipocytes matured following treatment with insulin, IBMX, and dexamethasone (D, green: CD31+, red: Oil red O). Adapted from Xu *et al.*[128]

The most complex of all vascularized tissues include the heart, lungs, and cardiovascular systems, which require every type of cell from muscle to endothelial to generate functional organs. Gelatin and alginate biopolymers laden with aortic valve interstitial and smooth muscle cells afforded a complex *in vitro* model of the aortic valve.[134] Microextrusion bioprinting of these two cell types into specifically patterned regions of an aortic valve model resulted in expression of biomarkers in location-specific regions of the scaffold, as seen in **Figure 4.9**.[134] Similar scaffolds synthesized with PEG-diacrylate and alginate also yielded sophisticated aortic valve structures.[135] Bioprinting with complex cell types to form complex scaffolds closely mimicked native biological tissue and afforded high-fidelity models to examine normal and disease-state tissues.

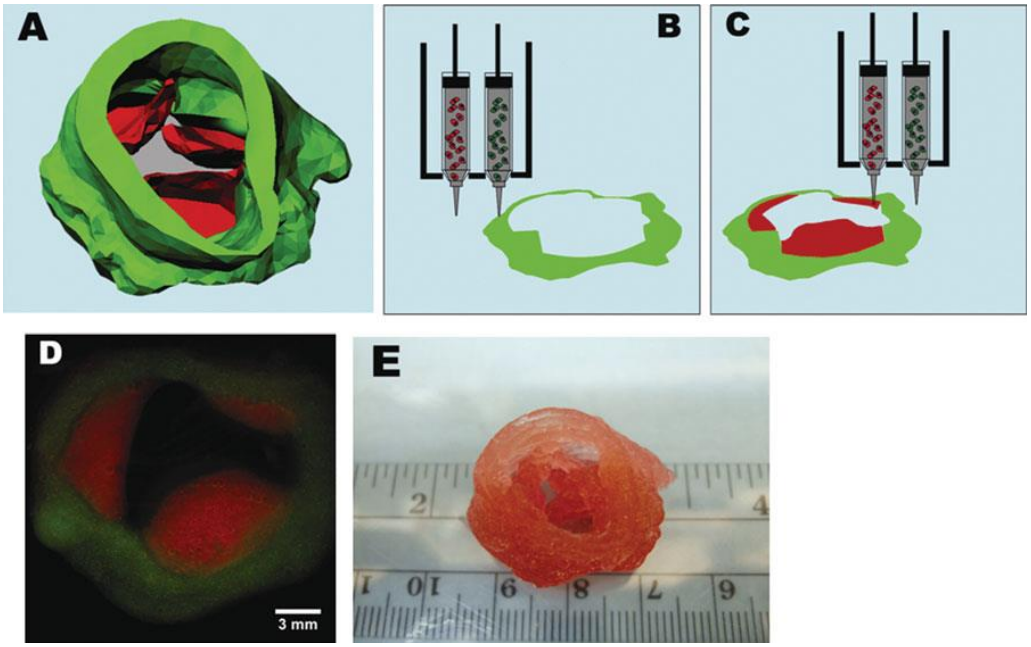

Figure 4.9. Aortic valve conduit bioprinting from micro-CT image (A) with both aortic valve root cells (B) and leaflet cells (C). D, E Fluorescence imaging revealed maintenance of conduit structure, with overall structure size mimicking that of native tissue. Adapted from Duan *et al.*[134]

Bioprinting necessitates the maintenance of cell viability throughout the printing process, which introduces a complex factor to successful AM. Factors such as time of print, cell concentration, oxygen diffusion, and temperature affect both the printing process as well as the viability of the cell.[123, 136] As an example, cell viability is maintained for longer times at reduced temperature, but the viscosity of cell-laden polymer solutions increases at lower temperatures, potentially hindering the printing process.[37, 136] The inclusion of these additional parameters makes printing challenging, but the resulting homogenous tissue scaffold avoids many problems faced in traditional AM of tissue scaffolds, such as cell gradients and diffusion-limited cell seeding.[123] A number of synthetic and natural polymers with their cellular counterparts exist currently (**Table 4.1**), providing a platform for future complex tissue generation through bioprinting.

Table 4.1. Bioprinting affords complex tissue generation utilizing both common cell types and increasingly complex cells.

Supramolecular Polymers for 3D Bioprinting				
Cell Type	**Printing Type**	**Polymer Base**	**Cell Concentration**	**References**
Structural Tissues				
Skin (Fibroblasts, Epidermal)	Microextrusion	Gelatin, PEG	2×10^6	63
		Agarose, PEG, HA	2.5×10^7	45
		PEG, amino acid-acrylic acid	-	73, 74
		Gelatin, Alginate, Fibrinogen	1×10^6	126
		Fibrinogen	7×10^4, 6×10^6	137
		Gelatin	5×10^6	138
		Gelatin, Alginate	-	139
	Inkjet	Alginate, EDTA blood plasma	3.33×10^7	127
		Alginate, Gelatin	1×10^6	140
Chondrocytes	Microextrusion	Poly(HPMAm-lactate)-PEG	5×10^6	69
		HA, dextran	5×10^6	52
		Gelatin, Gellan Gum	$1\text{-}2 \times 10^7$	82
		HA-poly(NIPAAM)	6×10^6	141
		Polyethyleneimine, Alginate	5×10^6	142
		Fibrinogen, Gelatin, HA	4×10^7	143
		Alginate, PCL	1×10^6	144
		HA, CS, Poly(HPMAm-lactate)-PEG	$1.5\text{-}2 \times 10^7$	145
	Inkjet	Gelatin	1×10^6	64
Stem Cells				
Mesenchymal Stem Cells	Inkjet	Gelatin	1×10^6	124
		PEG, Polypeptide	6×10^6	125
	Microextrusion	HA	5×10^6	44
		Gelatin	5×10^5	146
			5×10^6	138
		Collagen, Gelatin	-	147
		Fibrinogen, Gelatin	$0.1\text{-}10 \times 10^6$	148
		Collagen, Alginate, Gelatin	2×10^6	149
		Gelatin, HA, CS	1.5×10^7	50
		Gelatin, Alginate, Chitosan	2×10^6	150
		Silk Fibroin, Gelatin	$2\text{-}5 \times 10^6$	151

	Vat Photopolymerization	Gelatin	5×10^6	[152]
Embryonic Stem Cells	Microextrusion	Gelatin, Alginate	1×10^6	[153]
Adipose Stem Cells	Microextrusion	Gelatin, Alginate, Fibrinogen	3×10^7	[128]
			1×10^6	[154]
		Alginate	1×10^6	[121]
		Alginate, Gelatin	3×10^6	[155]
		Collagen	1×10^6	[156]
Glioma Stem Cell	Microextrusion	Fibrinogen, Gelatin, Alginate	5×10^5	[157]
Amniotic Fluid-Derived Stem Cells	Microextrusion	Gelatin, Fibrinogen, HA	5×10^6	[143]
Avascular Tissues				
Neuron	Microextrusion	Gellan Gum	1×10^6	[54]
		Fibrinogen, HA	2×10^5	[158]
		Alginate	5×10^5	[159]
		Agarose, Alginate, Chitosan	1×10^7	[160]
Myoblast	Microextrusion	Fibrinogen, Gelatin, HA	3×10^6	[143]
Anterior Pituitary	Inkjet	Polypeptide, DNA	-	[161]
Metabolic Tissues				
Kidney	Microextrusion	Gelatin, PEO	5×10^6	[162]
		Gelatin, Alginate	2×10^6	[163]
Urethra	Inkjet	Fibrinogen, Gelatin, HA	1×10^7	[164]
Hepatocytes	Microextrusion	Gelatin	1.5×10^6	[129]
		Collagen	$0.2 – 1 \times 10^6$	[133]
		Gelatin, Alginate, Fibrinogen	1×10^7	[154]
Vascular Tissues				
Endothelial Cells	Laser-assisted	Alginate, Matrigel	5×10^7	[132]
	Microextrusion	Gelatin, PEG	5×10^6	[162]
		Fibrinogen	2×10^5	[165]
		Collagen	2×10^5	[133]
		Alginate, Gelatin	5×10^5	[90]
Aortic Valve	Microextrusion	Gelatin, Alginate	2×10^6	[134]
Cardiac Cells	Microextrusion	Gelatin, HA	3×10^7	[166]
Lung Fibroblast	Microextrusion	Collagen	$6\text{-}7.5 \times 10^5$	[133]

4.5 Effect of Supramolecular Polymers on Anisotropy

Improving anisotropy drives supramolecular AM research, which stems from a desire to create isotropic parts for final use (**Figure 4.10**). AM without supramolecular interactions generates distinct layers with a defined interface, often the weak point in the part. One method to aid in achieving material isotropy revolves around forming interpenetrating networks, where multiple supramolecular interactions or a combination of supramolecular interactions and chemical crosslinking act in parallel to form stiff networks. Wei *et al.* explored this idea through agar, polyacrylamide, and alginate in concert to form tough hydrogels.[167] Initially, the AM structure demanded hydrogen bonding interactions prevalent in the agar, followed by chemical crosslinking of the acrylamide monomers to form polyacrylamide networks. Furthermore, soaking the hydrogel in calcium chloride solution induced physical crosslinking of the alginate through electrostatic interactions.[167] Following ink-based printing and subsequent photo-crosslinking, Abbadessa *et al.* revealed an enhancement of mechanical properties upon the inclusion of both CS-methacrylate and triblock copolymer together, suggesting the presence of an interpenetrating network.[49]

Nature perfected the use supramolecular interactions to form complex structures that have both programmed anisotropy and isotropy specific to tissue types. Harnessing the power of nature, supramolecular interactions due to complementary DNA strands mended hydrogel layers in well-defined tissue scaffolds generated from inkjet bioprinting.[161] The use of polypeptides and DNA forms isotropic hydrogels with suitable mechanical integrity to sustain cell viability.[161] Combinations of natural polymers to form polyelectrolyte hydrogel scaffolds also approach properties of bulk materials. Gelatin and

chitosan combined to form extrudable polyelectrolyte hydrogels capable of sustaining skin fibroblast viability, interacting between layers to form a homogenous scaffold.[56]

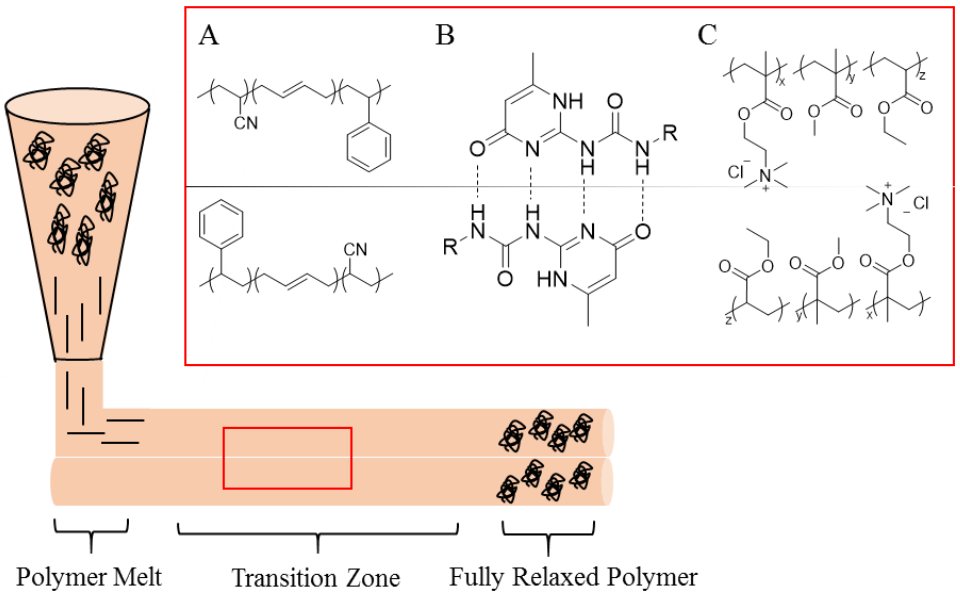

Figure 4.10. Effect of supramolecular polymers on anisotropy depends on the type of interaction that can occur between layers. Extrudable polymers with no supramolecular interactions, such as ABS (A) do not interact across the layers. Hydrogen bonding (B) or ionic associating (C) polymers have the ability to interact across boundaries to improve interfacial adhesion.

Zhu *et al.* described polyion hydrogels which approach tensile properties of the bulk material, suggesting the power of ionic interactions to maintain structure of the hydrogel.[100] Furthermore, these polyion complexes exhibited hysteresis, highlighting the polymers' ability to re-form ionic interactions after an applied load.[100] Additionally, this self-healing behavior along with comparable mechanical properties suggested isotropic behavior while offering the ability to precisely define 3D structure. The introduction of water into printed structures also imparts significant mobility to polymer chains, aiding in the formation of supramolecular interactions across layers.

4.6 Printing Hierarchical Structures

Biological tissues possess well-characterized hierarchy, with many built-in layers of structure on the molecular, cell, tissue, and organ level to create functional materials.[11, 38, 168] The role of designing hierarchical structures for improved mechanical properties as compared to bulk materials currently revolutionizes AM and its role in both biomedical materials and structural materials.[169] Currently, hierarchy imparted onto microfluidic structures printed with PEG diacrylate yielded high-fidelity parts that exhibit fluid mixing.[152] Mimicking the hierarchy of nature provides a structure with the capability to recreate tissues for use in biomedical applications such as organ replacement, drug discovery and delivery, and structural support materials.[170, 171]

Polyaniline demonstrated the potential to form these hierarchical structures through its crosslinked sheets. Dou *et al.* detailed the crosslinking of polyaniline with amino trimethylene phosphonic acid (ATMP) which acted to hold sheets of polyaniline in place during the extrusion AM process.[172] Furthermore, the structures produced were porous, which added a third level of complexity to the system, generating structure on the molecular, macromolecular, and feature scale.[172]

Nature is unmatched in the creation of hierarchical structures. Harnessing natural supramolecular materials to generate complex features starts to probe structures that closely mimic tissues and organs. Harnessing the ability of peptides to self-assemble into sheets and filaments, scaffolds with hierarchical structure effectively extruded to create both droplets and sheets (**Figure 4.11**).[173] The tiered nature of these scaffolds successfully cultured a variety of stem cell types as well as complex intestinal cells, highlighting the importance of hierarchical structures to *in vitro* cell and tissue

viability.[173] As tissue engineering moves towards more complex synthetic scaffolds, the introduction of hierarchical structure will provide biologically-robust hydrogels capable of mimicking complex natural tissues. With more biologically-sound synthetic hydrogels, the fields of synthetic organ replacement and disease characterization will progress rapidly.

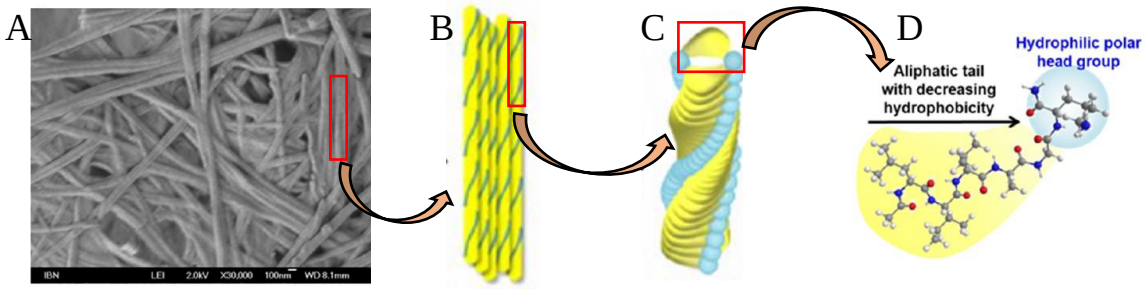

Figure 4.11. Hierarchical printing of peptide-based scaffolds. Scaffold structure (A) showing fibers which are composed of many β-sheets (B). β-sheets are then composed of a number of α-helices (C). α-helices are formed from short peptide sequences (D) designed for self-assembly. Adapted from Loo *et al.*[173]

4.7 Future Directions and Conclusions

Supramolecular polymers remain an emerging field of research, both in the creation of novel materials and the development of biologically-relevant scaffolds. Traditional tissue scaffolds suffer either from well-defined structure lacking fine features detectable by cells or supramolecular interactions that fail to provide well-defined structures. The combination of AM and supramolecular chemistry has the potential to develop hierarchical structures with levels of order spanning the entire sensing breadth of cells and creating synthetic tissues capable of mimicking native human tissues. Conquering these ideas will drive the future of tissue engineering research and translation to the creation of synthetically grown organs suitable for transplant into humans.

References

1. Aida, T.; Meijer, E. W.; Stupp, S. I., Functional Supramolecular Polymers. *Science* **2012,** 335, (6070), 813-817.
2. Brunsveld, L.; Folmer, B.; Meijer, E.; Sijbesma, R., Supramolecular polymers. *Chemical Reviews* **2001,** 101, (12), 4071-4098.
3. Faul, C. F.; Antonietti, M., Ionic self-assembly: Facile synthesis of supramolecular materials. *Advanced Materials* **2003,** 15, (9), 673-683.
4. Li, S.-L.; Xiao, T.; Lin, C.; Wang, L., Advanced supramolecular polymers constructed by orthogonal self-assembly. *Chemical Society Reviews* **2012,** 41, (18), 5950-5968.
5. Johnson, E. R.; Keinan, S.; Mori-Sanchez, P.; Contreras-Garcia, J.; Cohen, A. J.; Yang, W., Revealing noncovalent interactions. *Journal of the American Chemical Society* **2010,** 132, (18), 6498-6506.
6. Khademhosseini, A.; Langer, R., Microengineered hydrogels for tissue engineering. *Biomaterials* **2007,** 28, (34), 5087-5092.
7. Lutolf, M.; Hubbell, J., Synthetic biomaterials as instructive extracellular microenvironments for morphogenesis in tissue engineering. *Nature biotechnology* **2005,** 23, (1), 47-55.
8. Kaur, S.; Sandhu, S.; Dhillon, S. K.; Makhni, S. K., TISSUE ENGINEERING AND ITS FUTURE PERSPECTIVE IN THERAPEUTIC MEDICINE-A BRIEF REVIEW. *Journal of Advanced Medical and Dental Sciences Research* **2016,** 4, (4), 159.
9. Yang, S.; Leong, K.-F.; Du, Z.; Chua, C.-K., The design of scaffolds for use in tissue engineering. Part II. Rapid prototyping techniques. *Tissue engineering* **2002,** 8, (1), 1-11.
10. Sears, N.; Dhavalikar, P.; Seshadri, D.; Cosgriff-Hernandez, E., A Review of 3D Printing of Tissue Engineering Constructs. *Tissue engineering. Part B, Reviews* **2016**.
11. Guven, S.; Chen, P.; Inci, F.; Tasoglu, S.; Erkmen, B.; Demirci, U., Multiscale assembly for tissue engineering and regenerative medicine. *Trends in Biotechnology* **2015,** 33, (5), 269-279.
12. Lengalova, A.; Vesel, A.; Feng, Y.; Sencadas, V., Biodegradable Polymers for Medical Applications. *International Journal of Polymer Science* **2016**.
13. Hubbell, J. A., Biomaterials in tissue engineering. *Bio/technology (Nature Publishing Company)* **1995,** 13, (6), 565-576.
14. Gunatillake, P. A.; Adhikari, R., Biodegradable synthetic polymers for tissue engineering. *Eur Cell Mater* **2003,** 5, (1), 1-16.
15. Hutmacher, D. W., Scaffolds in tissue engineering bone and cartilage. *Biomaterials* **2000,** 21, (24), 2529-2543.
16. Makris, E. A.; Gomoll, A. H.; Malizos, K. N.; Hu, J. C.; Athanasiou, K. A., Repair and tissue engineering techniques for articular cartilage. *Nature Reviews Rheumatology* **2015,** 11, (1), 21-34.
17. Liu, X.; Ma, P. X., Polymeric Scaffolds for Bone Tissue Engineering. *Annals of Biomedical Engineering* **2004,** 32, (3), 477-486.
18. Yin, X.; Mead, B. E.; Safaee, H.; Langer, R.; Karp, J. M.; Levy, O., Engineering Stem Cell Organoids. *Cell stem cell* **2016,** 18, (1), 25-38.

19. Vogel, V.; Sheetz, M., Local force and geometry sensing regulate cell functions. *Nature reviews Molecular cell biology* **2006,** 7, (4), 265-275.
20. Van Vlierberghe, S.; Dubruel, P.; Schacht, E., Biopolymer-based hydrogels as scaffolds for tissue engineering applications: a review. *Biomacromolecules* **2011,** 12, (5), 1387-1408.
21. Lewis, P. L.; Shah, R. N., 3D Printing for Liver Tissue Engineering: Current Approaches and Future Challenges. *Current Transplantation Reports* **2016,** 3, (1), 100-108.
22. Gilmour, A.; Woolley, A.; Poole-Warren, L.; Thomson, C.; Green, R., A critical review of cell culture strategies for modelling intracortical brain implant material reactions. *Biomaterials* **2016,** 91, 23-43.
23. Rouwkema, J.; Khademhosseini, A., Vascularization and angiogenesis in tissue engineering: beyond creating static networks. *Trends in biotechnology* **2016**.
24. Ogle, B. M.; Bursac, N.; Domian, I.; Huang, N. F.; Menasché, P.; Murry, C. E.; Pruitt, B.; Radisic, M.; Wu, J. C.; Wu, S. M., Distilling complexity to advance cardiac tissue engineering. *Science Translational Medicine* **2016,** 8, (342), 342ps13-342ps13.
25. Griffith, L. G.; Naughton, G., Tissue engineering--current challenges and expanding opportunities. *Science* **2002,** 295, (5557), 1009-1014.
26. Wobma, H.; Vunjak-Novakovic, G., Tissue engineering and regenerative medicine 2015: a year in review. *Tissue Engineering Part B: Reviews* **2016,** 22, (2), 101-113.
27. Do, A. V.; Khorsand, B.; Geary, S. M.; Salem, A. K., 3D printing of scaffolds for tissue regeneration applications. *Advanced healthcare materials* **2015,** 4, (12), 1742-1762.
28. Guvendiren, M.; Molde, J.; Soares, R. M. D.; Kohn, J., Designing Biomaterials for 3D Printing. *ACS Biomaterials Science & Engineering* **2016**.
29. Studart, A. R., Additive manufacturing of biologically-inspired materials. *Chemical Society Reviews* **2016,** 45, (2), 359-376.
30. Stansbury, J. W.; Idacavage, M. J., 3D printing with polymers: Challenges among expanding options and opportunities. *Dental Materials* **2016,** 32, (1), 54-64.
31. Murphy, S. V.; Atala, A., 3D bioprinting of tissues and organs. *Nat Biotech* **2014,** 32, (8), 773-785.
32. Lim, J. Y.; Donahue, H. J., Cell sensing and response to micro-and nanostructured surfaces produced by chemical and topographic patterning. *Tissue engineering* **2007,** 13, (8), 1879-1891.
33. Migler, K., Polymer Additive Manufacturing and Rheology. **2016**.
34. Jose, R. R.; Rodriguez, M. J.; Dixon, T. A.; Omenetto, F.; Kaplan, D. L., Evolution of Bioinks and Additive Manufacturing Technologies for 3D Bioprinting. *ACS Biomaterials Science & Engineering* **2016**.
35. Tang, D.; Tare, R. S.; Yang, L.-Y.; Williams, D. F.; Ou, K.-L.; Oreffo, R. O. C., Biofabrication of bone tissue: approaches, challenges and translation for bone regeneration. *Biomaterials* **2016,** 83, 363-382.
36. Carrow, J. K.; Gaharwar, A. K., Bioinspired Polymeric Nanocomposites for Regenerative Medicine. *Macromolecular Chemistry and Physics* **2015,** 216, (3), 248-264.
37. Kumar, A.; Mandal, S.; Barui, S.; Vasireddi, R.; Gbureck, U.; Gelinsky, M.; Basu, B., Low temperature additive manufacturing of three dimensional scaffolds for

bone-tissue engineering applications: Processing related challenges and property assessment. *Materials Science and Engineering: R: Reports* **2016,** 103, 1-39.
38. Webber, M. J.; Appel, E. A.; Meijer, E.; Langer, R., Supramolecular biomaterials. *Nature materials* **2016,** 15, (1), 13-26.
39. Radhakrishnan, J.; Subramanian, A.; Krishnan, U. M.; Sethuraman, S., Injectable and 3D Bioprinted Polysaccharide Hydrogels: From Cartilage to Osteochondral Tissue Engineering. *Biomacromolecules* **2016**.
40. Necas, J.; Bartosikova, L.; Brauner, P.; Kolar, J., Hyaluronic acid (hyaluronan): a review. *Veterinarni medicina* **2008,** 53, (8), 397-411.
41. Collins, M. N.; Birkinshaw, C., Hyaluronic acid based scaffolds for tissue engineering—A review. *Carbohydrate Polymers* **2013,** 92, (2), 1262-1279.
42. Smeds, K. A.; Grinstaff, M. W., Photocrosslinkable polysaccharides for in situ hydrogel formation. *Journal of biomedical materials research* **2001,** 54, (1), 115-121.
43. Ouyang, L.; Highley, C. B.; Rodell, C. B.; Sun, W.; Burdick, J. A., 3D Printing of Shear-Thinning Hyaluronic Acid Hydrogels with Secondary Cross-Linking. *ACS Biomaterials Science & Engineering* **2016**.
44. Highley, C. B.; Rodell, C. B.; Burdick, J. A., Direct 3D Printing of Shear-Thinning Hydrogels into Self-Healing Hydrogels. *Advanced Materials* **2015,** 27, (34), 5075-5079.
45. Skardal, A.; Zhang, J.; Prestwich, G. D., Bioprinting vessel-like constructs using hyaluronan hydrogels crosslinked with tetrahedral polyethylene glycol tetracrylates. *Biomaterials* **2010,** 31, (24), 6173-6181.
46. Jung, H.; Park, J. S.; Yeom, J.; Selvapalam, N.; Park, K. M.; Oh, K.; Yang, J.-A.; Park, K. H.; Hahn, S. K.; Kim, K., 3D Tissue Engineered Supramolecular Hydrogels for Controlled Chondrogenesis of Human Mesenchymal Stem Cells. *Biomacromolecules* **2014,** 15, (3), 707-714.
47. Shim, J.-H.; Jang, K.-M.; Hahn, S. K.; Park, J. Y.; Jung, H.; Oh, K.; Park, K. M.; Yeom, J.; Park, S. H.; Kim, S. W., Three-dimensional bioprinting of multilayered constructs containing human mesenchymal stromal cells for osteochondral tissue regeneration in the rabbit knee joint. *Biofabrication* **2016,** 8, (1), 014102.
48. Wang, D.-A.; Varghese, S.; Sharma, B.; Strehin, I.; Fermanian, S.; Gorham, J.; Fairbrother, D. H.; Cascio, B.; Elisseeff, J. H., Multifunctional chondroitin sulphate for cartilage tissue–biomaterial integration. *Nature materials* **2007,** 6, (5), 385-392.
49. Abbadessa, A.; Blokzijl, M.; Mouser, V.; Marica, P.; Malda, J.; Hennink, W.; Vermonden, T., A thermo-responsive and photo-polymerizable chondroitin sulfate-based hydrogel for 3D printing applications. *Carbohydrate polymers* **2016,** 149, 163-174.
50. Costantini, M.; Idaszek, J.; Szöke, K.; Jaroszewicz, J.; Dentini, M.; Barbetta, A.; Brinchmann, J. E.; Święszkowski, W., 3D bioprinting of BM-MSCs-loaded ECM biomimetic hydrogels for in vitro neocartilage formation. *Biofabrication* **2016,** 8, (3), 035002.
51. Sun, G.; Shen, Y.-I.; Ho, C. C.; Kusuma, S.; Gerecht, S., Functional groups affect physical and biological properties of dextran-based hydrogels. *Journal of Biomedical Materials Research Part A* **2010,** 93A, (3), 1080-1090.
52. Pescosolido, L.; Schuurman, W.; Malda, J.; Matricardi, P.; Alhaique, F.; Coviello, T.; van Weeren, P. R.; Dhert, W. J.; Hennink, W. E.; Vermonden, T., Hyaluronic acid

and dextran-based semi-IPN hydrogels as biomaterials for bioprinting. *Biomacromolecules* **2011,** 12, (5), 1831-1838.
53. Grasdalen, H.; Smidsrød, O., Gelation of gellan gum. *Carbohydrate Polymers* **1987,** 7, (5), 371-393.
54. Lozano, R.; Stevens, L.; Thompson, B. C.; Gilmore, K. J.; Gorkin, R.; Stewart, E. M.; in het Panhuis, M.; Romero-Ortega, M.; Wallace, G. G., 3D printing of layered brain-like structures using peptide modified gellan gum substrates. *Biomaterials* **2015,** 67, 264-273.
55. Morris, V. B.; Nimbalkar, S.; Younesi, M.; McClellan, P.; Akkus, O., Mechanical Properties, Cytocompatibility and Manufacturability of Chitosan:PEGDA Hybrid-Gel Scaffolds by Stereolithography. *Annals of Biomedical Engineering* **2016**, 1-11.
56. Ng, W. L.; Yeong, W. Y.; Naing, M. W., Polyelectrolyte gelatin-chitosan hydrogel optimized for 3D bioprinting in skin tissue engineering. *2016* **2016,** 2, (1).
57. Müller, W. E.; Tolba, E.; Schröder, H. C.; Neufurth, M.; Wang, S.; Link, T.; Al-Nawas, B.; Wang, X., A new printable and durable N, O-carboxymethyl chitosan–Ca 2+–polyphosphate complex with morphogenetic activity. *Journal of Materials Chemistry B* **2015,** 3, (8), 1722-1730.
58. Kuo, C. K.; Ma, P. X., Ionically crosslinked alginate hydrogels as scaffolds for tissue engineering: Part 1. Structure, gelation rate and mechanical properties. *Biomaterials* **2001,** 22, (6), 511-521.
59. Lee, H.; Hong, S. H.; Ahn, D. J., Stable patterning of sensory agarose gels using inkjet printing. *Macromolecular Research* **2015,** 23, (1), 124-127.
60. Antoine, E. E.; Vlachos, P. P.; Rylander, M. N., Tunable collagen I hydrogels for engineered physiological tissue micro-environments. *PloS one* **2015,** 10, (3), e0122500.
61. Klotz, B. J.; Gawlitta, D.; Rosenberg, A. J.; Malda, J.; Melchels, F. P., Gelatin-Methacryloyl Hydrogels: Towards Biofabrication-Based Tissue Repair. *Trends in biotechnology* **2016,** 34, (5), 394-407.
62. Schuurman, W.; Levett, P. A.; Pot, M. W.; van Weeren, P. R.; Dhert, W. J.; Hutmacher, D. W.; Melchels, F. P.; Klein, T. J.; Malda, J., Gelatin-methacrylamide hydrogels as potential biomaterials for fabrication of tissue-engineered cartilage constructs. *Macromolecular bioscience* **2013,** 13, (5), 551-561.
63. Rutz, A. L.; Hyland, K. E.; Jakus, A. E.; Burghardt, W. R.; Shah, R. N., A Multimaterial Bioink Method for 3D Printing Tunable, Cell-Compatible Hydrogels. *Advanced Materials* **2015,** 27, (9), 1607-1614.
64. Hoch, E.; Hirth, T.; Tovar, G. E.; Borchers, K., Chemical tailoring of gelatin to adjust its chemical and physical properties for functional bioprinting. *Journal of Materials Chemistry B* **2013,** 1, (41), 5675-5685.
65. Bai, T.; Sun, F.; Zhang, L.; Sinclair, A.; Liu, S.; Ella-Menye, J.-R.; Zheng, Y.; Jiang, S., Restraint of the Differentiation of Mesenchymal Stem Cells by a Nonfouling Zwitterionic Hydrogel. *Angewandte Chemie International Edition* **2014,** 53, (47), 12729-12734.
66. Schultz, A. R.; Lambert, P. M.; Chartrain, N. A.; Ruohoniemi, D. M.; Zhang, Z.; Jangu, C.; Zhang, M.; Williams, C. B.; Long, T. E., 3D Printing Phosphonium Ionic Liquid Networks with Mask Projection Microstereolithography. *ACS Macro Letters* **2014,** 3, (11), 1205-1209.

67. Wang, B.; Benitez, A. J.; Lossada, F.; Merindol, R.; Walther, A., Bioinspired Mechanical Gradients in Cellulose Nanofibril/Polymer Nanopapers. *Angewandte Chemie* **2016**, n/a-n/a.
68. Chen, H.; Hou, S.; Ma, H.; Li, X.; Tan, Y., Controlled gelation kinetics of cucurbit[7]uril-adamantane cross-linked supramolecular hydrogels with competing guest molecules. *Scientific Reports* **2016,** 6, 20722.
69. Censi, R.; Schuurman, W.; Malda, J.; Di Dato, G.; Burgisser, P. E.; Dhert, W. J.; Van Nostrum, C. F.; Di Martino, P.; Vermonden, T.; Hennink, W. E., A Printable Photopolymerizable Thermosensitive p (HPMAm-lactate)-PEG Hydrogel for Tissue Engineering. *Advanced Functional Materials* **2011,** 21, (10), 1833-1842.
70. Hung, K. C.; Tseng, C. S.; Hsu, S. h., Synthesis and 3D Printing of Biodegradable Polyurethane Elastomer by a Water-Based Process for Cartilage Tissue Engineering Applications. *Advanced healthcare materials* **2014,** 3, (10), 1578-1587.
71. Hung, K.-C.; Tseng, C.-S.; Dai, L.-G.; Hsu, S.-h., Water-based polyurethane 3D printed scaffolds with controlled release function for customized cartilage tissue engineering. *Biomaterials* **2016,** 83, 156-168.
72. Gao, L.; Gao, Y.; Lin, Y.; Ju, Y.; Yang, S.; Hu, J., A Charge-Transfer-Induced Self-Healing Supramolecular Hydrogel. *Chemistry–An Asian Journal* **2016**.
73. Wei, Q.; Xu, M.; Liao, C.; Wu, Q.; Liu, M.; Zhang, Y.; Wu, C.; Cheng, L.; Wang, Q., Printable hybrid hydrogel by dual enzymatic polymerization with superactivity. *Chemical Science* **2016,** 7, (4), 2748-2752.
74. Wei, Q.; Xu, W.; Liu, M.; Wu, Q.; Cheng, L.; Wang, Q., Viscosity-controlled printing of supramolecular-polymeric hydrogels via dual-enzyme catalysis. *Journal of Materials Chemistry B* **2016**.
75. Domingos, M.; Chiellini, F.; Gloria, A.; Ambrosio, L.; Bartolo, P.; Chiellini, E., Effect of process parameters on the morphological and mechanical properties of 3D Bioextruded poly(ε-caprolactone) scaffolds. *Rapid Prototyping Journal* **2012,** 18, (1), 56-67.
76. Hart, L. R.; Li, S.; Sturgess, C.; Wildman, R.; Jones, J. R.; Hayes, W., 3D Printing of Biocompatible Supramolecular Polymers and their Composites. *ACS Applied Materials & Interfaces* **2016,** 8, (5), 3115-3122.
77. Dankers, P. Y.; Harmsen, M. C.; Brouwer, L. A.; Van Luyn, M. J.; Meijer, E., A modular and supramolecular approach to bioactive scaffolds for tissue engineering. *Nature materials* **2005,** 4, (7), 568-574.
78. Chimene, D.; Lennox, K. K.; Kaunas, R. R.; Gaharwar, A. K., Advanced Bioinks for 3D Printing: A Materials Science Perspective. *Annals of Biomedical Engineering* **2016,** 44, (6), 2090-2102.
79. Chung, R.-J.; Hsieh, M.-F.; Perng, L.-H.; Cheng, Y.-L.; Hsu, T.-J., MESHED SCAFFOLDS MADE OF α, α′ -BIS(2-HYDROXYETHYL METHACRYLATE) POLY(ETHYLENE GLYCOL) THROUGH 3D STEREOLITHOGRAPHY. *Biomedical Engineering: Applications, Basis and Communications* **2013,** 25, (05), 1340002.
80. Jeong, C. G.; Atala, A., 3D Printing and Biofabrication for Load Bearing Tissue Engineering. In *Engineering Mineralized and Load Bearing Tissues*, Springer: 2015; pp 3-14.

81. Akkineni, A. R.; Ahlfeld, T.; Funk, A.; Waske, A.; Lode, A.; Gelinsky, M., Highly Concentrated Alginate-Gellan Gum Composites for 3D Plotting of Complex Tissue Engineering Scaffolds. *Polymers* **2016,** 8, (5), 170.
82. Mouser, V. H.; Melchels, F. P.; Visser, J.; Dhert, W. J.; Gawlitta, D.; Malda, J., Yield stress determines bioprintability of hydrogels based on gelatin-methacryloyl and gellan gum for cartilage bioprinting. *Biofabrication* **2016,** 8, (3), 035003.
83. Keller, A.; Stevens, L.; Wallace, G. G., 3D Printed Edible Hydrogel Electrodes. *MRS Advances* **2016,** 1, (08), 527-532.
84. Liu, Y.; Liu, Y.; Hamid, Q.; Hamid, Q.; Snyder, J.; Snyder, J.; Wang, C.; Wang, C.; Sun, W.; Sun, W., Evaluating fabrication feasibility and biomedical application potential of in situ 3D printing technology. *Rapid Prototyping Journal* **2016,** 22, (6), 947-955.
85. Stein, N.; Saathoff, T.; Antoni, S.-T.; Schlaefer, A., Creating 3D gelatin phantoms for experimental evaluation in biomedicine. *Current Directions in Biomedical Engineering* **2015,** 1, (1), 331-334.
86. Rodriguez, M. J.; Brown, J.; Giordano, J.; Lin, S. J.; Omenetto, F. G.; Kaplan, D. L., Silk based bioinks for soft tissue reconstruction using 3-dimensional (3D) printing with in vitro and in vivo assessments. *Biomaterials* **2016**.
87. Ahlfeld, T.; Akkineni, A. R.; Förster, Y.; Köhler, T.; Knaack, S.; Gelinsky, M.; Lode, A., Design and fabrication of complex scaffolds for bone defect healing: combined 3D plotting of a calcium phosphate cement and a growth factor-loaded hydrogel. *Annals of Biomedical Engineering* **2016**, 1-13.
88. Lin, K.-F.; He, S.; Song, Y.; Wang, C.-M.; Gao, Y.; Li, J.-Q.; Tang, P.; Wang, Z.; Bi, L.; Pei, G.-X., Low-Temperature Additive Manufacturing of Biomimic Three-Dimensional Hydroxyapatite/Collagen Scaffolds for Bone Regeneration. *ACS applied materials & interfaces* **2016,** 8, (11), 6905-6916.
89. Lode, A.; Meyer, M.; Brüggemeier, S.; Paul, B.; Baltzer, H.; Schröpfer, M.; Winkelmann, C.; Sonntag, F.; Gelinsky, M., Additive manufacturing of collagen scaffolds by three-dimensional plotting of highly viscous dispersions. *Biofabrication* **2016,** 8, (1), 015015.
90. Akkineni, A. R.; Ahlfeld, T.; Lode, A.; Gelinsky, M., A versatile method for combining different biopolymers in a core/shell fashion by 3D plotting to achieve mechanically robust constructs. *Biofabrication* **2016,** 8, (4), 045001.
91. Khaled, S. A.; Burley, J. C.; Alexander, M. R.; Roberts, C. J., Desktop 3D printing of controlled release pharmaceutical bilayer tablets. *International Journal of Pharmaceutics* **2014,** 461, (1–2), 105-111.
92. Vogler, E. A., Protein adsorption in three dimensions. *Biomaterials* **2012,** 33, (5), 1201-1237.
93. Nesti, L. J.; Li, W.-J.; Shanti, R. M.; Jiang, Y. J.; Jackson, W.; Freedman, B. A.; Kuklo, T. R.; Giuliani, J. R.; Tuan, R. S., Intervertebral disc tissue engineering using a novel hyaluronic acid–nanofibrous scaffold (HANFS) amalgam. *Tissue Engineering Part A* **2008,** 14, (9), 1527-1537.
94. Pietrzak, K.; Isreb, A.; Alhnan, M. A., A flexible-dose dispenser for immediate and extended release 3D printed tablets. *European Journal of Pharmaceutics and Biopharmaceutics* **2015,** 96, 380-387.

95. Albarahmieha, E.; Qia, S.; Craig, D., Hot Melt Extruded Transdermal Films based on Amorphous Solid Dispersions in Eudragit RS PO: The Inclusion of Hydrophilic Additives to Develop Moisture-Activated Release Systems. *International Journal of Pharmaceutics* **2016**.
96. Zhang, F., Melt-Extruded Eudragit® FS-Based Granules for Colonic Drug Delivery. *AAPS PharmSciTech* **2016,** 17, (1), 56-67.
97. Nernplod, T.; Akkaramongkolporn, P.; Sriamornsak, P. In *Preparation of Eudragit® L Beads for Intragastric Floating Drug Delivery*, Advanced Materials Research, 2015; Trans Tech Publ: 2015; pp 79-82.
98. Vo, A. Q.; Feng, X.; Morott, J. T.; Pimparade, M. B.; Tiwari, R. V.; Zhang, F.; Repka, M. A., A novel floating controlled release drug delivery system prepared by hot-melt extrusion. *European Journal of Pharmaceutics and Biopharmaceutics* **2016,** 98, 108-121.
99. Yang, Y.; Chen, Y.; Wei, Y.; Li, Y., 3D printing of shape memory polymer for functional part fabrication. *The International Journal of Advanced Manufacturing Technology* **2015**, 1-17.
100. Zhu, F.; Cheng, L.; Yin, J.; Wu, Z.; Qian, J.; Fu, J.; Zheng, Q., 3D printing of ultra-tough polyion complex hydrogels. *ACS Applied Materials & Interfaces* **2016**.
101. Maher, P.; Keatch, R.; Donnelly, K.; Mackay, R.; Paxton, J., Construction of 3D biological matrices using rapid prototyping technology. *Rapid Prototyping Journal* **2009,** 15, (3), 204-210.
102. Boere, K. W. M.; Visser, J.; Seyednejad, H.; Rahimian, S.; Gawlitta, D.; van Steenbergen, M. J.; Dhert, W. J. A.; Hennink, W. E.; Vermonden, T.; Malda, J., Covalent attachment of a three-dimensionally printed thermoplast to a gelatin hydrogel for mechanically enhanced cartilage constructs. *Acta Biomaterialia* **2014,** 10, (6), 2602-2611.
103. Hong, S.; Sycks, D.; Chan, H. F.; Lin, S.; Lopez, G. P.; Guilak, F.; Leong, K. W.; Zhao, X., 3D printing of highly stretchable and tough hydrogels into complex, cellularized structures. *Advanced Materials* **2015,** 27, (27), 4035-4040.
104. Bakarich, S. E.; Beirne, S.; Wallace, G. G.; Spinks, G. M., Extrusion printing of ionic–covalent entanglement hydrogels with high toughness. *Journal of Materials Chemistry B* **2013,** 1, (38), 4939-4946.
105. Allen, P. B.; Khaing, Z.; Schmidt, C. E.; Ellington, A. D., 3D Printing with Nucleic Acid Adhesives. *ACS biomaterials science & engineering* **2014,** 1, (1), 19-26.
106. Skoog, S. A.; Goering, P. L.; Narayan, R. J., Stereolithography in tissue engineering. *Journal of Materials Science: Materials in Medicine* **2014,** 25, (3), 845-856.
107. Pal, K.; Sagiri, S. S.; Singh, V. K.; Behera, B.; Banerjee, I.; Pramanik, K., Natural Polymers: Tissue Engineering. *Drug delivery* **2015,** 39, 40.
108. Elomaa, L.; Pan, C.-C.; Shanjani, Y.; Malkovskiy, A.; Seppala, J. V.; Yang, Y., Three-dimensional fabrication of cell-laden biodegradable poly(ethylene glycol-co-depsipeptide) hydrogels by visible light stereolithography. *Journal of Materials Chemistry B* **2015,** 3, (42), 8348-8358.
109. Fedorovich, N. E.; Swennen, I.; Girones, J.; Moroni, L.; Van Blitterswijk, C. A.; Schacht, E.; Alblas, J.; Dhert, W. J., Evaluation of photocrosslinked lutrol hydrogel for tissue printing applications. *Biomacromolecules* **2009,** 10, (7), 1689-1696.

110. Pyo, S.-H.; Wang, P.; Zhu, W.; Hwang, H.; Warner, J. J.; Chen, S., Continuous Optical 3D Printing of Green Aliphatic Polyurethanes. *ACS Applied Materials & Interfaces* **2016**.
111. Petrochenko, P. E.; Torgersen, J.; Gruber, P.; Hicks, L. A.; Zheng, J.; Kumar, G.; Narayan, R. J.; Goering, P. L.; Liska, R.; Stampfl, J., Laser 3D printing with sub-microscale resolution of porous elastomeric scaffolds for supporting human bone stem cells. *Advanced healthcare materials* **2015,** 4, (5), 739-747.
112. Sirrine, J. M.; Pekkanen, A. M.; Nelson, A. M.; Chartrain, N. A.; Williams, C. B.; Long, T. E., 3D-printable biodegradable polyester tissue scaffolds for cell adhesion. *Australian Journal of Chemistry* **2015,** 68, (9), 1409-1414.
113. Yue, J.; Zhao, P.; Gerasimov, J. Y.; van de Lagemaat, M.; Grotenhuis, A.; Rustema-Abbing, M.; van der Mei, H. C.; Busscher, H. J.; Herrmann, A.; Ren, Y., 3D-Printable Antimicrobial Composite Resins. *Advanced Functional Materials* **2015,** 25, (43), 6756-6767.
114. Zawko, S. A.; Suri, S.; Truong, Q.; Schmidt, C. E., Photopatterned anisotropic swelling of dual-crosslinked hyaluronic acid hydrogels. *Acta Biomaterialia* **2009,** 5, (1), 14-22.
115. Suri, S.; Schmidt, C. E., Photopatterned collagen–hyaluronic acid interpenetrating polymer network hydrogels. *Acta Biomaterialia* **2009,** 5, (7), 2385-2397.
116. Gonçalves, J. L. D. S.; Valandro, S. R.; Wu, H.-F.; Lee, Y.-H.; Mettra, B.; Monnereau, C.; Cavalheiro, C. C. S.; Pawlicka, A.; Focsan, M.; Lin, C.-L. In *3D printing of natural organic materials by photochemistry*, SPIE OPTO, 2016; International Society for Optics and Photonics: 2016; pp 97450E-97450E-7.
117. Placone, J. K.; Navarro, J.; Laslo, G. W.; Lerman, M. J.; Gabard, A. R.; Herendeen, G. J.; Falco, E. E.; Tomblyn, S.; Burnett, L.; Fisher, J. P., Development and Characterization of a 3D Printed, Keratin-Based Hydrogel. *Annals of biomedical engineering* **2016**, 1-12.
118. Pawar, A. A.; Saada, G.; Cooperstein, I.; Larush, L.; Jackman, J. A.; Tabaei, S. R.; Cho, N.-J.; Magdassi, S., High-performance 3D printing of hydrogels by water-dispersible photoinitiator nanoparticles. *Science advances* **2016,** 2, (4), e1501381.
119. Lee, J. M.; Yeong, W. Y., Design and Printing Strategies in 3D Bioprinting of Cell-Hydrogels: A Review. *Advanced Healthcare Materials* **2016**.
120. Guvendiren, M.; Molde, J.; Soares, R. M.; Kohn, J., Designing biomaterials for 3D printing. *ACS Biomaterials Science & Engineering* **2016**.
121. Yeo, M.; Ha, J.; Lee, H.; Kim, G., Fabrication of hASCs-laden structures using extrusion-based cell printing supplemented with an electric field. *Acta Biomaterialia* **2016,** 38, 33-43.
122. Kani, M. H.; Chan, E.-C.; Young, R. C.; Butler, T.; Smith, R.; Paul, J. W., 3D Cell Culturing and Possibilities for Myometrial Tissue Engineering. *Annals of Biomedical Engineering* **2016**, 1-12.
123. Vanderburgh, J.; Sterling, J. A.; Guelcher, S. A., 3D Printing of Tissue Engineered Constructs for In Vitro Modeling of Disease Progression and Drug Screening. *Annals of biomedical engineering* **2016**, 1-16.
124. Gurkan, U. A.; El Assal, R.; Yildiz, S. E.; Sung, Y.; Trachtenberg, A. J.; Kuo, W. P.; Demirci, U., Engineering Anisotropic Biomimetic Fibrocartilage Microenvironment

by Bioprinting Mesenchymal Stem Cells in Nanoliter Gel Droplets. *Molecular Pharmaceutics* **2014,** 11, (7), 2151-2159.
125. Gao, G.; Yonezawa, T.; Hubbell, K.; Dai, G.; Cui, X., Inkjet-bioprinted acrylated peptides and PEG hydrogel with human mesenchymal stem cells promote robust bone and cartilage formation with minimal printhead clogging. *Biotechnology Journal* **2015,** 10, (10), 1568-1577.
126. Pourchet, L. J.; Thepot, A.; Albouy, M.; Courtial, E. J.; Boher, A.; Blum, L. J.; Marquette, C. A., Human Skin 3D Bioprinting Using Scaffold-Free Approach. *Advanced Healthcare Materials* **2016**.
127. Koch, L.; Deiwick, A.; Schlie, S.; Michael, S.; Gruene, M.; Coger, V.; Zychlinski, D.; Schambach, A.; Reimers, K.; Vogt, P. M., Skin tissue generation by laser cell printing. *Biotechnology and bioengineering* **2012,** 109, (7), 1855-1863.
128. Xu, M.; Wang, X.; Yan, Y.; Yao, R.; Ge, Y., An cell-assembly derived physiological 3D model of the metabolic syndrome, based on adipose-derived stromal cells and a gelatin/alginate/fibrinogen matrix. *Biomaterials* **2010,** 31, (14), 3868-3877.
129. Billiet, T.; Gevaert, E.; De Schryver, T.; Cornelissen, M.; Dubruel, P., The 3D printing of gelatin methacrylamide cell-laden tissue-engineered constructs with high cell viability. *Biomaterials* **2014,** 35, (1), 49-62.
130. Homan, K. A.; Kolesky, D. B.; Skylar-Scott, M. A.; Herrmann, J.; Obuobi, H.; Moisan, A.; Lewis, J. A., Bioprinting of 3D Convoluted Renal Proximal Tubules on Perfusable Chips. *Scientific Reports* **2016,** 6, 34845.
131. Kinstlinger, I. S.; Miller, J. S., 3D-printed fluidic networks as vasculature for engineered tissue. *Lab on a Chip* **2016,** 16, (11), 2025-2043.
132. Guillotin, B.; Souquet, A.; Catros, S.; Duocastella, M.; Pippenger, B.; Bellance, S.; Bareille, R.; Rémy, M.; Bordenave, L.; Amédée, J., Laser assisted bioprinting of engineered tissue with high cell density and microscale organization. *Biomaterials* **2010,** 31, (28), 7250-7256.
133. Lee, J. W.; Choi, Y.-J.; Yong, W.-J.; Pati, F.; Shim, J.-H.; Kang, K. S.; Kang, I.-H.; Park, J.; Cho, D.-W., Development of a 3D cell printed construct considering angiogenesis for liver tissue engineering. *Biofabrication* **2016,** 8, (1), 015007.
134. Duan, B.; Hockaday, L. A.; Kang, K. H.; Butcher, J. T., 3D Bioprinting of heterogeneous aortic valve conduits with alginate/gelatin hydrogels. *Journal of Biomedical Materials Research Part A* **2013,** 101A, (5), 1255-1264.
135. Hockaday, L.; Kang, K.; Colangelo, N.; Cheung, P.; Duan, B.; Malone, E.; Wu, J.; Girardi, L.; Bonassar, L.; Lipson, H., Rapid 3D printing of anatomically accurate and mechanically heterogeneous aortic valve hydrogel scaffolds. *Biofabrication* **2012,** 4, (3), 035005.
136. Hölzl, K.; Lin, S.; Tytgat, L.; Van Vlierberghe, S.; Gu, L.; Ovsianikov, A., Bioink properties before, during and after 3D bioprinting. *Biofabrication* **2016,** 8, (3), 032002.
137. Cubo, N.; Garcia, M.; del Cañizo, J. F.; Velasco, D.; Jorcano, J. L., 3D bioprinting of functional human skin: production and in vivo analysis. *Biofabrication* **2016,** 9, (1), 015006.
138. Bhuthalingam, R.; Lim, P. Q.; Irvine, S. A.; Agrawal, A.; Mhaisalkar, P. S.; An, J.; Chua, C. K.; Venkatraman, S., A novel 3D printing method for cell alignment and differentiation. *International Journal of Bioprinting* **2015,** 1, (1).

139. Huang, S.; Yao, B.; Xie, J.; Fu, X., 3D bioprinted extracellular matrix mimics facilitate directed differentiation of epithelial progenitors for sweat gland regeneration. *Acta biomaterialia* **2016,** 32, 170-177.
140. Arai, K.; Tsukamoto, Y.; Yoshida, H.; Sanae, H.; Mir, T. A.; Sakai, S.; Yoshida, T.; Okabe, M.; Nikaido, T.; Taya, M., The development of cell-adhesive hydrogel for 3D printing. *International Journal of Bioprinting* **2016,** 2, (2).
141. Kesti, M.; Müller, M.; Becher, J.; Schnabelrauch, M.; D'Este, M.; Eglin, D.; Zenobi-Wong, M., A versatile bioink for three-dimensional printing of cellular scaffolds based on thermally and photo-triggered tandem gelation. *Acta biomaterialia* **2015,** 11, 162-172.
142. You, F.; Wu, X.; Zhu, N.; Lei, M.; Eames, B. F.; Chen, X., 3D Printing of Porous Cell-Laden Hydrogel Constructs for Potential Applications in Cartilage Tissue Engineering. *ACS Biomaterials Science & Engineering* **2016,** 2, (7), 1200-1210.
143. Kang, H.-W.; Lee, S. J.; Ko, I. K.; Kengla, C.; Yoo, J. J.; Atala, A., A 3D bioprinting system to produce human-scale tissue constructs with structural integrity. *Nature biotechnology* **2016,** 34, (3), 312-319.
144. Kundu, J.; Shim, J. H.; Jang, J.; Kim, S. W.; Cho, D. W., An additive manufacturing-based PCL–alginate–chondrocyte bioprinted scaffold for cartilage tissue engineering. *Journal of tissue engineering and regenerative medicine* **2015,** 9, (11), 1286-1297.
145. Abbadessa, A.; Mouser, V. H.; Blokzijl, M. M.; Gawlitta, D.; Dhert, W. J.; Hennink, W. E.; Malda, J.; Vermonden, T., A synthetic thermo-sensitive hydrogel for cartilage bioprinting and its biofunctionalization with polysaccharides. *Biomacromolecules* **2016**.
146. Yang, L.; Shridhar, S. V.; Gerwitz, M.; Soman, P., An in vitro vascular chip using 3D printing-enabled hydrogel casting. *Biofabrication* **2016,** 8, (3), 035015.
147. Du, M.; Chen, B.; Meng, Q.; Liu, S.; Zheng, X.; Zhang, C.; Wang, H.; Li, H.; Wang, N.; Dai, J., 3D bioprinting of BMSC-laden methacrylamide gelatin scaffolds with CBD-BMP2-collagen microfibers. *Biofabrication* **2015,** 7, (4), 044104.
148. Kolesky, D. B.; Homan, K. A.; Skylar-Scott, M. A.; Lewis, J. A., Three-dimensional bioprinting of thick vascularized tissues. *Proceedings of the National Academy of Sciences* **2016,** 113, (12), 3179-3184.
149. Park, J. Y.; Shim, J.-H.; Choi, S.-A.; Jang, J.; Kim, M.; Lee, S. H.; Cho, D.-W., 3D printing technology to control BMP-2 and VEGF delivery spatially and temporally to promote large-volume bone regeneration. *Journal of Materials Chemistry B* **2015,** 3, (27), 5415-5425.
150. Huang, J.; Fu, H.; Wang, Z.; Meng, Q.; Liu, S.; Wang, H.; Zheng, X.; Dai, J.; Zhang, Z., BMSCs-laden gelatin/sodium alginate/carboxymethyl chitosan hydrogel for 3D bioprinting. *RSC Advances* **2016,** 6, (110), 108423-108430.
151. Das, S.; Pati, F.; Choi, Y.-J.; Rijal, G.; Shim, J.-H.; Kim, S. W.; Ray, A. R.; Cho, D.-W.; Ghosh, S., Bioprintable, cell-laden silk fibroin–gelatin hydrogel supporting multilineage differentiation of stem cells for fabrication of three-dimensional tissue constructs. *Acta biomaterialia* **2015,** 11, 233-246.
152. Liu, J.; Hwang, H. H.; Wang, P.; Whang, G.; Chen, S., Direct 3D-printing of cell-laden constructs in microfluidic architectures. *Lab on a Chip* **2016,** 16, (8), 1430-1438.

153. Ouyang, L.; Yao, R.; Zhao, Y.; Sun, W., Effect of bioink properties on printability and cell viability for 3D bioplotting of embryonic stem cells. *Biofabrication* **2016,** 8, (3), 035020.
154. Zhao, X.; Du, S.; Chai, L.; Xu, Y.; Liu, L.; Zhou, X.; Wang, J.; Zhang, W.; Liu, C.-H.; Wang, X., Anti-cancer drug screening based on a adipose-derived stem cell/hepatocyte 3D printing technique. *Journal of Stem Cell Research & Therapy* **2015,** 2015.
155. Wang, X.-F.; Lu, P.-J.; Song, Y.; Sun, Y.-C.; Wang, Y.-G.; Wang, Y., Nano hydroxyapatite particles promote osteogenesis in a three-dimensional bio-printing construct consisting of alginate/gelatin/hASCs. *RSC Advances* **2016,** 6, (8), 6832-6842.
156. Kim, Y. B.; Lee, H.; Kim, G. H., Strategy to Achieve Highly Porous/Biocompatible Macroscale Cell Blocks, Using a Collagen/Genipin-bioink and an Optimal 3D Printing Process. *ACS Applied Materials & Interfaces* **2016,** 8, (47), 32230-32240.
157. Dai, X.; Ma, C.; Lan, Q.; Xu, T., 3D bioprinted glioma stem cells for brain tumor model and applications of drug susceptibility. *Biofabrication* **2016,** 8, (4), 045005.
158. England, S.; Rajaram, A.; Schreyer, D. J.; Chen, X., Bioprinted fibrin-factor XIII-hyaluronate hydrogel scaffolds with encapsulated Schwann cells and their in vitro characterization for use in nerve regeneration. *Bioprinting* **2016**.
159. Schirmer, K. S.; Gorkin III, R.; Beirne, S.; Stewart, E.; Thompson, B. C.; Quigley, A. F.; Kapsa, R. M.; Wallace, G. G., Cell compatible encapsulation of filaments into 3D hydrogels. *Biofabrication* **2016,** 8, (2), 025013.
160. Gu, Q.; Tomaskovic-Crook, E.; Lozano, R.; Chen, Y.; Kapsa, R. M.; Zhou, Q.; Wallace, G. G.; Crook, J. M., Functional 3D Neural Mini-Tissues from Printed Gel-Based Bioink and Human Neural Stem Cells. *Advanced healthcare materials* **2016**.
161. Li, C.; Faulkner-Jones, A.; Dun, A. R.; Jin, J.; Chen, P.; Xing, Y.; Yang, Z.; Li, Z.; Shu, W.; Liu, D., Rapid Formation of a Supramolecular Polypeptide–DNA Hydrogel for In Situ Three-Dimensional Multilayer Bioprinting. *Angewandte Chemie International Edition* **2015,** 54, (13), 3957-3961.
162. Irvine, S. A.; Agrawal, A.; Lee, B. H.; Chua, H. Y.; Low, K. Y.; Lau, B. C.; Machluf, M.; Venkatraman, S., Printing cell-laden gelatin constructs by free-form fabrication and enzymatic protein crosslinking. *Biomedical microdevices* **2015,** 17, (1), 1-8.
163. Ouyang, L.; Yao, R.; Chen, X.; Na, J.; Sun, W., 3D printing of HEK 293FT cell-laden hydrogel into macroporous constructs with high cell viability and normal biological functions. *Biofabrication* **2015,** 7, (1), 015010.
164. Zhang, K.; Fu, Q.; Yoo, J.; Chen, X.; Chandra, P.; Mo, X.; Song, L.; Atala, A.; Zhao, W., 3D bioprinting of urethra with PCL/PLCL blend and dual autologous cells in fibrin hydrogel: an in vitro evaluation of biomimetic mechanical property and cell growth environment. *Acta Biomaterialia* **2016**.
165. Parker, P.; Moya, M.; Wheeler, E. *Development and Optimization of Viable Human Platforms through 3D Printing*; Lawrence Livermore National Laboratory (LLNL), Livermore, CA: 2015.
166. Gaetani, R.; Feyen, D. A.; Verhage, V.; Slaats, R.; Messina, E.; Christman, K. L.; Giacomello, A.; Doevendans, P. A.; Sluijter, J. P., Epicardial application of cardiac

progenitor cells in a 3D-printed gelatin/hyaluronic acid patch preserves cardiac function after myocardial infarction. *Biomaterials* **2015,** 61, 339-348.
167. Wei, J.; Wang, J.; Su, S.; Wang, S.; Qiu, J.; Zhang, Z.; Christopher, G.; Ning, F.; Cong, W., 3D printing of an extremely tough hydrogel. *RSC Advances* **2015,** 5, (99), 81324-81329.
168. Egan, P.; Ferguson, S. J.; Shea, K. In *DESIGN AND 3D PRINTING OF HIERARCHICAL TISSUE ENGINEERING SCAFFOLDS BASED ON MECHANICS AND BIOLOGY PERSPECTIVES*, Proceedings of the 28th International Conference on Design Theory and Methodology, 2016; 2016; p 24.
169. Dimas, L. S.; Bratzel, G. H.; Eylon, I.; Buehler, M. J., Tough Composites Inspired by Mineralized Natural Materials: Computation, 3D printing, and Testing. *Advanced Functional Materials* **2013,** 23, (36), 4629-4638.
170. Tibbitt, M. W.; Rodell, C. B.; Burdick, J. A.; Anseth, K. S., Progress in material design for biomedical applications. *Proceedings of the National Academy of Sciences* **2015,** 112, (47), 14444-14451.
171. Zhu, M.; Li, K.; Zhu, Y.; Zhang, J.; Ye, X., 3D-printed hierarchical scaffold for localized isoniazid/rifampin drug delivery and osteoarticular tuberculosis therapy. *Acta Biomaterialia* **2015,** 16, 145-155.
172. Dou, P.; Liu, Z.; Cao, Z.; Zheng, J.; Wang, C.; Xu, X., Rapid synthesis of hierarchical nanostructured Polyaniline hydrogel for high power density energy storage application and three-dimensional multilayers printing. *Journal of Materials Science* **2016,** 51, (9), 4274-4282.
173. Loo, Y.; Lakshmanan, A.; Ni, M.; Toh, L. L.; Wang, S.; Hauser, C. A., Peptide bioink: self-assembling nanofibrous scaffolds for three-dimensional organotypic cultures. *Nano letters* **2015,** 15, (10), 6919-6925.

Chapter 5. Characterization of Peptide Coatings Adhered to Synthetic Fibers: A Versatile Model for Peptide Nucleic Acids

(Published in International Journal of Adhesion and Adhesives, **2017**, **75**, 17-22)

Allison M. Pekkanen[†1], Ryan J. Mondschein[†2], Denis Guenette[3], Nrusingh Mohaptra[3], Timothy E. Long[2]

[1]Biomedical Engineering and Mechanics, Virginia Tech, Blacksburg, VA 24061

[2]Macromolecules Innovation Institute, Department of Chemistry, Virginia Tech, Blacksburg, VA 24061

[3]Techulon, Inc. Blacksburg, VA 24061

*To whom correspondence should be addressed. E-mail: telong@vt.edu. TEL: (540) 231-2480 FAX: (540) 231-8517

†These authors contributed equally to the work

5.1 Abstract

Peptide nucleic acids (PNAs) are an emerging family of biomaterials designed to specifically target and treat diseased cells, most commonly in the antimicrobial-resistant bacteria MRSA. While PNAs offer great promise for the elimination of these bacteria, they are significantly more expensive than traditional peptides and often do not provide a functional handle for analysis. In this work, a model peptide (KFFCCQ) was developed to evaluate peptide coatings adhered to fibrous surfaces with multiple functional handles, i.e. the presence of a sulfur atom in cysteine and an aromatic ring in phenylalanine, to predict the durability of PNA coatings on 50/50 nylon/cotton blends (NyCo), which are commonly used in clothing and medical attire. Following elemental analysis through XPS and EDX-SEM, rinses were performed on the fabrics and the subsequent release of

peptide was evaluated with UV-Vis. As expected, elevated temperature and increased time resulted in higher KFFCCQ release levels from the NyCo fibers. Finally, EDX-SEM examined the presence of KFFCCQ following rinse cycles, revealing that a higher level of KFFCCQ is released from nylon fibers as compared to cotton fibers. This evaluation proves the utility of KFFCCQ as a preliminary model to evaluate adhesion and release of peptides from nylon and cotton fibrous surfaces.

Textiles are a vital component to modern-day life and efficient modification of both synthetic and natural fibers is a crucial science and engineering concern. Most notably, dyes, antibacterials, and stain-resistant coatings must both adhere to woven fibers and survive external aqueous environments and mechanical agitation.[1-6] These coatings range in function from color fade resistance to therapeutic use.[6, 7] Recently, silver nanoparticles and tailored polymers as antibacterial coatings on fabrics justify the importance of developing and understanding biomaterial coatings and release profiles.[3, 5, 8] The characterization of fiber coatings and their resistance to multiple aqueous washing cycles is crucial to evaluate any new potential textile.

Although traditional antibacterial coatings offer precedence, they are often deemed too broad a class of antimicrobials, leading to the subsequent loss of naturally occurring bacteria on skin.[8] Peptide nucleic acids (PNAs) are an emerging biologic moiety that possess the potential to selectively eradicate numerous diseases.[9-13] DNA base pairs covalently attached to a peptide backbone reminiscent of proteins compose PNAs, harnessing the ability to combine the therapeutic function of DNA/RNA and

protein.[9] Their action varies on the specific application, but their main attraction is their specificity to target organisms. For example, Sato et al. described the use of PNAs as siRNA carriers to deliver these sensitive genes directly to the nucleus of cells.[14] More commonly, drug-resistant bacteria, such as Methicillin-resistant Staphylococcus aureus (MRSA), requires PNAs for treatment.[12] These PNAs eliminate specific targets within MRSA, such as FtsZ, allowing other bacteria to survive.[12]

Due to the high cost and often difficult characterization of PNA samples, developing simpler and cheaper model peptides to study the adhesion to fibers is important. Despite the complex nature of PNAs, peptides successfully model the action of PNA onto fiber surfaces. The peptide backbone, as well as short peptide sequences typically found in PNAs, effectively model the action of PNAs without the significant cost. PNAs typically contain two separate functional sequences in the backbone. First is the cell-penetrating peptide (CPP) sequence, typically incorporating high amounts of cationic charge through lysine or arginine incorporation. Second is the active inhibiting sequence, specific to targeting pathways or signals from a particular target, such as MRSA. Therefore, our unique design of a model peptide contains both a lysine residue to mimic charge density, as well as cysteine and phenylalanine for easy analytical analysis. This yielded a peptide with similar charge density to PNAs, while maintaining the peptide backbone suitable for coating and adhesive analysis (KFFCCQ, EnoGene Biotech Co Ltd).[15, 16] UV-Vis spectroscopy detected phenylalanine residues while elemental analysis, such as X-ray Photoelectron Spectroscopy (XPS, PHI Quantera SXM) or scanning electron microscopy (SEM, FEI Quanta 600 FEG) equipped with electron

dispersive X-ray spectroscopy (EDX, Bruker with Silicon Drifted Detector), identified sulfur atoms present in the cysteine residues.[17]

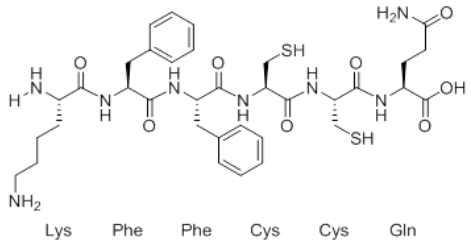

Figure 5.1: Model peptide consisting of Lysine-Phenylalanine-Phenylalanine-Cysteine-Cysteine-Glutamine (KFFCCQ) sequence.

XPS analysis of neat fabrics confirmed the lack of sulfur atoms present in commercially available 100 % cotton, 100 % nylon, or a 50/50 nylon/cotton (NyCo) blend, as shown in **Table 5.1**. All fibers showed a silicon signal, likely arising from a protective coating from a pre-treatment. NyCo samples reveal a magnesium peak, likely arising from dye or coating used on the fabric as demonstrated by a lack of magnesium upon bleach treatment.[18] Elemental analysis proves crucial to confirm KFFCCQ presence after coating procedures. Following characterization of neat fibers and validation of the lack of interference in elemental signal from the fibers, the NyCo sample was identified for detailed study.

Sample	C1s	N1s	O1s	F1s	Na1s	Mg2s	Si2p	P2p	S2p	Cl2p	Ca2p
Cotton	74.95	0.33	24.65	0	0.14	0	0.51	0	0.19	0	0.23
Cotton (Autoclaved)	71.63	1.3	22.73	2.41	0.13	0	0.97	0.26	0	0	0.57
Nylon	74.11	9.44	14.73	0	0	0	1.38	0	0	0	0.34
Nylon (Autoclaved)	70.4	8.63	18.07	0.42	0	0	2.23	0	0	0	0.24
NyCo	83.43	1.72	13.31	0	0	0.44	0.54	0	0	0.15	0.4
NyCo (Autoclaved)	78.03	3.18	15.84	0	0	0.34	2.31	0	0	0	0.3
NyCo (Bleached)	74.96	5.87	11.71	0	0.88	0	0.41	0	0.14	6.04	0

Table 5.1: XPS analysis of Cotton (neat & autoclaved), Nylon (neat & autoclaved), and 50/50 Nylon/Cotton (NyCo) (neat, autoclaved, and bleached) revealing the presence of coatings and dyes. XPS confirms the utility in the model peptide through the lack of elemental interference from fibers.

Pad-dry and pad-dry-cure techniques proved viable methods to coat KFFCCQ to NyCo fibers.[7, 19, 20] To compare these techniques, NyCo was soaked in aqueous 0.1 wt % or 0.5 wt % KFFCCQ solution for 30 min, with gentle agitation every 10 min. Pad-dry proceeded to dry the samples at 95 °C for 1 h, while pad-dry-cure placed the samples at 95 °C for 90 s followed by 150 °C for 60 s. Both pad-dry and pad-dry-cure methods sufficiently adhered the KFFCCQ to the 50/50 NyCo blend, with no discernible difference noticed between techniques. **Table 5.2** demonstrates changes in global elemental compositions (through XPS analysis) of fibers after adhering the peptide coating with varying weight percent KFFCCQ. As expected, 0.5 wt % KFFCCQ elicited higher sulfur content than 0.1 wt %, indicating a higher incorporation. The lack of variation between pad-dry and pad-dry-cure techniques for KFFCCQ incorporation suggests utility in the reduced-time pad-dry-cure method notwithstanding potential changes in function.[7]

Sample	C1s	N1s	O1s	Si2p	S2p	Cl2p
0.1 wt % Pad Dry	76.68	2.91	18.26	2.16	0	0
0.1 wt % Pad Dry Cure	80.24	4.2	14.06	0.86	0.41	0.22
0.5 wt % Pad Dry	74.01	5.4	17.43	2.14	0.73	0.3
0.5 wt % Pad Dry Cure	79.85	4.36	13.35	1.52	0.71	0.2

Table 5.2: XPS analysis of NyCo samples treated with 0.1 and 0.5 weight percent model peptide solutions, undergoing both pad dry and pad dry cure methods.

A broad S2p binding energy peak at 164 eV confirmed the retention of cysteine residues adhered to fiber surfaces following 0.5 wt % pad-dry and pad-dry-cure procedures, as shown in **Figure 5.2.**[21] Importantly, the high resolution XPS verified the absence of disulfide bonds potentially formed during the coating process. The retention of a broad S2p binding energy peak at 164 eV confirmed the structure of cysteine and preservation of KFFCCQ structure upon coating.[21]

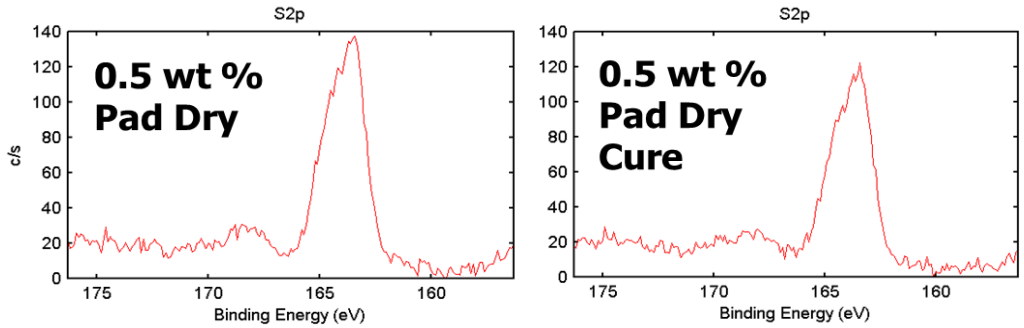

Figure 5.2: High resolution sulfur analysis performed on NyCo samples with 0.5 wt % pad-dry and pad-dry-cure treatment reveals retention of peptide structure upon coating.

SEM provided further confirmation of the utility of both pad-dry and pad-dry-cure techniques as compared to neat NyCo fibers. As seen in **Figure 5.3a**, cotton presented as rough, twisting fibers, while nylon presented smooth, cylindrical fibers. As seen in **Figure 5.3b-d**, the surface morphology of both fiber types after coating suggested successful adhesion of KFFCCQ throughout the NyCo sample. Regions of pad-dry samples exhibited bridging between fibers, while pad-dry-cure samples retain well-

defined morphology. These images indicate slight differences in both KFFCCQ content as well as coating morphology, suggestive of nuanced differences between the techniques not seen with XPS.

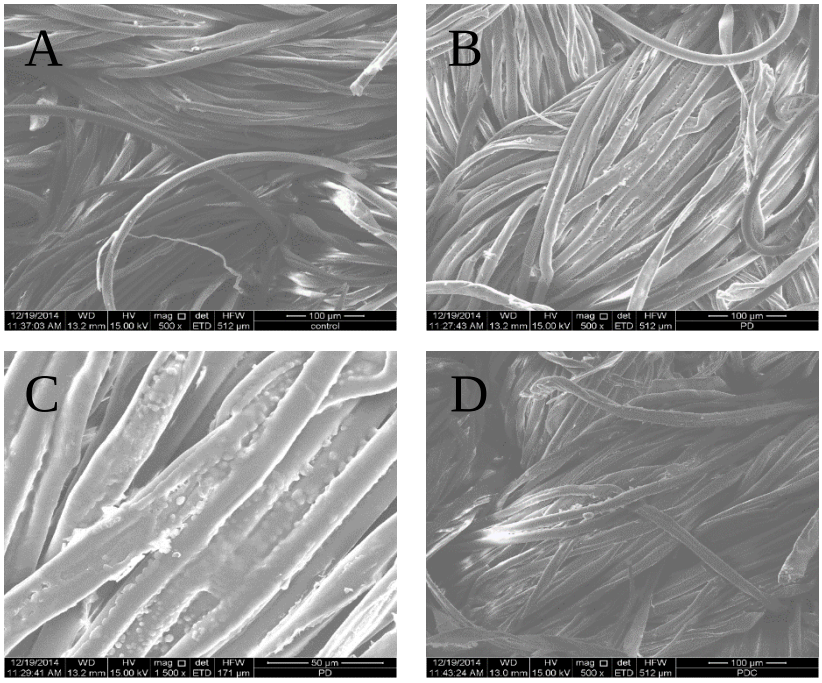

Figure 5.3: A. 500x SEM images of 50/50 Nylon/Cotton fibers treated with water. B. 500x SEM image of Pad-Dry 0.5 wt % model peptide treated NyCo fibers. A change in morphology is seen in the coating and bumpy, rough features. C. 1500x SEM image of Pad-Dry 0.5 wt % model peptide treated NyCo fibers. A change in morphology is seen in the coating and rough features. D. 500x SEM image of Pad-Dry-Cure 0.5 wt % model peptide treated NyCo fibers. A change in morphology is seen in the rough features on the fibers.

In conjunction with SEM imaging, EDX elemental analysis confirmed the presence of sulfur atoms on fiber surfaces after coating, as shown in **Figure 5.4**. **Figure 5.4a** depicted neat NyCo fibers and revealed a lack of sulfur present in the sample, in concordance with XPS performed on neat fabric. Predictably, following both pad-dry and pad-dry-cure procedures, a sulfur peak appeared, indicative of successful peptide adhesion (**Figure 5.4b-c**). EDX provided insight into elemental composition across the

entire depth of the fabric sample, as a thin coating present only on the surface would not produce a detectable signal. XPS and EDX together provided evidence that KFFCCQ is adhering to and coating both nylon and cotton fibers throughout the bulk of the sample.

The phenylalanine residues in KFFCCQ provide a metric to quantitatively determine release of KFFCCQ from NyCo fibers after aqueous rinsing. Absorbance of phenylalanine at 237 nm in water yielded a concentration-dependent absorption profile, which accurately probed samples of low concentration. The absorbance profile up to 2 mg/mL follows the linear fit

$$Absorbance = 0.2818c + 0.0317$$

where c indicates the concentration of KFFCCQ in mg/mL. KFFCCQ follows a linear fit at dilute concentrations, affording a method sensitive to low concentrations of peptide.

KFFCCQ-loaded NyCo was prepared by soaking in aqueous 0.5 wt % solution of KFFCCQ for 30 min with agitation every 10 min, followed by drying at 55 °C for 1 h. Dried, coated fabrics were rapidly stirred at 44 °C, 25 °C, or 16 °C in water for 0, 16, or 21 min. UV-Vis absorption (**Figure 5)** provided quantitative analysis of released KFFCCQ following lyophilization of collected water samples (n=3). KFFCCQ-loaded fabrics subjected to this rinse cycle exhibited a loss of peptide, with a rinse cycle performed at 44 °C for 16 min providing the most significant release of KFFCCQ from NyCo fibers, indicating a rapid release from fibers. Furthermore, NyCo subjected to a rinse cycle at 16 °C and 25 °C show marginal release from NyCo fibers, indicating warmer water disrupts KFFCCQ binding to a higher degree than colder water, as adhesion is most likely due to hydrogen bonding. Future studies revolve around the peptide-fiber binding mechanism.

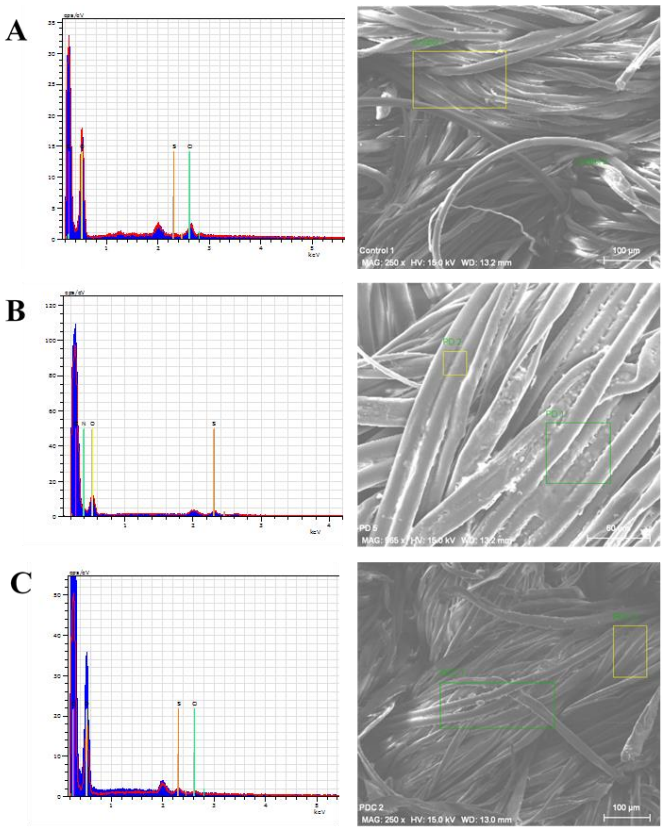

Figure 5.4: A. EDX analysis on SEM images of water treated NyCo fibers B. 0.5 weight % pad dry treated NyCo fibers C. 0.5 weight % pad dry cure treated NyCo fibers confirming the presence of KFFCCQ after coating steps.

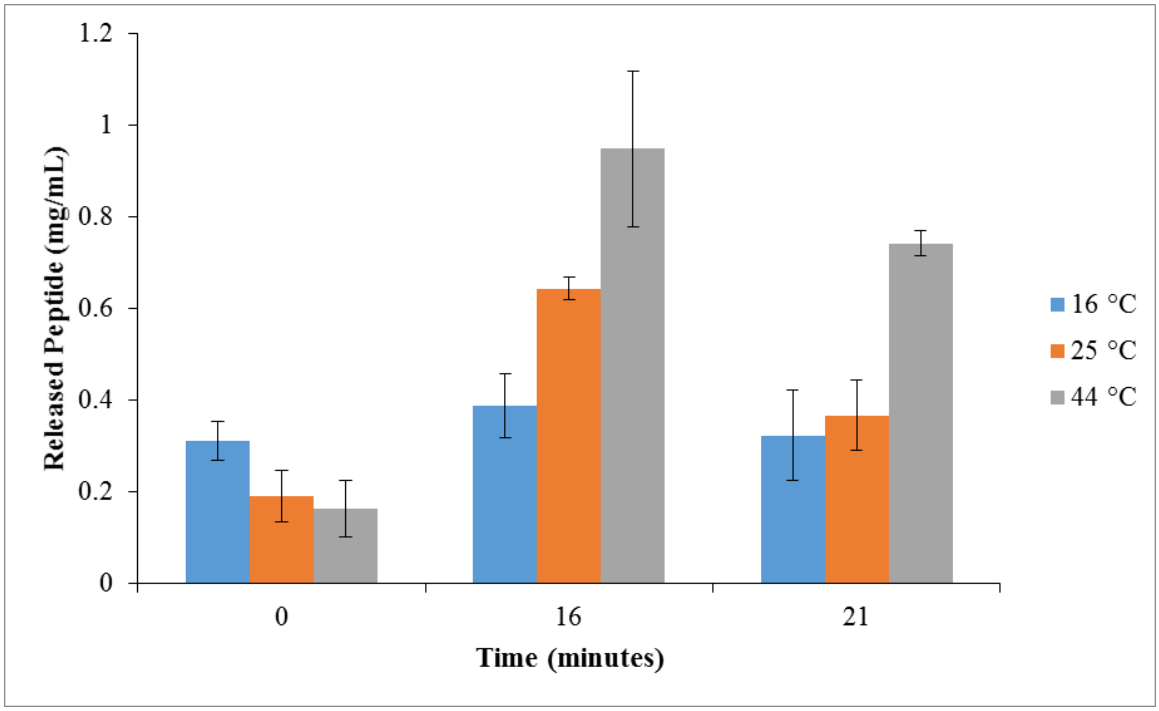

Figure 5.5: Total amount of peptide released from fiber surfaces as a function of temperature and time indicating an increase in the amount of release of KFFCCQ with increasing temperature and time (n = 3).

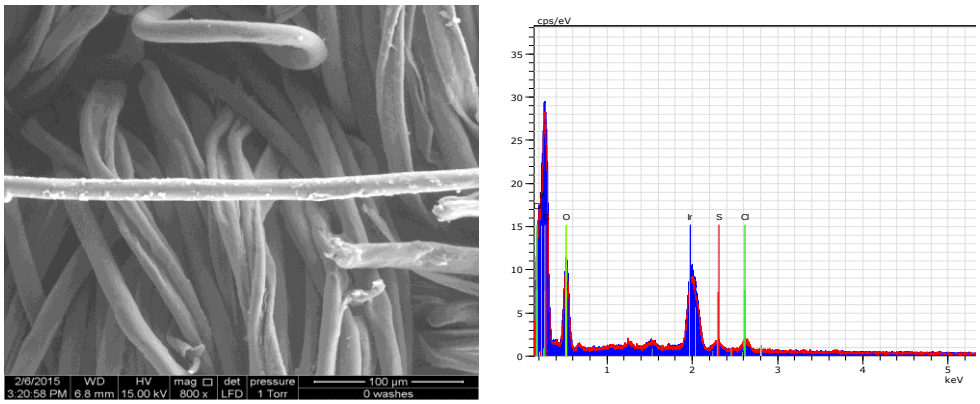

Figure 6. Control fabric and corresponding EDS for survivability studies which confirms the presence of KFFCCQ on fiber surfaces. The protruding nylon fiber provides a metric to compare between samples.

Rinse cycles at 25 °C for 20 min provided a metric of resistance of KFFCCQ coating to repeated rinse cycles (1, 3, 5, 10, and 15 rinse steps followed by drying at 55 °C for 30 min). For visual analysis of KFFCCQ release, nylon fibers protruding from the fabric surface provide a consistent metric. **Figure 5.6** depicts a protruding fiber coated in KFFCCQ with corresponding EDX analysis indicating its presence. **Figure 5.7** shows images of KFFCCQ-coated NyCo after repeated rinse cycles, indicating a loss of KFFCCQ from nylon fibers over time. The sulfur peak seen with EDX diminishes as the number of rinse cycles increases, in concordance with the qualitative images. Interestingly, cotton fibers did not exhibit this trend, as shown in Figure 8. Cotton fibers retain KFFCCQ at a similar level regardless of number of rinse cycles, suggesting a stronger adhesion to cotton fibers as compared to nylon fibers, either from chemical interactions such as hydrogen bonding or due to surface topology.[22] This model could also be utilized to predict the release of peptide from fabric to skin, postulating that a coating adhered to nylon fibers would be exposed to the skin before those adherent to cotton fibers.

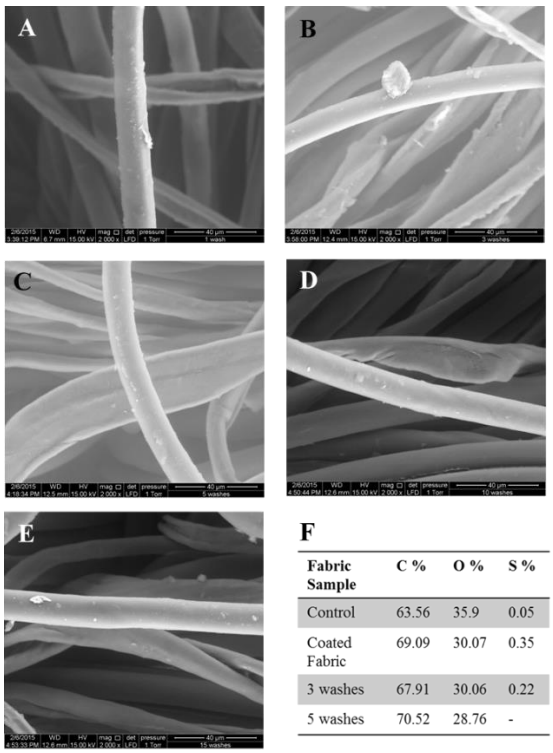

F

Fabric Sample	C %	O %	S %
Control	63.56	35.9	0.05
Coated Fabric	69.09	30.07	0.35
3 washes	67.91	30.06	0.22
5 washes	70.52	28.76	-

Figure 5.7: Model peptide coating on exposed nylon fibers as a function of number of rinse cycles, with 1 rinse (A) 3 rinses (B), 5 rinses (C), 10 rinses (D), and 15 rinses (E) examined. F. EDX confirms bulk loss of peptide as the number of rinse cycles increases.

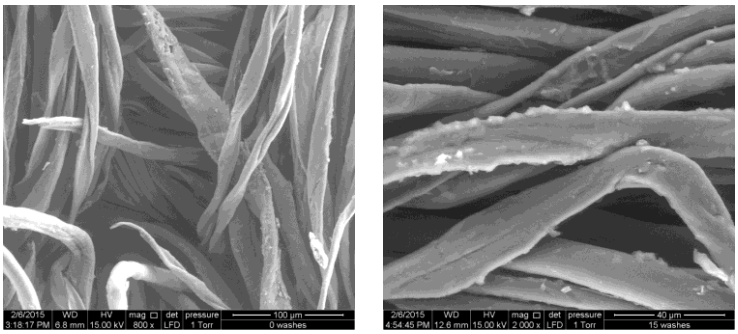

Figure 5.8: Cotton fibers after 0 rinses (left) and 15 rinses (right) indicating retention of the model peptide after multiple rinse cycles suggesting longevity of the coating.

The combination of elemental analysis through XPS and EDX, SEM imaging, and UV-Vis quantitative absorbance revealed both the KFFCCQ adhesion to NyCo fibers and its subsequent release following rinse cycles. While additional studies are needed for full evaluation of peptide release during more vigorous conditions, this study provided an

initial metric for evaluation of peptide coatings and release from fibers. The utilization of this model peptide KFFCCQ provides an inexpensive alternative for testing PNA adhesion to fiber surfaces, while also allowing for coating durability and efficacy studies.

5.2 Acknowledgements

The authors would like to think Steve McCartney for his assistance with SEM, Andrew Giordani for his assistance with XPS, and the US Army Research Office for funding to complete this work.

References

1 Martin, T, Kooi, S, Chang, S, Sedransk, K and Gleason, K, "Initiated chemical vapor deposition of antimicrobial polymer coatings." Biomaterials, 28 (6) 909-915 (2007)

2 Blyth, RC and Ucci, PA, "Stain resistant nylon fibers." US Patent 4,680,212, (1987)

3 Perelshtein, I, Applerot, G, Perkas, N, Guibert, G, Mikhailov, S and Gedanken, A, "Sonochemical coating of silver nanoparticles on textile fabrics (nylon, polyester and cotton) and their antibacterial activity." Nanotechnology, 19 (24) 245705 (2008)

4 Heisey, C, Wightman, J, Pittman, E and Kuhn, H, "Surface and adhesion properties of polypyrrole-coated textiles." Text Res J, 63 (5) 247-256 (1993)

5 MacKeen, PC, Person, S, Warner, SC, Snipes, W and Stevens, S, "Silver-coated nylon fiber as an antibacterial agent." Antimicrob Agents Ch, 31 (1) 93-99 (1987)

6 Xiao, X, Liu, X, Cao, G, Zhang, C, Xia, L, Xu, W and Xiao, S, "Atomic layer deposition TiO2/Al2O3 nanolayer of dyed polyamide/aramid blend fabric for high intensity UV light protection." Polym Eng Sci, 55 (6) 1296-1302 (2015)

7 Zhou, C-E, Kan, C-w, Yuen, C-wM, Matinlinna, JP, Tsoi, JK-h and Zhang, Q, "Plasma treatment applied in the pad-dry-cure process for making rechargeable antimicrobial cotton fabric that inhibits S. Aureus." Text Res J, 1-14 (2015)

8 Xue, C-H, Chen, J, Yin, W, Jia, S-T and Ma, J-Z, "Superhydrophobic conductive textiles with antibacterial property by coating fibers with silver nanoparticles." Appl Surf Sci, 258 (7) 2468-2472 (2012)

9 Nielsen, PE, Egholm, M and Buchardt, O, "Peptide nucleic acid (PNA). A DNA mimic with a peptide backbone." Bioconjugate Chem, 5 (1) 3-7 (1994)

10 Gaylord, BS, Heeger, AJ and Bazan, GC, "DNA detection using water-soluble conjugated polymers and peptide nucleic acid probes." P Natl Acad Sci, 99 (17) 10954-10957 (2002)

11 Wang, J, Palecek, E, Nielsen, PE, Rivas, G, Cai, X, Shiraishi, H, Dontha, N, Luo, D and Farias, PA, "Peptide nucleic acid probes for sequence-specific DNA biosensors." J Am Chem Soc, 118 (33) 7667-7670 (1996)

12 Meng, J, Da, F, Ma, X, Wang, N, Wang, Y, Zhang, H, Li, M, Zhou, Y, Xue, X and Hou, Z, "Antisense growth inhibition of methicillin-resistant Staphylococcus aureus by locked nucleic acid conjugated with cell-penetrating peptide as a novel FtsZ inhibitor." Antimicrob Agents Ch, 59 (2) 914-922 (2015)

13 Machado, A, Castro, J, Cereija, T, Almeida, C and Cerca, N, "Diagnosis of bacterial vaginosis by a new multiplex peptide nucleic acid fluorescence in situ hybridization method." PeerJ, 3 e780 (2015)

14 Sato, T, Sato, Y, Iwai, K, Kuge, S, Teramae, N and Nishizawa, S, "Fluorescence Imaging of siRNA Delivery by Peptide Nucleic Acid-based Probe." Anal Sci, 31 (4) 315-320 (2015)

15 Margus, H, Arukuusk, P, Langel, Ul and Pooga, M, "Characteristics of Cell-Penetrating Peptide/Nucleic Acid Nanoparticles." Mol Pharm, 13 (1) 172-179 (2016)

16 Nakase, I, Takeuchi, T and Futaki, S, "Cell Penetrating Peptides for Chemical Biological Studies." Cell-Penetrating Peptides: Methods and Protocols, pp. 387-396. (2015)
17 Williams, SR, Lepene, BS, Thatcher, CD and Long, TE, "Synthesis and Characterization of Poly(ethylene glycol)−Glutathione Conjugate Self-Assembled Nanoparticles for Antioxidant Delivery." Biomacromolecules, 10 (1) 155-161 (2009)
18 Ida, S and Endo, N, "Method for coloring fibrous material composed of phenolic resins." US Patent 3,918,901, (1975)
19 Liu, Y, Ma, K, Li, R, Ren, X and Huang, T, "Antibacterial cotton treated with N-halamine and quaternary ammonium salt." Cellulose, 20 (6) 3123-3130 (2013)
20 Perelshtein, I, Perkas, N and Gedanken, A, "Ultrasonic Coating of Textiles by Antibacterial and Antibiofilm Nanoparticles." Handbook of Ultrasonics and Sonochemistry, pp. 1-27. (2016)
21 Girardeaux, C, Zammatteo, N, Art, M, Gillon, B, Pireaux, J and Caudano, R, "Amination of poly (ethylene-terephthalate) polymer surface for biochemical applications." Plasmas Polym, 1 (4) 327-346 (1996)
22 Yu, Y, Yuan, J, Wang, Q, Fan, X, Wang, P and Cui, L, "A study of surface morphology and structure of cotton fibres with soluble immobilized-cellulase treatment." Fiber Polym, 15 (8) 1609-1615 (2014)

Chapter 6. Counterion Effect Upon Charged Poly(ether ester) Ionomers for Extrusion 3D Printing

(Published in ACS Applied Materials and Interfaces, **2017**)

Allison M. Pekkanen[1], Callie Zawaski[2], Abby R. Whittington[1,3], Christopher B. Williams[2], and Timothy E. Long[*]

Department of Chemistry and Macromolecules Innovation Institute, Virginia Tech, Blacksburg, VA 24061

[1]School of Biomedical Engineering and Sciences, Virginia Tech, Blacksburg, VA 24061

[2]Department of Mechanical Engineering, Virginia Tech, Blacksburg, VA 24061

[3]Department of Materials Science and Engineering, Virginia Tech, Blacksburg, VA 24061

*To whom correspondence should be addressed. E-mail: telong@vt.edu. TEL: (540) 231-2480

FAX: (540) 231-8517

Keywords: poly(ethylene glycol), ionomers, fused deposition modeling, additive manufacturing

6.1 Abstract

Water-soluble polymers as sacrificial supports for additive manufacturing (AM) facilitate complex features in printed objects. Few water-soluble polymers beyond poly(vinyl alcohol) enable material extrusion AM. In this work, charged poly(ether ester)s with tailored rheological and mechanical properties serve as novel materials for extrusion-based AM at low temperatures. Melt transesterification of poly(ethylene glycol) (PEG, 8k) and dimethyl 5-sulfoisophthalate afforded poly(ether ester)s of sufficient molecular weight to impart mechanical integrity. Quantitative ion exchange

provided a library of poly(ether ester)s with varying counterions, including both monovalent and divalent cations. Dynamic mechanical and tensile analysis revealed an insignificant difference in mechanical properties for these polymers below the melting temperature, suggesting an insignificant change in final part properties. Rheological analysis, however, revealed the advantageous effect of divalent countercations (Ca^{2+}, Mg^{2+} and Zn^{2+}) in the melt state and exhibited an increase in viscosity of two orders-of-magnitude. Furthermore, time-temperature-superposition identified an elevation in modulus, melt viscosity, and flow activation energy, suggesting intramolecular interactions between polymer chains and a higher apparent molecular weight. In particular, extrusion of poly(PEG_{8k}-co-CaSIP) revealed vast opportunities for extrusion AM of well-defined parts. The unique melt rheological properties highlighted these poly(ether ester) ionomers as ideal candidates for low-temperature material extrusion additive manufacturing of water-soluble parts.

6.2 Introduction

The prevalence of ion-containing polymers in both traditional and emerging applications enables widespread use in water-purification membranes, drug delivery agents, and conductive materials.[1] Significant research into novel, ion-containing monomers and novel combinations of established monomers, generates a large family of polymers for these high impact applications.[2] Incorporation of charge into a variety of polymer backbones permits tailoring of polymeric structures to address specific needs.[3] For example, Gao et al. synthesized charged poly(ethylene glycol) (PEG)-based polyurethanes, which displayed drastically different mechanical properties when

compared to inclusion of charge into PEG-based ammonium ionenes.[4] The presence of ions dramatically influences mechanical properties compared to neutral analogs.

The emerging technology of additive manufacturing (AM) focuses on tailoring part geometries and material properties for a customized product with well-defined features.[5] Compared to traditional subtractive processing methods, AM eliminates waste and creates well-defined, complex geometries not previously achievable.[6] Many different methods exist to fabricate a part layer, including vat photopolymerization, powder bed fusion, and material extrusion.[5] While vat photopolymerization continues to experience significant advances in new materials, established, commercial materials dominate many other printing types.[7] The applications accessible to AM expand through new materials development, paving the way to future personalized and on-demand printed parts.[7b]

Historically, thermoplastics dominate the most prevalent form of AM, material extrusion.[7a] A number of polymers, including acrylonitrile-butadiene-styrene (ABS) and polycarbonate, comprise a library of standardized printing parameters to control part geometry.[8] Commercially, material extrusion printers utilize these common polymers, which experience widespread use for the printing of end-use parts.[8b] ABS dominates commercial printing because of standardized printing parameters that generate well-defined parts.[9] Furthermore, in commercial AM systems, ABS co-extrudes with water-soluble support material, which selectively dissolved to achieve complex geometries not achievable through ABS printing alone.[10] Extrusion of support material requires temperature matching between the support and printed part, limiting materials selection. Currently, material extrusion research focuses on printing parameters and part mechanical properties, and the commercial availability of these materials makes them a

logical choice to develop in-house, rapid prototypers.[11] New polymer development for material extrusion AM lags behind other forms of AM, resulting in a disconnect to support emerging applications. This unique facet of material extrusion compared to other methods of AM makes research into new polymers extremely valuable.

Material extrusion generally does not result in potentially harmful byproducts, which plagues other methods of AM.[12] As a result of the decreased toxicity concern, extrudable water-soluble and biodegradable polymers act as small molecule delivery agents for biological applications.[13] These polymers, found in nature and synthetic chemistry, include poly(ethylene glycol) (PEG), poly(lactide-co-glycolide), and poly(vinyl alcohol) (PVOH).[14] A number of water-soluble polymers enable delivery of genes or water-insoluble drugs, which have previously exhibited low bioavailability to the human body.[13a, 13c, 15] Few examples exist of water-soluble polymers which have suitable rheological and mechanical properties necessary for AM via material extrusion.[16] Commercially, PVOH offers sufficient rheological properties to act as a water-soluble filament for material extrusion at high temperatures, necessitating the development of additional materials for low temperature printing of water-soluble material extrusion parts.[17] Furthermore, the incorporation of small molecules, such as drug or biological moieties, requires a processing temperature window below 75 °C, inaccessible for printing PVOH that prints above 200 °C.[18] Currently, water-soluble support materials dissolve upon completion of the print to afford complex structures that were previously unattained.[19] Previous research does not focus on printing water-soluble support materials, as the resolution and printability of these features is not vital to the integrity of

the final part. However, the need for bio-active materials with complex structures highlights the need for materials suitable for low-temperature extrusion.

Currently, there lacks a fundamental understanding in the role of charge in extrusion-based AM, suggesting a need for a new class of extrusion materials.[20] Supramolecular materials, including either hydrogen-bonding or charge-containing monomers, lack exploration in additive manufacturing, particularly in the field of material extrusion.[18] Interactions between polymer chains during the layer-by-layer process influence both printability and isotropy of the final printed part. Charge interactions and hydrogen bonding enable physical crosslinks between layers, which will presumably affect the integrity of a printed part. Currently, material extrusion utilizes only the commercial, charged polymer Eudagrit® and failed to investigate the role of ionic interactions to enhance printability.[20b] Therefore, a fundamental investigation of charge-containing polymers with low-temperature melt extrusion alongside water solubility presents a unique facet for material extrusion research.

Poly(ether ester)s represent a promising class of water-soluble polymers, with previous research utilizing these systems in ion exchange and battery applications.[21] In previous work, low molecular weight PEG and dimethyl 5-sulfoisophthalate (SIP) afforded a family of ionic poly(ether ester)s.[21a, 21c, 21d] An exchange to varying monovalent counter cations revealed a modulation of conductivity and ion exchange potential. Other reports imparted SIP into PTMO-segmented copolymers for the enhancement of mechanical properties, stressing the importance of charge inclusion on material strength.[21d, 22] As a result, charged polymers drive research to develop robust

water-soluble polymers for low-temperature material extrusion with potential to reduce anisotropy in printed parts.

This work focuses on the synthesis and characterization of water soluble poly(ether ester)s for low-temperature material extrusion. Low melting and processing temperatures permits the incorporation of additional biological molecules. The poly(ether ester)s undergo quantitative ion exchange to monovalent and divalent counterions to manipulate rheological responses and enhance processability. In particular, the exchange to divalent counter cations induces a significant increase in melt viscosity, which is key to successful filament printing. Furthermore, this exchange does not affect the room-temperature, bulk properties of the material, indicating a change in counterion does not affect final printed part properties. These copolymers represent a new class of materials suitable for low-temperature, material extrusion, which impart functionality and water solubility to the printed part.

6.3 Materials and Methods

6.3.1 Materials. Poly(ethylene glycol) (PEG_{8k}) (Sigma-Aldrich, M_n = 8,000 g/mol) and dimethyl 5-sulfoisophthalate sodium salt (SIP, Sigma-Aldrich, 98 %) were dried overnight in a vacuum oven at 50-60 °C before use. Sodium acetate (NaOAc) (Sigma-Aldrich, ≥99.0 %) was used as received. Titanium tetra(isopropoxide) was purchased from Sigma-Aldrich, and a 0.01 g/mL or 0.0132 g/mL titanium solution in anhydrous 1-butanol was prepared according to previous procedures. Potassium chloride, calcium chloride, zinc acetate, and magnesium chloride were received from Sigma-Aldrich and used as received. Cellulose dialysis tubing (MWCO = 3,500 g/mol) was obtained from

Fisher Scientific and cut into usable lengths. All solvents were received from Spectrum and were used as received. Nitrogen gas (Praxair, 99.999 %) was used as received.

6.3.2 Analytical Methods. Differential scanning calorimetry (DSC) was performed with a nitrogen flow of 50 mL/min at a heating rate of 10 °C/min and a cooling rate of 100 °C/min on a TA instruments Q1000 DSC calibrated using indium (mp = 156.60 °C) and zinc (mp = 419.47 °C) standards. The maximum of the melting endotherm afforded melting temperatures. Thermogravimetric analysis (TGA) was performed using a TA Instruments Q50 from 25 – 600 °C with a heating rate of 10 °C/min. Dynamic mechanical analysis (DMA) was performed on a TA Instruments Q800 dynamic mechanical analyzer in tension mode. Experiments were conducted at a temperature ramp of 3 °C/min with a frequency of 1 Hz, an oscillatory amplitude of 10 μm, and a static force of 0.01 N. Rheological analysis was performed on a TA Instruments AR G2 rheometer using 25 mm, disposable, aluminum, parallel plates under air. Melt stability experiments were run at an angular frequency of 1 rad/s with oscillatory strain of 1 %. Zero-shear viscosity measurements were performed at 78 °C with angular frequencies ranging from 0.1 – 100 rad/s with an oscillatory strain of 1 %. Time-temperature superposition was performed from 70 – 170 °C (10 °C per step), with samples loaded at 120 °C. Angular frequencies ranged from 1 – 100 rad/s at 1 % strain under air with a reference temperature of 100 °C. PEG_{8k} viscosity was measured using a concentric cylinder geometry surrounded by a water-heated jacket operating at 78 °C with frequencies ranging from 0.1-100 rad/s under a constant 1 % strain. Tensile testing was performed on film-pressed dogbones with an Instron 5500R with a crosshead motion of 5 mm/min and an initial grip-to-grip separation of 26.75 mm. Molecular weight was performed by size exclusion chromatography (SEC)

through Agilent aquagel-oh columns and in conjunction with a Waters 2414 refractive index detector and Wyatt miniDAWN Treos MALS. Polymers were dissolved in 54/23/23 v/v/v H_2O/MeOH/Acetic acid buffered with 0.1 M NaOAc at 1 mg/mL (dn/dc = 0.2524). Polymer solutions filtered through a 0.45 µm PTFE filter were analyzed at 30 °C and a flow rate of 1 mL/min. Statistical testing utilizing Analysis of Variance (ANOVA) with a Tukey's HSD revealed significant differences between groups and was calculated using JMP Statistical software.

6.3.3 Synthesis of poly(PEG8k-co-NaSIP). Reactions were conducted in a single-necked, 100-mL, round-bottomed flask equipped with a distillation apparatus (dried overnight in a 150 °C oven), overhead stirrer equipped with a metal stirrod, and nitrogen inlet. PEG_{8k} (1 mol eq.) and SIP (1 mol eq.) were dried in a vacuum oven (60 °C) overnight before use. PEG_{8k}, SIP, and NaOAc (0.1:1 mole ratio NaOAc:SIP) were added to the flask. Titanium tetra(isopropoxide) (40 ppm) was added and used to catalyze the reaction. Degassing and purging with nitrogen three times allowed the synthesis to proceed oxygen free. The flask was submerged into a silicone oil bath under constant nitrogen purge until the reactants were covered, and the reaction proceeded at 180 °C until all reactants were molten (~5 min). Vacuum was then applied until a pressure of 0.15 mmHg was achieved and the reaction stirred from 180 – 196 °C for 2 h. The resulting viscous polymer was isolated and used without further purification. **Scheme 6.1** illustrates the overall synthetic strategy.

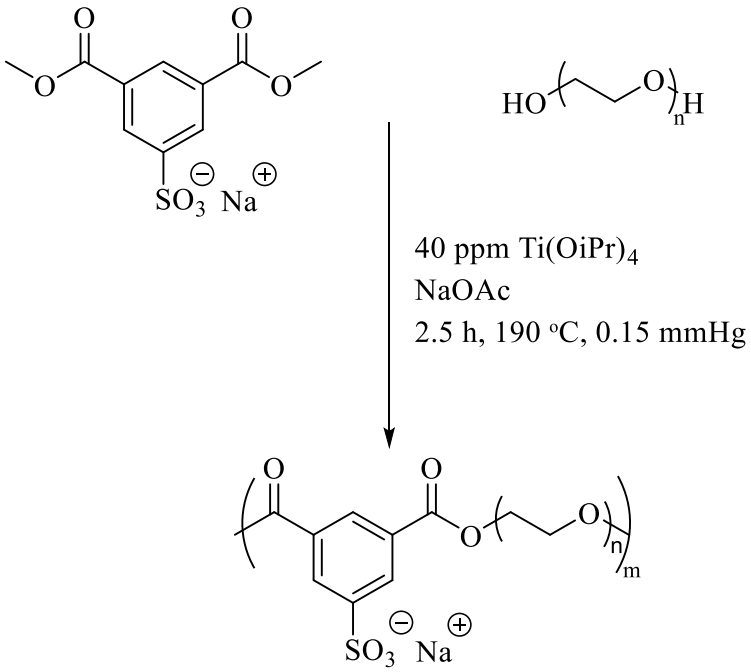

Scheme 6.1. Melt transesterification of poly(ethylene glycol) and sulfonated isophthalate (SIP) to yield ion-containing poly(ether ester)s.

6.3.4 Ion exchange of poly(PEG8k-co-NaSIP). All polymers were exchanged following a similar procedure (**Scheme 6.2**), with poly(PEG_{8k}-co-CaSIP) used as an example. A solution of 10 wt % poly(PEG_{8k}-co-NaSIP) in water was prepared and separated equally into cellulose dialysis tubing (MWCO: 3,500 g/mol). 5 M eq $CaCl_2$ was added to the tubing and water surrounding polymers changed on days 1, 2, and 3. Poly(PEG_{8k}-co-CaSIP) was then allowed to equilibrate against RO water for 3 additional days. The resulting aqueous solution was frozen and lyophilized until a constant weight was achieved. The white, fluffy polymer was isolated and used without further purification. Poly(PEG_{8k}-co-KSIP) was prepared with KCl, poly(PEG_{8k}-co-ZnSIP) was prepared with $Zn(OAc)_2$, and poly(PEG_{8k}-co-MgSIP) was prepared with $MgCl_2$.

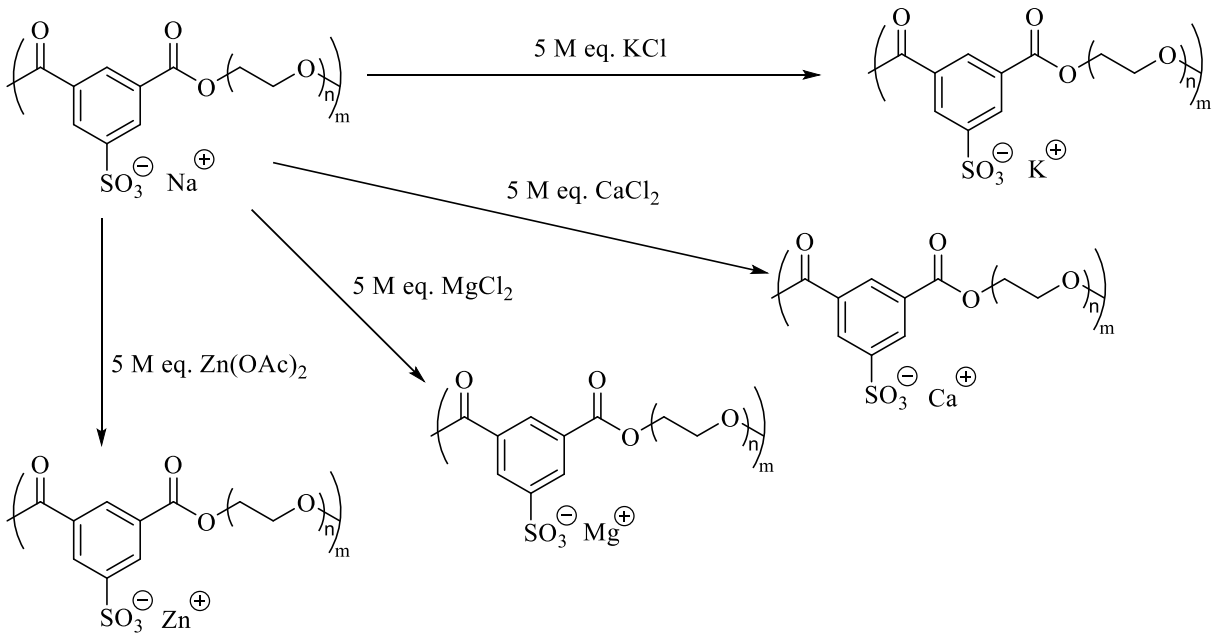

Scheme 6.2. Ion exchange of poly(PEG_{8k}-co-NaSIP) to a range of counterions is accomplished through dialysis in water with excess salt on days 1-3. Each polymer is equilibrated against water for days 4-6 to ensure removal of excess salt.

6.3.5 Compression molding poly(ether ester)s. Polymers were melt pressed between two 16 mil stainless steel plates layered with Kapton® films using a PHI Q-230H manual hydraulic compression press. A Rexco Partall® Power Glossy Liquid mold release agent was applied to the Kapton® films to prevent poly(ether ester)s adhesion. Samples were heated for ~3 min at 90 °C before the top plate was added. After a ~1 min isotherm at 90 °C, 4 press-release cycles were performed, the first two utilizing 5 tons of force and the second two using 10 tons of force. The films were removed from the stainless steel plates and allowed to slowly cool to room temperature between the Kapton® films.

6.3.6 Water Solubility. A novel method to calculate polymer structure water solubility based on complete dissolution was implemented. Polymers were weighed (~3 g), placed in a cylindrical silicone mold (16 mm height and 22.5 mm diameter), and heated in an oven until melted (approximately 80 °C for 30 min). The molten polymers were left in

the oven to cool overnight producing smooth surfaces. Each polymer sample was wrapped in a nylon mesh and suspended in excess DI H_2O with agitation. The amount of time for complete polymer dissolution was determined by physical and optical inspection for any remaining solid or gel like substances in the nylon mesh. Relative dissolution rate was calculated as follows:

$$Dissolution\ Rate\left(\frac{mg}{cm^2 * min}\right) = \frac{Initial\ Mass\ (mg)}{Initial\ Surface\ Area\ (cm^2) * Complete\ Dissolution\ Time\ (min)}$$

Cylindrical polymer dissolution studies were performed in triplicate and errors are presented as standard deviations unless otherwise noted. Minitab 17 was used for Pearson correlation analysis where appropriate and ANOVA with $p < 0.05$ determined statistical significance. Complete dissolution time was determined for poly(PEG_{8k}-co-CaSIP) infills by placing each printed part in a nylon mesh as described above.

6.3.7 Filament Processing. Poly(PEG_{8k}-co-CaSIP) filament was created using a desktop scale single screw extruder set to a single temperature of 70 °C. The white, fluffy polymer was fed directly into the extruder, processed and pelletized, before using the pellets to create filament. A conveyor belt was used to pull the filament to a diameter of 1.75 mm from a 2 mm diameter die. Forced convection was used along the conveyor belt and the extruder hopper to accelerate solidification and maintain a circular cross section. Finished filament was stored and sealed with desiccant.

6.3.8 Material Extrusion Printing from Filament. The poly(PEG_{8k}-co-CaSIP) filament was printed using a direct drive system with an E3D all-metal-hot-end with a 0.4 mm diameter nozzle. A hot end temperature of 70 °C using a glass bed heated to 40 °C achieved successful prints. Surface treatment by adhering tape with sufficient surface

roughness to the glass was used to improve first layer adhesion. Forced convection was used to improve part quality of small features.

6.4 Results and Discussion

Melt transesterification with titanium catalyst afforded poly(PEG_{8k}-co-NaSIP) through typical melt polymerization as shown in **Scheme 6.1.** Advantageously, neither reactant has a boiling point at the reaction temperature, allowing for application of vacuum and subsequent removal of the methanol byproduct to occur as soon as the reactants reached the molten state. In contrast to conventional melt polymerization, this transesterification reaction did not require time in the melt prior to application of vacuum, providing a facile route to charged poly(ether ester)s at significantly shortened times. A heterogeneous melt formed at the onset, which clarified as the reaction proceeded. Insolubility of SIP in PEG at any molecular weight suggested that transesterification solubilized SIP in the melt.

Following polymerization, quantitative ion exchange occurred with a 10 wt % aqueous solution of poly(PEG_{8k}-co-NaSIP). To ensure homogeneity between samples, splitting of one large batch of poly(PEG_{8k}-co-NaSIP) allowed direct comparison between samples without variation in precursor molecular weight or molecular weight distribution. For each ion exchange, the weight of the polymer sample translated to the theoretical number of moles of sodium. Addition of 5 M eq salt (KCl, $MgCl_2$, $CaCl_2$, and $Zn(OAc)_2$) to aqueous solutions is shown in **Scheme 6.2**. The solutions dialyzed against water for 6 d, with additional 5 M eq salt added on days 2 and 3. A large excess of salt

ensured complete ion exchange and equilibrations against water on days 4, 5, and 6 drove out excess salt.

Thermal, Molecular Weight, and Solubility Analysis. DSC analysis conducted on the series of poly(ether ester)s showed that neither the melting temperature nor the % crystallinity calculated from DSC changed significantly upon ion exchange (**Table 1**).[41] In comparison to neat PEG_{8k}, both the melting temperature and % crystallinity decreased substantially, suggesting that low concentrations of ionic groups disrupted PEG_{8k} crystallinity. Restriction of the polymer crystallinity likely arises due to the increased molecular weight and incorporation of charged groups. Consistency between % crystallinity enabled evaluation of potential differences between polymer samples below T_m, as any differences between the samples directly resulted from the counterion.

Sample	***T_g (°C)***	***T_m (°C)***	***ΔH_f (J/g)***	***Crystallinity (%)***	***Young's Modulus (MPa)***	***% Elongation***	***Dissolution Rate ($mg/cm^2/min$)***
Poly(PEG_{8k}-co-NaSIP)	-42	55	92	47	225 ± 26	47 ± 20	2.7 ± 0.1
Poly(PEG_{8k}-co-KSIP)	-44	54	99	50	185 ± 10	24 ± 6	2.3 ± 0.1
Poly(PEG_{8k}-co-CaSIP)	-44	57	98	50	210 ± 21	22 ± 13	2.5 ± 0.1
Poly(PEG_{8k}-co-ZnSIP)	-45	55	99	50	172 ± 12	12 ± 1.6	3.0 ± 0.2
Poly(PEG_{8k}-co-MgSIP)	-46	55	89	45	190 ± 12	55 ± 19	-
PEG_{8k}	-	64	175	89	-	-	8.3 ± 0.5

Table 6.1. Thermomechanical properties of ion exchanged poly(PEG_{8k}-co-NaSIP) evaluated with DSC (T_m), DMA(T_g), and tensile measurements. Crystallization percentages as determined by DSC, calculated from 100% crystalline PEO sample with a $\Delta H_{f,c}$ = 196.8 J/g.[41] PEG_{8k} does not successfully form films capable for DMA or tensile analysis.

In addition to thermal characterization, molecular weight of the samples determined by SEC revealed minor changes in molecular weight upon ion exchange, as shown in **Table 6.2**. SEC failed to detect a significant drop in molecular weight following dialysis. Each unimodal elution peak revealed only slight variations between samples, potentially deriving from varied ionic charge and size affecting polymer coil dimensions. Changes in polymeric coiling arose from varying counterion and concentration, which indicate a possible crown ether effect commonly seen in PEG polyethers.[42, 43] Differences in polymer coiling likely affected the scattering peak used to calculate absolute molecular weight from SEC. Since this series of polymers derived from the same batch and no significant drop in molecular weight observed, polymer properties obtained from film and melt rheological properties elucidated the effect of counter cation.

Sample	M_n (g/mol)	M_w (g/mol)	Đ
Poly(PEG_{8k}-co-NaSIP)	16,400	23,700	1.4
Poly(PEG_{8k}-co-KSIP)	11,700	16,900	1.4
Poly(PEG_{8k}-co-CaSIP)	12,600	22,000	1.8
Poly(PEG_{8k}-co-ZnSIP)	23,300	32,400	1.4
Poly(PEG_{8k}-co-MgSIP)	9,600	20,300	2.1

Table 6.2. Molecular weight of ion exchanged poly(PEG_{8k}-co-NaSIP) measured by SEC show insignificant changes in molecular weight with ion exchange.

Control PEG dissolution experiments (consisting of neat PEG from 8 g/mol to 100 g/mol) revealed a molecular weight dependence on dissolution rate (**Figure 6.S1**). A range of PEG number-average molecular weights provided facile comparison with poly(PEG_{8k}-co-XSIP) samples which possessed molecular weights ranging from 17 g/mol to 32 /mol (**Table 6.2**). Dissolution studies with ionomers revealed a range of

dissolution rates, from poly(PEG_{8k}-co-ZnSIP) with the fastest to poly(PEG_{8k}-co-KSIP) with the slowest (**Table 6.1, Figure 6.S2**). Interestingly, an opposite trend exists between the ion-exchanged samples and dissolution rate, where decreased molecular weights resulted in slower dissolution rates. Pearson correlation studies comparing ionic charge (+1 versus +2) to dissolution rate revealed a positive medium strength of correlation (r = 0.446), suggesting dissolution rate increases with increasing ionic charge. Likely, the interaction between ions and PEG_{8k} influences dissolution, providing an additional metric for tailored dissolution.

Thermomechanical Analysis. DMA evaluated viscoelastic behavior below melting temperature (T_m), as shown in **Figure 6.1**. DMA, performed at 1 Hz and 3 °C/min, detected a glass transition temperature (T_g) near -44 °C for all samples, similar to pure PEG (**Table 6.1**).[44] Thermomechanical properties below T_m revealed insignificant change as a function of counterion. Slight variations in storage modulus at low temperatures did not distinguish monovalent from divalent cations, suggesting that ionic exchanges to divalent counterions did not affect the glassy state of the materials. The similarities between samples corroborated the comparable crystallinity percentages, and suggested that PEG drives the behavior of the polymers in the solid state. The broad T_g's of these polymers (calculated from tan delta) and lack of a plateau at temperatures above T_g further suggested that ionic associations did not influence solid-state properties. The low concentration of ions in the samples (~0.3 mol %) likely prevented significant ionic aggregation, which in turn did not perturb the solid-state properties of the poly(ether ester)s. The modulus in this region constantly decreased until flow, suggesting a dominance of PEG in the thermomechanical properties of the polymers. The insignificant

difference between samples allowed for material selection based solely on melt extrusion conditions without affecting part behavior at room temperature.

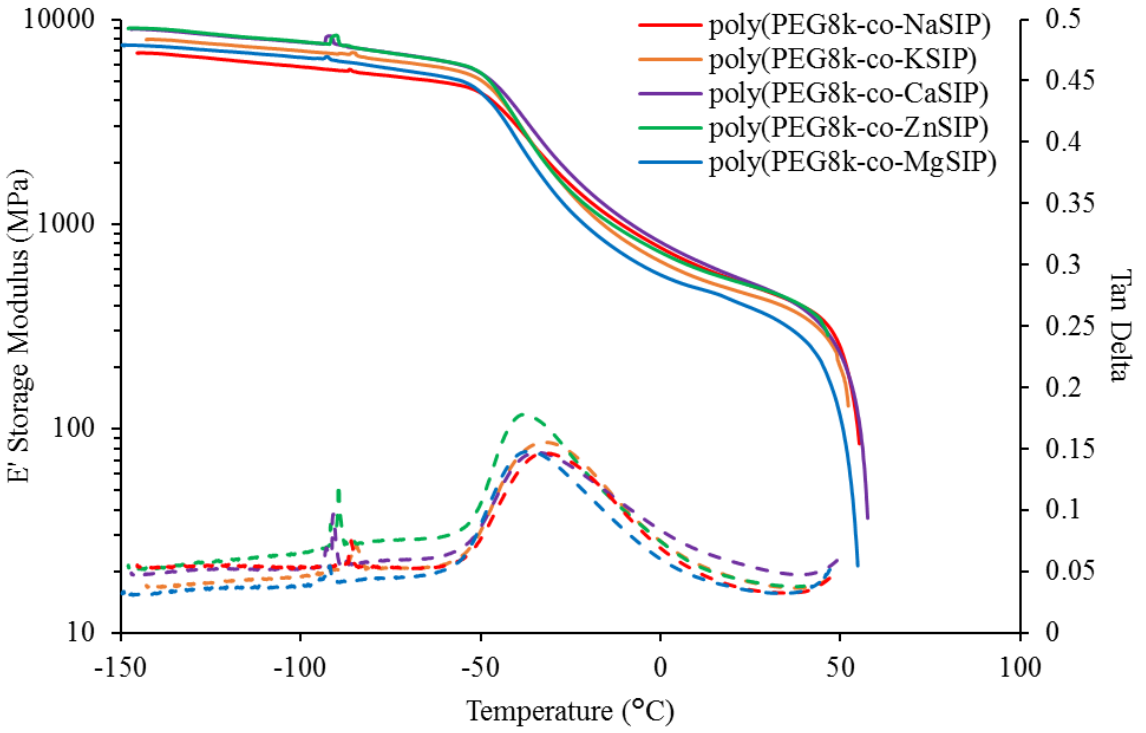

Figure 6.1. Dynamic mechanical analysis of ion-exchanged poly(PEG_{8k}-co-NaSIP) shows insignificant changes between the samples in the solid state. Solid lines represent E' storage modulus behavior and dashed lines represent tan delta.

To further confirm the similarity between polymer samples in the bulk film state, tensile measurements of film-punched dogbones revealed both the Young's modulus and the elongation of polymer samples before break, as shown in **Table 6.1**. Only poly(PEG_{8k}-co-ZnSIP) demonstrated a significant change in Young's modulus upon ion exchange, which again suggested that PEG drives the solid behavior. The presence of ionic groups in the polymer sample lent structural integrity as compared to commercial PEG homopolymers, highlighted through the lack of attainable tensile data from neat PEG samples up to M_n = 35,000 g/mol. Despite the low concentrations of ions in the

polymer samples, they played a large role in the structural integrity of the samples. The inclusion of ionic groups allowed for a much lower molecular weight polymer (~25,000 g/mol charged vs. 100,000 g/mol uncharged) to achieve favorable mechanical properties and processing capabilities. Analysis of SIP-terminated poly(XSIP-b-PEG_{8k}-b-XSIP) prepared under similar reaction conditions highlighted this trend. Thermal characterization showed a decrease in melting temperature and crystallinity and an increase in melt viscosity as compared to PEG_{8k}, suggesting the successful introduction of ionic groups into the polymer structure (**Table 6.S1, Figure 6.S3**). The inclusion of ionic groups enabled this enhanced mechanical properties at a lower molecular weight.

Rheological Characterization. Rheological characterization of ion-exchanged poly(ether ester)s performed at 78 °C revealed significant changes in melt viscosity with varying counterions, as seen in **Figure 6.2**. An exchange to monovalent counterions, such as potassium, revealed insignificant change in melt viscosity. However, divalent counterions induced a marked increase in melt viscosity. Poly(PEG_{8k}-co-CaSIP) exhibited the highest melt viscosity, suggesting the strongest ionic interactions. Ionic exchange to poly(PEG_{8k}-co-MgSIP) and poly(PEG_{8k}-co-ZnSIP) both experienced an increase in melt viscosity by one order-of-magnitude. All of these ionomers exhibited a melt viscosity larger than neat 8k and 35k PEG, suggesting a significant influence of ionic groups on melt viscosity. Calcium ions presumably demonstrated a propensity to form larger crown ethers, likely increasing the amount of salt present relative to magnesium and zinc samples and thus changing the melt viscosity of the final polymer.[45]

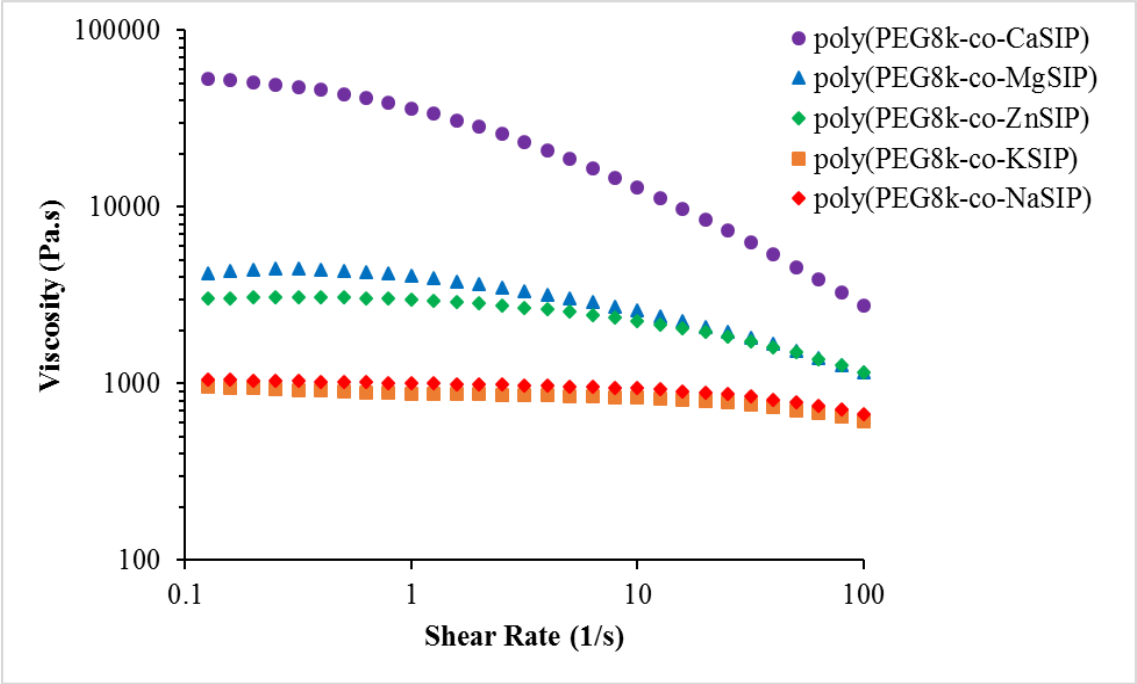

Figure 6.2. Ion exchange of poly(PEG_{8k}-co-NaSIP) has a dramatic effect on melt viscosity to lend a higher apparent molecular weight. Samples were measured at 78 °C.

To confirm the hypothesis of enhanced ionic interactions upon exchange to divalent cations, time-temperature-superposition (TTS) of monovalent counterion poly(PEG_{8k}-co-XSIP) revealed a lack of crossover from G' to G" over a range of temperatures and angular frequencies (**Figure 6.S4**). The sodium and potassium counterions failed to induce physical crosslinking between polymer chains in the samples, highlighting their inability to aggregate and construct chain mobility. When exchanged to divalent counter cations, a crossover of G' and G" suggested physical crosslinks and indicated a degree of association between charges (**Figure 6.3**). In these polymers, the physical crosslinks restricted chain mobility causing a significant increase in melt viscosity. The divalent cations interacted with two sulfonate groups simultaneously, the majority of which are between two polymer chains because of low ion concentrations. Physical crosslinking caused enhanced melt viscosity seen in polymers exchanged with divalent cations, without changes in molecular weight,

dispersity, or morphology. Melt stability elucidated this phenomena, with poly(PEG_{8k}-co-CaSIP) exhibiting an increased melt viscosity over time (**Figure 6.S6**). Excess calcium present in the crown ether domain of the polymer samples induced an increase in melt viscosity over time. When molten, calcium ions previously associated with one or no sulfonate group coupled between two sulfonate groups, thus affecting the number of physical crosslinks in the polymer sample and restricting chain mobility.

The Arrhenius fits of shift factors (a_T) calculated from poly(ether ester)s indicated a separation between monovalent and divalent cations (**Table 6.S2**). Divalent counter cations provided a higher energy barrier for polymer flow as compared to monovalent counterions, which also suggested a higher association strength. Most interestingly, poly(PEG_{8k}-co-MgSIP) exhibited the strongest ionic interactions, contrary to zero-shear viscosity experiments, which suggested calcium ions exhibited the strongest ionic interactions. Examination of the TTS viscosity data corroborated the higher viscosity seen in the poly(PEG_{8k}-co-MgSIP) during the TTS experiment (**Figure 6.S6**). The varied thermal history experienced by the polymers in shear sweep versus TTS experiments explained the differences in viscosity between the two experiments. Poly(ether ester)s experienced an elevated temperature upon loading (120 °C) during TTS experiments versus zero-shear viscosity experiments. As seen in **Figure 6.S6**, poly(PEG_{8k}-co-MgSIP) exhibited a crossover point upon cooling, suggesting a variation in ionic associations upon the application of heat. This further supported the claim of significant ionic presence in the PEG domain due to a kinetic effect during dialysis, as ionic groups further associated between two sulfonate groups upon thermal annealing during TTS. A higher association resulted from this thermal step and a shift to lower frequency in crossover

showed a change in chain relaxation. These results highlighted the effect the divalent counterions have on the melt properties of the polymers.

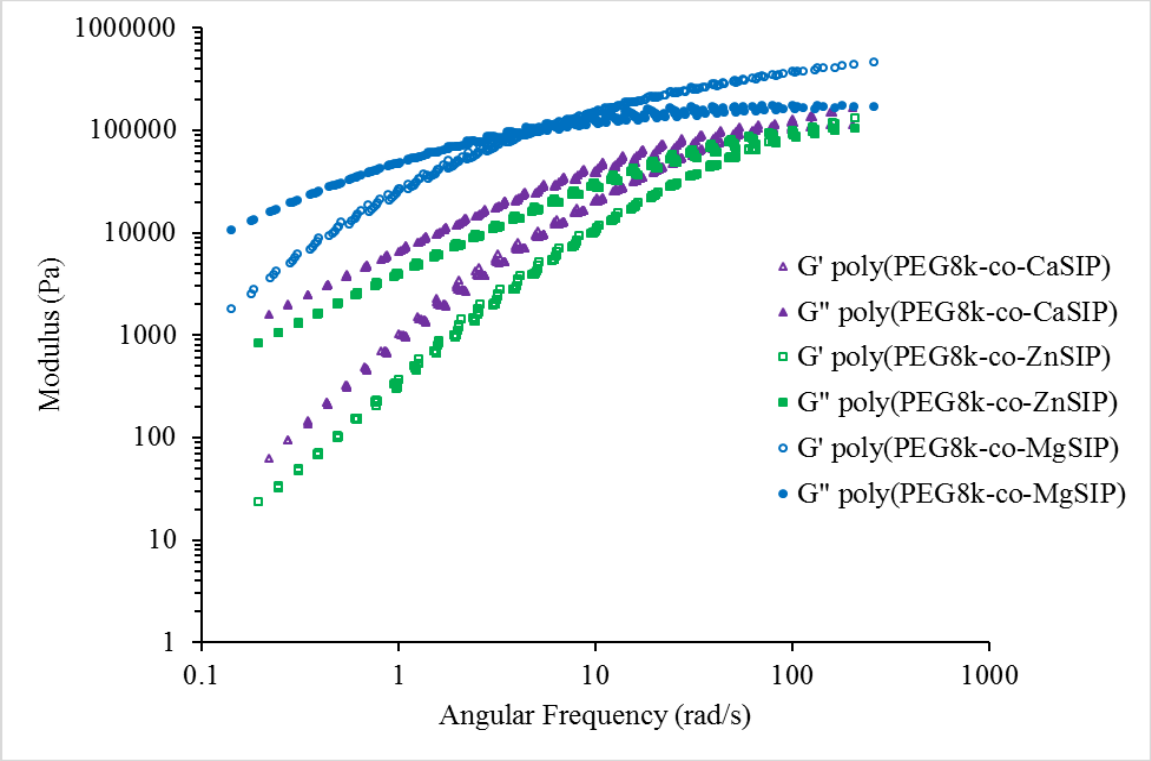

Figure 6.3. Divalent counterions show crossover points in TTS at high frequency, indicating ionic association. Magnesium counterions exhibit the strongest binding as indicated by the shift in the crossover points.

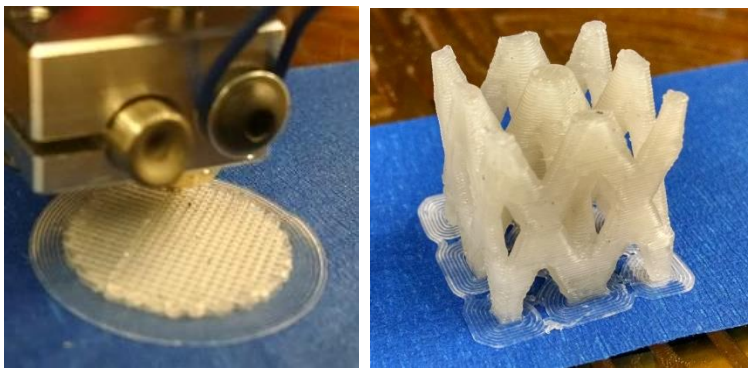

Figure 6.4. poly(PEG8k-co-CaSIP) exhibits printability through extrusion 3D printing, affording well-defined structures.

Material Extrusion Additive Manufacturing. A single screw extruder operating at 70 °C afforded filament of poly(PEG_{8k}-co-CaSIP) of constant diameter (1.8 ± 0.1 mm). Following successful filament formation, extrusion AM of poly(PEG_{8k}-co-CaSIP) produced well-defined parts. The poly(PEG_{8k}-co-CaSIP) exhibited minimal oozing upon stopping and starting the print, as evidenced in **Figure 6.4.** Furthermore, parts exhibited fine features distinguishable upon printing through a 0.4 mm diameter nozzle. This polymer is the first example of successful low-temperature material extrusion utilizing melted filament, with the maximum printing temperature not exceeding 70 °C. In conjunction with its low printing temperature, poly(PEG_{8k}-co-CaSIP) effectively printed ~15 °C above its melting point, a unique processing characteristic for any application due to the polymer's high viscosity. The sharp transition between molten and solid state, revealed in DSC permitted processing of this polymer at relatively low temperatures. Furthermore, the melt viscosity of poly(PEG_{8k}-co-CaSIP) contributed significantly to the high fidelity of the final printed part, as high viscosity limited flow after extrusion. These viscoelastic properties enabled the filament to act as a piston to drive successful material extrusion. Finally, the small temperature difference between printer (70 °C) and environment (30-40 °C) increased the time to fall below T_m, hindering many other polymers' ability to print at a low temperature. Low temperatures demand a polymer that is capable of surviving an elongated solidification time while maintaining shape. The effect of counterion on the processing conditions and resulting material properties of 3D printed parts is the focus of current and future study. Parts printed using poly(PEG_{8k}-co-CaSIP) ranging from 0 % infill to 100 % infill provided dissolution of post-processed ionomer (**Figure 6.S10**). As expected, the printed part with 0 % infill dissolved in

approximately 8 min, while the 100 % infilled polymer dissolved in 103 min. Coupling polymers and print design, material extrusion facilitates tailored dissolution for controlled release applications. The unique high melt viscosity combined with a sharp melting transition temperature of poly(PEG_{8k}-co-CaSIP) are well suited for low-temperature material extrusion.

6.5 Conclusion

This study examined the introduction of low concentrations of anions into PEG to afford poly(ether ester) ionomers. The effect of divalent ions on the thermomechanical properties of poly(ether ester)s revealed an insignificant effect as a function of counterion. Even at low ion concentrations, these polymers demonstrated a substantial change in melt rheological properties while retaining PEG-like bulk properties below T_m. Furthermore, introduction of divalent ions significantly enhanced the processability for extrusion AM, as evidenced through the creation of complex parts. This family of poly(ether ester)s represents a new class of water-soluble, ion-containing polymers with sufficient mechanical properties for successful low temperature material extrusion.

6.6 Acknowledgements

The authors would like to thank Joseph M. Dennis for helpful discussions throughout the project.

6.7 Supplemental Information

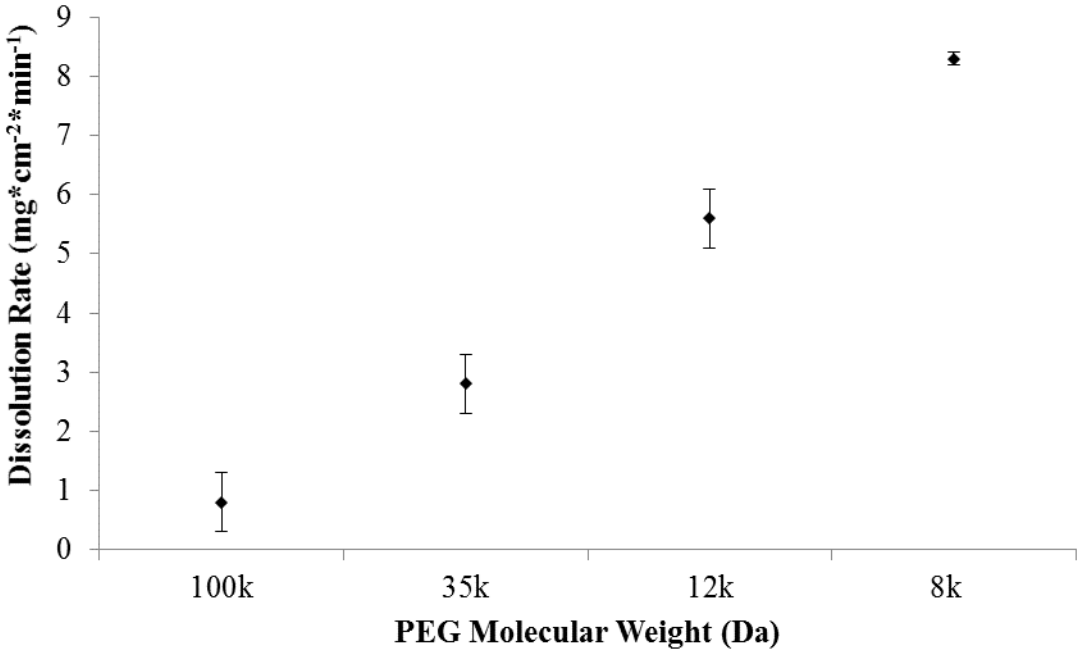

Figure 6.S1. Dissolution rates of neat PEG. As molecular weight decreases, dissolution rates increase, so less time is required to dissolve lower molecular weight PEGs. All rates are statistically significant ($p<0.05$).

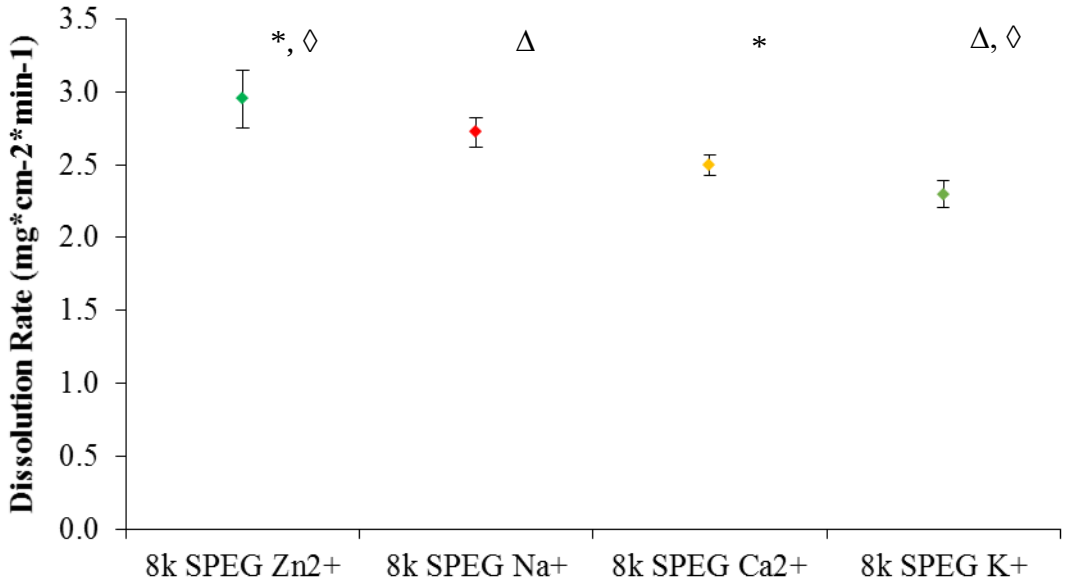

Figure 6.S2. Dissolution rates of ion exchanged SPEGs. As molecular weight decreases, dissolution rates decrease, so less time is required to dissolve lower molecular weight SPEGs. "*", "Δ" and "◊" represent the pairs that are statistically significant ($p < 0.05$).

Sample	T_m (°C)	Crystallinity (%)
PEG_{8k}	64	89
Poly(NaSIP-b-PEG_{8k}-b-NaSIP)	54	50
Poly(CaSIP-b-PEG_{8k}-b-CaSIP)	56	41

Table 6.S1. Thermal characterization of poly(XSIP-b-PEG_{8k}-b-XSIP) reveals a decrease in both melting temperature and % crystallinity as compared to neat PEG_{8k}.

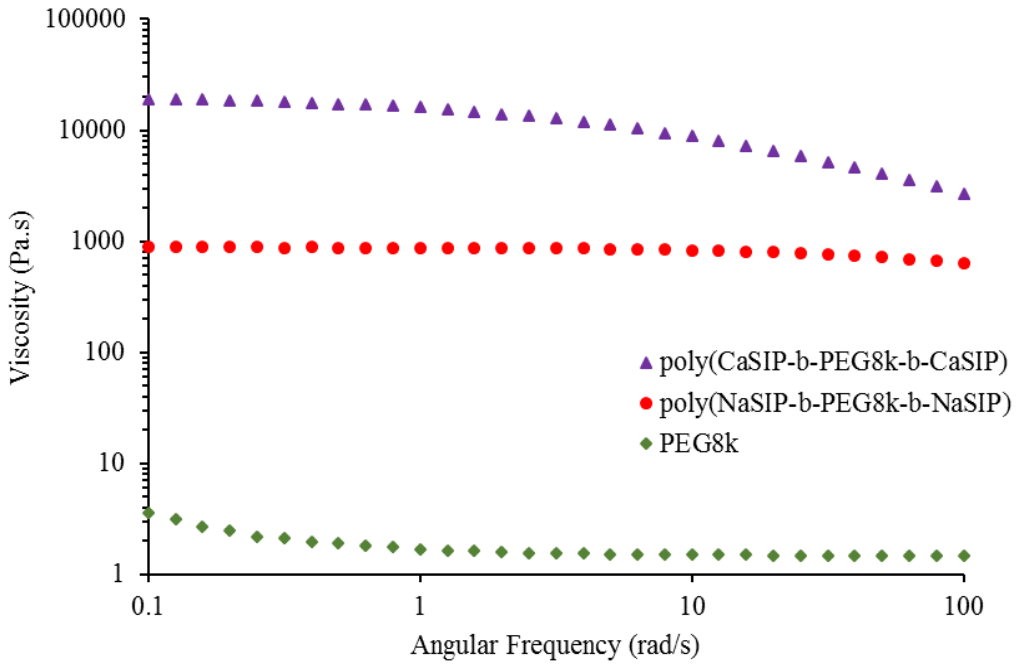

Figure 6.S3. Rheological measurements of poly(XSIP-b-PEG_{8k}-b-XSIP) reveal orders-of-magnitude changes between neat PEG_{8k}, Na counter cations, and Ca counter cations, indicating a significant contribution of ions to rheological properties.

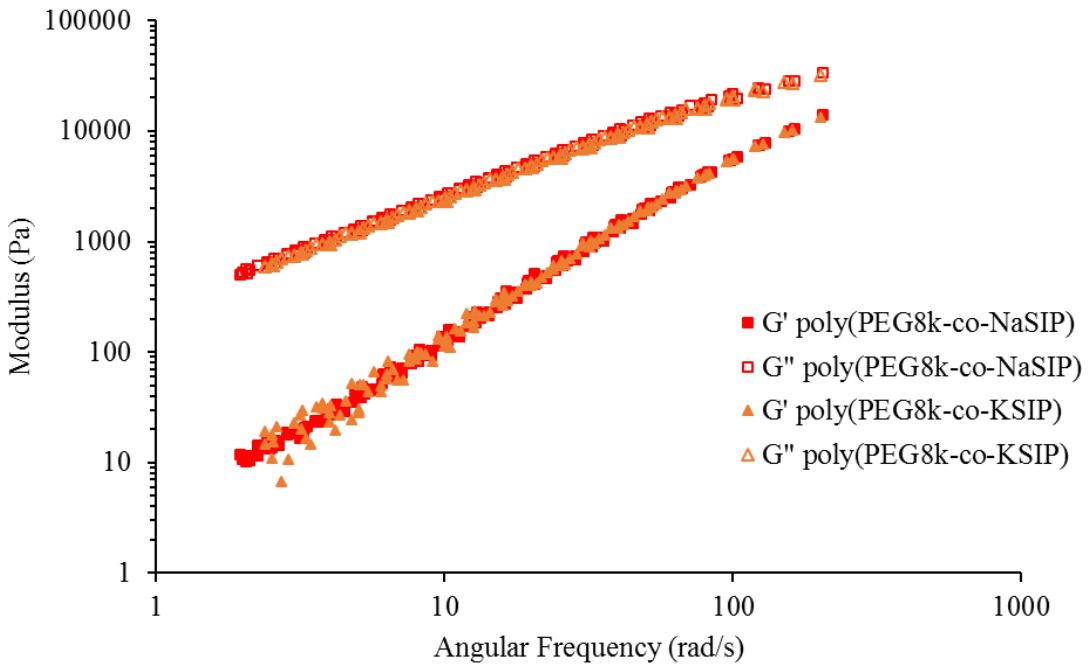

Figure 6.S4. Monovalent ions do not exhibit crossover points in modulus under time-temperature superposition and insignificant difference between the two samples, suggesting a lack of physical crosslinking.

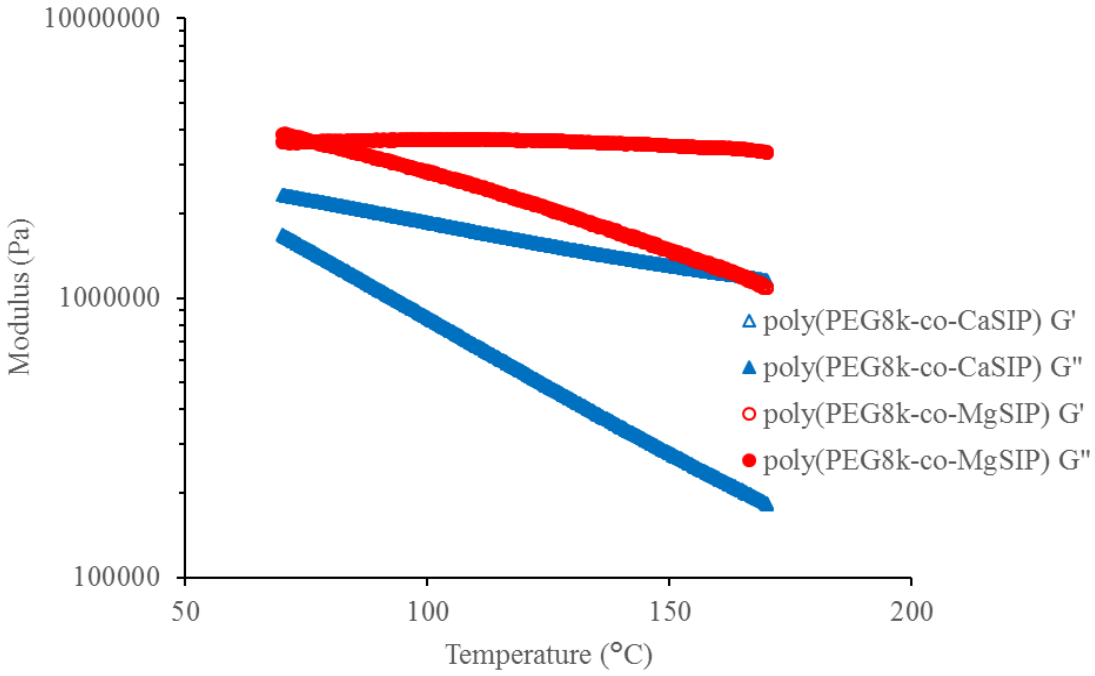

Figure 6.S5. Cooling curves under constant shear sweep reveal crossover points in poly(PEG_{8k}-co-MgSIP) not present in poly(PEG_{8k}-co-CaSIP).

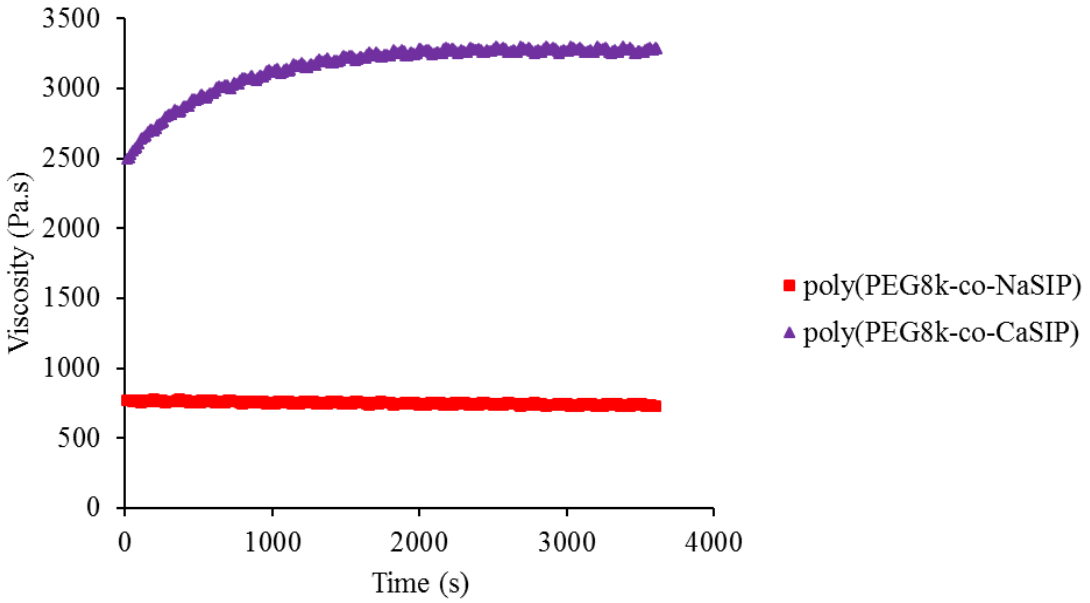

Figure 6.S6. Melt stability experiments reveal an increase in viscosity of poly(PEG8k-co-CaSIP), suggesting ionic mobility to increase the number of physical crosslinks which does not occur for monovalent counterions.

Sample	Activation Energy (kJ/mol)
Poly(PEG_{8k}-co-NaSIP)	22.1
Poly(PEG_{8k}-co-KSIP)	23.1
Poly(PEG_{8k}-co-CaSIP)	27.9
Poly(PEG_{8k}-co-ZnSIP)	30.5
Poly(PEG_{8k}-co-MgSIP)	37.6

Table 6.S2. Activation energies as calculated from Arrhenius fits of TTS curves. All fits have $R^2 > 0.99$.

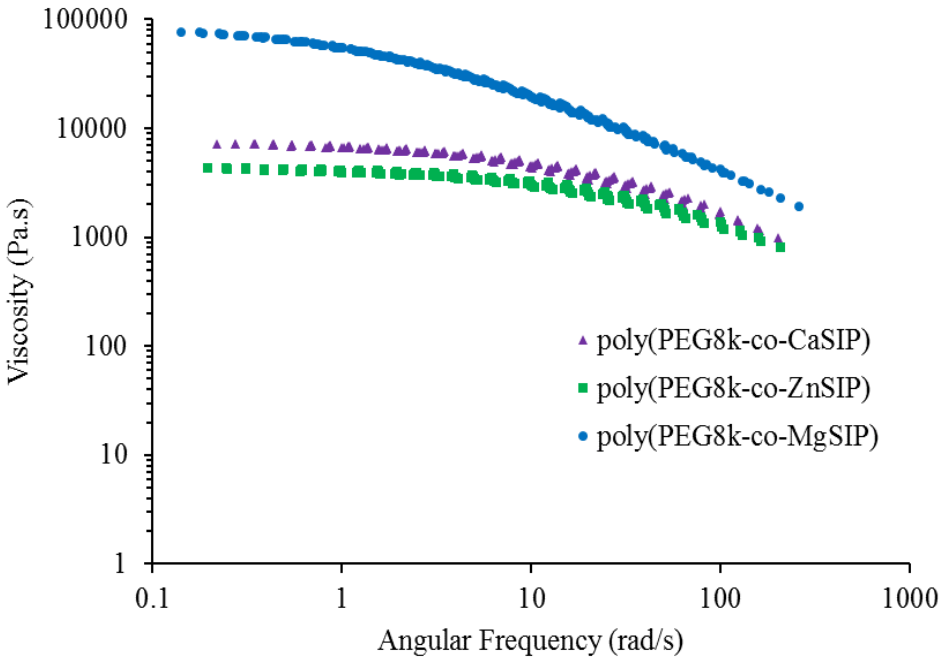

Figure 6.S7. Rheological data during TTS experiment reveals a change in viscosity compared to shear sweep experiments, further corroborating a thermal effect on polymer properties.

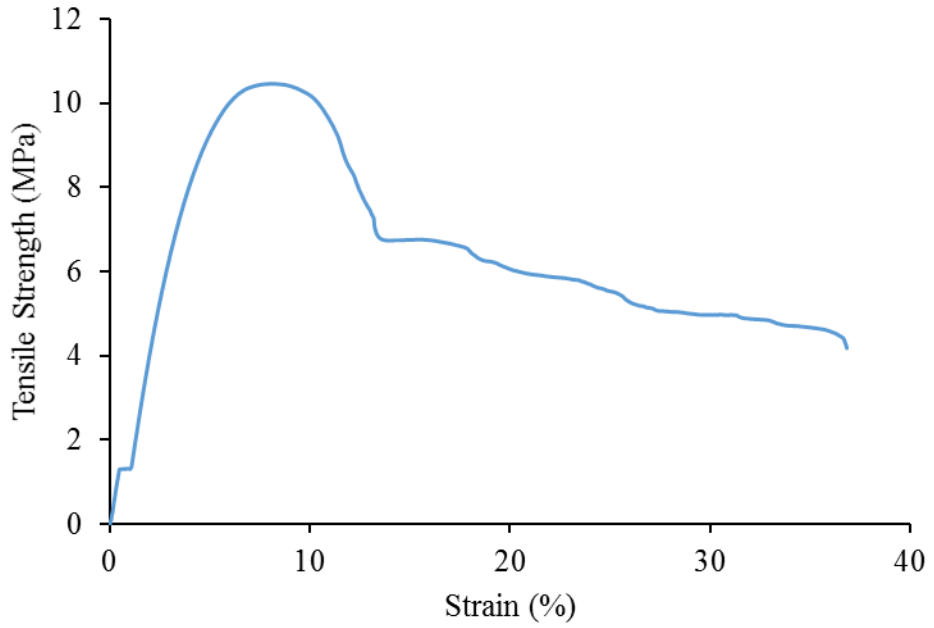

Figure 6.S8. Representative tensile curve showing stress-strain behavior of poly(PEG8k-co-MgSIP). All polymer samples exhibit similar stress-strain behavior.

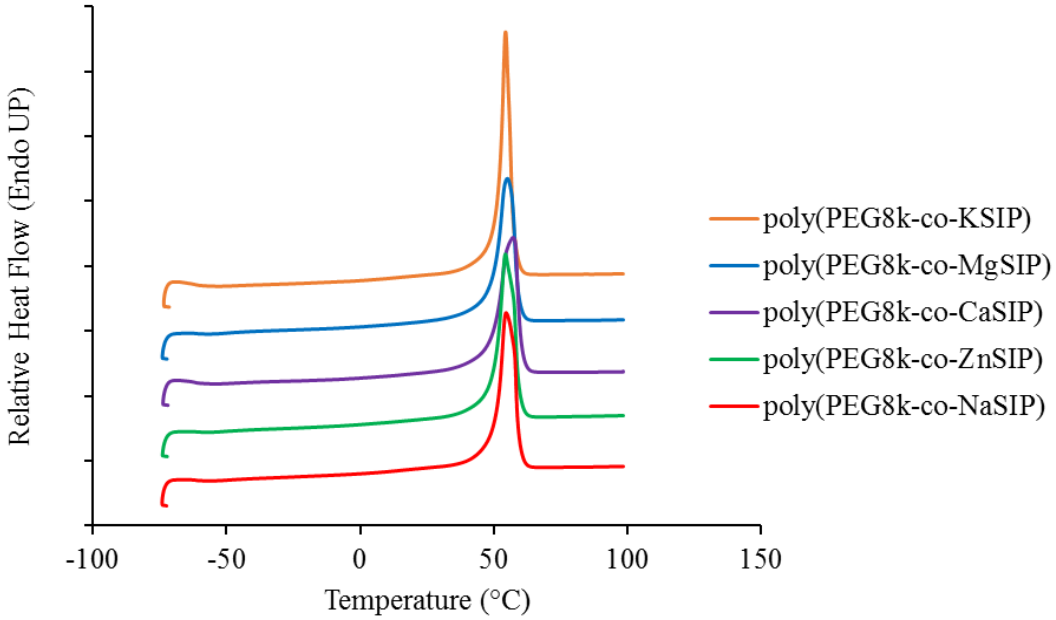

Figure 6.S9. DSC traces of ion exchanged samples showing broad melting endotherms. The data have been arbitrarily shifted to ease readability.

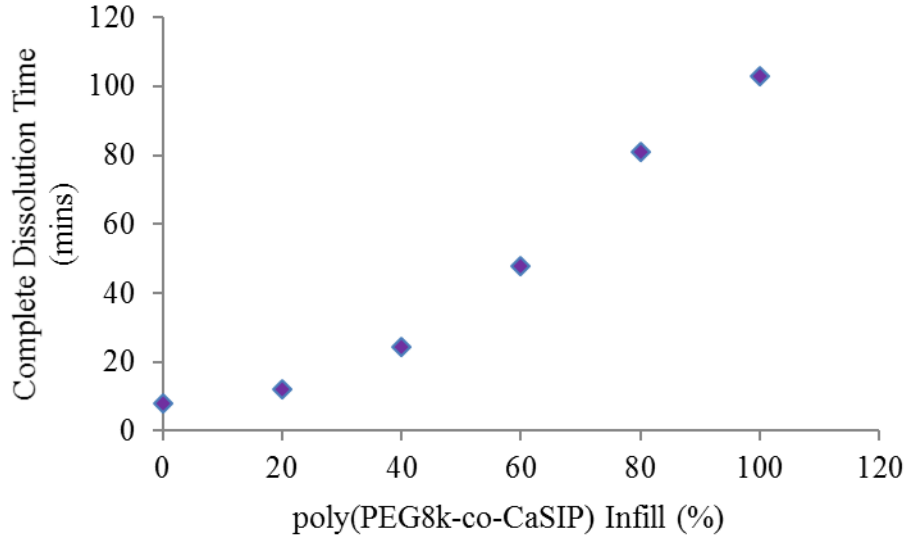

Figure 6.S10. Infill dissolution reveals increased printed part infill amounts result in longer dissolution times.

References

1. Eisenberg, A., *Ion-containing Polymers: Physical Properties and Structure*. Elsevier: 2012; Vol. 2.
2. Hickner, M. A., Water-mediated Transport in Ion-containing Polymers. *J. Polym. Sci., Part B: Polym. Phys.* **2012,** 50, (1), 9-20.
3. Kobayashi, M.; Ishikawa, T.; Takahara, A., Adhesion and Tribological Characteristics of Ion-Containing Polymer Brushes Prepared by Controlled Radical Polymerization. *Polym. Adhes., Frict., Lubr.* **2013**, 59-82.
4. Kamcev, J.; Galizia, M.; Benedetti, F. M.; Jang, E.-S.; Paul, D. R.; Freeman, B. D.; Manning, G. S., Partitioning of Mobile Ions Between Ion Exchange Polymers and Aqueous Salt Solutions: Importance of Counter-ion Condensation. *Phys. Chem. Chem. Phys.* **2016,** 18, (8), 6021-6031.
5. Kumar, T. S.; Madhumathi, K.; Rajkamal, B.; Zaheatha, S.; Malar, A. R.; Bai, S. A., Enhanced Protein Delivery by Multi-ion Containing Eggshell Derived Apatitic-alginate Composite Nanocarriers. *Colloids Surf., B* **2014,** 123, 542-548.
6. Nelson, A. M.; Long, T. E., Synthesis, Properties, and Applications of Ion-Containing Polyurethane Segmented Copolymers. *Macromol. Chem. Phys.* **2014,** 215, (22), 2161-2174.
7. Zhang, M.; Zhang, M.; Moore, R. B.; Long, T. E., Influence of Charge Placement on the Thermal and Morphological Properties of Sulfonated Segmented Copolyesters. *Polymer* **2013,** 54, (14), 3521-3528.
8. Choi, U. H.; Runt, J., Structures in Ion-Containing Polymers. *Encyclopedia of Polymeric Nanomaterials* **2015**, 2345-2351.
9. Tamami, M.; Hemp, S. T.; Zhang, K.; Zhang, M.; Moore, R. B.; Long, T. E., Poly (ethylene glycol)-based Ammonium Ionenes Containing Nucleobases. *Polymer* **2013,** 54, (6), 1588-1595.
10. Gao, R.; Zhang, M.; Dixit, N.; Moore, R. B.; Long, T. E., Influence of Ionic Charge Placement on Performance of Poly (ethylene glycol)-based Sulfonated Polyurethanes. *Polymer* **2012,** 53, (6), 1203-1211.
11. Hopkinson, N.; Hague, R.; Dickens, P., *Rapid Manufacturing: An Industrial Revolution for the Digital Age*. John Wiley & Sons: 2006.
12. Gao, W.; Zhang, Y.; Ramanujan, D.; Ramani, K.; Chen, Y.; Williams, C. B.; Wang, C. C.; Shin, Y. C.; Zhang, S.; Zavattieri, P. D., The Status, Challenges, and Future of Additive Manufacturing in Engineering. *Computer-Aided Design* **2015,** 69, 65-89.
13. Wong, K. V.; Hernandez, A., A Review of Additive Manufacturing. *ISRN Mechanical Engineering* **2012,** 2012.
14. Vaezi, M.; Seitz, H.; Yang, S., A Review on 3D Micro-additive Manufacturing Technologies. *Int. J. Adv. Manuf. Technol.* **2013,** 67, (5-8), 1721-1754.
15. Schultz, A. R.; Lambert, P. M.; Chartrain, N. A.; Ruohoniemi, D. M.; Zhang, Z.; Jangu, C.; Zhang, M.; Williams, C. B.; Long, T. E., 3D Printing Phosphonium Ionic Liquid Networks with Mask Projection Microstereolithography. *ACS Macro Lett.* **2014,** 3, (11), 1205-1209.
16. Sirrine, J. M.; Pekkanen, A. M.; Nelson, A. M.; Chartrain, N. A.; Williams, C. B.; Long, T. E., 3D-Printable Biodegradable Polyester Tissue Scaffolds for Cell Adhesion. *Aust. J. Chem.* **2015,** 68, (9), 1409-1414.

17. Montero, M.; Roundy, S.; Odell, D.; Ahn, S.-H.; Wright, P. K. In *Material Characterization of Fused Deposition Modeling (FDM) ABS by Designed Experiments*, Proceedings of rapid prototyping and manufacturing conference, SME, 2001; 2001; pp 1-21.
18. Smith, W. C.; Dean, R. W., Structural Characteristics of Fused Deposition Modeling Polycarbonate Material. *Polym. Test.* **2013,** 32, (8), 1306-1312.
19. Eujin Pei, D.; Meisel, N. A.; Williams, C. B., Design and Assessment of a 3D Printing Vending Machine. *Rapid Prototyping Journal* **2015,** 21, (5), 471-481.
20. Durgun, I.; Ertan, R., Experimental Investigation of FDM Process for Improvement of Mechanical Properties and Production Cost. *Rapid Prototyping Journal* **2014,** 20, (3), 228-235.
21. Mohamed, O. A.; Masood, S. H.; Bhowmik, J. L., Optimization of Fused Deposition Modeling Process Parameters: A Review of Current Research and Future Prospects. *Adv. Manuf.* **2015,** 3, (1), 42-53.
22. Oskui, S. M.; Diamante, G.; Liao, C.; Shi, W.; Gan, J.; Schlenk, D.; Grover, W. H., Assessing and Reducing the Toxicity of 3D-Printed Parts. *Environ. Sci. Technol. Lett.* **2015,** 3, (1), 1-6.
23. Allen, M. H.; Day, K. N.; Hemp, S. T.; Long, T. E., Synthesis of Folic Acid-Containing Imidazolium Copolymers for Potential Gene Delivery Applications. *Macromol. Chem. Phys.* **2013,** 214, (7), 797-805.
24. Allen, M. H.; Hemp, S. T.; Long, T. E., Polymeric Imidazoles and Imidazoliums in Nanomedicine: Comparison to Ammoniums and Phosphoniums. In *Applications of Ionic Liquids in Polymer Science and Technology*, Springer: 2015; pp 231-266.
25. Hemp, S. T.; Allen Jr, M. H.; Smith, A. E.; Long, T. E., Synthesis and Properties of Sulfonium Polyelectrolytes for Biological Applications. *ACS Macro Lett.* **2013,** 2, (8), 731-735.
26. Brough, C.; Miller, D. A.; Keen, J. M.; Kucera, S. A.; Lubda, D.; Williams III, R. O., Use of Polyvinyl Alcohol as a Solubility-enhancing Polymer for Poorly Water Soluble Drug Delivery (part 1). *AAPS PharmSciTech* **2016,** 17, (1), 167-179.
27. Kim, S. W.; Petersen, R. V.; Feijen, J., Polymeric Drug Delivery Systems. *Drug Design* **2016,** 10, 193-250.
28. Hemp, S. T.; Smith, A. E.; Bryson, J. M.; Allen Jr, M. H.; Long, T. E., Phosphonium-containing Diblock Copolymers for Enhanced Colloidal Stability and Efficient Nucleic Acid Delivery. *Biomacromolecules* **2012,** 13, (8), 2439-2445.
29. Melocchi, A.; Parietti, F.; Loreti, G.; Maroni, A.; Gazzaniga, A.; Zema, L., 3D Printing by Fused Deposition Modeling (FDM) of a Swellable/erodible Capsular Device for Oral Pulsatile Release of Drugs. *J. Drug Delivery Sci. Technol.* **2015,** 30, 360-367.
30. Zhou, Z.; Salaoru, I.; Morris, P.; Gibbons, G., Development of a Direct Feed Fused Deposition Modelling Technology for Multi-material Manufacturing. *19th International Conference on Material Forming – ESAFORM* **2016**.
31. Skowyra, J.; Pietrzak, K.; Alhnan, M. A., Fabrication of Extended-release Patient-tailored Prednisolone Tablets via Fused Deposition Modelling (FDM) 3D Printing. *Eur. J. Pharm. Sci.* **2015,** 68, 11-17.
32. Hermes, F.; Bernhardt, S.; Poppe, D.; Schmitt, G.; Pridoehl, M.; Loehden, G., Maleic Anhydride Copolymers as Soluble Support Material for Fused Deposition Modelling (FDM) Printer. In Google Patents: 2014.

33. Dudek, P., FDM 3D Printing Technology in Manufacturing Composite Elements. *Arch. Metall. Mater.* **2013,** 58, (4), 1415-1418.
34. Bakarich, S. E.; Balding, P.; Gorkin Iii, R.; Spinks, G. M.; in het Panhuis, M., Printed Ionic-covalent Entanglement Hydrogels from Carrageenan and an Epoxy Amine. *RSC Adv.* **2014,** 4, (72), 38088-38092.
35. Pietrzak, K.; Isreb, A.; Alhnan, M. A., A flexible-dose dispenser for immediate and extended release 3D printed tablets. *Eur. J. Pharm. Biopharm.* **2015,** 96, 380-387.
36. Chen, Q.; Masser, H.; Shiau, H.-S.; Liang, S.; Runt, J.; Painter, P. C.; Colby, R. H., Linear Viscoelasticity and Fourier Transform Infrared Spectroscopy of Polyether–Ester–Sulfonate Copolymer Ionomers. *Macromolecules* **2014,** 47, (11), 3635-3644.
37. Roach, D. J.; Dou, S.; Colby, R. H.; Mueller, K. T., Nuclear Magnetic Resonance Investigation of Dynamics in Poly(ethylene oxide)-based Lithium Polyether-ester-sulfonate Ionomers. *J. Chem. Phys.* **2012,** 136, (1), 014510.
38. Tudryn, G. J.; O'Reilly, M. V.; Dou, S.; King, D. R.; Winey, K. I.; Runt, J.; Colby, R. H., Molecular Mobility and Cation Conduction in Polyether–Ester–Sulfonate Copolymer Ionomers. *Macromolecules* **2012,** 45, (9), 3962-3973.
39. Wang, W.; Tudryn, G. J.; Colby, R. H.; Winey, K. I., Thermally Driven Ionic Aggregation in Poly(ethylene oxide)-Based Sulfonate Ionomers. *J. Am. Chem. Soc.* **2011,** 133, (28), 10826-10831.
40. Szymczyk, A.; Roslaniec, Z., Sulfonated Poly(ether–block–ester) Ionomers with Anions in the Polyester Hard Segments. *Polym. Adv. Technol.* **1999,** 10, (10), 579-587.
41. Pielichowski, K.; Flejtuch, K., Differential Scanning Calorimetry Studies on Poly(ethylene glycol) with Different Molecular Weights for Thermal Energy Storage Materials. *Polym. Adv. Technol.* **2002,** 13, (10-12), 690-696.
42. Hancock, R. D., A Molecular Mechanics Study of the Selectivity of Crown Ethers for Metal Ions on the Basis of their Size. *J. Inclusion Phenom. Mol. Recognit. Chem.* 17, (1), 63-80.
43. Junk, P. C.; Steed, J. W., A Structural Study of Calcium, Strontium and Barium Crown Ether Complexes. *J. Coord. Chem.* **2007,** 60, (10), 1017-1028.
44. Hancock, B. C.; Zografi, G., The Relationship Between the Glass Transition Temperature and the Water Content of Amorphous Pharmaceutical Solids. *Pharm. Res.* **1994,** 11, (4), 471-477.
45. Gámez, F.; Hurtado, P.; Martínez–Haya, B.; Berden, G.; Oomens, J., Vibrational Study of Isolated 18-crown-6 ether Complexes with Alkaline-earth Metal Cations. *Int. J. Mass Spectrom.* **2011,** 308, (2–3), 217-224.

Chapter 7. Charged Polycaprolactone Copolymers as Bioadhesive Wound Glue

Allison M. Pekkanen[1], Kilian Horatz[2], Kevin Drummey[3], and Timothy E. Long[1,3]*

[1]School of Biomedical Engineering and Sciences, Virginia Tech, Blacksburg, VA 24061

[2]University of Cologne, Cologne, Germany

[3]Macromolecules Innovation Institute, Department of Chemistry, Virginia Tech, Blacksburg, VA 24061

*To whom correspondence should be addressed. Email: telong@vt.edu Phone: (540) 231-2480 Fax: (540) 231-8517

Keywords: Bioadhesive, polycaprolactone, wound glue, ionomer

7.1 Abstract

Scientists continue to examine and promote the field of wound healing to aid patients in expediting the healing process and eliminating scar formation. To this end, only a few wound glue solutions exist in clinical practice, including fibrin glue and cyanoacrylates. The development of a biodegradable, biocompatible wound glue is of great clinical need. Transesterification of polycaprolactone diols and sulfonated isophthalate afforded polyester ionomers with melting temperatures around 50 °C. These ionomers suppress inherent PCL crystallinity and provide potential sites for physical crosslinking between polymer chains. PCL ionomers exhibit increased rheological and tensile modulus compared to high molecular weight PCL controls, likely due to the presence of ionic aggregates. Furthermore, when soaked in phosphate buffered saline, the PCL ionomers exhibited substantially increased compressive modulus, likely due to physical crosslinking from phosphate salts. Time-temperature superposition revealed

adherence to the Dahlquist criterion, supported by 180 ° peel testing. Finally, biological evaluation revealed cell attachment and proliferation, suggesting the ability of cells to infiltrate into wound space. These PCL-based ionomers possess great potential to perform as biodegradable wound glue.

7.2 Introduction

The field of wound healing and characterization continues to draw significant new research due to the complexity and broad need of wound healing solutions.[1, 2] Examination of infiltrating cells, released cytokines, and fluid movement throughout the wound healing process remains an active area of research, with some complexities yet unknown.[1] Psychological stress and other underlying factors provide new clinical insights into the complexities of wounds and their healing.[3] Tissue engineering to develop *in vitro* wound healing models to test potential new therapies and cellular behavior continues to progress at a rapid pace.[4] Coupling clinical research with novel tissue engineering scaffolds positions the creation of next generation wound healing solutions. New solutions to aid in expediting wound healing stem from both the understanding of wound healing processes and tissue-level characterization.

Currently, cyanoacrylates act as the commercial standard for wound glue. While offering superior adhesion to wound tissue, cyanoacrylates suffer from potential toxicity arising from the release in formaldehyde and difficulty in application by clinicians.[5-7] Dong et al. exhibited electrospinning of cyanoacrylate wound glues directly into the injury site to reduce this toxicity, alleviating some, but not all, toxicity concerns.[8] Alongside toxicity concerns, cyanoacrylates suffer from a lack of degradation to allow

native tissue infiltration.[9] Fibrin wound glue also experiences widespread use due to its natural occurrence during the wound healing process.[10, 11] While providing significant tissue adhesion, fibrin glues fail from potential hypersensitivity due to its position in the blood clotting cascade.[11, 12] Excess fibrin impacts surrounding healthy tissue through errant activation of the clotting cascade, potentially causing an overresponse to the injured area.[12] While many wound healing solutions currently experience clinical practice, the potential for improved toxicity and biological response generates areas of current research.

Polycaprolactone (PCL) experiences a large portion of tissue engineering solutions due to its processability and biodegradability.[13] The inherent nature of the ester bond present in PCL backbones, coupled with their high molecular weight, renders them biodegradable over long time scales.[13] In particular, PCL recently served in additive manufacturing of tissue scaffolds such as trachea and other permanent scaffolds.[14-17] PCL facilitated tissue scaffold generation through numerous additive manufacturing techniques, highlighting its versatility throughout many processing conditions.[15-17] Its strong precedence as a biomedical tissue scaffold inspires it as an optimal choice for biological applications. While high molecular weight PCL promoted widespread use in biological applications, lower molecular weight PCL remains unexplored.[18] Lower molecular weight PCL provides opportunities for biological solutions with a faster degradation timeline, but lacks mechanical integrity hallmark of traditional PCL tissue scaffolds. Due to this shortened degradation timeline, lower molecular weight PCL catalyzes use in wound healing applications.

Ion-containing polymers revolutionize common applications and find themselves in a large range of applications, including membrane separations, batteries, and biological applications.[19] The addition of charge in traditional polymer chemistry presents polymers with enhanced processability at significantly lower molecular weight compared to their non-charged counterparts.[20] Furthermore, precisely-tuned structure tailors polymers for specific applications, changing the polymer backbone and charge-inclusion groups.[21] Physical crosslinking, present through ionic aggregates, aids in the processability and resulting properties of the ionomers and provides a facile route to restrict chain mobility when molten.[21, 22] Chen et al. detailed the synthesis and characterization of poly(ether ester) ionomers with sulfonated isophthalate for lithium ion transport, which exhibited significant ionic aggregation.[22] This ionic aggregation gave rise to significantly improved properties compared to their non-charged analogs, highlighting the large effect of ionic groups on polymer properties.[22]

This work describes the synthesis and characterization of a PCL-based ionomer for wound healing applications. Transesterification of PCL diols with sulfonated isophthalate (SIP) afforded polymers of sufficient film-forming molecular weight. When compared to high molecular weight PCL, enhanced melt viscosity and modulus arose from the inclusion of charge. Furthermore, compressive modulus increased significantly when soaked in phosphate buffered saline (PBS) for 48 h, revealing the power of charge in the properties of these ionomers. 180° peel testing revealed a significant increase in peel strength at elevated temperatures and cell studies elucidated favorable attachment to film surfaces. This novel ionomer represents the future of clinical wound healing due to its favorable processability and application compared to commercial standards.

7.3 Materials and Methods

7.3.1. Materials. Polycaprolactone (PCL) diols and sulfonated isophthalate (SIP) were dried overnight in a vacuum oven (50-60 °C) before use. Sodium acetate (NaOAc, Sigma-Aldrich, >99.0 %), PCL (MW = 80,000 g/mol), and dimethyl isophthalate (DMI) were purchased from Sigma-Aldrich and used as received. Titanium tetra(isopropoxide) was purchased from Sigma-Aldrich, and a 0.0132 g/mL titanium solution in anhydrous 1-butanol was prepared according to previous procedures. MDA-MB-231 human breast cancer cells were purchased from ATCC. Sterile phosphate buffered saline, Dulbecco's Modified Eagle Medium, Fetal Bovine Serum, Penicillin/Streptomycin, and 0.25 % Trypsin/EDTA were purchased from Life Technologies and used as received. A CellTiter Glo® cell viability assay was purchased from Promega and used according to manufacturer's protocol. All solvents were received from Spectrum and used as received. Nitrogen and carbon dioxide gas (Praxair, 99.999 %) was used as received.

7.3.2. Analytical Methods. Differential scanning calorimetry (DSC) was performed with a nitrogen flow of 50 mL/min and a heating rate of 10 °C/min on a TA Instruments Q1000 DSC calibrated with indium (mp = 156.60 °C) and zinc (mp = 419.47 °C) standards. Glass transition temperatures (T_g) were calculated as the inflection point and melting temperatures (T_m) calculated as the peak maximum of the melting endotherm. Thermogravimetric analysis (TGA) was performed using a TA Instruments Q50 from 25 – 600 °C with a heating rate of 10 °C/min. Dynamic mechanical analysis (DMA) was performed on a TA Instruments Q800 dynamic mechanical analyzer in tension or compression mode. Tensile experiments were conducted at a temperature ramp of 3 °C/min with a frequency of 1 Hz, an oscillatory amplitude of 10 μm, and a static force of

0.01 N. Samples for compression experiments were formed by melting into a 2-dram vial to form cylinders. Wet samples were soaked in phosphate buffered saline (PBS) for 48 h and blotted gently before loading onto the sample stage. Compression experiments were conducted with a frequency sweep from 0.1 – 10 Hz at a temperature of 37 °C, an oscillatory amplitude of 70 μm and a static force of 0.01 N. Rheological analysis was performed on a TA Instruments AR G2 rheometer using 25 mm disposable aluminum parallel plates under air. Zero-shear viscosity measurements were performed at 100 °C with angular frequencies ranging from 0.1 – 100 rad/s with a constant strain of 1 % and a 1000 μm gap. Time-temperature superposition was performed from 100 – 30 °C, with 10 °C/step and angular frequencies ranging from 1 – 100 rad/s at constant 1 % strain under air. WLF shifts were calculated from a reference temperature of 40 °C and were used to transpose data (1 Hz) to be in reference to temperature. Scanning electron microscopy (SEM) was performed on a Jeol Neoscope JCM-5000 benchtop SEM in high vacuum mode.

7.3.3. Synthesis of poly(PCLnk-co-SIP). Reactions were conducted in a 100-mL round-bottomed flask equipped with an overhead stirrer and metal stirrod, distillation apparatus, and nitrogen inlet. All glassware was dried in a 150 °C oven overnight. PCL_{nk} (1 mol eq.) and SIP (1 mol eq.) were dried overnight in a vacuum oven (50-60 °C) before use. PCL_{nk}, SIP, and NaOAc (0.1:1 mole ratio NaOAc:SIP) were charged to the round-bottomed flask. Titanium tetra(isopropoxide) (40 ppm) was added and used to catalyze the reaction. Degassing and purging with nitrogen three times removed oxygen and allowed the reaction to proceed oxygen-free. The flask was submerged in a silicone oil bath heated to 170 °C under constant nitrogen purge until all reactants were molten (~ 10 min). Vacuum

was then applied until a pressure of 0.15 mmHg was achieved and the reaction stirred from 170 – 190 °C for 2 h. The resulting viscous polymer was isolated and used without further purification. **Scheme 7.1** depicts the overall synthetic strategy.

7.3.4. Synthesis of poly(PCL500-co-DMI) non-charged analog. Reactions were conducted in a 100-mL round-bottomed flask equipped with a metal stirrod, overhead stirrer, and distillation apparatus. Glassware and PCL_{500} were dried overnight in a 150 °C oven and 60 °C vacuum oven, respectively, to remove moisture. PCL_{500} and DMI were charged to the round-bottomed flask, and titanium tetra(isopropoxide) was added (40 ppm) to catalyze the transesterification. Three degassing and purge cycles provided an oxygen-free environment for the reaction. The flask was submerged in a silicone oil bath heated to 170 °C and stirred under nitrogen purge for 2.5 h. Following the nitrogen step, vacuum was applied (0.15 mmHg) and the reaction proceeded for an additional 2 h. The product was removed from the round-bottomed flask and used without further purification. **Scheme 7.2** depicts the overall synthetic strategy.

7.3.5. Compression molding PCL and PCL copolymers. Polymers were melt pressed between two 16 mil stainless steel plates layered with Kapton® films using a PHI Q-230H manual hydraulic compression press. A Rexco Partall ® Power Glossy Liquid mold release agent was applied to the Kapton® films to prevent polyester adhesion following press. Samples were heated for ~ 3 min at 90 °C before the top plate was added. After ~ 1 min equilibration period at 90 °C, 4 press-release cycles were performed, the first two utilizing 5 tons of force and the second two using 10 tons of force. The films were removed from the stainless steel plates and allowed to cool to room

temperature between the Kapton® films. The resulting films were used without further modification.

7.3.6. Peel Testing. Poly(PCL_{1k}-co-SIP) films were cast from chloroform at 4.3 wt % directly onto Mylar sheets, with thickness controlled with a draw-down blade set to 86 μm. Films were dried for 15 min at 25 °C and subsequently placed into a 37 °C oven with vacuum overnight. Mylar sections were cut into 1 inch strips and placed on stainless steel plates pre-warmed to 45 °C. Films were allowed to adhere to stainless steel plates for 5 min. 180° peel testing was conducted on a ChemInstruments Adhesion/Release Tester AR1000. Data was taken as an average and standard deviation of n = 6 readings.

7.3.7. Maintenance of cells. MDA-MB-231 human breast cancer cells were cultured in Dulbecco's Modified Eagle Medium supplemented with F12, fetal bovine serum (FBS), and penicillin-streptomycin (1 %). Cells were cultured at 37 °C and 5 % CO_2 in a humidified atmosphere on T-75 tissue-culture treated plates. When ~80 % confluent, MDA-MB-231 cell media was removed, cells were washed with PBS, and 0.25 % Trypsin-EDTA solution added to detach cells from the plate.

7.3.8. Cytotoxicity Analysis. Following trypsinization, MDA-MB-231 cells were centrifuged and counted using a hemocytometer. 25,000 cells were seeded into each well of a 24-well tissue-culture-treated plate and allowed to attach and proliferate for 24 h. PCL films were sterilized by soaking in 70/30 % ethanol/water solutions followed by soaks in fresh culture medium to remove ethanol. Sections of film were placed on top of MDA-MB-231 cells and allowed to interact with cells for 24 h. PCL films were removed and fresh medium added to each well. After allowing the media to come to room temperature, equal volume of Cell Titer Glo® reagent was added to each well. Each well

was then subsampled 3 times into a 96 well plate and analyzed using a SpectraMax G2 plate reader in luminescence mode. Viability is calculated as percentages compared to untreated controls cells cultured on the same plate.

7.3.9. Cell Attachment. Following trypsinization, MDA-MB-231 cells were seeded directly onto sections of sterilized PCL film in a 24-well non-tissue-culture-treated plate at 25,000 cells/well. An equivalent number of cells were also placed in adjacent wells to provide a negative/competitive control and onto a tissue-culture-treated plate to serve as a positive control. After 24 h incubation, PCL films were removed and subsequently used for analysis. A Cell Titer Glo® assay was completed in accordance to manufacturer's protocol. Briefly, equivalent volumes of Cell Titer Glo® reagent and cell media (at 25 °C) were placed onto control cell and PCL films. After a 10 min incubation, each well was subsampled into a 96-well plate and quantified using a SpectraMax G2 plate reader in luminescence mode. Percent attachment is calculated as percentages compared to positive control cells.

7.3.10. Cell Imaging. MDA-MB-231 human breast cancer cells were seeded onto PCL films as above. Following 24 h incubation, PCL films were removed from wells and attached cells subsequently fixed for 30 min in 3.7 % paraformaldehyde in PBS. Cells were rehydrated in fresh PBS for 5 min three times and slowly dehydrated with PBS-ethanol mixtures until pure ethanol washes. The films were dried at 25 °C overnight to remove any residual ethanol. Cell imaging was performed on a Nikon JEOL JCM-5000 Benchtop Scanning Electron Microscope (SEM) to visualize cell attachments on PCL films.

7.4 Results and Discussion

High molecular weight PCL induced widespread use in biological applications due to its high modulus and processability to form well-defined tissue scaffolds. The polyester backbone of PCL renders it biodegradable and lends biocompatible functionality to the resulting tissue scaffolds. Over time, smaller molecular weight by-products undergo excretion through liver metabolism and kidney filtration, resulting in a resorbable tissue scaffold which degrades as surround tissue regenerates. Melt polymerization of PCL diols and SIP proceeded to form viscous polymer melts. The application of vacuum on molten reactants proceeded immediately due to the high boiling points of staring materials. This accelerated reaction protocol provided high volumes of polymer sample in short times for subsequent analysis. The resulting white polymer enabled immediate analysis without further purification. Molecular weight characterization proved elusive due to the polymer insolubility in common organic solvents.

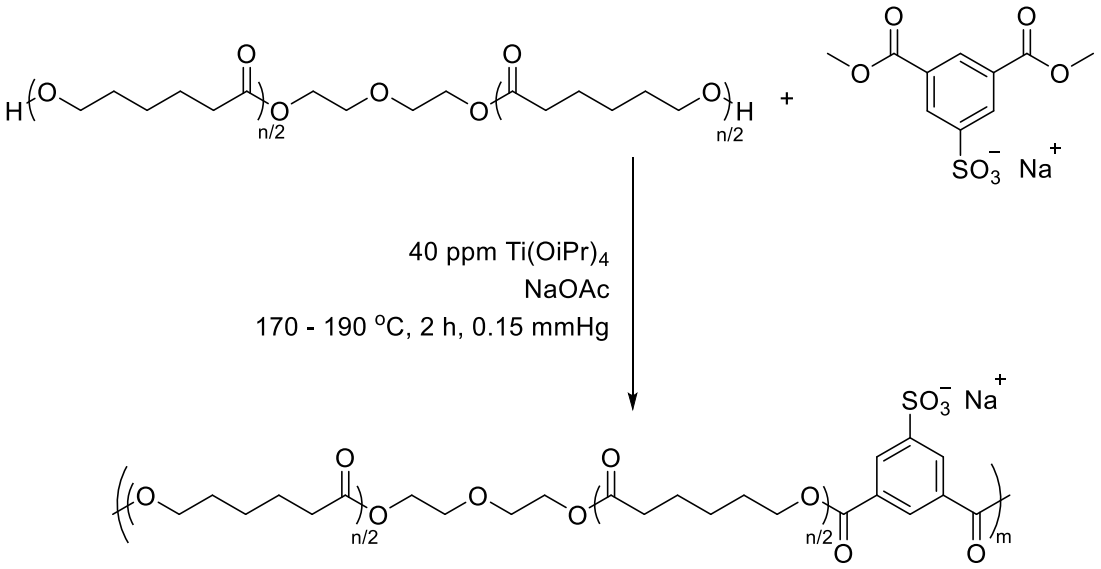

Scheme 7.1. Synthesis of copolyesters through melt transesterification of polycaprolactone (PCL) diols and dimethyl 5-sulfoisophthalate (SIP).

Thermal analysis, conducted by DSC, revealed T_g's similar to that of unmodified PCL homopolymers, suggesting a dominance of PCL in thermal behavior. Polymerization of PCL diols of molecular weight 500 g/mol revealed complete suppression of PCL crystallinity prominent in high molecular weight PCL homopolymers (**Table 7.1**). Polymers containing PCL diols of molecular weight 1,000 g/mol however, maintain some degree of polymer crystallinity. Interestingly, the introduction of charge also depressed the melting temperature of PCL by ~10 °C. T_m of poly(PCL_{1k}-co-SIP) demonstrated PCL dominance of thermal properties, highlighted when compared to the melting endotherms observed in PCL_{1k} oligomers. To highlight the importance of charge to impart mechanical integrity to PCL copolymers, dimethyl isophthalate (DMI) provided a non-charged analog to SIP. As evidenced in **Table 7.1**, DMI suppressed crystallinity of copolyesters and resulted in a viscous liquid upon polymerization.

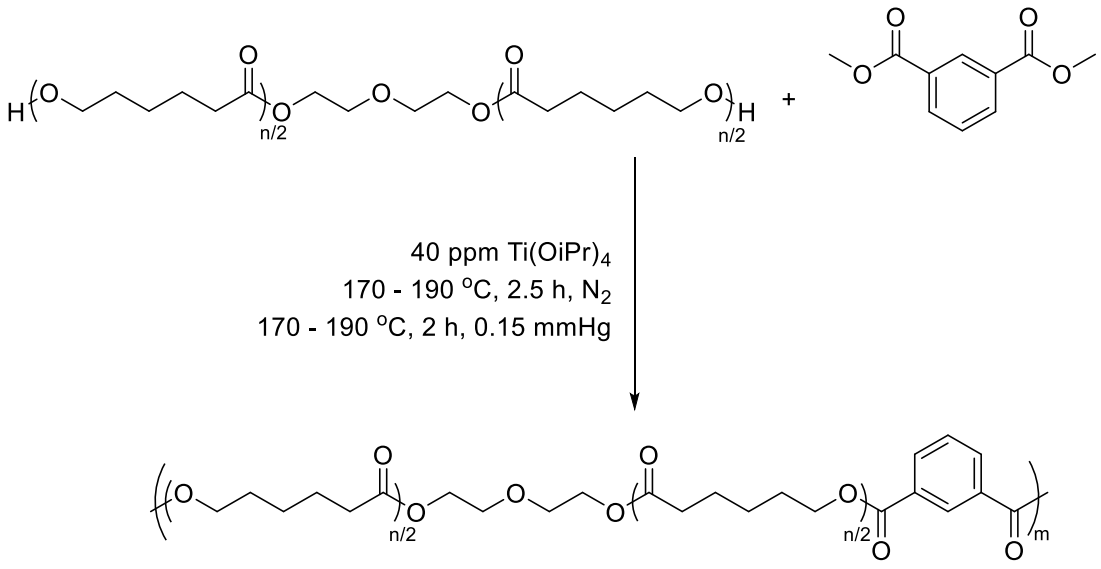

Scheme 7.2. Synthesis of non-charged analog poly(PCL_{500}-co-DMI) proceeded through traditional melt transesterification.

Compression molding of molten PCL_{80k} and poly(PCL_{1k}-co-SIP) resulted in mechanically stable polymer films for further analysis. Poly(PCL_{500}-co-SIP) compression molded films exhibited significant latent molten time during cooling, likely due to the lack of crystallinity present in the copolyester to stabilize the film following press-release cycles. Poly(PCL_{1k}-co-SIP), however, provided mechanically robust films due to its inherent crystallinity upon cooling and enabled subsequent analysis.

	T_g (DSC) (°C)	T_m (DSC) (°C)	% Crystallinity	T_g (DMA) (°C)
Poly(PCL_{500}-co-SIP)	-57	-	-	-
Poly(PCL_{1k}-co-SIP)	-63	44	28	-37
Poly(PCL_{500}-co-DMI)	-52	-	-	-
PCL_{80k}	-	56	52	-43
PCL_{1k}	-	35, 44	57	-

Table 7.1. Thermal characterization through differential scanning calorimetry showing depressed melting points and % crystallinity upon addition of charge.

Melt rheology of charged copolyesters revealed increased moduli by 2 orders-of-magnitude compared to high molecular weight PCL (**Figure 7.1**). Each of the polymers exhibited a G'-G" crossover point, a hallmark of high molecular weight polymers. Despite the lack of molecular weight information for the charged PCL copolyesters, they are likely well below 80,000 g/mol due to the nature of these step-growth polymerizations. The presence of crossover points in each of the charged copolyesters highlights the influence of charge in the resulting moduli. As expected, the moduli of poly(PCL_{500}-co-SIP) is greater than that of poly(PCL_{1k}-co-SIP) due to the increase in charge density imparted from lower molecular weight PCL diol precursors. In these

copolymers, ionic groups present on the polymer backbone potentially form physical crosslinks between polymer chains. In this scenario, ions between adjacent chains interact to restrict chain mobility in the polymer melt, influencing the moduli of the polymers and their subsequent G'-G" crossover points.

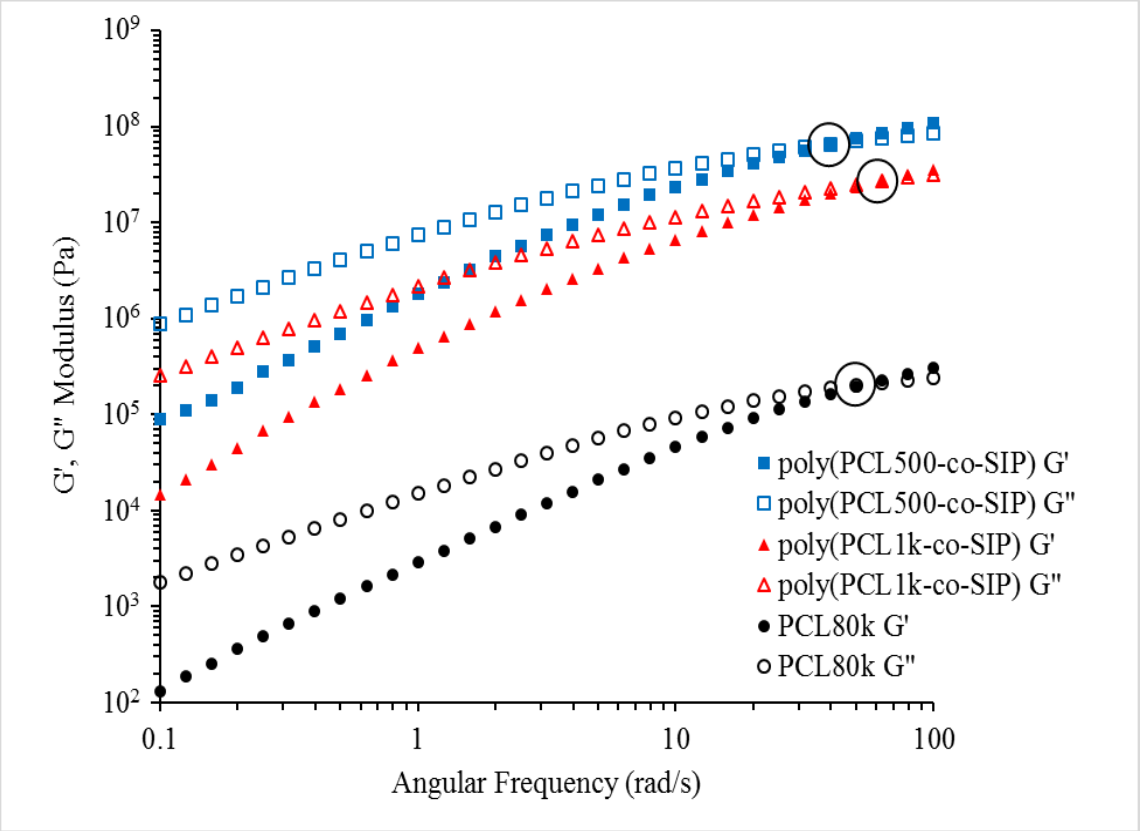

Figure 7.1. Rheological characterization reveals enhanced storage and loss modulus upon addition of ionic groups.

Similarly, melt viscosity increased by two orders-of-magnitude upon the addition of charged groups into the copolyesters, despite lower assumed molecular weights (**Figure 7.2**). Furthermore, as seen with the moduli of charged copolyesters, the lower molecular weight PCL diol reactants resulted in increased charge density and a significant increase in melt viscosity. In addition to increased melt viscosity, each of the PCL copolyesters exhibited shear thinning, also characteristic of high molecular weight polymers. PCL_{80k} also revealed shear thinning, confirming the molecular weight behavior

and highlighting the role of charge in the melt properties of the copolyesters. Due to the high viscosity and amorphous nature of poly(PCL_{500}-co-SIP), poly(PCL_{1k}-co-SIP) provided a valuable charged copolyester for mechanical testing.

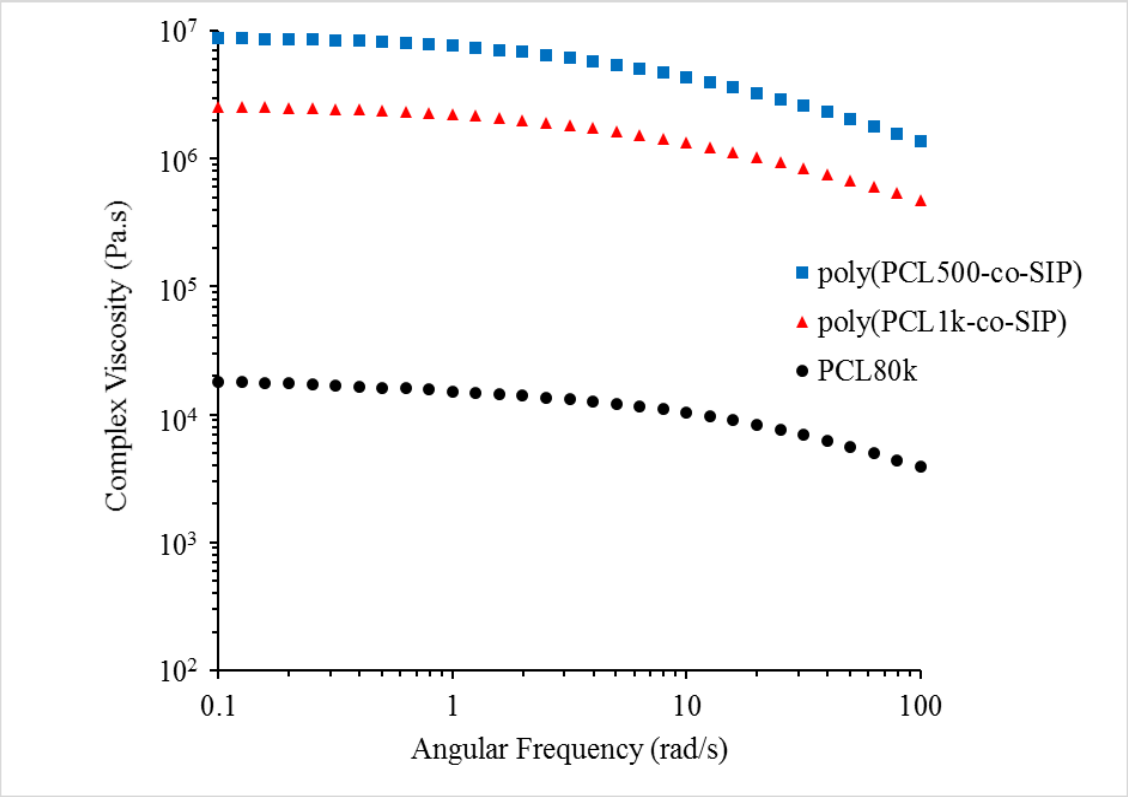

Figure 7.2. Viscosity analysis reveals an increase by two orders-of-magnitude upon addition of sulfonate ions into PCL at 100 °C.

Dynamic mechanical analysis of poly(PCL_{1k}-co-SIP) and PCL_{80k} films revealed an increase in plateau storage modulus upon the addition of charge (**Figure 7.3**). In the temperature window between the T_g and flow temperatures, poly(PCL_{1k}-co-SIP) exhibited an increased E' modulus, likely due to the presence of charge in the copolyester films. In particular, in the temperature window of use (25- 37 °C), the charged copolyester possessed a modulus nearly double that of high molecular weight PCL. The enhanced properties of poly(PCL_{1k}-co-SIP) compared to high molecular weight PCL

arises from the presence of ionic aggregation, confirmed through small angle X-ray scattering (**Figure 7.S3**). Ionic aggregates provide the basis for both enhanced compressive modulus as well as improved tensile and rheological modulus. The large peak in high molecular weight PCL arises from the crystallinity present in these polymers. The suppression of this characteristic peak also confirms results seen in DSC of decreased crystallinity upon the inclusion of charge.

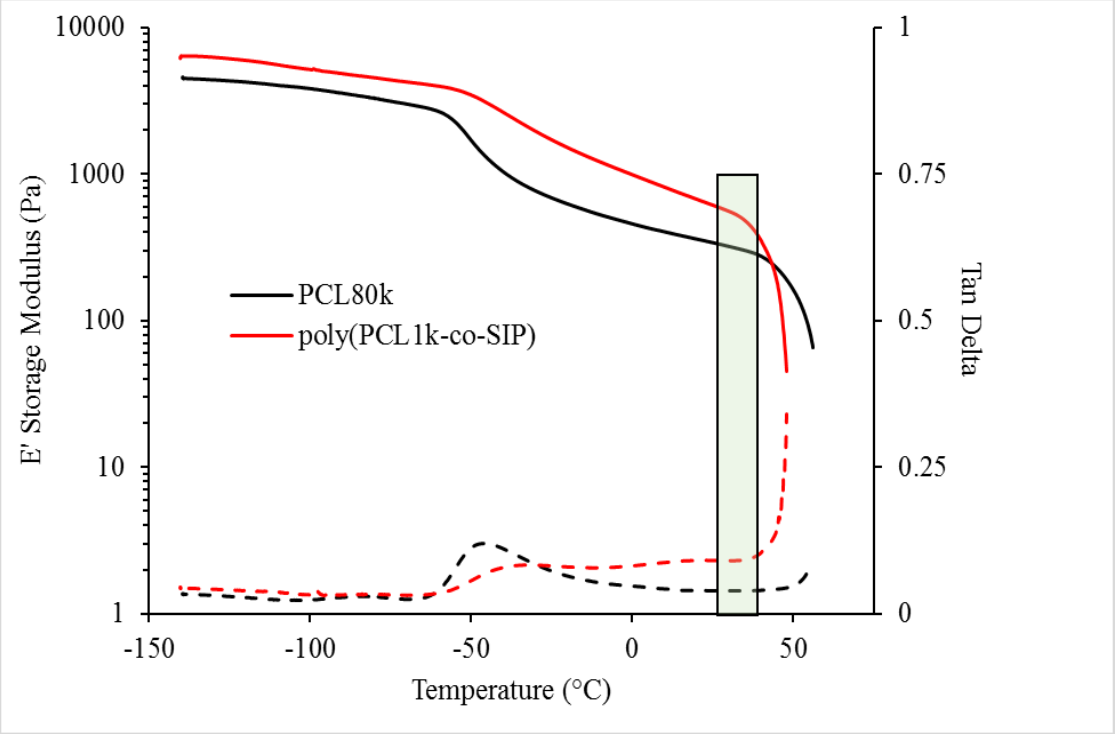

Figure 7.3. Dynamic mechanical analysis reveals enhanced plateau modulus upon the addition of charge. The green box highlights the temperature window of use (25 – 37 °C).

In addition to tensile analysis, the response of polymers to compressive load impacts potential biological applications (**Figure 7.4**). In the dry state, poly(PCL_{1k}-co-SIP) and PCL_{80k} both exhibit a compressive modulus ~ 20 Pa over a range of frequencies at 37 °C. Poly(PCL_{1k}-co-SIP) exhibited a slight but insignificant increase in modulus in response to increased frequency. Both PCL polyester samples were analyzed again

following a soak in PBS for 48 h. Following soaks, PCL_{80k} revealed a slight decrease in compressive storage modulus with a similar response to applied frequencies due to the presence of water and PBS salts. Poly(PCL_{1k}-co-SIP), however, revealed an enhancement of compressive modulus and a strong response to applied frequency, with compressive moduli approaching 100 Pa at 10 Hz. This increased compressive modulus following PBS soaks likely arises through interactions between the charged copolyester backbone and the salts in PBS.[23] Non-charged PCL_{80k} submerged in PBS did not induce significant interactions between polymer backbone and PBS salts and likely excludes PBS from the center of the polymer disc. Charged copolyesters, however, interact with the salts in PBS to induce slight swelling upon submersion, potentially affecting the intramolecular interactions between polymer chains.[23] In particular, PBS formulations contain divalent phosphate salts which could form physical crosslinks between polymer chains, leading to an enhanced compressive modulus following soaks.

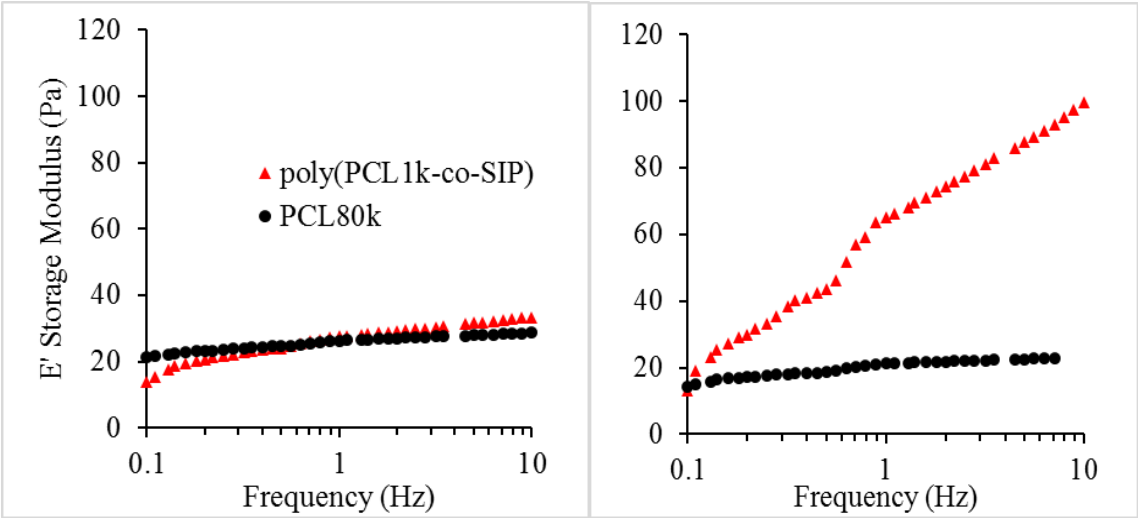

Figure 7.4. A. Dry compression mechanical analysis reveals similar storage modulus between PCL homopolymer and charged PCL copolyester. B. Wet compression mechanical analysis shows enhanced storage modulus for charged PCL copolyesters and depressed storage modulus of PCL homopolymer upon soaking in phosphate buffered saline for 48 h.

Due to the superior properties of poly(PCL_{1k}-co-SIP) ionomers, investigations of their role as bioadhesives showed great promise. Time-temperature superposition analysis of poly(PCL_{1k}-co-SIP) revealed adherence to WLF parameter fits, despite significant charge and the presence of crystallinity (**Figure 7.S1**). Rheological shear sweeps over the temperature range of 100 – 30 °C revealed a G'-G" crossover point and shear thinning characteristic of high molecular weight polymers and similar to that observed before. Upon transformation to a temperature-dependent behavior (utilizing WLF parameters and a frequency of 1 Hz), the G' storage modulus as a function of temperature adhered to the Dahlquist criterion for pressure-sensitive adhesives. Furthermore, while poly(PCL_{1k}-co-SIP) exhibited G' moduli near 0.3 MPa at room temperature, its modulus decreases at the application temperature of 37 °C. This decrease in modulus enhances adhesion, particularly to rough surfaces often seen in the human body and wounds. Furthermore, as shown in **Figure 7.5**, at 37 °C a crossover point is reached where G" is higher than G', suggesting the potential for polymer flow into wound crevasses to increase adhesion to harmed tissues.

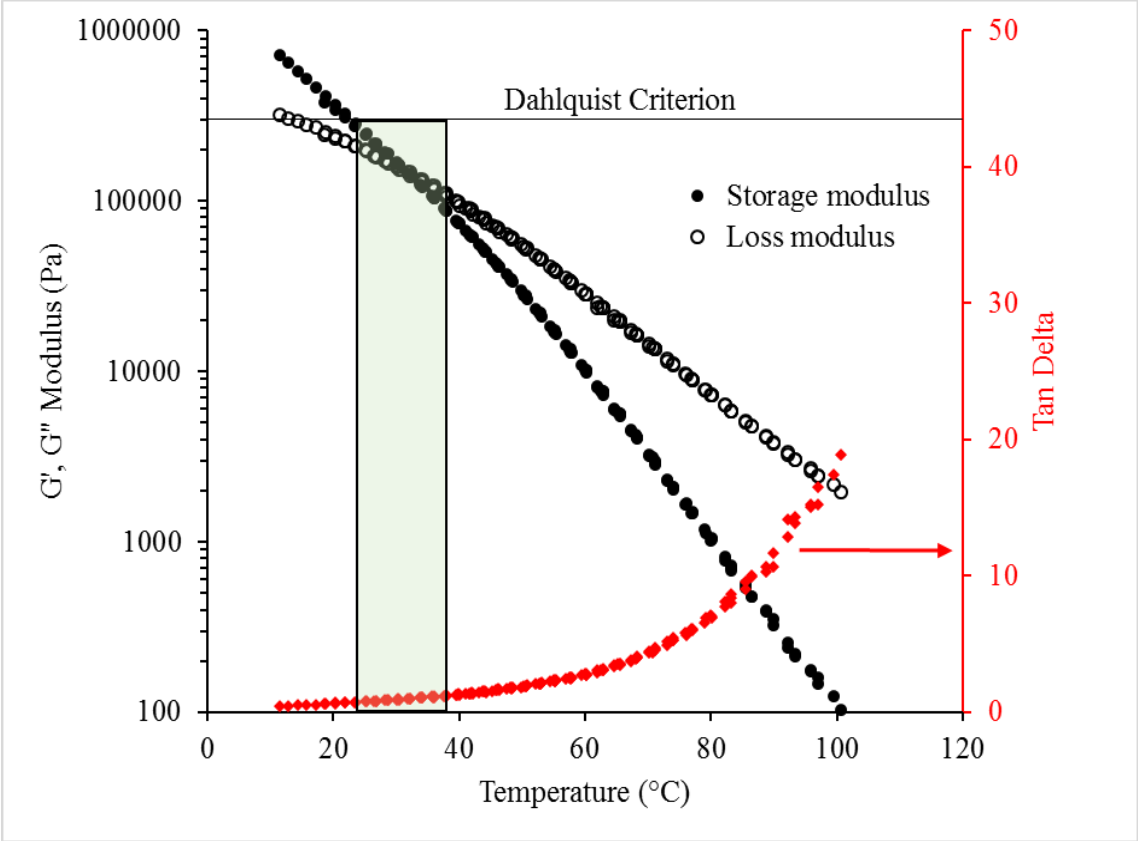

Figure 7.5. Time-temperature superposition analysis reveals adherence to the Dahlquist criterion for adhesives. The green box highlights the temperature window of use (25 – 37 °C).

180° peel testing revealed peel strength of 108 ± 90 g/in for poly(PCL_{1k}-co-SIP) at ~45 °C from stainless steel plates. While the peel strength of the polymer film remains decreased compared to conventional tape, poly(PCL_{1k}-co-SIP) films remain promising tissue adhesives. Room temperature peel strength remains unattainable due to a lack of adhesion to either Mylar or stainless steel plates. When placed on a hydrated surface, such as gelatin, poly(PCL_{1k}-co-SIP) films transfer cleanly from the Mylar to the gelatin, suggesting a role of water in the film adhesive properties. Poly(PCL_{1k}-co-SIP) provides a facile polymer film for clinician application while providing adhesion and enhanced compressive properties once introduced to the injured tissue. Clinicians handling poly(PCL_{1k}-co-SIP) films would fail to witness significant adhesion to skin or gloves

during the application process, but upon warming and contact with water present in tissue, poly(PCL_{1k}-co-SIP) transforms into an effective adhesive.

While material and adhesive properties remain vital for an effective wound glue, biological evaluation remains of vital importance to tissue healing. Cytotoxic evaluation against MDA-MB-231 human breast cancer cells provided a metric of cellular response for wound healing. As seen in **Figure 7.S1**, viability of human breast cancer cells decreases significantly compared to untreated control cells, but remains above 80 %. This change in viability likely arises from slight variations in oxygen permeability due to the presence of poly(PCL_{1k}-co-SIP) film on top of cells. While encouraging, cell attachment remains the most important metric for successful wound healing, due to the presence of infiltrating cells into wound space. As seen in **Figure 7.6**, poly(PCL_{1k}-co-SIP) facilitated significantly increased cell adhesion compared to non-tissue-culture-treated 24-well plates. Increased cell adhesion results in decreased time required to heal the wound, as the poly(PCL1k-co-SIP) film provides sites for cell attachment alongside biodegradation potential due to its decreased molecular weight.

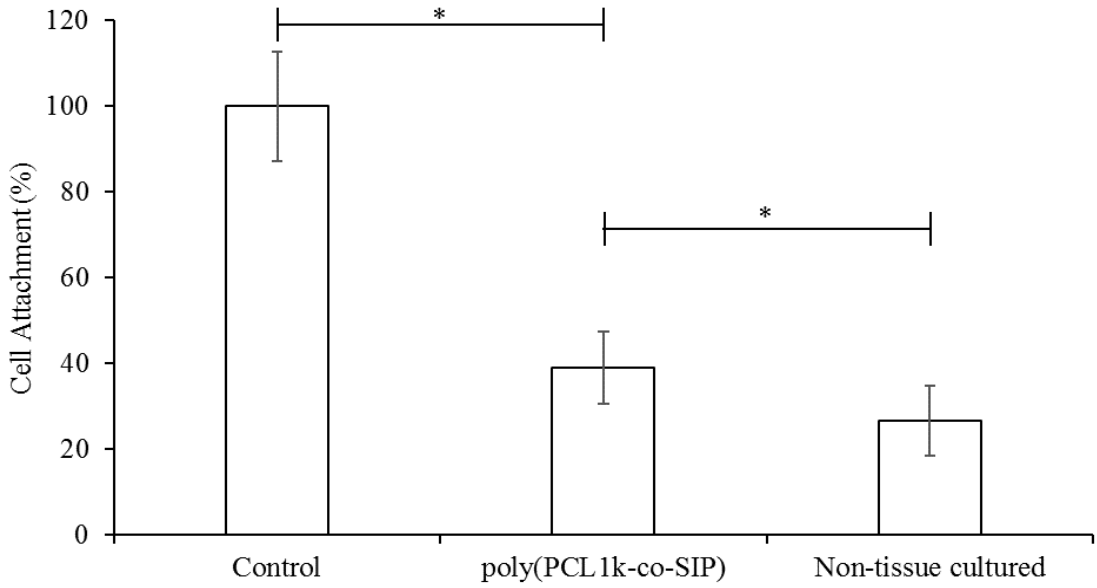

Figure 7.6. Poly(PCL_{1k}-co-SIP) facilitates cell attachment significantly better than non-tissue culture treated plates, providing anchors for infiltration (n = 3). Asterisks represent samples that are statistically different ($p < 0.05$).

SEM imaging provided visualization of MDA-MB-231 human breast cancer cell attachment onto poly(PCL_{1k}-co-SIP) films, seen in **Figure 7.7**. Microcracks along the film surface provided sites for cell infiltration and attachment and facilitated the start of cell migration along the film surface. Cell attachments, as well as secreted protein, allowed for the indirect evaluation of cell health due to the morphology characteristic of MDA-MB-231 cells. The films themselves remained flat, with only small cracks (likely due to the sterilization or dehydration process) present on film surfaces. The ability of cells to successfully attach to poly(PCL_{1k}-co-SIP) films confirmed the promise of these films to act as effective wound glue.

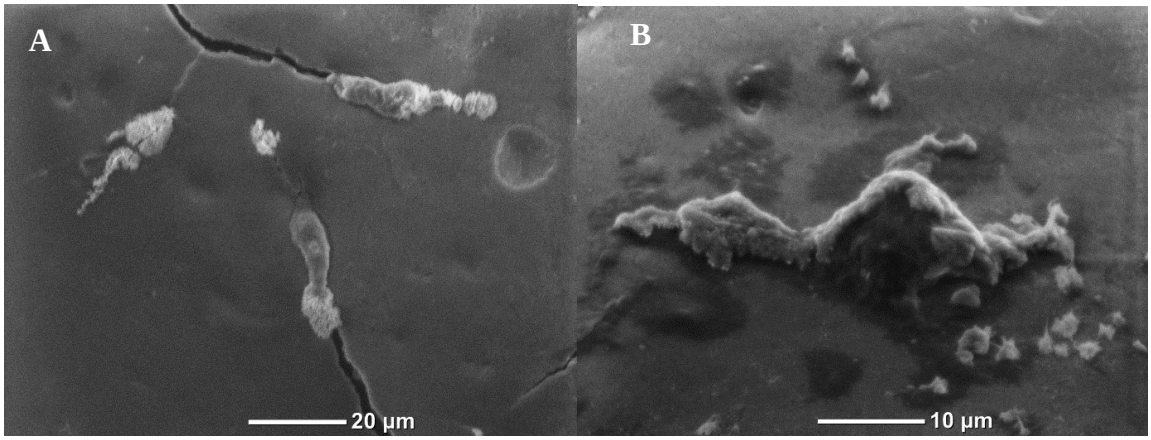

Figure 7.7. SEM imaging reveals MDA-MB-231 propensity to attach along cracks in poly(PCL_{1k}-co-SIP) (a) as well as protruding cell attachments for migration (b).

7.5 Conclusion

Wound healing continues to plague millions of people, with limited options for effective, non-toxic care. Synthesis of poly(PCL_{nk}-co-SIP) polyester ionomers provided polymers with enhanced rheological modulus and viscosity for successful melt processing. Furthermore, the inclusion of charge into PCL afforded copolyesters with increased tensile and compressive modulus, especially upon PBS soaking for 48 h. 180° peel testing revealed a favorable peel strength around body temperature, significantly improved compared to 25 °C and suggesting potential to improve adhesion in a hydrated state. Finally, cell screening against MDA-MB-231 human breast cancer cells revealed cell attachment onto poly(PCL_{1k}-co-SIP) films. Poly(PCL_{1k}-co-SIP) represents the future of wound healing through increased adhesion to patient tissues while minimizing tackiness observed by clinicians.

7.6 Acknowledgements

The authors would like to thank Samantha Talley for her help with SAXS and Ryan Mondschein for helpful discussions. This work was funded in part by the NSF Research Experience for Undergraduates, Chemists at the Food-Energy-Water Nexus.

7.7 Supplemental Information

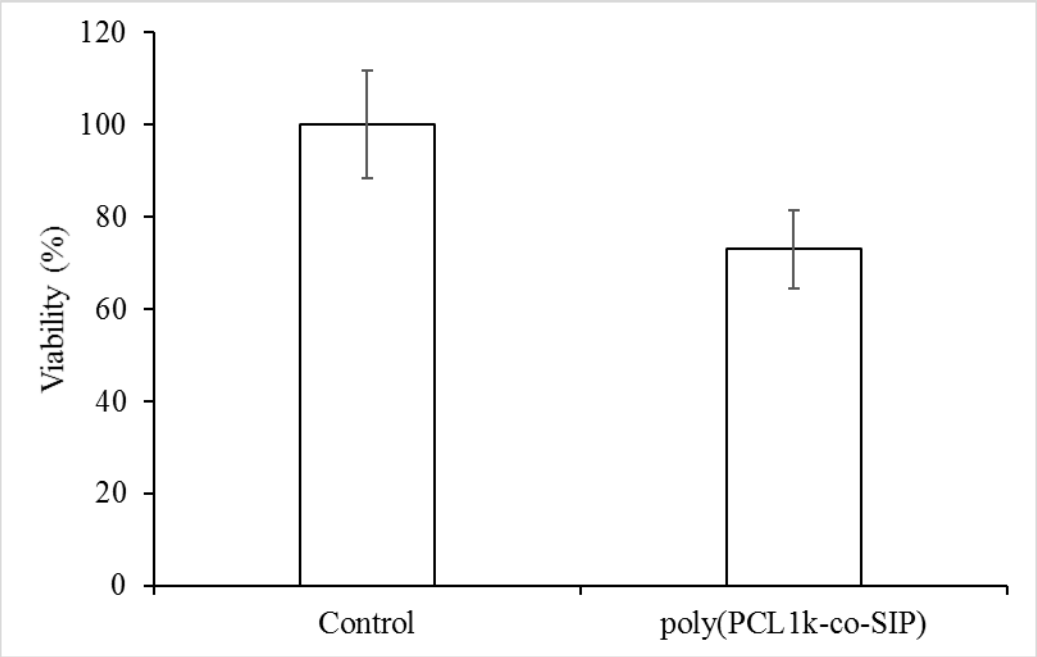

Figure 7.S1. Cell viability of MDA-MB-231 cells cultured underneath poly(PCL_{1k}-co-SIP) films reveals significantly decreased cell viability compared to control cells, likely due to slight inhibition of oxygen transport throughout the well ($n = 3$, $p < 0.05$). Statistical difference evaluated by ANOVA followed by Tukey's HSD.

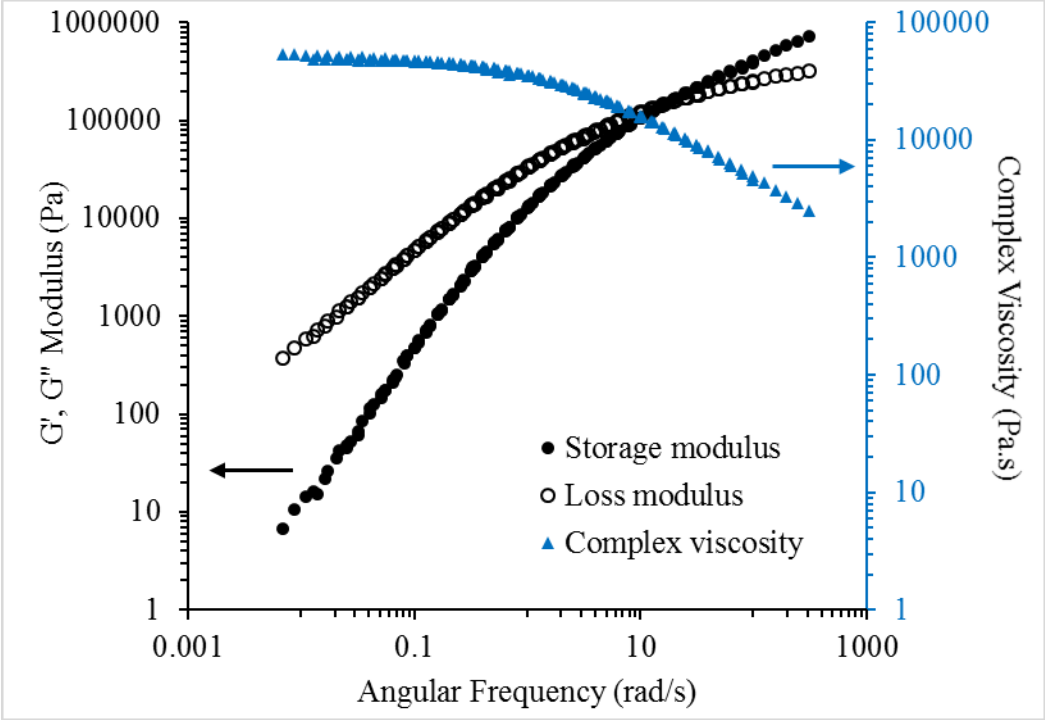

Figure 7.S2. Analysis of poly(PEG1k-co-SIP) reveals adherence to time-temperature superposition.

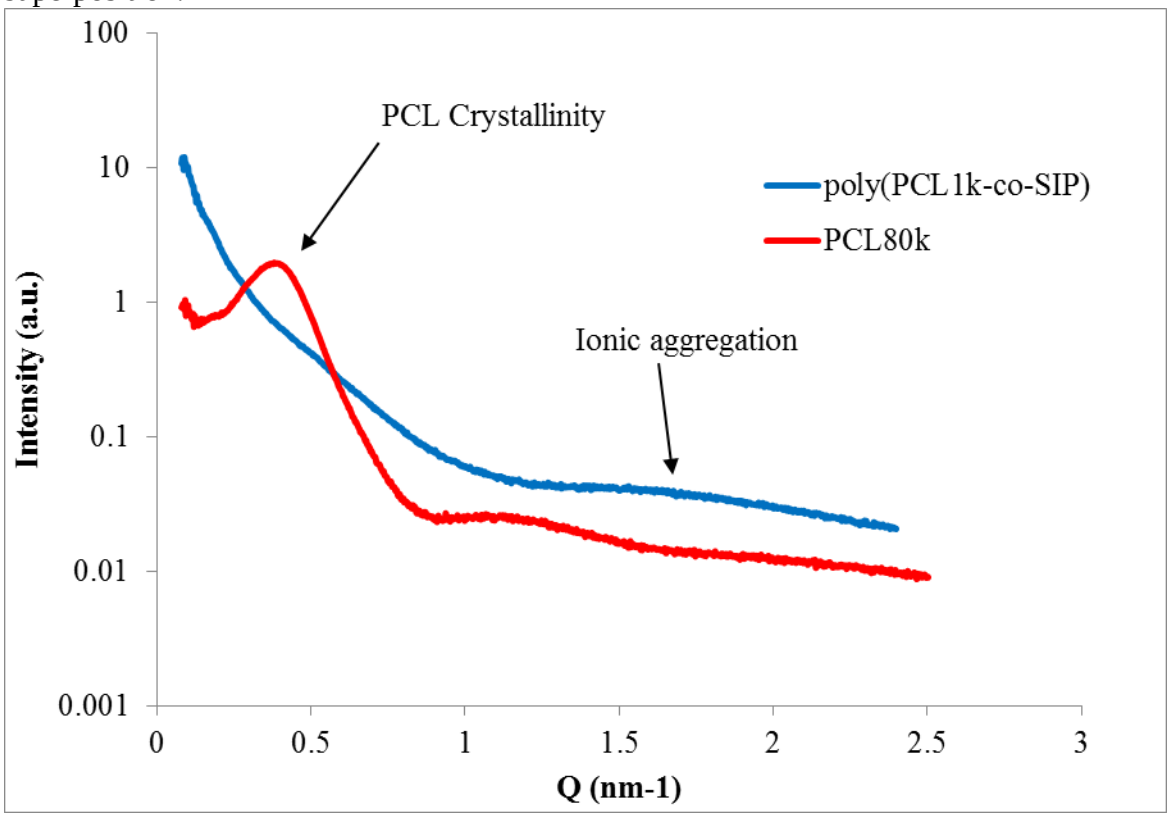

Figure 7.S3. Small angle X-ray scattering reveals ionic aggregation in poly(PCL_{1k}-co-SIP) compared to high molecular weight PCL.

References

1. Broughton 2nd, G.; Janis, J. E.; Attinger, C. E., The basic science of wound healing. *Plastic and reconstructive surgery* **2006,** 117, (7 Suppl), 12S-34S.
2. Diegelmann, R. F.; Evans, M. C., Wound healing: an overview of acute, fibrotic and delayed healing. *Front Biosci* **2004,** 9, (1), 283-289.
3. Kiecolt-Glaser, J. K.; Marucha, P. T.; Mercado, A.; Malarkey, W. B.; Glaser, R., Slowing of wound healing by psychological stress. *The Lancet* **1995,** 346, (8984), 1194-1196.
4. Gonzalez-Andrades, M.; Alonso-Pastor, L.; Mauris, J.; Cruzat, A.; Dohlman, C. H.; Argüeso, P., Establishment of a novel in vitro model of stratified epithelial wound healing with barrier function. *Scientific reports* **2016,** 6.
5. Bhende, S.; Rothenburger, S.; Spangler, D. J.; Dito, M., In vitro assessment of microbial barrier properties of Dermabond® topical skin adhesive. *Surgical infections* **2002,** 3, (3), 251-257.
6. Lefèvre, S.; Valois, A.; Truchetet, F., Allergic contact dermatitis caused by Dermabond®. *Contact Dermatitis* **2016,** 75, (4), 240-241.
7. Yagnatovsky, M.; Pham, H.; Rokito, A.; Jazrawi, L.; Strauss, E., Type IV hypersensitivity reactions following Dermabond adhesive utilization in knee surgery: A Report of Three Cases. *The Physician and Sportsmedicine* **2017**, 1-4.
8. Dong, R.; Qin, C.; Qiu, X.; Yan, X.; Yu, M.; Cui, L.; Zhou, Y.; Zhang, H.; Jiang, X.; Long, Y., In situ precision electrospinning as an effective delivery technique for cyanoacrylate medical glue with high efficiency and low toxicity. *Nanoscale* **2015,** 7, (46), 19468-19475.
9. Hee Park, D.; Bum Kim, S.; Ahn, K. D.; Yong Kim, E.; Jun Kim, Y.; Keun Han, D., In vitro degradation and cytotoxicity of alkyl 2-cyanoacrylate polymers for application to tissue adhesives. *Journal of applied polymer science* **2003,** 89, (12), 3272-3278.
10. Kouketsu, A.; Nogami, S.; Fujiwara, M.; Mori, S.; Yamauchi, K.; Hashimoto, W.; Miyashita, H.; Kurihara, J.; Kawai, T.; Higuchi, K., Clinical evaluations of autologous fibrin glue and polyglycolic acid sheets as oral surgical wound coverings after partial glossectomy. *Journal of Cranio-Maxillofacial Surgery* **2016,** 44, (8), 964-968.
11. Whelan, D.; Caplice, N.; Clover, A., Fibrin as a delivery system in wound healing tissue engineering applications. *Journal of Controlled Release* **2014,** 196, 1-8.
12. Wagers, S. S.; Norton, R. J.; Rinaldi, L. M.; Bates, J. H.; Sobel, B. E.; Irvin, C. G., Extravascular fibrin, plasminogen activator, plasminogen activator inhibitors, and airway hyperresponsiveness. *The Journal of clinical investigation* **2004,** 114, (1), 104-111.
13. Lam, C. X.; Hutmacher, D. W.; Schantz, J. T.; Woodruff, M. A.; Teoh, S. H., Evaluation of polycaprolactone scaffold degradation for 6 months in vitro and in vivo. *Journal of biomedical materials research Part A* **2009,** 90, (3), 906-919.
14. Chang, J. W.; Park, S. A.; Park, J. K.; Choi, J. W.; Kim, Y. S.; Shin, Y. S.; Kim, C. H., Tissue-engineered tracheal reconstruction using three-dimensionally printed artificial tracheal graft: preliminary report. *Artificial organs* **2014,** 38, (6).
15. Elomaa, L.; Teixeira, S.; Hakala, R.; Korhonen, H.; Grijpma, D. W.; Seppälä, J. V., Preparation of poly (ε-caprolactone)-based tissue engineering scaffolds by stereolithography. *Acta biomaterialia* **2011,** 7, (11), 3850-3856.

16. Eshraghi, S.; Das, S., Mechanical and microstructural properties of polycaprolactone scaffolds with one-dimensional, two-dimensional, and three-dimensional orthogonally oriented porous architectures produced by selective laser sintering. *Acta Biomaterialia* **2010,** 6, (7), 2467-2476.
17. Williams, J. M.; Adewunmi, A.; Schek, R. M.; Flanagan, C. L.; Krebsbach, P. H.; Feinberg, S. E.; Hollister, S. J.; Das, S., Bone tissue engineering using polycaprolactone scaffolds fabricated via selective laser sintering. *Biomaterials* **2005,** 26, (23), 4817-4827.
18. Niu, Y.; Chen, K. C.; He, T.; Yu, W.; Huang, S.; Xu, K., Scaffolds from block polyurethanes based on poly (ε-caprolactone)(PCL) and poly (ethylene glycol)(PEG) for peripheral nerve regeneration. *Biomaterials* **2014,** 35, (14), 4266-4277.
19. Duncan, A. J.; Leo, D. J.; Long, T. E., Beyond Nafion: charged macromolecules tailored for performance as ionic polymer transducers. *Macromolecules* **2008,** 41, (21), 7765-7775.
20. Kang, H.; Lin, Q.; Armentrout, R. S.; Long, T. E., Synthesis and characterization of telechelic poly (ethylene terephthalate) sodiosulfonate ionomers. *Macromolecules* **2002,** 35, (23), 8738-8744.
21. Bartels, J.; Wang, J.-H. H.; Chen, Q.; Runt, J.; Colby, R. H., Segmental Dynamics of Ethylene Oxide-Containing Polymers with Diverse Backbone Chemistries. *Macromolecules* **2016,** 49, (5), 1903-1910.
22. Chen, Q.; Masser, H.; Shiau, H.-S.; Liang, S.; Runt, J.; Painter, P. C.; Colby, R. H., Linear viscoelasticity and Fourier transform infrared spectroscopy of polyether–ester–sulfonate copolymer ionomers. *Macromolecules* **2014,** 47, (11), 3635-3644.
23. Valliant, E. M.; Gagnier, D.; Dickey, B. T.; Boyd, D.; Filiaggi, M. J., Calcium polyphosphate as an additive to zinc-silicate glass ionomer cements. *Journal of biomaterials applications* **2015,** 30, (1), 61-70.

Chapter 8. Biologically-Derived, Environmentally-Friendly Polyureas to Enable Rapid Nitrogen Delivery to Plants

Allison M. Pekkanen[1], Joseph M. Dennis[2], Lindsey J. Anderson[2], Ryan J. Mondschein[2], Robert B. Moore[2], Timothy E. Long[1,2]*

[1]School of Biomedical Engineering and Sciences, Virginia Tech, Blacksburg, VA 24061

[2]Macromolecules Innovation Institute, Department of Chemistry, Virginia Tech, Blacksburg, VA 24061

* To whom correspondence should be addressed. E-mail: telong@vt.edu. TEL: (540) 231-2480 Fax: (540) 231-8517

Keywords: Poly(ethylene glycol), Urea, Nitrogen, Hydrogen Bonding

8.1 Abstract

Nitrogen availability for plants while reducing or eliminating harmful runoff remains an important aspect of both plant scientists and chemists. The creation of polymeric ammonia sources realizes the long sought-after controlled release of nitrogen-containing fertilizers. Poly(urea)s, commonly synthesized from isocyanates, act as ammonia sources but require toxic catalyst and precursor chemicals. Melt polycondensation provided high molecular weight poly(ether urea)s suitable for water-soluble ammonia release. Thermomechanical and rheological analysis proved the poly(ether urea)s potential as melt-processable materials with low melting points. Variable temperature Fourier transform infrared spectroscopy confirmed urea hydrogen bonding, accounting for mechanical properties not commonly seen with poly(ethylene glycol). Ammonia release studies revealed significant polymer degradation at short (< 1 month) time scales, highlighting the role of poly(ethylene glycol) in the availability of

urea groups. These poly(ether urea)s represent a significant potential for successful delivery of nitrogen to plants at short time scales.

8.2 Introduction

The uptake of ammonium into plant cells catalyzes a wide variety of biochemical reactions, most notably the formation of amino acids including glutamine and glutamate.[1, 2] Atmospheric nitrogen fixation, nitrate reduction, and direct uptake provide substantial ammonium ions for plant metabolism.[1] The use of nitrogen fertilizers sustains crop production suitable to meet demands of human consumption.[3] Individual plant or crop type along with the availability of water dictates the nitrogen content required for successful plant growth.[3] Overuse of nitrogen fertilizers to promote further crop growth and yield saturates plant roots and limits overall plant growth.[3, 4] Furthermore, the overuse of fertilizers results in significant nitrogen runoff, which initiates aquatic ecosystem breakdowns and significant growth of algae.[5, 6] The generation of sustained-release fertilizers to regulate the release of nitrogen remains a vital concern for both farmers and scientists.

Polymeric nitrogen sources, notably polyureas, generate sustained and delayed release of ammonium to limit fertilizer overuse.[7] The urea group proved valuable in the improvement of mechanical properties compared to urethanes through reversible bidentate hydrogen bonding.[8] Typical polymerization of urea involves the use of toxic isocyanates to couple diamines, leading also to the use of solvent and heavy metal catalysts.[7, 9] Reactions performed at elevated temperature and pressure or in the presence of catalyst yield polyureas from carbon dioxide and diamines.[9-13] Tang et al. described a

two-step poly(urea ester)s synthesis from urea-containing diols formed from melt reactions of urea and amino alcohols.[14] Dennis et al. demonstrated the power of melt polycondensation of urea with diamines to couple EDTA and diaminooctane to afford film-forming polymers suitable for low levels of ammonia release.[15] While these previous reports generated significant interest in the field of polyureas, the need for a faster releasing ammonia from processable, environmentally-friendly polymers still exists.

Poly(ethylene glycol) (PEG) continues to experience widespread use in biological fields due to its strong track record of biocompatibility and inertness in the human body.[16] The staunch hydrophilic nature of PEG coupled with its chain flexibility renders many polymers containing PEG water soluble.[17] This chain flexibility and water solubility potentially increases ammonia availability for plants. The inert nature of PEG also provides a polymer backbone suitable for plant interactions. PEG facilitated drought conditions in controlled studies of plant health and growth in low water conditions.[18, 19] Large concentrations of PEG prevented significant water uptake by plant roots and allowed for mediated drought control.[18, 19] PEG also generated increased concentrations of reactive oxygen species, though this remained limited at low PEG concentrations.[18] Furthermore, ethylene glycols remain inert when present in runoff, limiting disturbances to the native aquatic ecosystems.[20] While the elimination of runoff inspires current research, the elimination of potentially harmful downstream effects presents a path to rapidly restoring aquatic ecosystems.[20, 21] PEG's precedence as an material in plant biology motivates its use as a potential controlled release nitrogen source.

This work details the synthesis and characterization of poly(ether urea)s as a potential nitrogen source for plants. Melt polycondensation provided poly(ether urea)s

with varying PEG molecular weight without the need for solvent or catalyst. Rheological and thermomechanical characterization proved the utility of hydrogen bonding within PEG backbones to significantly enhance properties compared to high molecular weight PEG. Finally, ammonia release characterized through incubation with urease revealed significant polymer degradation over short time scales. Coupling solvent and catalyst-free synthesis with significant polymer degradation provided polymers suitable for sustained nitrogen release to plants.

8.3 Materials and Methods

8.3.1 Materials. Poly(ethylene glycol) diamine (PEG-diamine, MW = 2,000 g/mol, 6,000 g/mol, 10,000 g/mol) and urea were purchased from Sigma Aldrich and used directly. Urease from Canavalia ensiformis (Jack bean) - Type III powder and an ammonia assay kit were purchased from Sigma-Aldrich. Phosphate buffered saline (PBS) was purchased from Life Technologies.

8.3.2 Analytical Techniques. ^{1}H NMR was performed on a Varian Unity Nuclear Magnetic Resonance instrument at ambient temperature in $DMSO_{d6}$. Differential scanning calorimetry (DSC) was performed on a TA Instruments Q2000 with a heat/cool/heat cycle of 10 °C/min, 100 °C/min, and 10 °C/min, respectively. The melting temperature was calculated as the maximum of the melting endotherm. Dynamic mechanical analysis (DMA) was conducted on a TA Instruments Q800 DMA in tension mode with a temperature ramp of 3 °C/min, a static force of 0.01 N, and an oscillatory strain of 1 Hz. Rheological experiments were performed on an Ares G2 rheometer in oscillation mode with 25 mm parallel plates and a constant strain of 1 % under air.

Variable temperatures IR was performed on a Varian 670-IR spectrometer (DTGS detector) 51 with Pike Technologies variable temperature GladiATRTM attachment (Diamond crystal). The spectra were collected at 4 cm^{-1} resolution and as an average of 32 scans. The samples were subjected to a temperature ramp of 1 °C /min, starting from 30 °C to 190 °C and FTIR spectra were collected every 10 °C beginning from 30 °C.

8.3.3 Synthesis of poly(ether urea)s. All polymers were prepared in a similar manner, with poly(PEG_{2k}-co-urea) used as an example. 2 g PEG_{2k}-diamine (0.001 moles, 1 eq.) and 60 mg urea (0.001 moles, 1 eq.) were introduced into a 100 mL round-bottomed flask equipped with a metal stirrod, distillation apparatus, gas inlet, and overhead stirrer. Degassing and purging with nitrogen gas three times allowed the reaction to proceed oxygen-free. Under a constant nitrogen purge, the reaction was stirred at 80 rpm at 180 °C for 30 min. A temperature ramp of 200 °C for 30 min and 220 °C for 30 min allowed the reaction to remain molten. Following 30 min at 220 °C, vacuum was applied until 0.15 mmHg, at which time the temperature was increased to 250 °C. The reaction was allowed to stay under vacuum for 1 h, after which the heating source was removed and the reaction allowed to cool under vacuum overnight. The product was removed from the round-bottomed flask and used without further purification.

8.3.4 Melt pressing of poly(ether urea) films. Poly(ether urea) samples were dried overnight at 60 °C under vacuum before use. Polymers were pressed between two 16 mil stainless steel plates using a PHI Q-230H manual hydraulic compression press. Kapton® films and a Rexco Partall® Power Glossy Liquid mold release agent were used to prevent poly(ether urea) adhesion. Polymers were heated for ~3 min at 90 °C before the top plate was added. After a 1 min isotherm at 90 °C, 4 press-release cycles were performed, the

first two utilizing 5 tons of force and the second two using 10 tons of force. The films were removed from the stainless steel plates and allowed to cool slowly to room temperature between the Kapton® films. The resulting polymer films were used without further purification.

8.3.5 Ammonia Release. All polymers were dissolved in phosphate buffered saline supplemented with 500 U/mL urease from Canavalia ensiformis - Type III. Urease was introduced at 20 U/mg polymer sample and incubated at room temperature for either 1 week or 1 month. Following incubation, ammonia release was measured using an ammonia assay kit following the manufacturer's protocol. Briefly, 100 μL polymer sample with urease was added to 1 mL ammonia assay reagent and incubated for 5 min. Absorbance was read at 340 nm on a SpectraMax G2 plate reader in cuvette absorbance mode. 10 μL L-glutamate dehydrogenase was added to each cuvette and allowed to react for 5 min. After gentle mixing, the absorbance was read again at 340 nm. Calculation of the concentration of ammonia in each sample followed the manufacturer's calculations. % polymer remaining was calculated from the theoretical moles of ammonia released per mg polymer upon complete degradation, assuming 2 units of ammonia are released during each reaction of urea. Data is presented as average ± standard deviation with respect to weight percent urea incorporation. Statistical analysis was performed in JMP statistical software by an ANOVA test followed by Tukey's HSD ($\alpha = 0.05$) to determine differences between groups ($n = 3$).

8.4 Results and Discussion

The utilization of bio-sourced urea for the creation of poly(urea)s without the use of isocyanates and solvent introduces a vital aspect of polymer science. The creation of water-soluble poly(urea)s for ammonia release remains a vital concern to release high levels of ammonia in shorter time scales than other poly(urea)s. Polycondensation of urea and poly(ethylene glycol) diamine afforded a series of poly(ether urea)s suitable as water-soluble polymers for accelerated ammonia release (**Scheme 8.1**). The resulting brown, viscous polymer melts provided polymers suitable for further characterization.

^{1}H NMR of poly(ether urea)s provided confirmation of successful polymerization, as seen in **Figure 8.1.** The incorporation of urea functionality into poly(ethylene glycol) diamine presents a characteristic NMR shift. Integration of peak areas provides further confirmation of poly(ethylene glycol) diamine molecular weight between urea groups. Despite confirmation of polymerization, molecular weight information of the resulting polymers remains unattainable due to insolubility in any common size exclusion chromatography solvents.

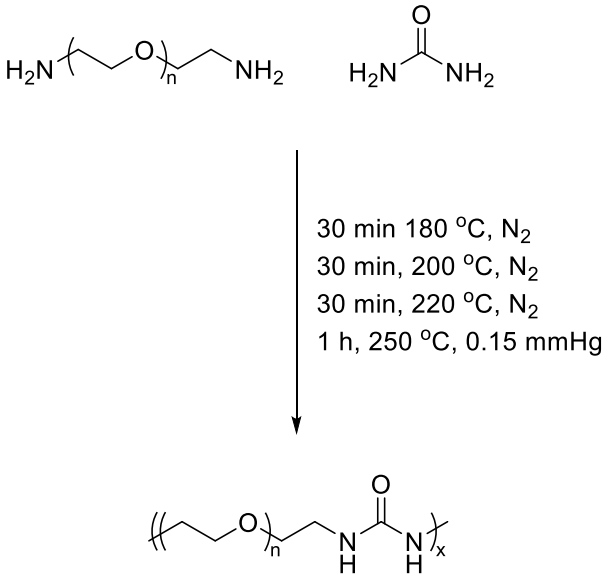

Scheme 8.1. Melt polycondensation of poly(ethylene glycol) and urea affords high molecular weight poly(ether urea)s.

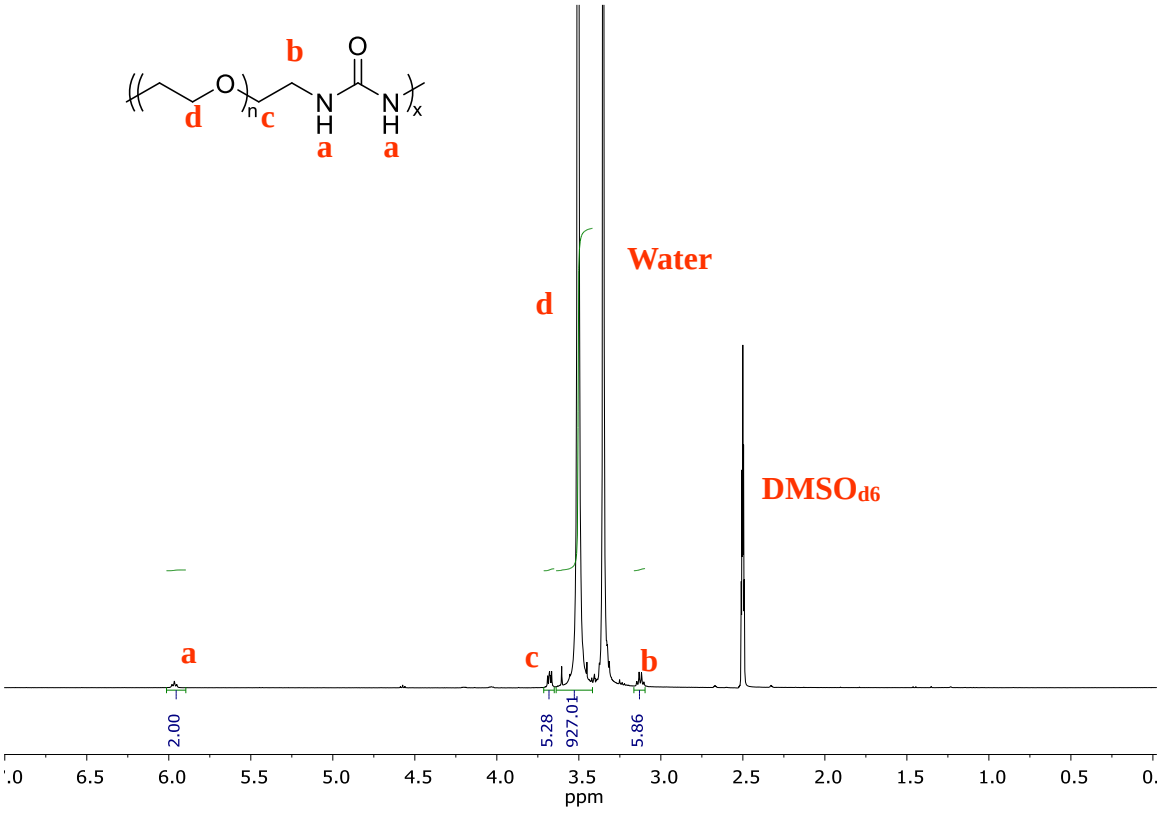

Figure 8.1. ^{1}H NMR analysis revealed successful polymerization.

DSC of poly(ether urea)s revealed the dominance of PEG in thermal transitions, evidenced by **Table 8.1**. As the PEG molecular weight increased, the melting temperature also increased. Furthermore, the % crystallinity of each sample, normalized to the theoretical PEG crystallinity, revealed an increase in crystallinity with increasing PEG-diamine molecular weight. As PEG-diamine molecular weight increases, the wt % urea functionality decreases and enables PEG chain mobility between urea groups. This chain mobility and the inherent hydrophilicity of PEG enable rapid dissolution in water at 1 mg/mL (**Table 8.1**). Total dissolution time decreases as wt % urea incorporation decreases, proving a larger role of chain flexibility and urea on dissolution compared to % crystallinity.

Sample	**Wt % Urea (%)**	**T_m (°C) (DSC)**	**% Crystallinity**	**T_g (°C) (DMA)**	**Dissolution Time**
Poly(PEG_{2k}-co-urea)	3	48	33.4	-34	17 min
Poly(PEG_{6k}-co-urea)	1	58	50.4	-37	13 min
Poly(PEG_{10k}-co-urea)	0.5	62	57.4	N.D.	11 min

Table 8.1. Thermal analysis revealed glass transition temperatures and melting temperatures of poly(ether urea)s. Only poly(ether urea)s without TEG-diamine exhibit water solubility.

Rheology of poly(ether urea)s provided information on their melt processability and indicated their potential as a moldable polymer. poly(ether urea)s exhibited ordering according to their levels of urea functionality, with poly(PEG_{2k}-co-urea) exhibiting the highest modulus and melt viscosity (**Figure 8.2, 8.S1**). Poly(PEG_{2k}-co-urea) and poly(PEG_{6k}-co-urea) each possessed a crossover point characteristic of high molecular weight polymers. Poly(PEG_{10k}-co-urea) failed to have a G”-G’ crossover point, due to

either potentially a lower molecular weight compared to other samples or a large effect of urea functionality on melt rheological properties. Melt viscosity of poly(ether urea)s revealed shear thinning and a high melt viscosity of poly(PEG_{2k}-co-urea) and poly(PEG_{6k}-co-urea) (**Figure 8.2**). Both poly(PEG_{2k}-co-urea) and poly(PEG_{6k}-co-urea) exhibited shear thinning and an onset of shear thinning at low angular frequencies, characteristic of high molecular weight polymers. Compared to polymers of similar composition and molecular weight, urea functionality provided an increased melt viscosity compared to their charged counterparts (cite SPEG). Poly(PEG_{10k}-co-urea) exhibited significantly decreased melt viscosity compared to either of its counterparts, likely due to a lower molecular weight. Despite this lowered molecular weight, the polymer continued to exhibit shear thinning, providing sufficient molecular weight to form films.

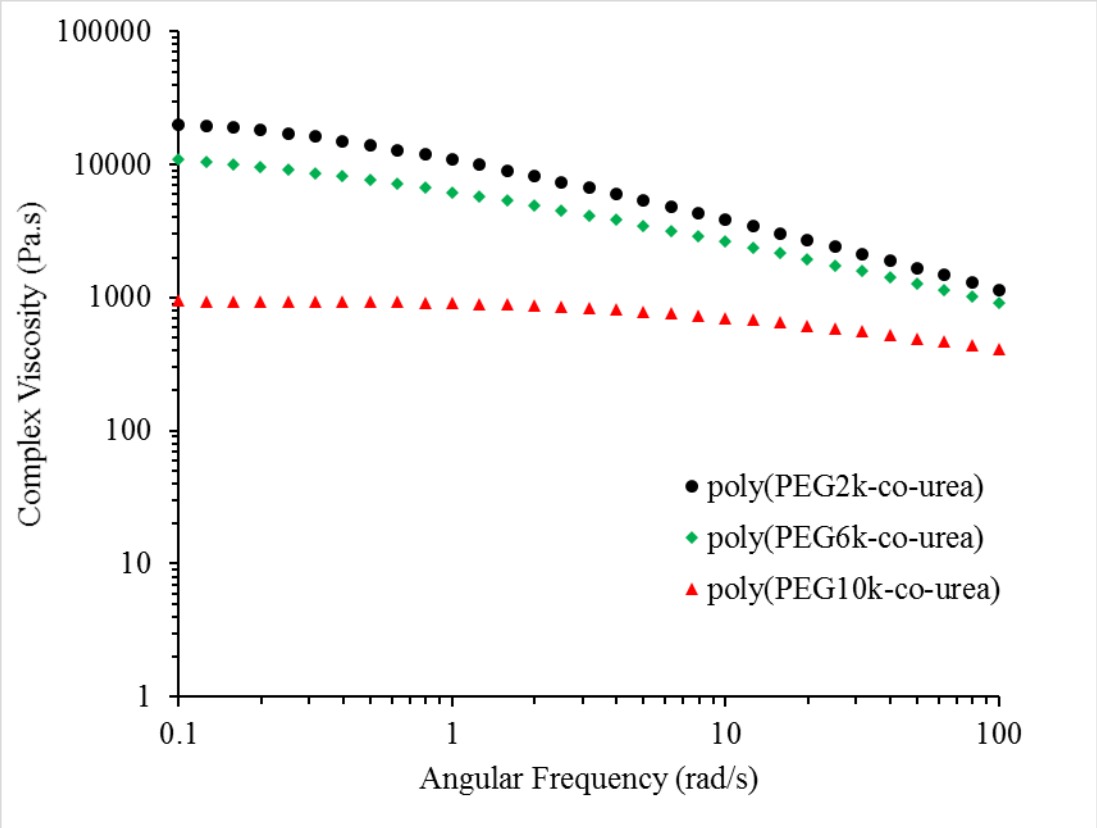

Figure 8.2. Increased melt viscosity resulted from inclusion of high mol % urea functionality.

Melt-pressed films of poly(PEG_{2k}-co-urea) and poly(PEG_{6k}-co-urea) provided optically, creasable clear films. The molecular weight of poly(PEG_{10k}-co-urea) proved insufficient to generate robust films. These films provided sample for dynamic mechanical analysis, shown in **Figure 8.3.** Urea functionality provided a slight increase in storage modulus with increased weight percent urea, while the onset of flow temperature remained consistent with PEG molecular weight. The flow temperatures of each polymer highlight the dominance of PEG in the thermal behavior of the samples. The chain flexibility and dominance of thermal properties of PEG likely drives this change in flow temperature between samples and results in the failure of films to sustain mechanical integrity until urea hydrogen bond disassociation. Due to low weight percent

incorporation of urea into PEG backbones, the urea groups likely failed to maintain film properties past PEG melting temperatures but provided sufficient hydrogen bonding to facilitate the formation of free-standing films.

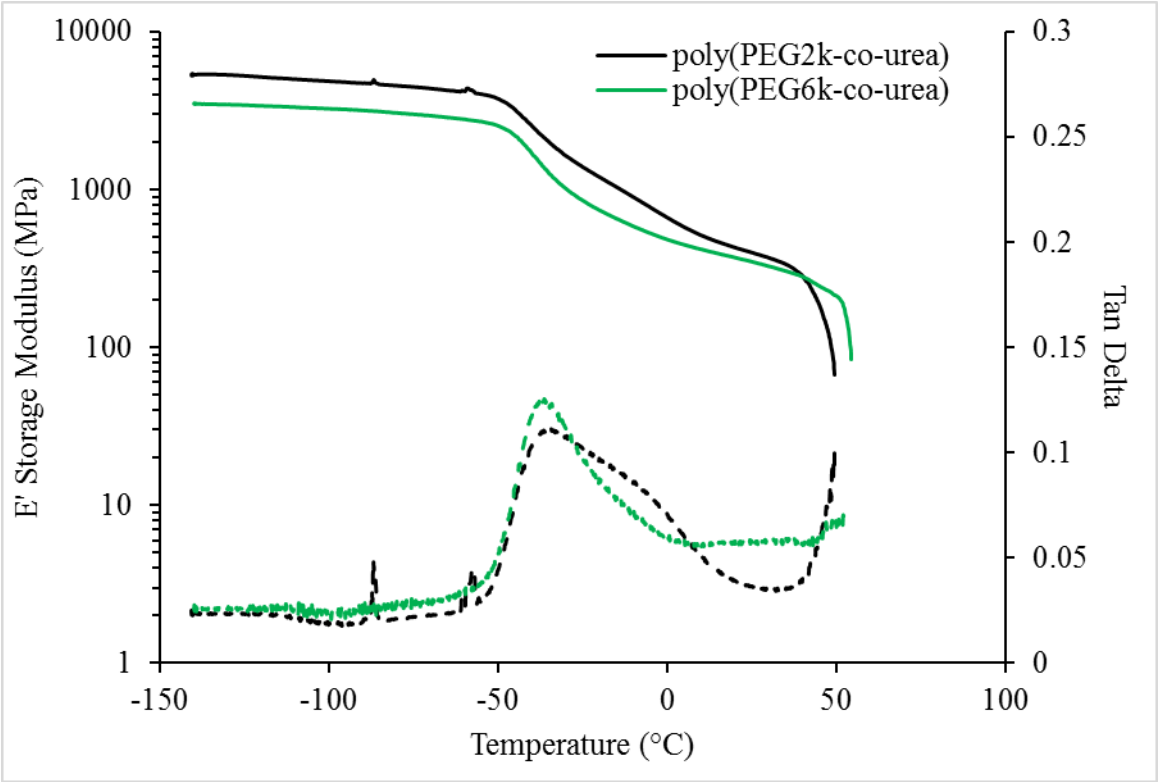

Figure 8.3. Dynamic mechanical analysis reveals storage moduli of poly(ether urea)s.

To confirm these hydrogen bonding interactions, variable temperature infrared spectroscopy (VT-FTIR) from 30 °C to 190 °C revealed the presence of urea interactions and free carbonyl species. As seen in **Figure 8.4**, the number of free carbonyl species increases as temperature increases, suggesting the labile nature of urea interactions. As the weight percent urea decreases, the relative number of bound and unbound carbonyls decreases, with the prevalence of free carbonyl groups increased in lower weight percent

urea samples. The variation in spectra with temperature confirms the presence of hydrogen bonding groups present on the polymer backbones and their labile nature.

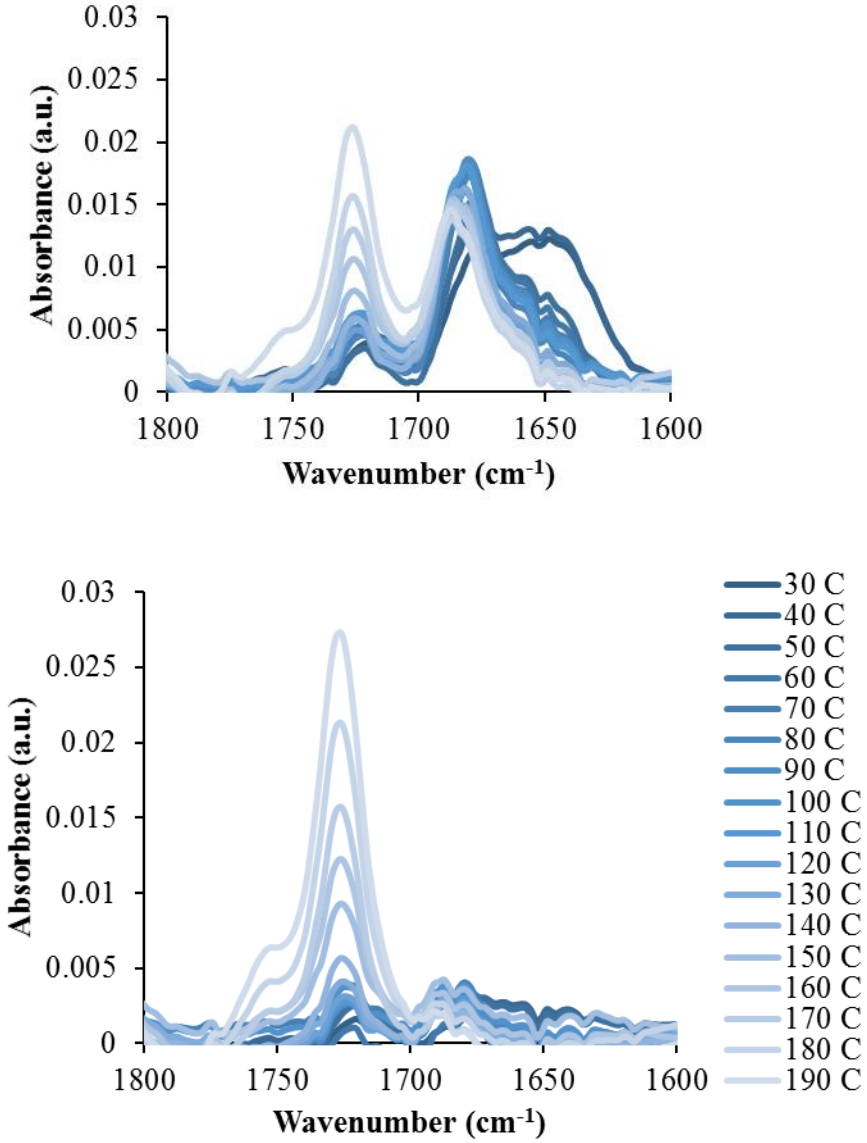

Figure 8.4. Variable temperature FTIR reveals hydrogen bonding interactions between urea groups. A. poly(PEG_{2k}-co-urea) B. poly(PEG_{10k}-co-urea)

The value of urea incorporation into PEG backbones lies in their great potential to act as a nitrogen source for plants. Ammonia release from these water-soluble poly(ether urea)s confirmed the availability of urea to act as a nitrogen source. After only one week at room temperature, urease releases sufficient urea to present significant polymer degradation (**Figure 8.5**). Interestingly, only four weeks of exposure to urease induced near complete polymer degradation and significant ammonia release. Compared to previous results of poly(urea) films' ability to release ammonia, the availability of urea for subsequent ammonia release remained much greater in these polymers.[10] As the weight percent urea decreases, the amount of ammonia required to degrade the polymer decreases, making each urea reduction more and more significant to total polymer degradation. After four weeks, close to 30 % of poly(PEG_{2k}-co-urea) remained, while poly(PEG_{10k}-co-urea) approached complete degradation and released significantly increased levels of ammonia.

Furthermore, compared to surface degradation of previous polyureas, both the water solubility and chain mobility afforded by these poly(ether urea)s increased the availability of urea for degradation by urease.[12] The urea enzyme operates through the incorporation of urea into a chamber which contains the enzyme active site.[17, 18] Once internalized, the enzyme catalyzes the reaction of urea into two molecules of ammonia which are subsequently released.[17, 18] The fate of ethylene glycol-based materials proved the environmentally-friendly aspect of these polymers, experiencing complete degradation into inert by-products within months in aquatic ecosystems. These polymers present biologically-friendly solutions as nitrogen sources within short time periods (<1 month).

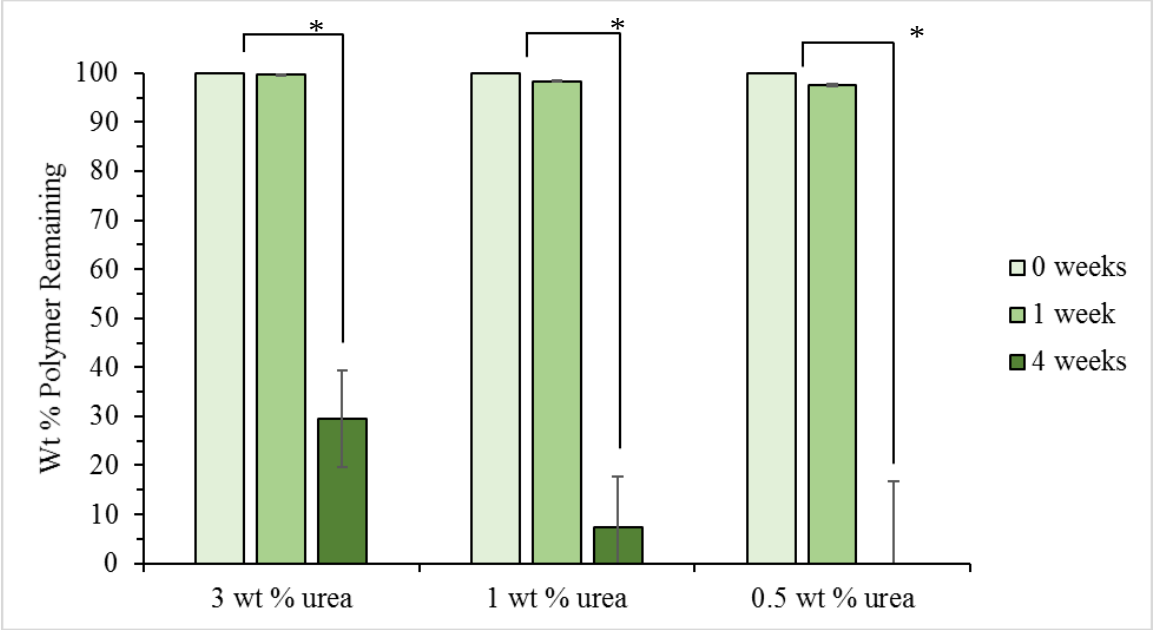

Figure 8.5. Ammonia release from polymers demonstrates dependence on wt % urea. After four weeks, near complete polymer degradation released significant levels of ammonia. * represents significant differences ($n = 3$, $p < 0.05$).

8.5 Conclusions

Water-soluble poly(ether urea)s show great promise as the next generation nitrogen feedstock for plants nutrients. Melt polycondensation provided poly(ether urea)s from biosourced feedstocks and without solvent, limiting environmental impacts. Compared to high molecular weight PEG, low weight percent incorporation of urea provided substantially different rheological and thermomechanical properties. Following incubation with urease, significant polymer degradation and ammonia release proved the utility of these poly(ether urea)s as a readily-available nitrogen source to sustain plant life.

8.6 Supplemental Information

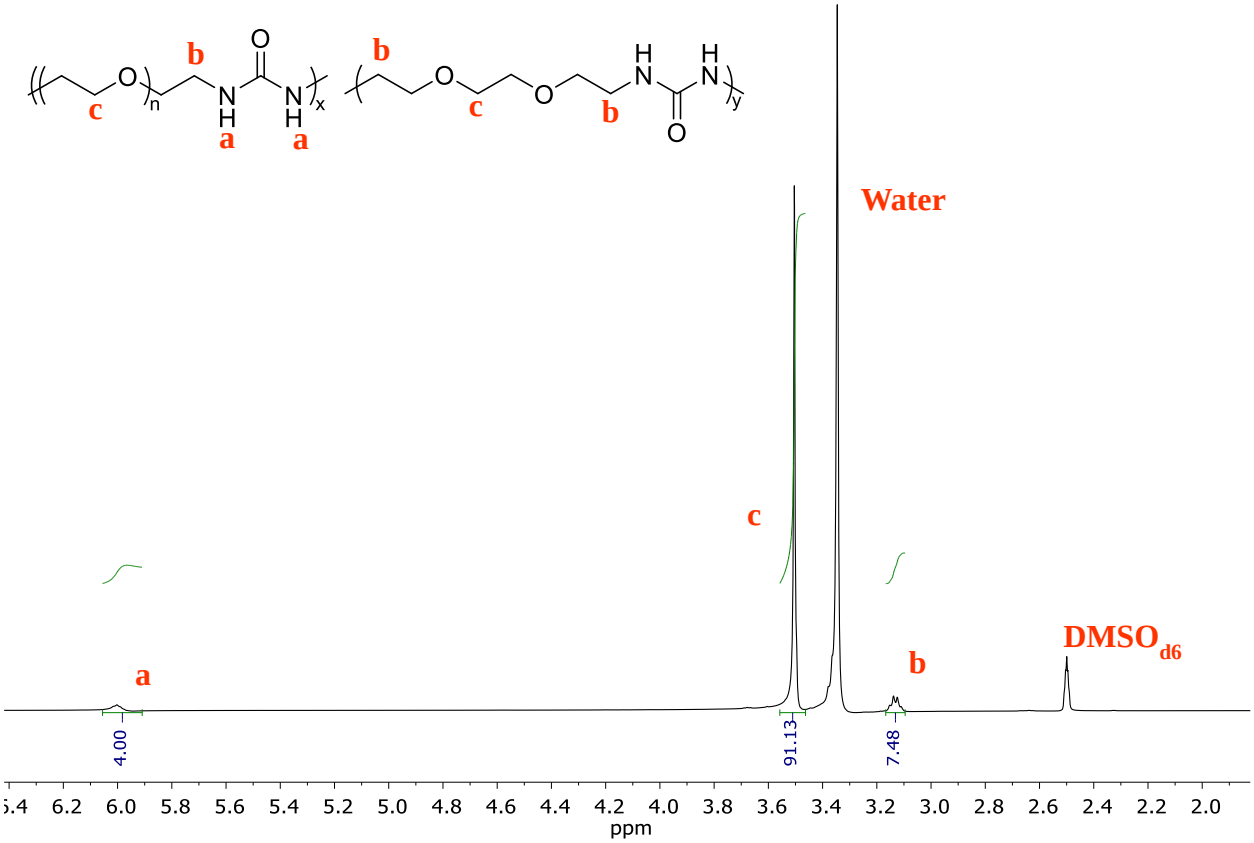

Sample	T_m (°C) (DSC)	Dissolution Time
Poly(PEG2k-co-EDBA-co-urea)	43, 103	DND

Figure 8.S1. ^{1}H NMR of poly(PEG_{2k}-co-EDBA-co-urea) reveals successful polymerization. Melting endotherms reveal favorable thermal properties but poly(PEG_{2k}-co-EDBA-co-urea) failed to dissolve in RO water.

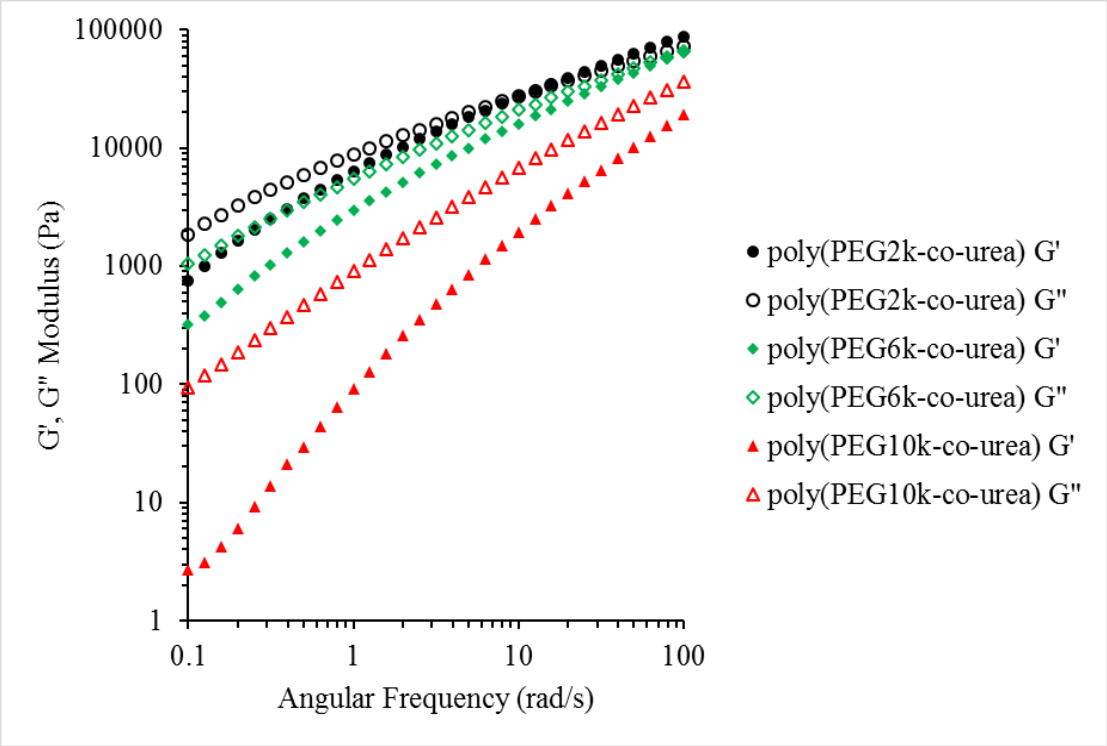

Figure 8.S2. Rheological analysis revealed crossover of G' and G" moduli.

References

1. Hirel, B.; Lea, P. J., Ammonia assimilation. In *Plant nitrogen*, Springer: 2001; pp 79-99.
2. Alain OURRY, J. H.; VOLENEC, J. J., Nitrogen Traffic During Plant Growth and Development. *Plant Nitrogen* **2013**, 255.
3. Lawlor, D. W.; Lemaire, G.; Gastal, F., Nitrogen, plant growth and crop yield. In *Plant nitrogen*, Springer: 2001; pp 343-367.
4. Kong, L.; Xie, Y.; Hu, L.; Si, J.; Wang, Z., Excessive nitrogen application dampens antioxidant capacity and grain filling in wheat as revealed by metabolic and physiological analyses. *Scientific Reports* **2017,** 7.
5. Zhu, Z.; Chen, D., Nitrogen fertilizer use in China–Contributions to food production, impacts on the environment and best management strategies. *Nutrient Cycling in Agroecosystems* **2002,** 63, (2), 117-127.
6. Zhang, F.; Chen, X.; Vitousek, P., Chinese agriculture: An experiment for the world. *Nature* **2013,** 497, (7447), 33-35.
7. Markusch, P. H.; Cline, R. L., Process for the production of polyurea encapsulated fertilizer particles and the encapsulated fertilizer particles produced by this process. In Google Patents: 1998.
8. Sheth, J. P.; Klinedinst, D. B.; Wilkes, G. L.; Yilgor, I.; Yilgor, E., Role of chain symmetry and hydrogen bonding in segmented copolymers with monodisperse hard segments. *Polymer* **2005,** 46, (18), 7317-7322.
9. Chiriac, C. I.; Tanasă, F., Polyureas. *Ullmann's Encyclopedia of Industrial Chemistry* **2000**.
10. Koji, K.; Yanosuke, I., Process for preparing linear polyureas. In Google Patents: 1961.
11. Koji, K.; Yanosuke, I., Linear polyureas prepared from the reaction of urea and two different alkylene diamines. In Google Patents: 1964.
12. Bouboulis, C. J.; Isidor, K.; White, C. M., Flexible polyureas. In Google Patents: 1968.
13. Bouboulis, C. J.; Isidor, K., Polyureas. In Google Patents: 1968.
14. Tang, D.; Chen, Z.; Correa-Netto, F.; Macosko, C. W.; Hillmyer, M. A.; Zhang, G., Poly (urea ester): A family of biodegradable polymers with high melting temperatures. *Journal of Polymer Science Part A: Polymer Chemistry* **2016,** 54, (24), 3795-3799.
15. Dennis, J. M.; Pekkanen, A. M.; Steinberg, L. I.; Long, T. E., Synthesis and Characterization of Isocyanate-free Biosourced Polyureas. *In Preparation* **2017**.
16. Turecek, P. L.; Bossard, M. J.; Schoetens, F.; Ivens, I. A., PEGylation of biopharmaceuticals: a review of chemistry and nonclinical safety information of approved drugs. *Journal of pharmaceutical sciences* **2016,** 105, (2), 460-475.
17. Lee, H.; Venable, R. M.; MacKerell, A. D.; Pastor, R. W., Molecular dynamics studies of polyethylene oxide and polyethylene glycol: hydrodynamic radius and shape anisotropy. *Biophysical journal* **2008,** 95, (4), 1590-1599.
18. de Araújo Silva, M. M.; Willadino, L.; dos Santos, D. Y. A. C.; Oliveira, A. F. M.; Camara, T. R., Response of Ricinus communis L. to in vitro water stress induced by polyethylene glycol. *Plant growth regulation* **2016,** 78, (2), 195-204.

19. He, Y.; Wu, J.; Lv, B.; Li, J.; Gao, Z.; Xu, W.; Baluška, F.; Shi, W.; Shaw, P. C.; Zhang, J., Involvement of 14-3-3 protein GRF9 in root growth and response under polyethylene glycol-induced water stress. *Journal of experimental botany* **2015**, erv149.
20. Kent, R. A.; Andersen, D.; Caux, P. Y.; Teed, S., Canadian water quality guidelines for glycols–An ecotoxicological review of glycols and associated aircraft anti-icing and deicing fluids. *Environmental Toxicology* **1999,** 14, (5), 481-522.
21. Switzenbaum, M. S.; Veltman, S.; Mericas, D.; Wagoner, B.; Schoenberg, T., Best management practices for airport deicing stormwater. *Chemosphere* **2001,** 43, (8), 1051-1062.
22. Follmer, C., Insights into the role and structure of plant ureases. *Phytochemistry* **2008,** 69, (1), 18-28.
23. Krajewska, B., Ureases I. Functional, catalytic and kinetic properties: A review. *Journal of Molecular Catalysis B: Enzymatic* **2009,** 59, (1), 9-21.

Chapter 9. Vat Photopolymerization of Physically Crosslinked Monomers: Printing Soluble 3D Parts from Monofunctional Monomers

Allison M. Pekkanen[1], Emily M. Wilts[2], Donald A. Aduba[3], Christopher B. Williams[3], Timothy E. Long[2]*

[1]School of Biomedical Engineering and Sciences, Virginia Tech, Blacksburg, VA 24061

[2]Department of Chemistry, Macromolecules Innovation Institute, Virginia Tech, Blacksburg, VA 24061

[3]Department of Mechanical Engineering, Virginia Tech, Blacksburg, VA 24061

*To whom correspondence should be addressed: E-mail: telong@vt.edu. TEL: (540) 231-2480 FAX: (540) 231-8517

Keywords: Vat photopolymerization, ionic liquid, ionic bonds, hydrogen bonding, 3D printing

9.1 Abstract

Additive manufacturing enables the creation of novel structures and geometries previously unattainable through traditional processing techniques. In particular, vat photopolymerization provides unprecedented resolution through the manipulation of light interactions with a photpolymer resin. Traditionally, chemical crosslinks generated a permanent network which possessed swelling capabilities but not dissolution potential. In this work, vat photopolymerization resins suitable for dissolution enable the formation of 3D parts suitable for complete dissolution. A library of monomers with varying ionic and hydrogen bonding potentials provided photopolymerized films sufficient for mechanical characterization. The rate of polymerization and the subsequent mechanical properties revealed a dependence of functionality on the resulting hydrogel. Vat

photopolymerization of the best candidate monomer, trimethylammonium ethyl acrylate chloride solution provided 3D parts with fine structure resolution. Layer structure evaluated through scanning electron microscopy revealed a lack of layering commonly observed with parts created through additive manufacturing. This method of creating dissolvable, water-laden structures through vat photopolymerization enables future research to enlarge the library of monomers and further improve structural resolution.

9.2 Introduction

Additive manufacturing (AM) provides a unique method for the creation of complex geometries which enable features to direct enhanced function.[1, 2] AM takes many forms, including material extrusion AM, selective laser sintering, and vat photopolymerization.[3, 4] Vat photopolymerization in particular operates through the manipulation of light to pattern vats of photopolymer containing photoinitiator into chemically crosslinked solids.[4] Upon the addition of light, chemical crosslinking occurs at the site of irradiation to form a solid network with a characteristic depth dependent on the light intensity, photoinitiator content, and presence of any photo-absorbers.[5-7] Vat photopolymerization remains desirable over other printing techniques due to the potential for nanometer-scale features unattainable by other printing techniques.[8] Furthermore, both a bottom-up and top-down approach can be imagined, with bottom-up printers relying on the slow removal of parts from a resin vat and top-down printers relying on the submersion of crosslinked parts into the remaining photopolymer solution.[9] Despite the breadth of part geometries available for vat photopolymerization, the technique requires a low viscosity, light-responsive polymer resin that traditionally required chemical

crosslinking to successfully form 3D parts.[9] Vat photopolymerization enabled the creation of fine features to control geometry and porosity throughout a resulting part, eliminating waste from traditional manufacturing and generating previously unattainable geometries.[10]

Controlled release of small molecules such biologics, drugs, or fertilizers revolves around selective dissolution as a function of time or stimuli.[11] Control of geometry and surrounding chemistry dictates the rate of dissolution and subsequently the rate of release.[12] The release of a drug or chemical can be tuned to rates driven by application-specific requirements, such as a sustained release or a delayed release formulation.[13] Tailoring selective biologic release for specific applications requires the use of precise control of matrix material degradation or dissolution.[14] Incorporation of sensitive drugs or biologics into these matrix materials requires processing steps designed to maintain function throughout the lifetime of manufacturing and sufficient function in the product.[15] As an example, heat-sensitive actives are not suitable for processing at elevated temperatures, limiting the selection of available matrix materials to those easily processed at low temperatures.[15] To date, only one example of controlled release formulations utilizing vat photopolymerization techniques exists, highlighting the utility of investigations surrounding this area.[16] AM provides new manufacturing techniques capable of precisely controlling dissolution and active release to potentially eliminate costly processing steps.

Supramolecular interactions enable the formation of non-covalent bonds between molecules and polymers alike. Commonly, ionic interactions and hydrogen bonding play a large role in the creation of complex structures through ionic aggregation and

multidentate hydrogen bonding motifs.[17] While these types of interactions remain less energetic than covalent bonds, they generate significant properties when melded in concert.[17] Supramolecular interactions play large roles in adhesive and biomedical applications due to their reversibility under stimuli and the breadth of interactions found in nature.[17-19] Specifically, the ability of supramolecular interactions to reduce or eliminate anisotropy in AM parts remains a focus of recent research.[20] The role of ionic liquids in vat photopolymerization processes revealed electrically-active parts while maintaining a large degree of crosslinking.[6] Liska et al. detailed the examination of monofunctional monomers for vat photopolymerization, but failed to realize well-defined parts without incorporation of chemical crosslinkers.[21] The ability to probe supramolecular interactions to form a well-defined 3-dimensional network without the need for chemical crosslinking remains unexplored.

In this work, the creation of dissolvable parts by vat photopolymerization additive manufacturing is realized. Monomer selection, dictated by supramolecular interactions, enabled the creation of water-laden gels. Characterization of the photopolymerization process proceeded through differential scanning calorimetry and rheology coupled with a light source. Tensile analysis revealed significant elongation of each photopolymerized gel, highlighting the role of water in the gels. Finally, vat photopolymerization of monomer solutions yielded well-defined printed parts which retained water solubility. This report enables future study into dissolvable parts created by vat photopolymerization for controlled released applications.

9.3 Materials and Methods

9.3.1 Materials. Trimethylammonium ethyl acrylate chloride solution (TMAEA, 80 wt % in water), 3-sulfopropyl acrylate potassium salt (SPAK), 2-acrylamido-2-methyl-1-propane sulfonic acid sodium salt (AASNa, 50 wt % in water), 2-acrylamido-2-methyl-1-propane sulfonic acid (AAS), and poly(ethylene glycol) methyl ether acrylate ($PEGMEA_{480}$) were obtained from Sigma-Aldrich. 2-hydroxyl-4'-(2-hydroxyethoxy)-2-methylpropiophenone (Irgacure 2959) was obtained from Sigma-Aldrich and dissolved in ethanol before use. Diphenyl(2,4,6-trimethylbenzoyl) phosphine oxide (TPO) was obtained from Sigma-Aldrich and dissolved in acetone before use. All solvents were purchased from Spectrum, Inc. and used as received.

9.3.2 Analytical Methods. Differential scanning calorimetry (DSC) was performed on a TA Instruments Q2000 with heat/cool/heat cycles of 10 °C/min, 100 °C/min, and 10 °C/min, respsectively. Samples were dried at 60 °C under vacuum prior to analysis. Glass transition temperatures (T_g's) and melting temperatures (T_m's) were calculated from the second heat inflection point and peak of the melting endotherm, respectively. Photocalorimetry was performed on a TA Instruments Q2000 with an Omnicure S2000 photo-attachment with fiber optic cable. T-zero pans were loaded as either sample pans or blank pans and equilibrated at 25 °C. Following a 1 min isotherm, 8 mW of 365 nm light was introduced to the pans. Following 5 min irradiation, the light was turned off and the background heat from the light noted. Integrations of the peaks minus the background signal afforded the heat of polymerization. Photorheology of polymerized monomer occurred on a TA Instruments DHR-2 Discovery Rheometer with photo attachment and 20 mm PDMS bottom plate with 20 mm disposable upper geometry. Samples were

equilibrated at 25 °C for 30 sec to provide baselines for all samples. Samples were oscillated at 1 Hz, providing sampling rates relevant for the second timescale. Following 30 sec, samples were irradiated at 8 mW and modulus monitored. The crossover point was determined as the first instance of storage modulus (G') exceeding loss modulus (G"). Monomer rheology was performed on an Ares G2 rheometer with a concentric cylinder geometry at 25 °C. Samples were oscillated from 10-100 rad/s, and viscosity values were compared at 12.5 rad/s (n = 3). Statistical testing was performed on JMP software with an ANOVA followed by a Tukey's HSD ($\alpha = 0.05$). Tensile testing was performed on film-punched dogbones from photocured films with a crosshead motion of 500 mm/min and grip-to-grip separation of 26.25 mm. Young's Modulus was calculated as the slope of the initial rise in strain and the percent elongation noted for each sample. Dynamic mechanical analysis was performed on a TA Instruments Q800 in tension mode. Samples were cooled with liquid nitrogen prior to loading. Samples were heated at 3 °C/min with a frequency of 1 Hz and a static force of 0.01 N. Dynamic light scattering (DLS) was performed on a Malvern ZetaSizer at room temperature with a backscattering angle of 145 ° and a wavelength of 435 nm.

9.3.3 Film Preparation. $PEGMEA_{480}$, TMAEA, and AASNa were used as received (0 wt %, 20 wt %, and 50 wt % water, respectively). AAS and SPAK were dissolved at 50 wt % water prior to use. To monomer solutions, 2 wt % photoinitiator in ethanol was added to catalyze the photopolymerization. Films were prepared by irradiation from a broad-band UV source (put specs here) until they were free-standing. Films were used for subsequent analysis without further purification.

9.3.4 Dissolution Testing. Sections of gel were placed in RO water at 1 mg/mL. The water was stirred rapidly and the time to full dissolution was noted. Data is presented as an average with a standard deviation of n = 3 samples.

9.3.5 Vat Photopolymerization. TMAEA (20 wt % water) and 2 wt % TPO in acetone were added to the chamber of an Autodesk Ember® stereolithographic, bottom-up, 3D printer. (put in light source) The first layer was irridiated for 5 sec to ensure adhesion to the stainless steel plate. The next four layers were irradiated for 2.5 sec. All subsequent layers were irradiated for 1.2 sec each. Between each layer, the bed was raised to allow fresh monomer solution onto the PDMS plate and to recoat the part. 50 μm layers were used for the sample.

9.3.6 Statistical Analysis. Statistical testing was performed using JMP software. An ANOVA test followed by a Tukey's HSD provided differences between treatment groups.

9.4 Results and Discussion

Traditional vat photopolymerization additive manufacturing processes utilize chemical crosslinking to ensure part fidelity upon printing. However, this process generates a permanent network unable to dissolve fully for controlled release applications. This permanent network enables controlled release via swelling mechanisms but remains as a network requiring removal. The utilization of physical crosslinks enables creation of dissolvable parts without the need for a chemical trigger or potentially harmful degradation products. Screening of ionic monomers in water afforded a range of acrylate and acrylamide monomers suitable for generation of physically-crosslinked 3D

printed parts. Equivalent structures in acrylate vs. acrylamide (SPAK, AASNa) as well as ionic vs. acid forms (AAS, AASNa) provided a library of potential monomer types with the potential to evaluate photopolymerized gel properties based on monomer structure (**Scheme 9.1**).

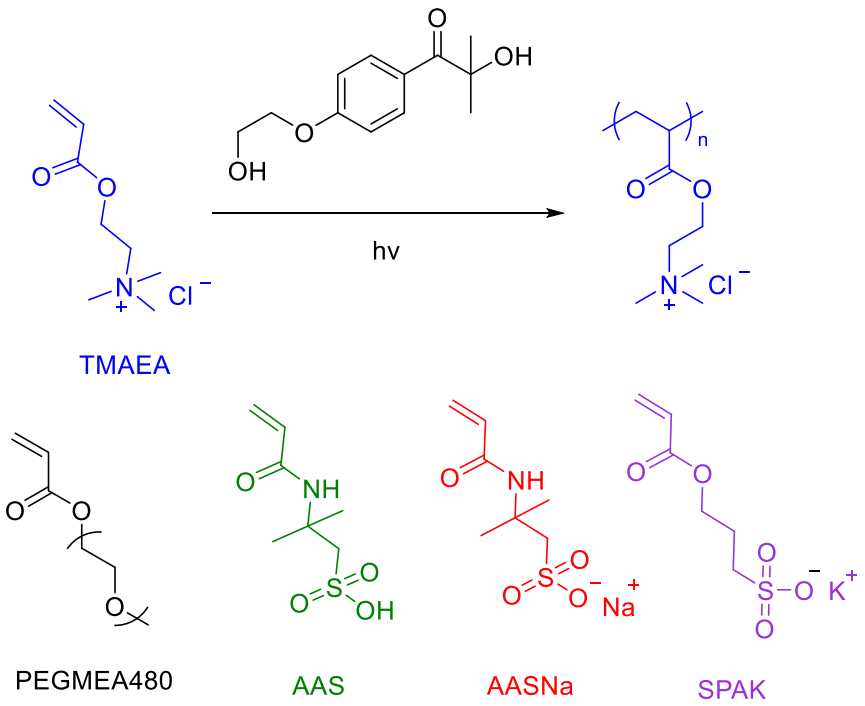

Scheme 9.1. Monomer selection and the photopolymerization process

Photo-DSC generated heat of polymerization as a function of irradiation time and allowed for estimations of conversion (**Figure 9.1**). TMAEA proved to evolve the most heat upon irradiation, potentially due to the slightly lower wt % water in the sample. However, $PEGMEA_{480}$ which contained no water, exhibited a broad peak and lower evolved heat of polymerization potentially due to lack of supramolecular interactions. Each of the acrylamide monomers (AAS and AASNa) experienced shorter times to peak heat flow compared to the equivalent acrylate (SPAK), suggesting a role of hydrogen

bonding in the polymerization process. Furthermore, utilizing a standard 18 kcal/mol of standard acrylate polymerizations, the percent conversion of each monomer revealed interesting trends (**Table 9.1**). As expected, the incorporation of water attenuated light from the instrument and prevented high conversion of samples with 50 wt % water. However, the percent conversion of the acid (AAS) versus the neutralized (SPAK, AASNa) monomers revealed the potential role of counterion in the conversion during photopolymerization.

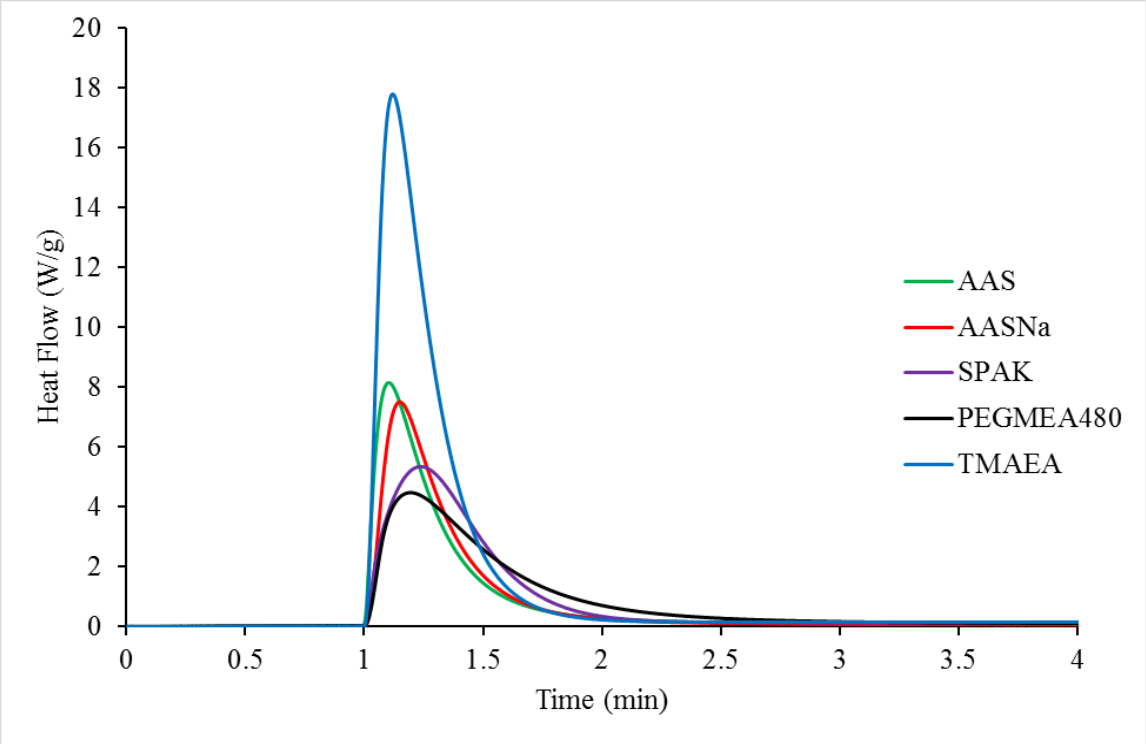

Figure 9.1. Photo-DSC of monomers for photpolymerization reveals an increase in polymerization rate for acrylamides vs. acrylates at equivalent water content (AAS, AASNa vs. SPAK). TMAEA exhibits the fastest polymerization and greatest endotherm. A representative graph for each monomer is shown (n = 3).

The discrepancies between monomers potentially arises from varied ionic aggregation in the monomer solution prior to polymerization (**Figure 9.S1**). As seen in dynamic light scattering, each of the ionic monomers exhibited larger aggregates as

compared to $PEGMEA_{480}$, suggesting a role in monomer aggregation for the successful formation of free-standing films. The size of each of these aggregates and their shape potentially direct both the kinetics of polymerization and the properties of the free-standing film.[22, 23] Further studies as to the particular mechanism and the potential extension of these monomers is currently underway.

Monomer	$\Delta H_{polymerization}$ (J/g)	Percent Conversion	Time to Peak (sec)	T_g (°C)
TMAEA	300 ± 10	71 ± 4 %	21 ± 12	-68
PEGMEA480	162 ± 2	89 ± 11 %	23 ± 8	-70
AAS	158 ± 22	39 ± 3 %	26 ± 12	-64
AASNa	157 ± 19	44 ± 3 %	29 ± 15	-68
SPAK	154 ± 7	39 ± 4 %	52 ± 27	-66

Table 9.1. Varied polymerization exotherms leads to varied percent conversions, largely controlled by the water content (n = 3). Each polymer has a similar dried T_g, suggesting similarities in the resulting polymers.

Differential scanning calorimetry of dried films provided confirmation of polymer transitions without the presence of water as a plasticizer (**Figure 9.S2**). The measured T_g's of each polymer remain near -70 °C for each polymer, suggesting similar polymeric properties (**Table 9.1**). Furthermore, the presence of T_g's in the polymer indicates successful polymerization of monomer to form polymer as the primary mechanism of film formation. $PEGMEA_{480}$ becomes crystalline in its polymerized state, suggesting a role of crystallinity in the creation of free-standing films. The polymerization of $PEGMEA_{480}$ results in a bottlebrush-type polymer, potentially playing a role in both the formation of films and their resulting crystallinity. Similarities in thermal transitions between each dried polymer allows for the comparison between samples based solely on wt % water and supramolecular interactions.

Photorheology of monomers revealed a trend in storage modulus as a function of monomer and wt % water (**Figure 9.2**). As suggested by the photo-DSC, TMAEA exhibited significantly increased storage modulus following polymerization compared to all other monomers. Both the rate of polymerization and increased conversion likely led to this enhanced storage modulus and fast crossover time, lending itself as the prime candidate for AM. Despite its lower wt % water, $PEGMEA_{480}$ failed to reach the same storage modulus as TMAEA, suggesting that the ionic interactions in TMAEA generated a stronger film than non-charged $PEGMEA_{480}$. Furthermore, as SPAK, AAS, and AASNa each possessed 50 wt % water, direct comparisons between acrylate, acrylamide, and the role of ions can be made. As confirmed from results of photo-DSC, SPAK exhibited a much slower rate of polymerization and thus a longer time to reach the G'-G" crossover point than either AAS or AASNa. This suggests the role of hydrogen bonding in the acrylamide monomers in the rate of formation of free-standing films. The role of ion incorporation into monomers also afforded gels of varied modulus, as seen in the comparison between AAS and AASNa. The presence of the sodium ion could potentially lead to larger ionic aggregates in monomer form, leading to a less-highly-physically-crosslinked film upon polymerization. When comparing AASNa to SPAK, the rate of polymerization potentially limits the growth of molecular weight after ~5 sec of AASNa, while SPAK continues to polymerize over much longer time scales. The acid form of the acrylamide monomer generated moduli similar of that experienced by $PEGMEA_{480}$ despite containing 50 wt % water. These results suggest that the ability of hydrogen bonding acrylamide functionalities coupled with smaller ions for decreased aggregate size leads to higher modulus in resulting films.

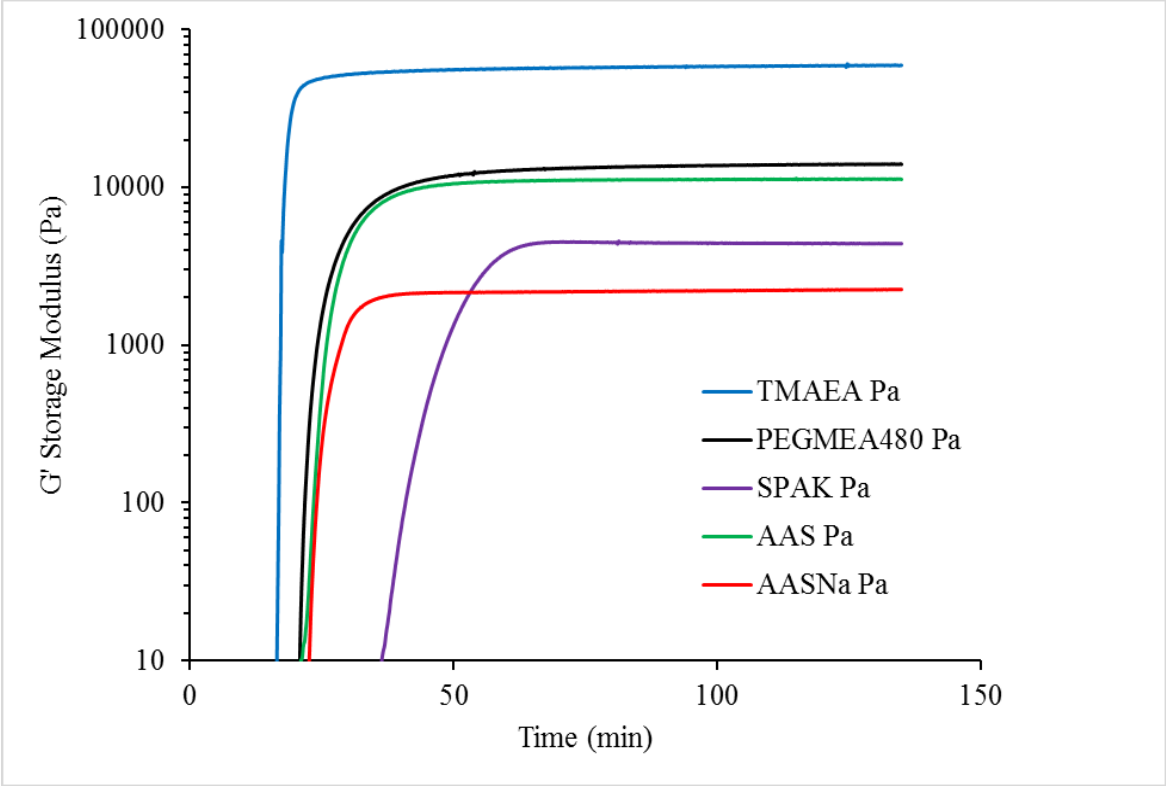

Figure 9.2. Photorheology of photopolymerization reveals storage modulus of photopolymerized gels. TMAEA exhibits the highest storage modulus following polymerization, suggesting its potential as a suitable monomer for vat photopolymerization additive manufacturing. Shown is a representative modulus curve (n = 3).

Rheology of monomer solutions revealed complex viscosity as a function of monomer concentration (**Figure 9.3**). The increased viscosity of TMAEA and AAS at monomer concentrations relevant to photopolymerization (80 wt % and 50 wt %, respectively) suggests a role of monomer viscosity on final film modulus. This viscosity decreased significantly upon the addition of water to monomer solutions (**Figure 9.S3 – 9.S6**), confirming aggregate presence in monomer solutions. Interestingly, AASNa and SPAK, which both contain large counterions, failed to exhibit this increase in viscosity at 50 wt % in water. This decreased viscosity corresponded to a decrease in final film

modulus (**Figure 9.2**), suggesting the potential for solution viscosity to aid in monomer selection for vat photopolymerization.

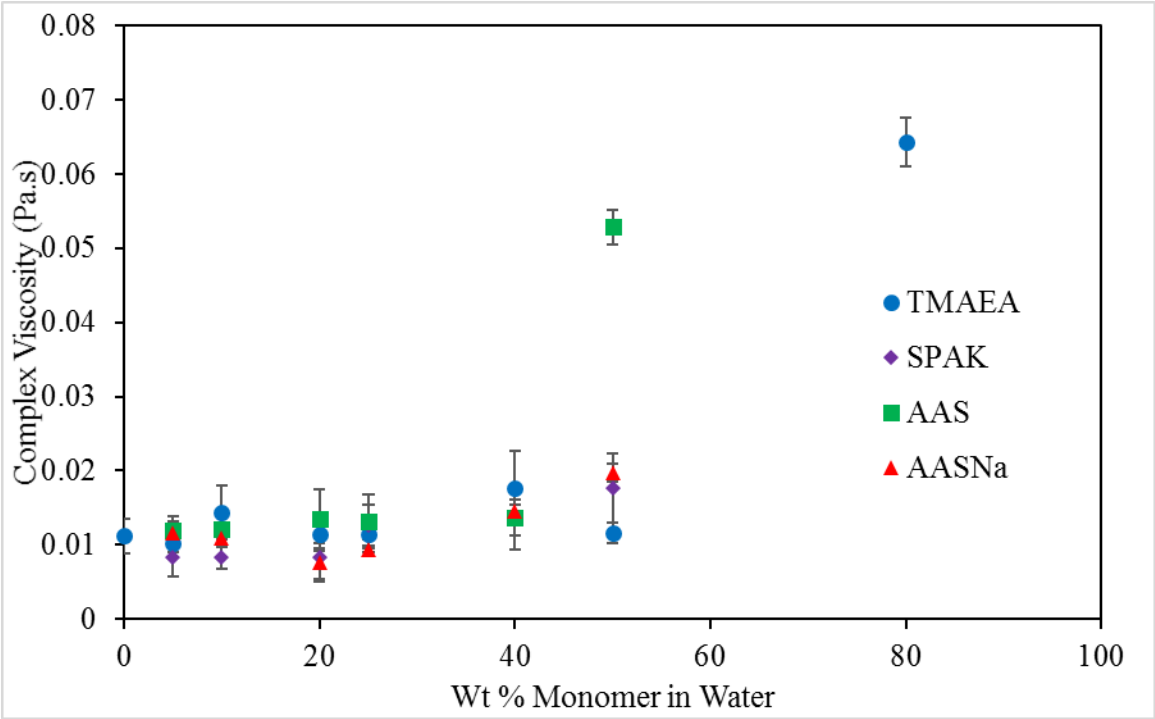

Figure 9.3. Concentric cylinder rheology provides complex viscosity of monomer solutions as a function of monomer concentration ($n = 3$, $p < 0.05$). TMAEA and AAS exhibit increased viscosity at photopolymerization concentration compared to AASNa and SPAK.

The role of physical crosslinks in the dissolution of photopolymerized parts remains an essential part of controlled release applications. The ability to dissolve in water was determined for each composition at 1 mg/mL until full dissolution was noted. As noted in **Table 9.2**, the time to full dissolution is dictated by acrylamides vs. acrylates (AAS, AASNa) rather than the presence of counterion. Interestingly, $PEGMEA_{480}$ failed to dissolve in water after more than 24 h, indicating a strong role of crystallinity in the integrity of these free-standing films. Despite the water-loving nature of PEG, the high degree of crystallinity in $PEGMEA_{480}$ gels rendered them water insoluble. Again, TMAEA exhibited the fastest dissolution time, potentially due to its lowered wt % water

and its ionic aggregation size. Water loss during the photopolymerization process as a result of heat evolution remains the topic of current and future investigations.

Sample	**Dissolution Time**	**Film Wt % Water**
AAS	27 ± 2.5 min	50
AASNa	30 ± 0.8 min	50
SPAK	43 ± 2.5 min	50
TMAEA	23 ± 0.8 min	20
$PEGMEA_{480}$	DND	0

Table 9.2. Dissolution results suggest a dependence on acrylamide functionality (n = 3). $PEGMEA_{480}$ does not dissolve in water under these conditions.

Following photorheology, TMAEA showed promise as a monomer for vat photopolymerization additive manufacturing. TMAEA modulus versus temperature (**Figure 9.4**) reveals thermal transitions of as-formed gels. When cooled, TMAEA gels exhibit a high E' storage modulus likely due to the presence of water in the gel. As calculated from the maximum of the tan delta, T_g depression due to the presence of water lowered the T_g to -82 °C. As the sample heated, the ice present in the gel melted around 0 °C and resulted in a significant drop in storage modulus. Furthermore, following melting, the water-containing gel remained intact with a lowered modulus. Interestingly, TMAEA gels retained modulus as the sample heated above 100 °C despite a loss of water from the gel. This maintenance of modulus through drying TMAEA gels indicated the potential to dry TMAEA parts created from vat photopolymerization without sacrificing structure. This drying step represents a crucial part of the 3D printing process, as TMAEA monomer resists drying to remove water before polymerization.

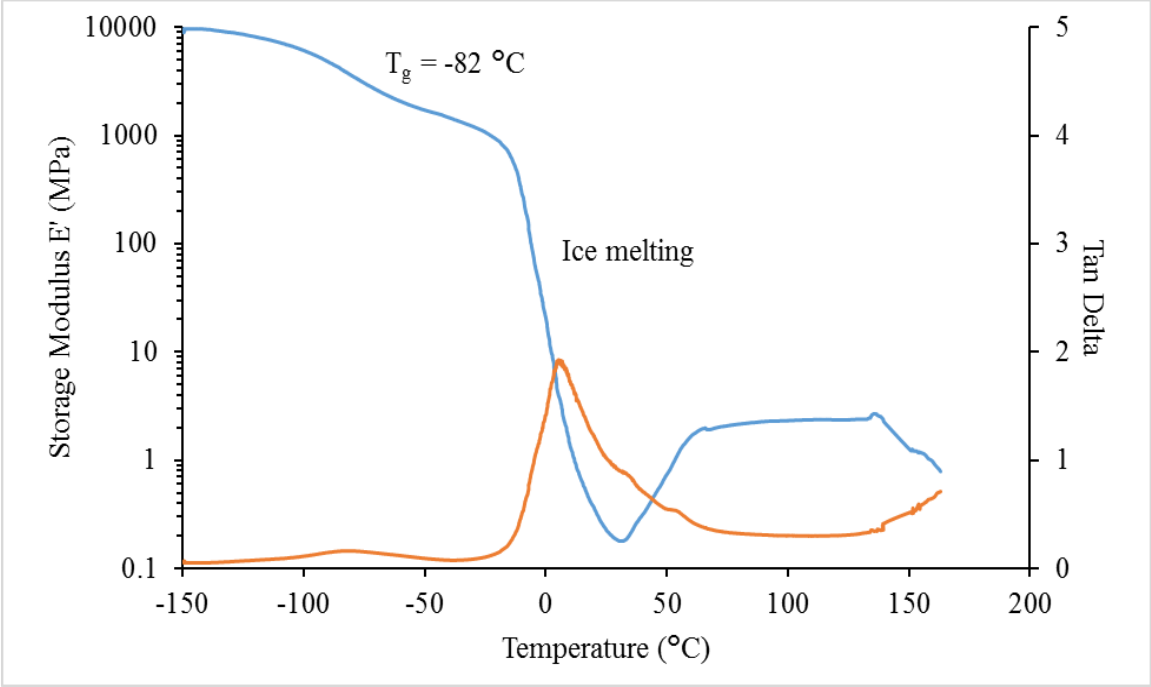

Figure 9.4. Thermomechanical analysis reveals water-plasticized T_g and stark loss in modulus due to ice melting. TMAEA films retain mechanical strength following the removal of water, suggesting the strength of ionic interactions.

Vat photopolymerization of TMAEA with 2 wt % TPO revealed the maintenance of fine features upon rapid printing. As the printing proceeded, residual TMAEA resided within the part interior and became trapped within the structure. Furthermore, overcure due to the rapid polymerization of TMAEA monomer likely played a role in part fidelity. Drying photopolymerized TMAEA also presents the opportunity to further generate radical polymerization, requiring future study. As shown in **Figure 9.5**, the top crenelations maintained fine feature resolution characteristic of vat photopolymerization. Due to the solubility of printed parts, uncured monomer remained within the printed part including drying steps before scanning electron microscopy. When examined further, the crenelations exhibit a surface roughness characteristic of the layer thickness dictated by the printer and as a result of light penetration within each layer. Despite this characteristic

surface roughness, distinct layers failed to develop, suggesting strong interlayer interactions and a blending of layers during the print process. The physical properties of printed parts rival those seen in bulk gels, suggesting a lack of anisotropy characteristic in traditional 3D printed parts.

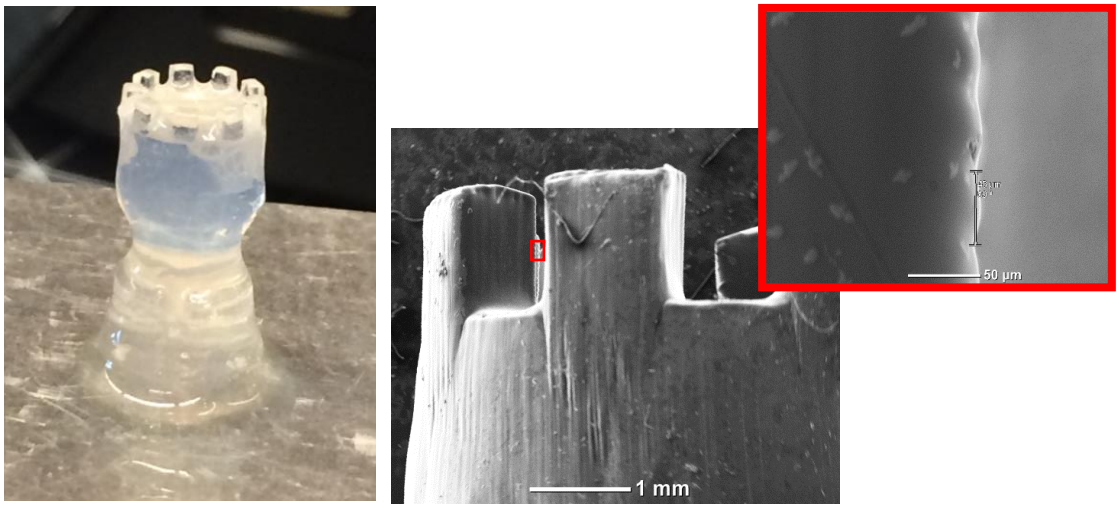

Figure 9.5. Vat photopolymerization of TMAEA results in well-defined features. B. SEM imaging reveals distinct crenelations and characteristic surface roughness relative to layer thickness.

9.5 Conclusion

To date, fully-soluble parts connected only through physical interaction and generated by vat photopolymerization fail to exist. This report details the characterization of water-soluble gels created through photopolymerization. A wide range of monomer selection afforded the development of a wide range of gel properties based on supramolecular interactions. Furthermore, preliminary vat photopolymerization produced parts with well-defined features and the absence of defined layers, paving the way for future work to examine the limits of resolution and properties afforded by this process.

9.6 Supplemental Information

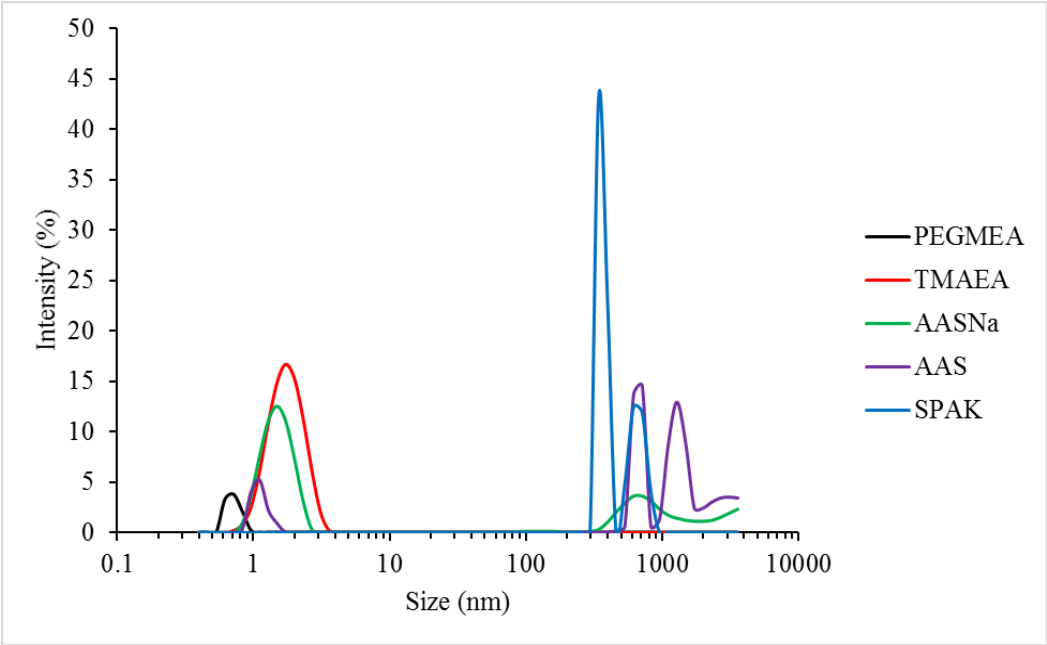

Figure 9.S1. Dynamic Light Scattering reveals ionic aggregation in monomer

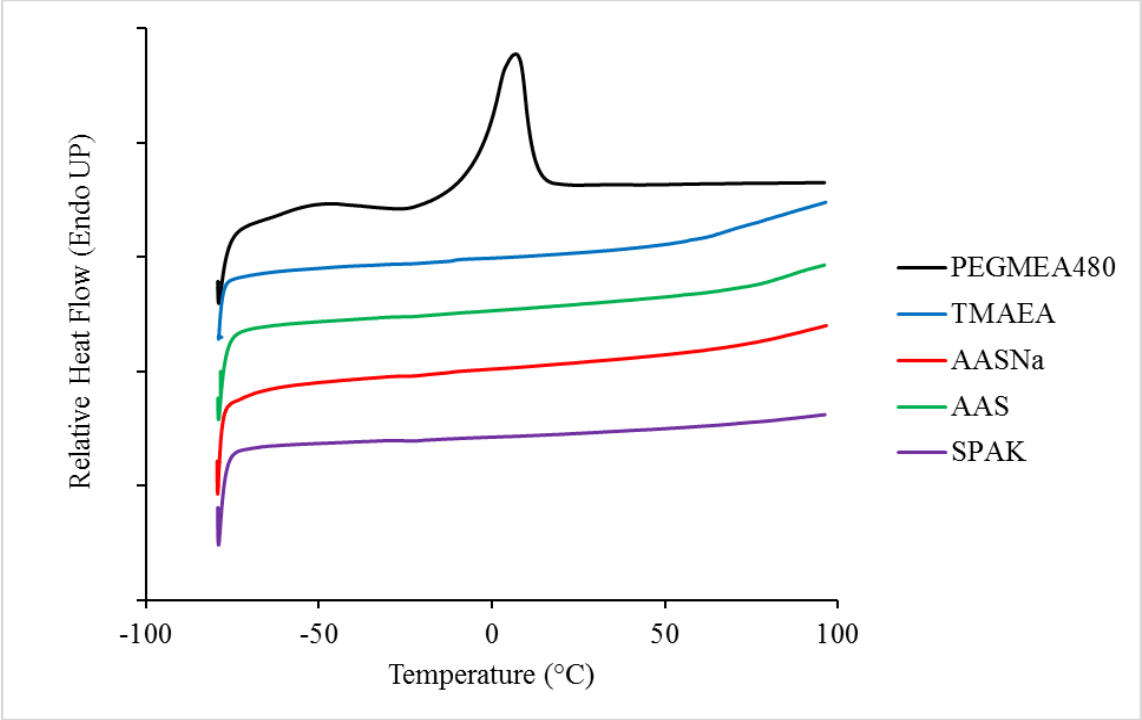

Figure 9.S2. DSC of dried polymers reveals low Tg's exhibited by all polymers. Curves have been manually shifted for clarity.

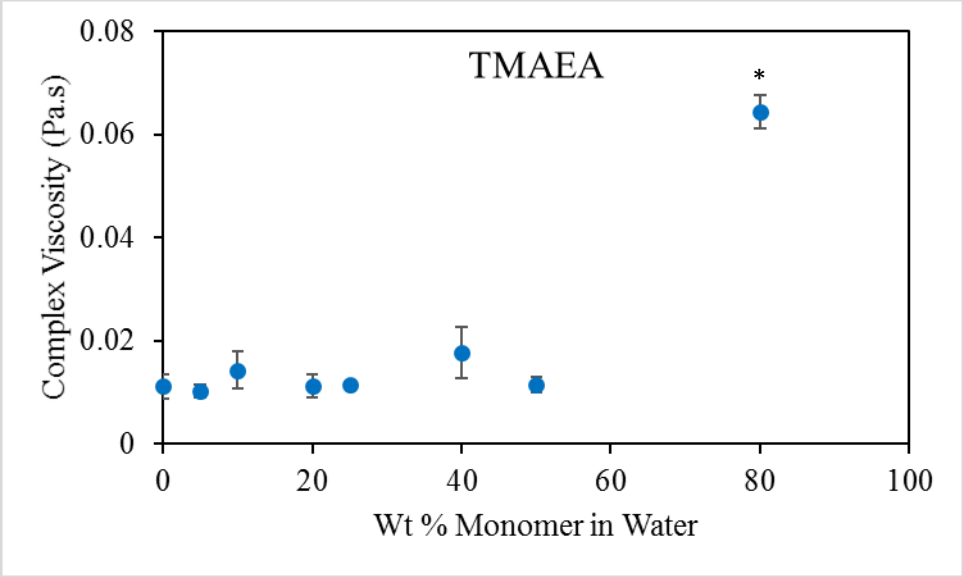

Figure 9.S3. Viscosity of TMAEA with varying concentration. 80 wt % TMAEA in water revealed a significantly increased viscosity compared to all other concentrations. ($n = 3$, $p < 0.05$)

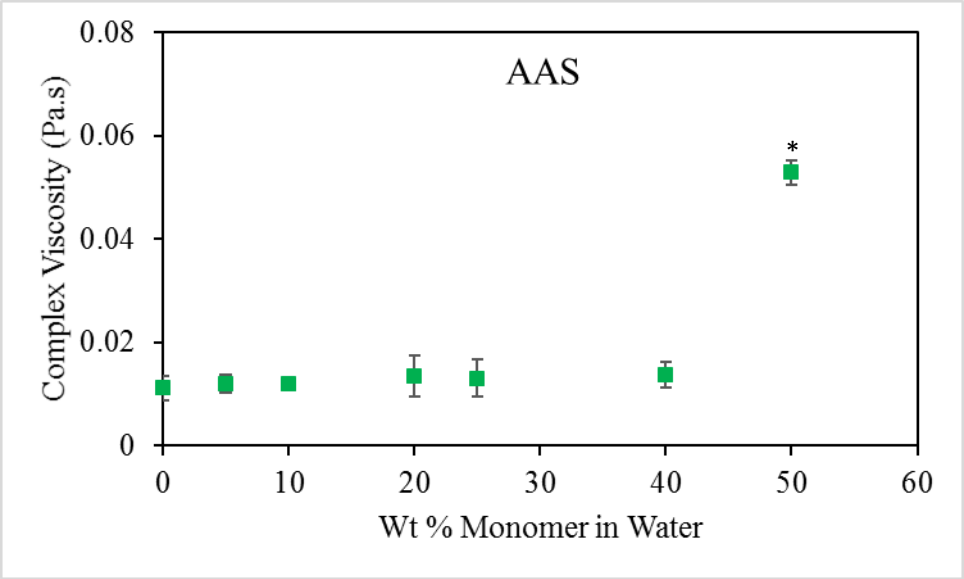

Figure 9.S4. Viscosity of AAS with varying concentration, revealing that 50 wt % AAS in water possesses a significantly increased viscosity compared to all other concentrations ($n = 3$, $p < 0.05$).

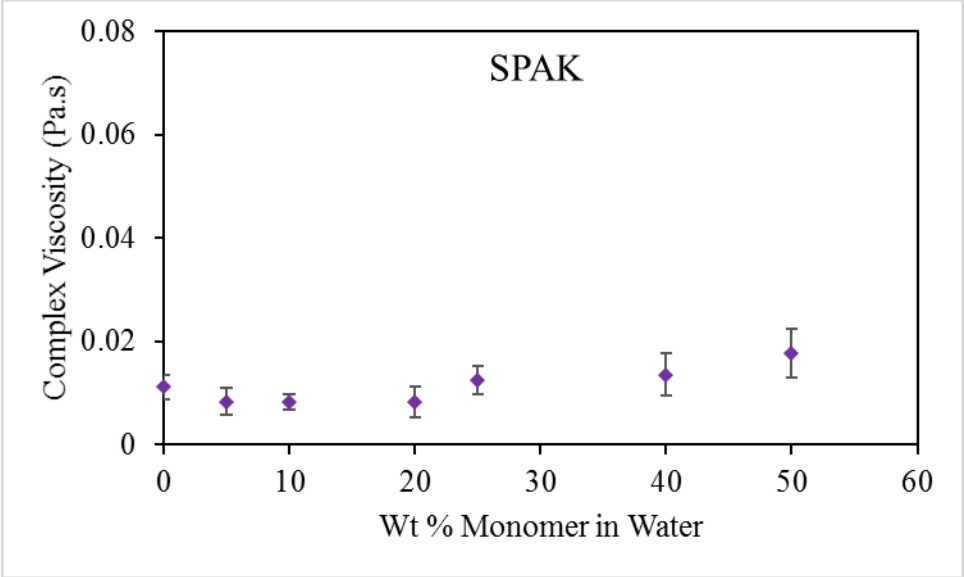

Figure 9.S5. Viscosity of SPAK in water revealed an insignificant change in viscosity with concentration ($n = 3$, $p < 0.05$).

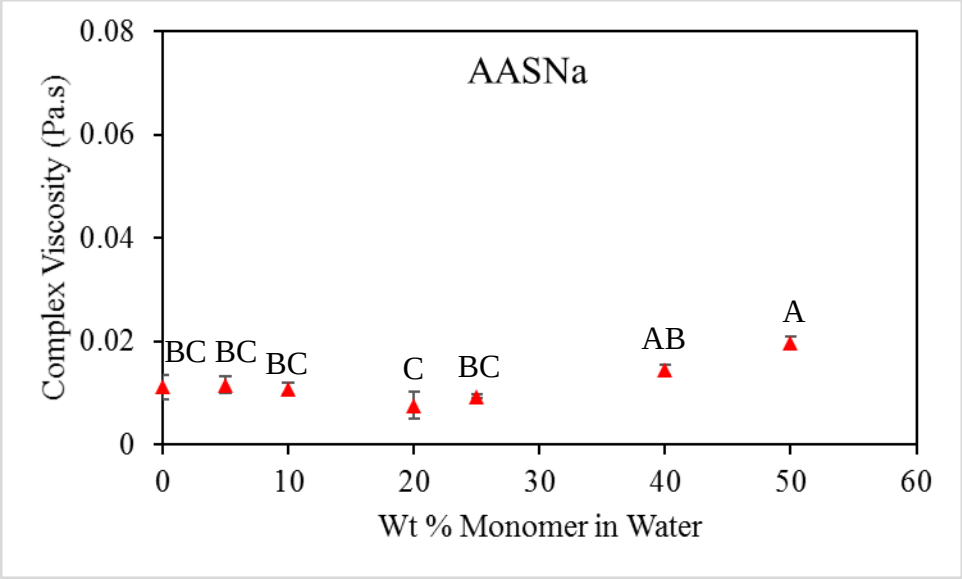

Figure 9.S6. Viscosity of AASNa revealed the effect of concentration on viscosity. Groups with the same letter are not statistically different ($n = 3$, $p < 0.05$). The effect of monomer concentration on viscosity remains less pronounced than TMAEA or AAS monomers.

References

1. Wegst, U. G.; Bai, H.; Saiz, E.; Tomsia, A. P.; Ritchie, R. O., Bioinspired structural materials. *Nature materials* **2015,** 14, (1), 23-36.
2. Compton, B. G.; Lewis, J. A., 3D-printing of lightweight cellular composites. *Advanced materials* **2014,** 26, (34), 5930-5935.
3. Chia, H. N.; Wu, B. M., Recent advances in 3D printing of biomaterials. *Journal of biological engineering* **2015,** 9, (1), 4.
4. Gross, B. C.; Erkal, J. L.; Lockwood, S. Y.; Chen, C.; Spence, D. M., Evaluation of 3D printing and its potential impact on biotechnology and the chemical sciences. In ACS Publications: 2014.
5. Lambert, P.; Chartrain, N.; Schultz, A.; Cooke, S.; Long, T.; Whittington, A.; Williams, C. In *Mask Projection Microstereolithography of Novel Biocompatible Polymers*, International Solid Freeform Fabrication Symposium: Austin, 2014; 2014; pp 974-990.
6. Schultz, A. R.; Lambert, P. M.; Chartrain, N. A.; Ruohoniemi, D. M.; Zhang, Z.; Jangu, C.; Zhang, M.; Williams, C. B.; Long, T. E., 3d printing phosphonium ionic liquid networks with mask projection microstereolithography. *ACS Macro Letters* **2014,** 3, (11), 1205-1209.
7. Sirrine, J. M.; Pekkanen, A. M.; Nelson, A. M.; Chartrain, N. A.; Williams, C. B.; Long, T. E., 3D-printable biodegradable polyester tissue scaffolds for cell adhesion. *Australian Journal of Chemistry* **2015,** 68, (9), 1409-1414.
8. Spadaccini, C. M.; Farquar, G.; Weisgraber, T.; Gemberling, S.; Fang, N.; Xu, J.; Alonso, M.; Lee, H., High resolution projection micro stereolithography system and method. In Google Patents: 2016.
9. Stansbury, J. W.; Idacavage, M. J., 3D printing with polymers: Challenges among expanding options and opportunities. *Dental Materials* **2016,** 32, (1), 54-64.
10. Gao, W.; Zhang, Y.; Ramanujan, D.; Ramani, K.; Chen, Y.; Williams, C. B.; Wang, C. C.; Shin, Y. C.; Zhang, S.; Zavattieri, P. D., The status, challenges, and future of additive manufacturing in engineering. *Computer-Aided Design* **2015,** 69, 65-89.
11. Khaled, S. A.; Burley, J. C.; Alexander, M. R.; Roberts, C. J., Desktop 3D printing of controlled release pharmaceutical bilayer tablets. *International journal of pharmaceutics* **2014,** 461, (1), 105-111.
12. Khaled, S. A.; Burley, J. C.; Alexander, M. R.; Yang, J.; Roberts, C. J., 3D printing of five-in-one dose combination polypill with defined immediate and sustained release profiles. *Journal of Controlled Release* **2015,** 217, 308-314.
13. Skowyra, J.; Pietrzak, K.; Alhnan, M. A., Fabrication of extended-release patient-tailored prednisolone tablets via fused deposition modelling (FDM) 3D printing. *European Journal of Pharmaceutical Sciences* **2015,** 68, 11-17.
14. Goyanes, A.; Chang, H.; Sedough, D.; Hatton, G. B.; Wang, J.; Buanz, A.; Gaisford, S.; Basit, A. W., Fabrication of controlled-release budesonide tablets via desktop (FDM) 3D printing. *International journal of pharmaceutics* **2015,** 496, (2), 414-420.
15. Okwuosa, T. C.; Stefaniak, D.; Arafat, B.; Isreb, A.; Wan, K.-W.; Alhnan, M. A., A lower temperature FDM 3D printing for the manufacture of patient-specific immediate release tablets. *Pharmaceutical research* **2016,** 33, (11), 2704-2712.

16. Wang, J.; Goyanes, A.; Gaisford, S.; Basit, A. W., Stereolithographic (SLA) 3D printing of oral modified-release dosage forms. *International journal of pharmaceutics* **2016,** 503, (1), 207-212.
17. Webber, M. J.; Appel, E. A.; Meijer, E.; Langer, R., Supramolecular biomaterials. *Nature materials* **2016,** 15, (1), 13-26.
18. Zhang, K.; Aiba, M.; Fahs, G. B.; Hudson, A. G.; Chiang, W. D.; Moore, R. B.; Ueda, M.; Long, T. E., Nucleobase-functionalized acrylic ABA triblock copolymers and supramolecular blends. *Polymer Chemistry* **2015,** 6, (13), 2434-2444.
19. Zhang, K.; Chen, M.; Drummey, K. J.; Talley, S. J.; Anderson, L. J.; Moore, R. B.; Long, T. E., Ureido cytosine and cytosine-containing acrylic copolymers. *Polymer Chemistry* **2016,** 7, (43), 6671-6681.
20. Highley, C. B.; Rodell, C. B.; Burdick, J. A., Direct 3D printing of shear-thinning hydrogels into self-healing hydrogels. *Advanced Materials* **2015,** 27, (34), 5075-5079.
21. Liska, R.; Schwager, F.; Maier, C.; Cano-Vives, R.; Stampfl, J., Water-soluble photopolymers for rapid prototyping of cellular materials. *Journal of Applied Polymer Science* **2005,** 97, (6), 2286-2298.
22. Noor, S. A. M.; Sun, J.; MacFarlane, D. R.; Armand, M.; Gunzelmann, D.; Forsyth, M., Decoupled ion conduction in poly (2-acrylamido-2-methyl-1-propane-sulfonic acid) homopolymers. *Journal of materials chemistry a* **2014,** 2, (42), 17934-17943.
23. Abdullah, M. M.; AlQuraishi, A. A.; Allohedan, H. A.; AlMansour, A. O.; Atta, A. M., Synthesis of novel water soluble poly (ionic liquids) based on quaternary ammonium acrylamidomethyl propane sulfonate for enhanced oil recovery. *Journal of Molecular Liquids* **2017,** 233, 508-516.

Chapter 10. Isocyanate-free Polyurethanes with Biologically Inert Byproducts (Unfinished)

Allison M. Pekkanen, Emily M. Wilts, Ryan J. Mondschein, Joseph M. Dennis, Timothy E. Long

[1]School of Biomedical Engineering and Sciences, Virginia Tech, Blacksburg, VA 24061

[2]Macromolecules Innovation Institute, Department of Chemistry, Virginia Tech, Blacksburg, VA 24061

*To whom correspondence should be addressed. E-mail: telong@vt.edu TEL: (540) 231-2480 FAX: (540) 231-8517

Keywords: Isocyanate-free, polyurethane, carbonyldiimidazole, poly(ethylene glycol)

10.1 Abstract

Polyurethanes continue to experience widespread use in both industry and academia as new formulations and methods arise for their formation. While a number of reports detail synthetic procedures to generate isocyanate-free polyurethanes, these reactions remain complex and lengthy. Herein, reactions between carbonyldiimidazole, diols, and diamines provides a library of polyurethanes created in a one-pot, water-tolerant reaction at room temperature. These polymers exhibit thermal transitions suited to the dominance of poly(ethylene glycol) in the systems. Furthermore, the presence of shear thinning and an increase in melt viscosity confirms the urethane linkage and the increase in molecular weight. Finally, the generation of an extended plateau window in dynamic mechanical analysis reveals the power of hydrogen bonding found in urethane functionalities. This method for creating isocyanate-free polyurethanes represents the next generation of facile, biologically-friendly polyurethane synthesis.

10.2 Introduction

Polyurethanes remain a commercially-viable solution for many common applications, most notably in the formation of polyurethane foams or in biomedical applications.[1] While the method and applications of polyurethanes are well precedented, novel polyurethanes, such as ion-containing polyurethanes, pique the interest of many scientists.[1-3] Typical polymerization to form polyurethanes requires an isocyanate coupled between a soft segment diol and a chain extender urethane to form a hard segment.[1, 4, 5] However, isocyanates require the use of dry solvent and heavy metal catalyst and pose health risks for employees responsible for polyurethane polymerizations.[4, 6] The movement away from isocyanates in the formation of polyurethanes poses a great scientific challenge to ensure safety for employees while also yielding high molecular weight polymer suitable for target applications.[4]

A number of synthetic options remain viable for the formation of isocyanate-free polyurethanes.[4, 6] Ring opening of cyclic carbonates provided a method for creating isocyanate-free polyurethanes with varied structure.[7] Recently, the formation of cyclic carbonates from renewable resources produced isocyanate-free poly(amide-hydroxyurethane)s with varied soft segment content.[8] Besse et al. discussed the formation of glycidyl-containing isosorbide oligomers to form biobased, high performance polyurethanes.[9] Alternatively, transurethanization from biscarbamates also provided an alternative to isocyanate-containing polyurethane synthesis.[4] Ring-opening or ring-elimination reactions to form polyurethanes from lactams enabled high molecular weight polymers with varied functionality and the formation of dendrimers.[10] In many of these

cases, however, the creation of a reactive precursor presents a challenge not suitable for many reactants.

1-1'-carbonyldiimidazole (CDI) reactions provide a facile synthetic route for the creation of diamines, carbonates, and ureas. A tolerance to water characterize reactions with CDI, making them highly attractive for facile and biologically-friendly synthetic procedures.[11, 12] Furthermore, the reaction of CDI with a diol or diamine is catalyzed at room temperature, removing the need for elevated or reduced temperature required for many reactions.[13, 14] CDI catalyzed the formation of peptide bonds for the polymerization of amino acids in aqueous environments.[11, 12] CDI also induced the formation of biodegradable carbonate crosslinks to produce biological tissue scaffolds at room temperature.[13] Carbamate and carbonate generation under mild conditions enables chemical manipulation for sensitive or biologic applications.[15, 16] CDI's role in the formation of cyclic carbonates serves as a platform for further examination to make polyurethanes directly.[6] These diverse reactions highlight the versatility and utility of CDI in polymerizations.

Poly(ethylene glycol) (PEG) generates significant interest to scientists due to its precedence as a biologically-inert material, both in the environment and the human body.[17, 18] PEG stimulated the formation of poly(ether ester) ionomers, polyureas, and soft segments of polyurethanes to impart water solubility and flexibility to common materials.[3, 19, 20] Numerous reports detail the utility of PEG in biological systems, including both those in the human body and in the environment.[21, 22 23] PEG's biological inert nature coupled with previous examination of polymeric properties dependent on low

concentrations of functional groups make it a suitable candidate to examine polyurethane properties from CDI reactions.

This work details the synthesis and characterization of PEG-containing polyurethanes through reactions with 1,1'-carbonyldiimidazole. Facile synthesis readily provides poly(PEG-urethane)s of varying PEG molecular weight. ^{1}H NMR confirmed successful polyurethane formation without significant reaction to form carbonates or ureas. DSC provided thermal transitions of the polyurethanes, which remain consistent to those previous examined. Rheological analysis reveals increased melt viscosity compared to neat PEG, further confirming the presence of hydrogen bonding and increased molecular weight. These polymers represent the next generation of facile, isocyanate-free polyurethane synthesis.

10.3 Materials and Methods

10.3.1 Materials. 1-1'-Carbonyldiimidazole (CDI), poly(ethylene glycol) (PEG, MW = 400, 1,000, and 4,000 g/mol), sodium chloride, 2-2-(ethylenedioxy)bis(ethylamine) (EDBA), and 1,4-benzenedimethanol (1,4-BDM) were purchased from Sigma-Aldrich and used as received. All solvents were purchased from Spectrum and used without further purification.

10.3.2 Analytical Methods. ^{1}H NMR was performed on a Varian Unity Nuclear Magnetic Resonance at ambient temperature in either $CDCl_3$ or $DMSO_{d6}$. Differential scanning calorimetry was performed on a TA Instruments Q2000 with a heating ramp of 10 °C/min and a cooling ramp of 100 °C/min, with the second heat used for all analysis. The glass transition temperatures (T_g) were calculated from the inflection point and

melting temperatures (T_m) were calculated as the maximum of the melting endotherm. Rheological experiments were performed on an Ares G2 rheometer in oscillation mode with 25 mm parallel plates and 1 % strain under air at either 150 °C or 75 °C. Dynamic mechanical analysis was performed on a TA Instruments Q800 in tension mode with a heating ramp of 3 °C/min, a 0.01 N static force, and an oscillation of 1 Hz. Compression molding of films was performed on a PHI Manual Hydraulic Press between Kapton® sheets at 225 °C. Films were cooled between the Kapton® sheets and used directly.

10.3.3 Polyurethane Synthesis. All polyurethanes were synthesized under similar conditions, with poly(ethylene glycol-urethane) used as an example. To a 250 mL round-bottomed flask equipped with magnetic stirring, 15 g of PEG_{1k} (0.015 moles, 1 eq.) and 150 mL $CHCl_3$ was added and allowed to fully dissolve. Addition of CDI (4.8645 g, 0.03 moles, 2 eq.) proceeded rapidly, and the reaction was allowed to stir for 30 min. TEG-diamine was added (2.223 g, 0.015 moles, 1 eq.) rapidly to facilitate the formation of urethane bonds. After stirring for 24 h, water was added to the reaction and stirred rapidly for 10 min. The polymer in $CHCl_3$ was the washed two additional times with water, followed by a wash in concentrated NaCl to remove residual water. The $CHCl_3$ was removed under reduced pressure and the resulting white polymer dried overnight at 50 °C under vacuum to remove residual chloroform.

10.4 Results and Discussion

Polyurethanes, commonly synthesized with isocyanates, represent a significant portion of commercial polymers and find use in a wide variety of applications. The elimination of toxic isocyanates and heavy metal catalysts remains of great concern, both for the end user and the chemical processing facilities. Previous work suggests several

ways to avoid isocyanates in the creation of polyurethanes but often requires multiple synthetic steps or complex precursor chemicals to realize these polymers. Reactions of diols with 1-1'-carbonyldiimidazole and the subsequent additions of diamines results in polyurethane product without the need for heavy metal catalysts or multiple steps (**Scheme 10.1**). Furthermore, imidazole, commonly found in biological systems, functions as the only byproduct of the reaction. Purification revolves around the removal of this imidazole through washing with water to yield pure polyurethane.

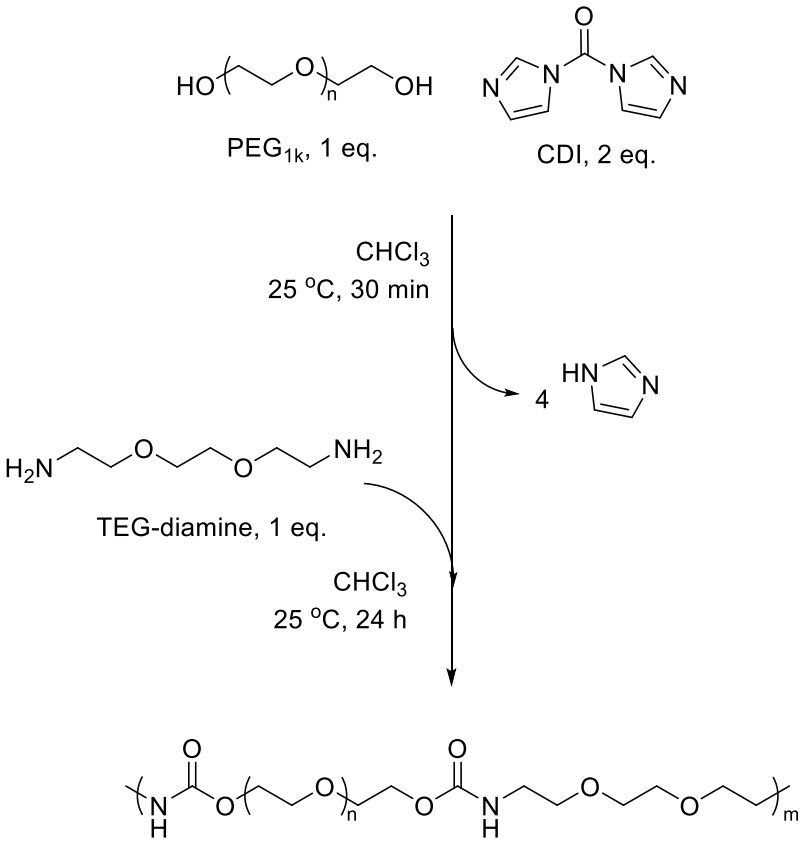

Scheme 10.1. Synthesis of PEG-based polyurethanes utilizing CDI reactions in one-pot.

^{1}H NMR confirms the successful polymerization utilizing CDI to form urethane bonds (**Figure 10.1)**. The peak at 5.5 ppm depends solely on the presence of urethane groups and serves to confirm successful polymerization. Furthermore, the purification process revealed the removal of residual imidazole created as a byproduct of the reaction as well as complete reaction from PEG-diimidazole to the polyurethane (**Figure 10.S1**). Furthermore, the order of addition in these studies ensures that the majority of polymer formed remains alternating between EDBA and the diol. The order of addition (or lack thereof) changes the number of possible reactions and functional groups formed (carbonates or ureas) between any two reactants. While a certain percentage of these reactions can occur during this stepwise synthesis, the majority of reactions occurring in the solution remain between diol and diamine to form polyurethane functional groups. This one-pot synthesis catalyzes the formation of isocyanate-free polyurethanes in high yield.

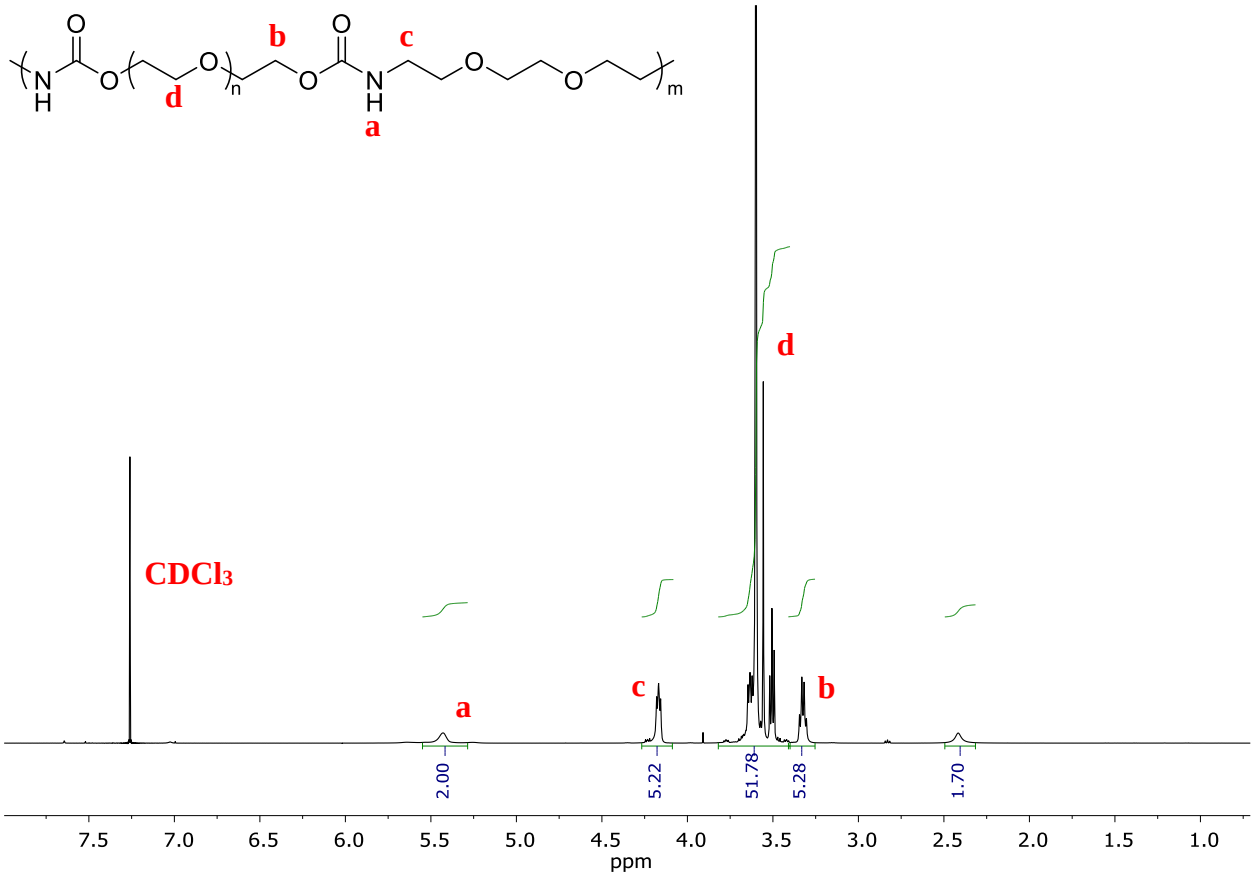

Figure 10.1. ^{1}H NMR reveals successful formation of urethane bonds from reactions with CDI.

While ^{1}H NMR serves as an effective tool to confirm the presence of urethane functionality, the polymeric properties derived from the reaction with CDI provide indications of conversion and molecular weight derived from these reactions. As seen in **Figure 10.2**, DSC reveals the presence of T_g's and T_m's characteristic of polymeric systems. The series of poly(PEG-urethane)s reveals the transition from amorphous poly(PEG_{400}-urethane) to semi-crystalline poly(PEG_{1k}-urethane) and poly(PEG_{4k}-urethane). Furthermore, the low levels of urethane functionality prevent significant deviations from neat PEG thermal properties. To address these concerns, polymerization of poly(1,4-BDM-urethane) demanded a higher number of coupling events to achieve

similar properties. The presence of a large melting endotherm in the first heat, followed by a quench-cooled amorphous polymer with a T_g of 13 °C aided in confirming CDI's ability to form higher molecular weight polymers (**Table 10.1**).

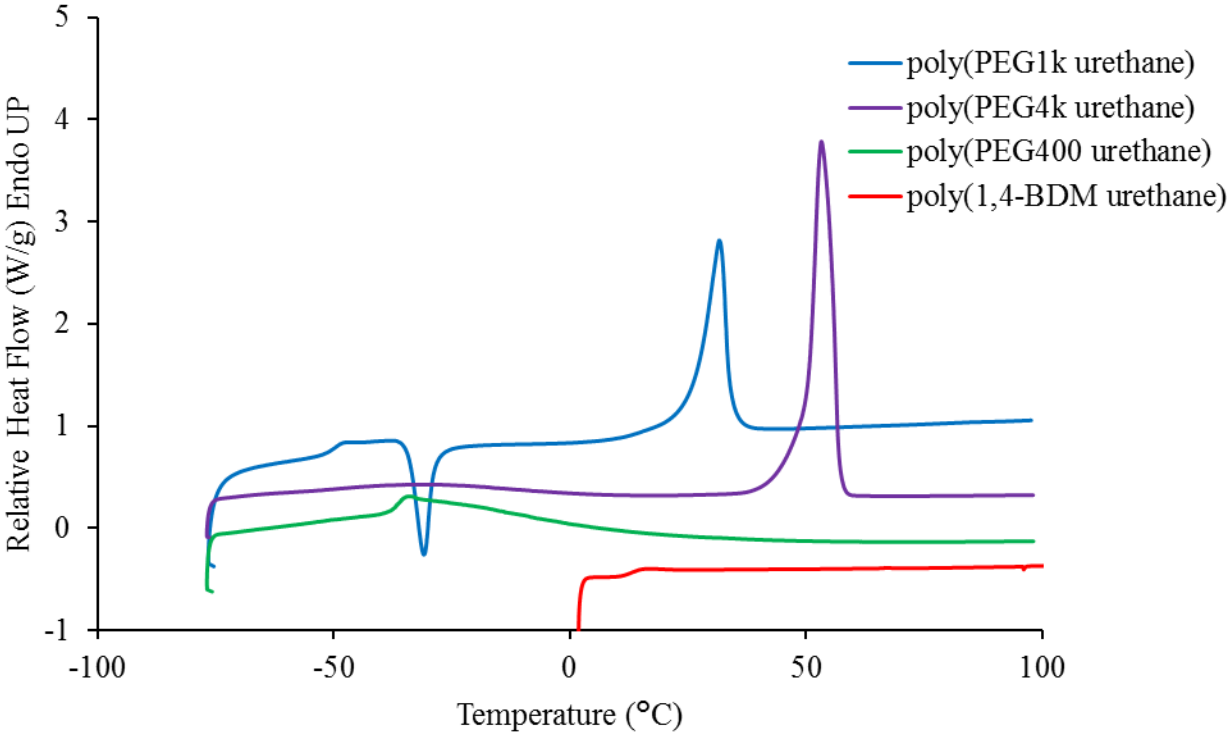

Figure 10.2. Differential scanning calorimetry reveals PEG dominance in thermal behavior of poly(PEG_{nk}-urethane)s. poly(1,4-BDM urethane) exhibits a crystalline melting peak during the first heat which is quenched during the cooling cycle.

Sample	***T_g (°C)***	***T_m (°C)***	***Wt % Urethane (%)***
Poly(PEG_{400} urethane)	-37	-	19.7
Poly(PEG_{1k} urethane)	-50	32	9.85
Poly(PEG_{4k} urethane)	-	53	2.81
Poly(1,4-BDM urethane)	13	-	35.1

Table 10.1. Polyurethanes reveal varied thermal behavior based on composition, calculated from DSC curves.

Melt rheological analysis of polyurethanes reveal an ordering of melt viscosity dependent on the weight percent urethane incorporation (**Table 10.1, Figure 10.3**). Both poly(PEG4k-urethane) and poly(1,4-BDM-urethane) experience shear thinning at 150 °C, highlighting the formation of higher molecular weight polymer. At these temperatures, poly(PEG-urethane) samples exhibit exceptionally low viscosity and modulus, requiring analysis at lower temperatures (**Figure 10.4**). When oscillated at 75 °C, poly(PEG-urethane) polymers exhibit ordering according to weight percent urethane incorporation, highlighting the role of hydrogen bonding in these systems. Furthermore, the melt viscosity at these temperatures aid in confirming higher molecular weight species compared to neat PEGs (**Figure 10.S2**). While failing to reach melt viscosities experienced by either polyureas or ionomers containing similar weight percent PEG, these polyurethanes reached significantly higher melt viscosities than neat PEG. While the hydrogen bonding in these polymers remains weaker than that experienced by other polymers, they represent the next generation in the formation of isocyanate-free polyurethanes.

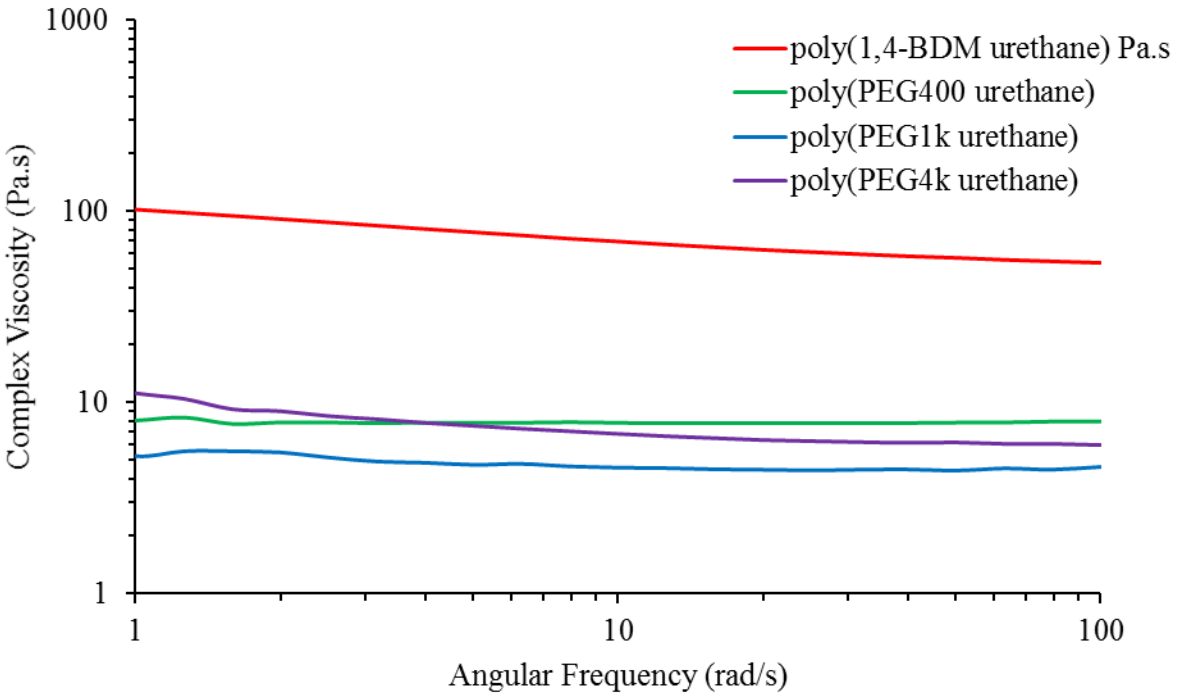

Figure 10.3. Rheological analysis reveals low melt viscosity at 150 °C of poly(PEG-urethane)s, suggesting weak interactions between urethane groups. The high concentration of urethane bonds in poly(1,4-BDM urethane) leads to a higher melt viscosity.

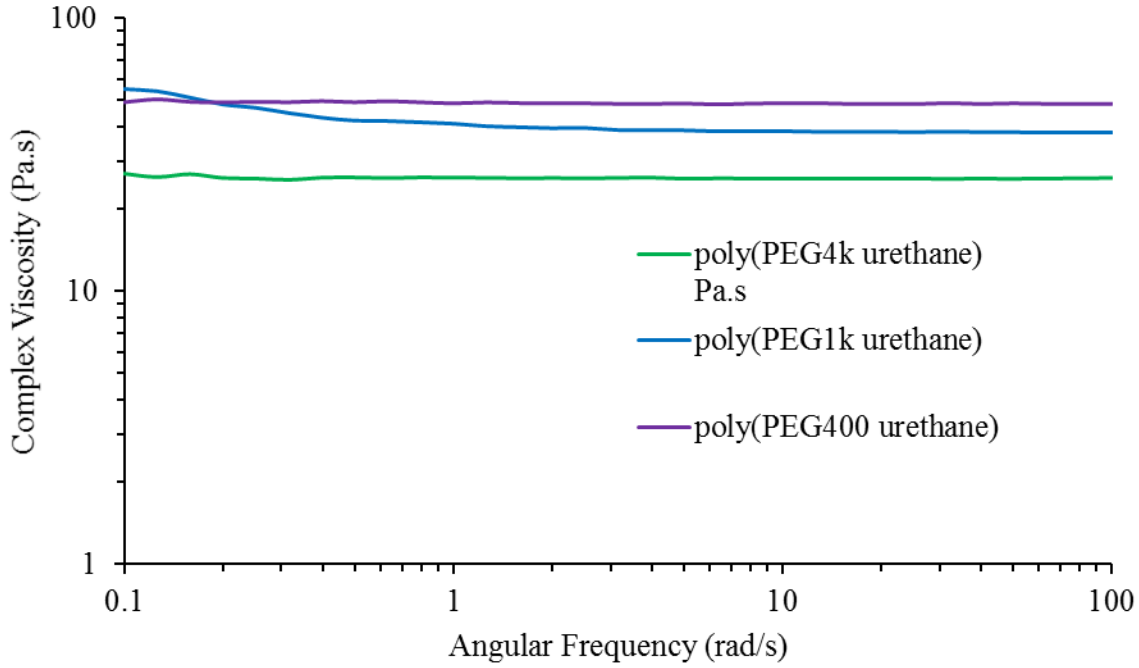

Figure 10.4. Rheological analysis at 75 °C reveals ordering of poly(PEG-urethane)s based on urethane content. The melt viscosity of these poly(PEG-urethane) samples approaches those seen in other PEG-based systems with supramolecular functionality.

Mechanical properties of polyurethanes remain of upmost importance for tailored performance. The characteristic hydrogen bonding motifs present in urethanes present unique mechanical properties extending above T_g's. As seen in **Figure 10.5**, DMA of poly(1,4-BDM urethane) highlights the extension of mechanical properties beyond the glass transition temperature in an amorphous quenched film. These properties, including those at room temperature, are dominated by hydrogen bonding and demonstrate the vast potential of these interactions to dictate polymeric properties. The potential to incorporate large amounts of hydrogen bonding into a polyurethane structure highlights the utility of the CDI reaction.

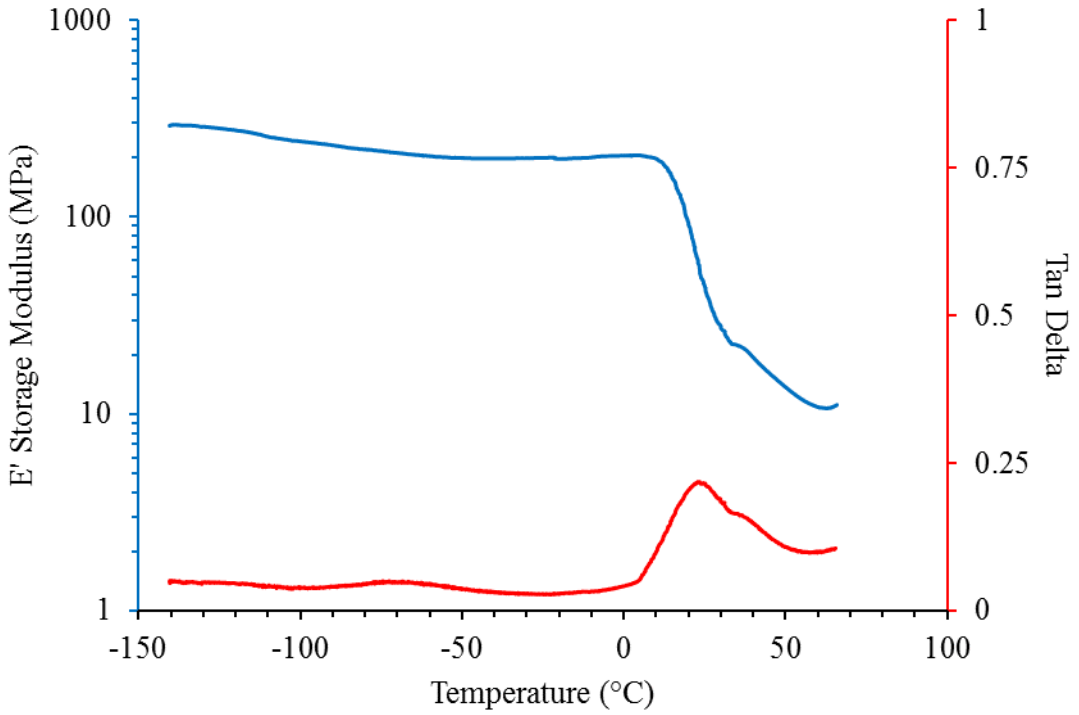

Figure 10.5. Dynamic mechanical analysis reveals extension of modulus above T_g, characteristic of hydrogen bonding's effect on mechanical properties.

10.5 Conclusions

Reactions between diols and diamines catalyzed by CDI proved fruitful in the formation of polyurethanes of significant molecular weight. Rheological analysis revealed a role in the weight percent urethane incorporation in the resulting melt viscosity. Furthermore, this method enables the formation of high molecular weight polyurethanes of varying functionality without the use of isocyanates or heavy metal catalysts.

10.6 Supplemental Information

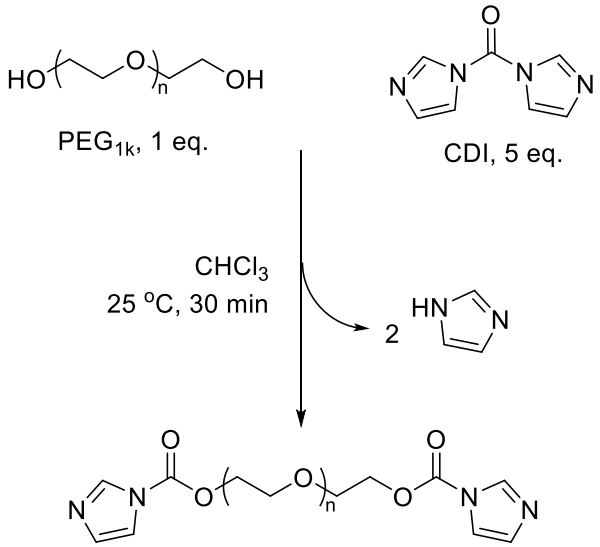

Scheme 10.S1. PEG reactions with CDI provide imidazole end-capped species.

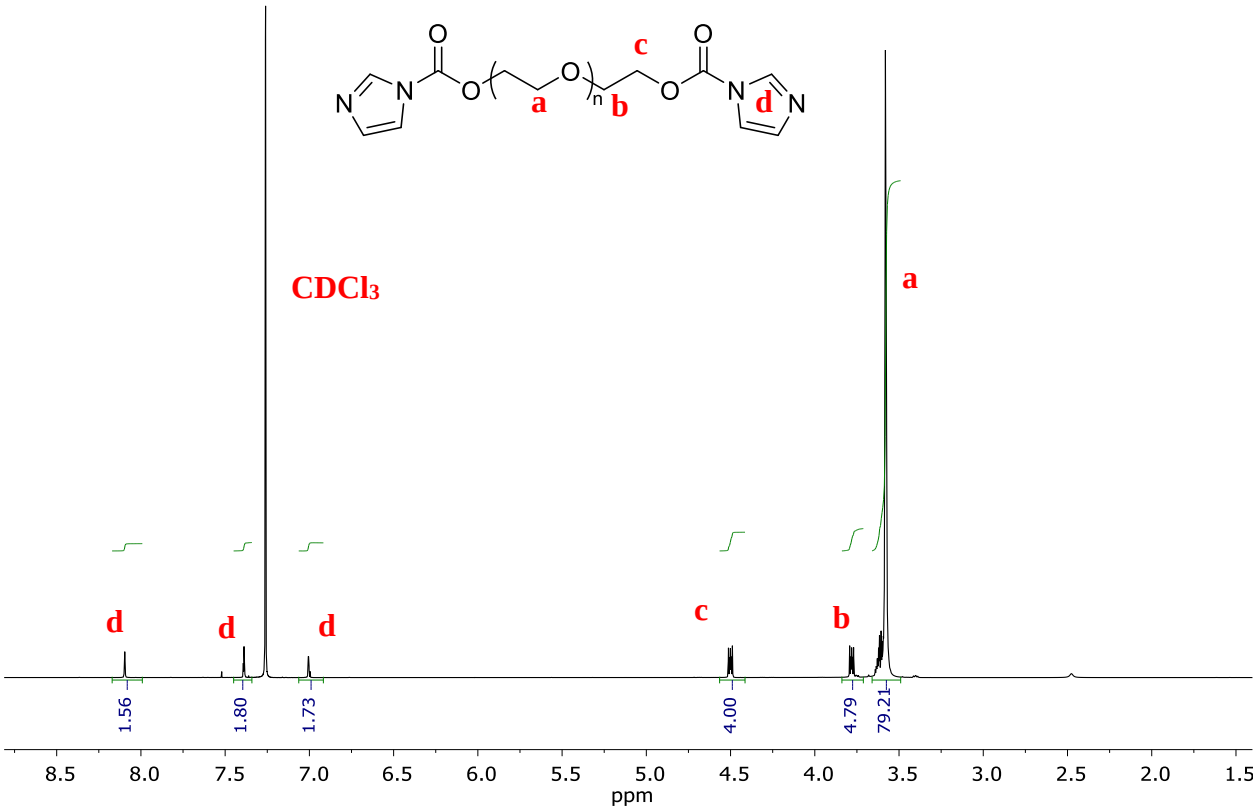

Figure 10.S1. Imidazole end-capped PEG confirms structure of diimidazole intermediate.

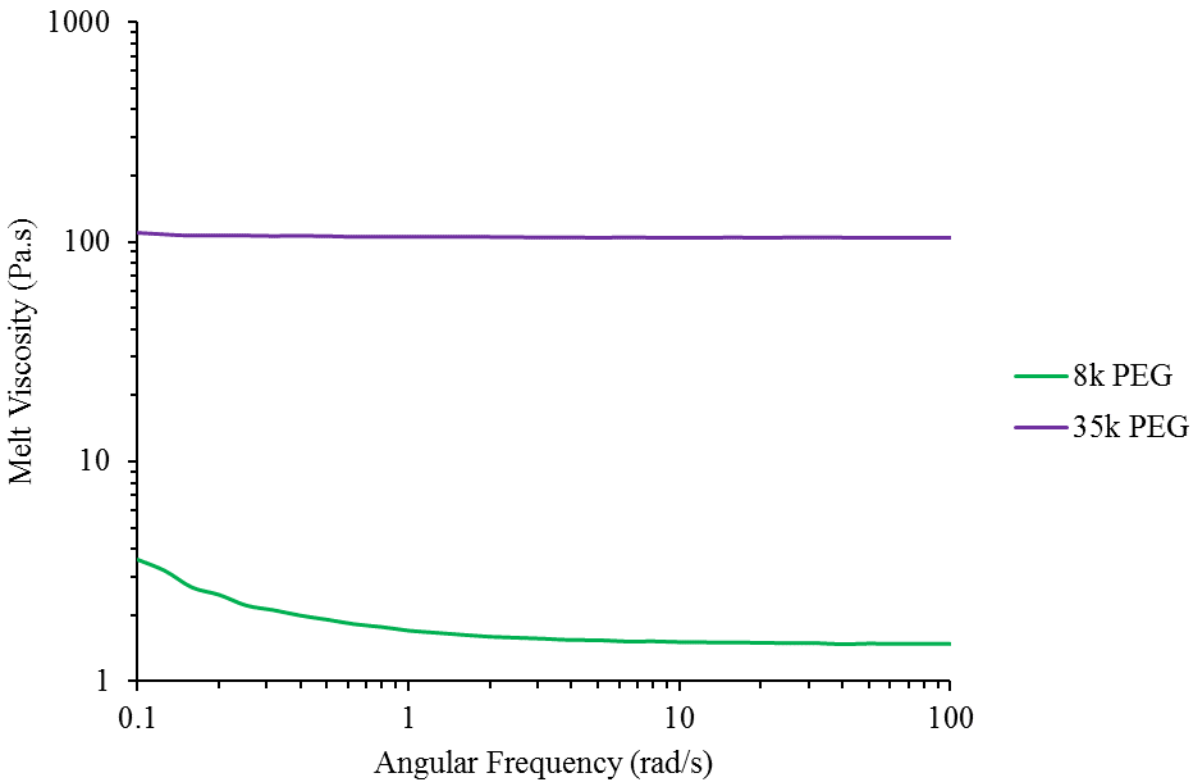

Figure 10.S2. Melt rheology of PEGs with varying molecular weight. Viscosity of 8k PEG remains below 10 Pa.s, highlighting the range of molecular weights generated by CDI reactions.

References

1. Nelson, A. M.; Long, T. E., Synthesis, Properties, and Applications of Ion-Containing Polyurethane Segmented Copolymers. *Macromolecular Chemistry and Physics* **2014,** 215, (22), 2161-2174.
2. Gao, R.; Zhang, M.; Dixit, N.; Moore, R. B.; Long, T. E., Influence of ionic charge placement on performance of poly (ethylene glycol)-based sulfonated polyurethanes. *Polymer* **2012,** 53, (6), 1203-1211.
3. Williams, S. R.; Wang, W.; Winey, K. I.; Long, T. E., Synthesis and morphology of segmented poly (tetramethylene oxide)-based polyurethanes containing phosphonium salts. *Macromolecules* **2008,** 41, (23), 9072-9079.
4. Maisonneuve, L.; Lamarzelle, O. a.; Rix, E.; Grau, E.; Cramail, H., Isocyanate-free routes to polyurethanes and poly (hydroxy urethane) s. *Chemical reviews* **2015,** 115, (22), 12407-12439.
5. Sheth, J. P.; Wilkes, G. L.; Fornof, A. R.; Long, T. E.; Yilgor, I., Probing the hard segment phase connectivity and percolation in model segmented poly (urethane urea) copolymers. *Macromolecules* **2005,** 38, (13), 5681-5685.
6. Rokicki, G.; Parzuchowski, P. G.; Mazurek, M., Non-isocyanate polyurethanes: synthesis, properties, and applications. *Polymers for Advanced Technologies* **2015,** 26, (7), 707-761.
7. Pyo, S.-H.; Persson, P.; Mollaahmad, M. A.; Sörensen, K.; Lundmark, S.; Hatti-Kaul, R., Cyclic carbonates as monomers for phosgene-and isocyanate-free polyurethanes and polycarbonates. *Pure and Applied Chemistry* **2011,** 84, (3), 637-661.
8. Zhang, K.; Nelson, A. M.; Talley, S. J.; Chen, M.; Margaretta, E.; Hudson, A. G.; Moore, R. B.; Long, T. E., Non-isocyanate poly (amide-hydroxyurethane) s from sustainable resources. *Green Chemistry* **2016,** 18, (17), 4667-4681.
9. Besse, V.; Auvergne, R.; Carlotti, S.; Boutevin, G.; Otazaghine, B.; Caillol, S.; Pascault, J.-P.; Boutevin, B., Synthesis of isosorbide based polyurethanes: An isocyanate free method. *Reactive and Functional Polymers* **2013,** 73, (3), 588-594.
10. Maier, S.; Loontjens, T.; Scholtens, B.; Mülhaupt, R., Carbonylbiscaprolactam: A Versatile Reagent for Organic Synthesis and Isocyanate-Free Urethane Chemistry. *Angewandte Chemie International Edition* **2003,** 42, (41), 5094-5097.
11. Ehler, K.; Orgel, L., N, N′-carbonyldiimidazole-induced peptide formation in aqueous solution. *Biochimica et Biophysica Acta (BBA)-Protein Structure* **1976,** 434, (1), 233-243.
12. Hill, A. R.; Orgel, L. E., Oligomerization of negatively-charged amino acids by carbonyldiimidazole. *Origins of Life and Evolution of Biospheres* **1996,** 26, (6), 539-545.
13. Mawad, D.; Stewart, E.; Officer, D. L.; Romeo, T.; Wagner, P.; Wagner, K.; Wallace, G. G., A single component conducting polymer hydrogel as a scaffold for tissue engineering. *Advanced Functional Materials* **2012,** 22, (13), 2692-2699.
14. Najemi, L.; Jeanmaire, T.; Zerroukhi, A.; Raihane, M., Isocyanate-free Route to Starch-graft-Polycaprolactone via Carbonyldiimidazole (CDI)-mediated End Group Conversion. *Starch-Stärke* **2010,** 62, (2), 90-101.
15. D'Addona, D.; Bochet, C. G., Preparation of carbamates from amines and alcohols under mild conditions. *Tetrahedron Letters* **2001,** 42, (31), 5227-5229.

16. Giammona, G.; Carlisi, B.; Pitarresi, G.; Fontana, G., Hydrophilic and hydrophobic polymeric derivatives of anti-inflammatory agents such as alclofenac, ketoprofen, and ibuprofen. *Journal of bioactive and compatible polymers* **1991,** 6, (2), 129-141.
17. Zalipsky, S., Functionalized poly (ethylene glycols) for preparation of biologically relevant conjugates. *Bioconjugate chemistry* **1995,** 6, (2), 150-165.
18. Ranucci, E.; Ferruti, P., A new synthetic method for amino-terminated poly (ethyleneglycol) derivatives. *Synthetic Communications* **1990,** 20, (19), 2951-2957.
19. Dennis, J. M.; Pekkanen, A. M.; Steinberg, L. I.; Long, T. E., Synthesis and Characterization of Isocyanate-free Biosourced Polyureas. *In Preparation* **2017**.
20. Pekkanen, A. M.; Zawaski, C.; Stevenson, A. T.; Dickerman, R.; Whittington, A. R.; Williams, C. B.; Long, T. E., Poly(ether ester) Ionomers as Water-Soluble Polymers for Material Extrusion Additive Manufacturing Processes. *ACS Applied Materials and Interfaces* **2017**.
21. Turecek, P. L.; Bossard, M. J.; Schoetens, F.; Ivens, I. A., PEGylation of biopharmaceuticals: a review of chemistry and nonclinical safety information of approved drugs. *Journal of pharmaceutical sciences* **2016,** 105, (2), 460-475.
22. Lee, H.; Venable, R. M.; MacKerell, A. D.; Pastor, R. W., Molecular dynamics studies of polyethylene oxide and polyethylene glycol: hydrodynamic radius and shape anisotropy. *Biophysical journal* **2008,** 95, (4), 1590-1599.
23. Kent, R. A.; Andersen, D.; Caux, P. Y.; Teed, S., Canadian water quality guidelines for glycols–An ecotoxicological review of glycols and associated aircraft anti-icing and deicing fluids. *Environmental Toxicology* **1999,** 14, (5), 481-522.

Chapter 11. Overall Conclusions

Design of biologically relevant materials, including both carbon and polymeric solutions, presents a grand challenge for scientists at the intersection of chemistry and biology. Prediction of biological responses to synthetic materials remains elusive, requiring testing of all new materials specific to their particular applications. In this work, water-soluble and dispersible materials proved valuable to direct biologic response, from microbiological chemotherapy response to release of ammonia from polymers to aid plant growth. Water-insoluble polymers proved useful as biological adhesives and showed potential as biodegradable wound glue.

During the development of novel materials, many reagents and byproducts of chemical reactions pose a great risk for toxicity, both in the end product and for workers handling the raw materials. The development of new methods for creating materials also drives the work of chemists at the intersection with biology. Isocyanate-free polyurethanes and polyureas, developed along without the need for heavy metal catalyst, provide next-generation polymers generated in a sustainable manner.

The intersection of chemistry and biology in the creation of new biological materials drives current and future research. Applications in biological fields present widespread materials needs requiring scientists that enable interdisciplinary research at this interface. These next-generation polymers enable material property and application development simultaneously, significantly enhancing innovation at the chemistry and biology interface.

List of Scientific Achievements:

- Developed and characterized the first theranostic carbon nanohorn, combining quantum dot imaging and cisplatin chemotherapy.
- Developed a protocol to measure peptide adhesion to fiber surfaces as a model to expensive peptide nucleic acids.
- Generated and characterized a water-soluble polymer suitable for low-temperature material extrusion additive manufacturing.
- Compared ionic interactions and hydrogen bonding's effect on poly(ethylene glycol) at low incorporations (< 5 wt %)
- Developed an ammonia-releasing polyurea capable of significant degradation within one month

Chapter 12. Suggested Future Work

12.1 Polyurea Tissue Scaffolds.

The creation of poly(urea)s without solvent or catalyst enables polymer formation without concern of biological toxicity. High molecular weight poly(urea)s formed through melt polycondensation provide water insoluble polymers suitable for biological tissue scaffolds. Incorporating low levels of hydrophobic chain stopper provides aliphatic carbon chain ends during the polymerization process which can be used to control molecular weight. Previous work in the Long group highlighted the role of long aliphatic chains to aid gene transfection from polymeric vectors, hypothesized through the insertion into biological membranes. Incorporation of two aliphatic chains of varying length provide insight into the role of aliphatic chain incorporation into cell attachment and subsequent proliferation. The urea functionality surrounding the aliphatic chains provides a hydrophilic backbone to potentially aid initial cell-scaffold interactions. The area of degraded tissue scaffolds, particularly with urea functionality, remains largely unknown and enables significant potential for regenerative medicine. The following experiments would enable this in-depth study:

- Synthesis of poly(urea)s with varied chain stopper (hexylamine vs. octadecylamine) (Scheme 12.1)

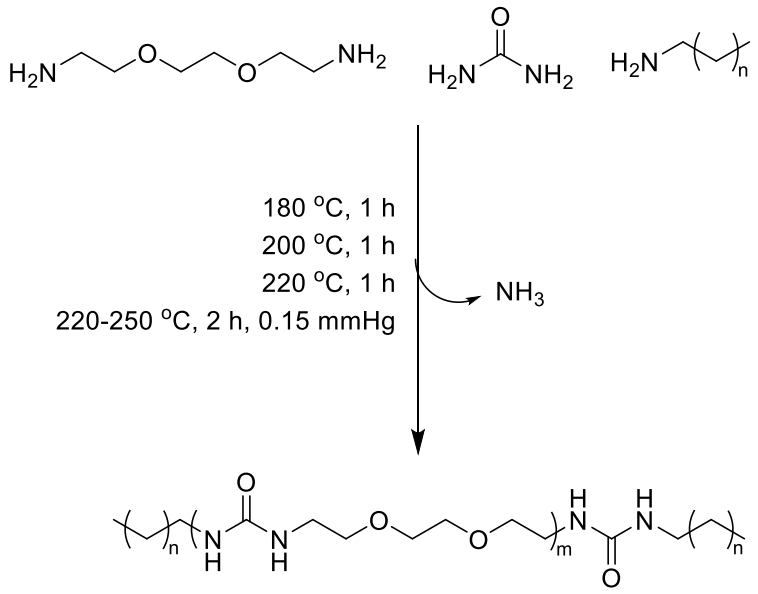

Scheme 12.1 Synthetic strategy for creation of polyureas with varied aliphatic chain ends through melt polymerization.

- Thermomechanical characterization to evaluate change in modulus at biological temperatures
- Evaluation of degradation or dissolution under biological media
- Probe cell attachment through cell seeding directly onto polymer films and analyze with both viability study and direct imaging
- Rheological characterization through frequency sweeps to probe the potential of these polymers for extrusion
- Extrusion additive manufacturing to create complex tissue scaffolds from filament to direct regenerative medicine

12.2 Fate of Polyureas in Soil

Upon completion of various poly(urea) synthesis and characterization, their fate and rate of ammonia release in soil samples remains unknown. In collaboration with

Professor Kang in Soil Science, the relative rate of ammonia release in complex media represents the logical next step. The rates presented in this work and others are an idealized system without compounding factors of bacteria and other enzymes found in common soil samples. Full investigation of nitrogen release and potential downstream effects of degraded polymer in soil samples requires further research. The following experiments would enable this in-depth study:

- A series of in-lab experiments controlling for soil type, water content, sunlight, and temperature to generate ammonia from polyureas should be conducted.
- The health of soil following long-term exposure to these polymers should also be examined. The quantity and quality of bacteria and minerals found in soil should be studied.
- The growth of plants before and after fertilization with these polymers should be examined. The health of plants should also be evaluated after exposure to polymers.
- Finally, large-scale field studies will provide relevant ecosystem effects that these polymers have on a larger scale. The concentration of ammonia in runoff water compared to typical nitrogen fertilizers will provide valuable insight into the utility of these polymers as nitrogen sources for plants.

12.3 PLGA-PEG Photocurable Oligomers for Degradable Tissue Scaffolds

Previous work developed by Evan Margaretta and myself reveals the creation of oligomers consisting of a poly(ethylene glycol) center block surrounded by poly(lactide-co-glycolide) outer blocks. The ring-opening polymerization readily occurs in the melt and can provide significant amounts of oligomer suitable for functionalization. The

functionalization with isocyanato ethyl methacrylate renders the oligomers photocurable while retaining a suitable viscosity for vat photopolymerization. The role of lactide and glycolide content on the realizable structural resolution, as well as the degradability of these scaffolds in aqueous media remains unknown. Furthermore, the ability of cells to recognize and attach successfully on the surface of these scaffolds remains unknown. The following experiments should be conducted to complete this in-depth study:

- A series of polymers synthesized with a short middle block PEG (Mw = 400 g/mol) and comparable molecular weight (~1100 g/mol) with varying lactide and glycolide content will provide significant variation in polymer structure. (**Scheme 12.2)**

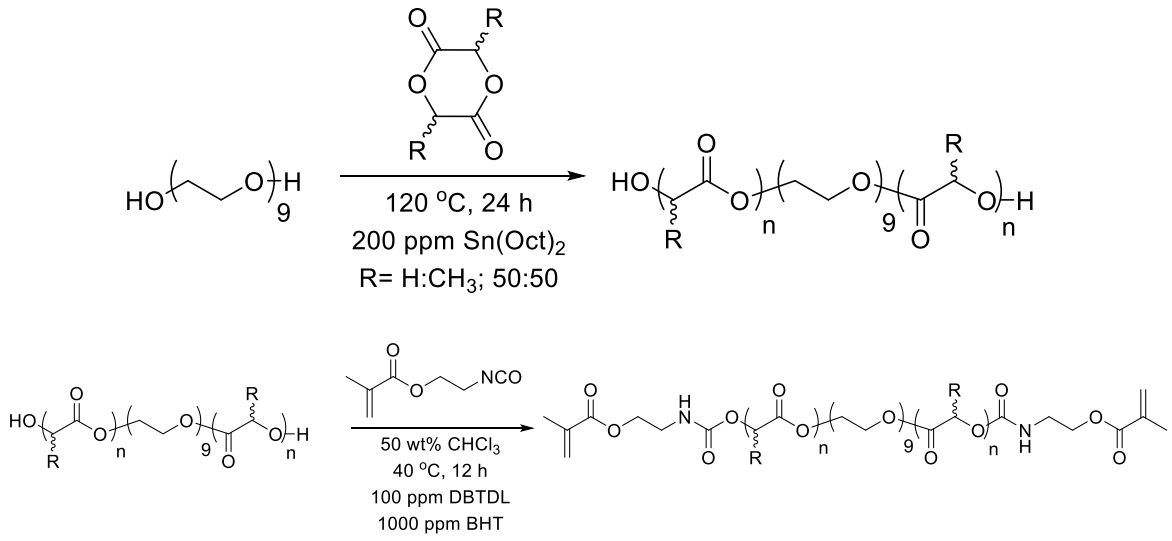

Scheme 12.2 Lactide ring-opening polymerization to form PLGA-PEG-PLGA triblock copolymers and their subsequent functionalization utilizing isocyanate coupling.

- Photocuring experiments, such as photo-DSC and photo-rheology, will probe the reaction kinetics of these photocuring reactions following functionalization to the methacrylate.

- Vat photopolymerization of the resulting oligomer will provide 3D structure. The resolution and printability of the resin can be fully examined. Furthermore, specified tissue scaffolds can be generated to examine the degradability of the resulting scaffold. (**Figure 12.1**)

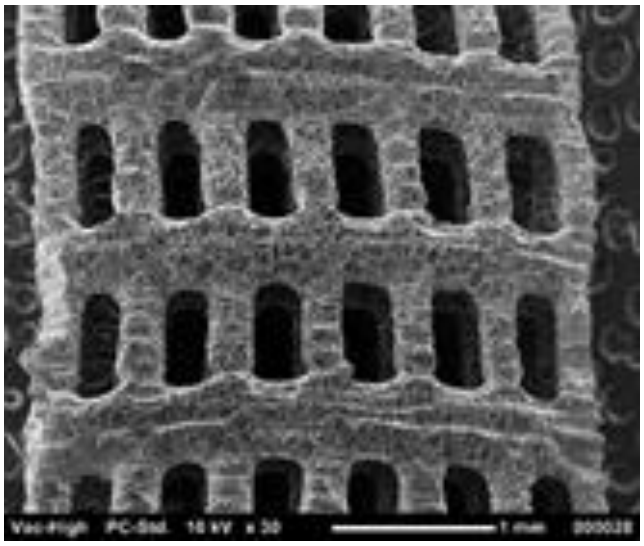

Figure 12.1 SEM imaging of a PLGA dimethacrylate shaped into a scaffold using vat photopolymerization. Refinement of printing parameters will provide insight into resolution and structure capabilities of this oligomer.

- Cell studies, including toxicity and cell attachment onto film surfaces, should first be conducted on photocured films. The potential degradation of the scaffolds should be probed with and without the presence of cells to determine the selective degradation of scaffolds in the presence of cellular stresses. Imaging of cells on these surfaces should also be conducted.

12.4 Further Exploration of CDI Reaction

Carbonyldiimidazole reacts readily with diols and diamines to form combinations of polyurea, polyurethanes, and polycarbonates. The order of addition of CDI and reactants directs the polymer structure and manipulation thereof could change properties drastically. Furthermore, the hard segment of polyurethanes can be tuned through the addition of varied diamines, as only properties of EDBA have been explored. Hard segments can be pre-formed *in situ* with the subsequent addition of soft segments to provide varied properties. The functional group tolerance and substitution has also yet to be fully explored in either polyureas, polyurethanes, or polycarbonates. The breadth of potential polymer structures generated through this reaction renders it a valuable tool for polymer chemists to develop new polymer structures without isocyanates. The following experiments should be conducted for this study:

- The order of addition of reactants to generate potential varied polymer structure should be probed. In particular the following compositions should be examined:
    - EDBA polyurea hard segments can be created by first introducing EDBA and CDI such that CDI end-capped hard segments are formed. Following this first step, the soft segment can then be added to link together hard segments. Solvent selection is key for these reactions to create segmented polyurethanes to ensure proper solvation throughout the reaction. (**Scheme 12.3**)

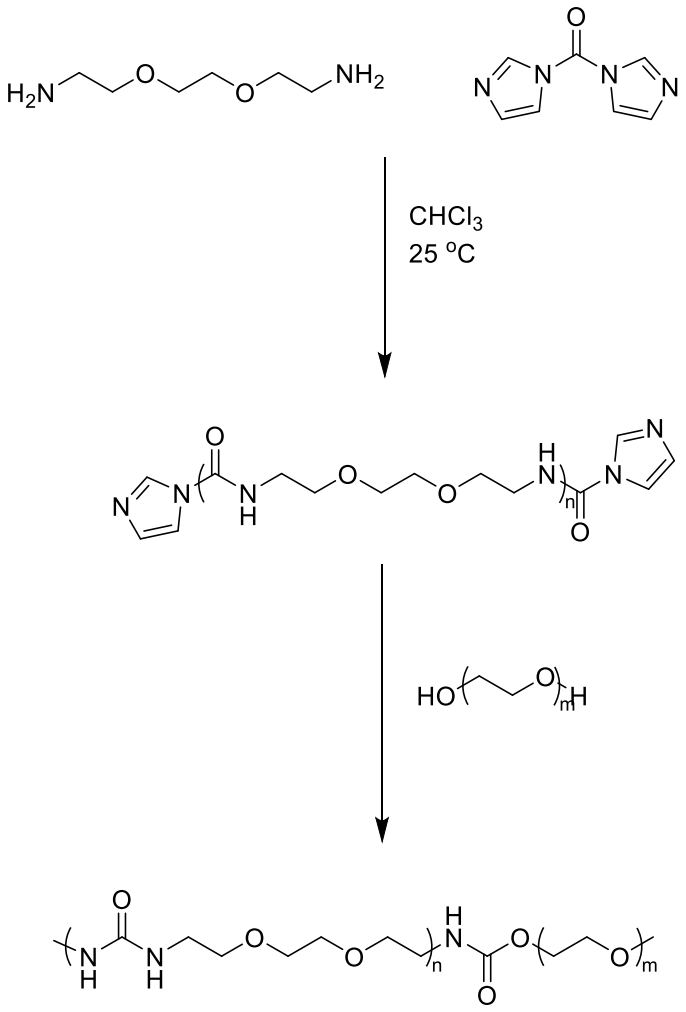

Scheme 12.3 Synthetic strategy to create segmented poly(urea urethane)s utilizing reaction with CDI.

- A polymer composed of only PEG oligomers linked by carbonate groups serves as a control for many PEG-based polymers presented here and provides a standard for degradation parameters for carbonate degradation.
- Molecular weight of polymers formed in the melt versus the CDI reaction of PEG-diamines to form polyureas should be fully characterized. Reaction parameters can be tuned to probe the limit of the CDI reaction in the formation of high molecular weight polymers.

- After polymerization, thermomechanical characterization of melt-pressed or solvent-cast films will provide important information as to the modulus of the polymers. Specifically, the extended plateau after T_g due to additional hydrogen bonding will aid in confirming the formation of segmented polyurethanes.
- For polyureas and polycarbonates, biodegradation should be examined. The effect of salts, cells, and mild acidic conditions on polymer degradation will provide further confirmation of polymer structure. The time scale of degradation will then dictate their biologic function, with applications ranging from tissue scaffolds for slow degrading polymers to drug delivery agents for those polymers that degrade in shorter time scales.
- Diacrylate formation from reactions of alcohol-containing acrylates and CDI provides a potential biodegradable diacrylate in one step. These diacrylates can be tuned to create diacrylates of suitable viscosity for vat photopolymerization additive manufacturing. Furthermore, the range of photo reactions and their printability provide another important metric. The ultimate degradation of the carbonate linkage to form degradable crosslinked networks for biological applications will prove vital. These set of reactions provides a facile degradable diacrylate synthesis with potential functional group tolerance to create novel diacrylates.